PolyPublie
Polytechnique Montréal

POLYTECHNIQUE MONTRÉAL
UNIVERSITÉ D'INGÉNIERIE

Titre: Title:	PEDOT:PSS-Based Soft Materials for Wearable Bioelectronic Applications
Auteur: Author:	Gayaneh Petrossian
Date:	2026
Type:	Mémoire ou thèse / Dissertation or Thesis
Référence: Citation:	Petrossian, G. (2026). PEDOT:PSS-Based Soft Materials for Wearable Bioelectronic Applications [Thèse de doctorat, Polytechnique Montréal]. PolyPublie. https://publications.polymtl.ca/76416/

Document en libre accès dans PolyPublie
Open Access document in PolyPublie

URL de PolyPublie: PolyPublie URL:	https://publications.polymtl.ca/76416/
Directeurs de recherche: Advisors:	Fabio Cicoira, & Hang Xu
Programme: Program:	Génie des matériaux

Ce fichier a été téléchargé à partir de PolyPublie, le dépôt institutionnel de Polytechnique Montréal
This file has been downloaded from PolyPublie, the institutional repository of Polytechnique Montréal

https://publications.polymtl.ca

POLYTECHNIQUE MONTRÉAL

affiliée à l'Université de Montréal

PEDOT:PSS-Based Soft Materials for Wearable Bioelectronic Applications

GAYANEH PETROSSIAN

Département de génie chimique

Thèse présentée en vue de l'obtention du diplôme de *Philosophiæ Doctor*

Génie des matériaux

Mai 2026

© Gayaneh Petrossian, 2026.

POLYTECHNIQUE MONTRÉAL

affiliée à l'Université de Montréal

Cette thèse intitulée :

PEDOT:PSS-Based soft Materials for Wearable Bioelectronic Applications

présentée par **Gayaneh PETROSSIAN**

en vue de l'obtention du diplôme de *Philosophiæ Doctor*

a été dûment acceptée par le jury d'examen constitué de :

Daria Camilla BOFFITO, présidente
Fabio CICOIRA, membre et directeur de recherche
Hang XU, membre et codirecteur de recherche
Sampada BODKHE, membre
Hyun-Joong CHUNG, membre externe

DEDICATION

Dedicated to my late father, my biggest cheerleader

ACKNOWLEDGEMENTS

I would like to thank my supervisor, Professor Fabio Cicoira, for the opportunity to conduct my doctoral research in his group at Polytechnique Montréal. I appreciate the independence I had throughout this work to develop my research ideas and grow as a researcher. Your support over the years, as well as your confidence in my research abilities, allowed me to carry out the work presented in this thesis. I would also like to thank my co-supervisor, Professor Hang Xu, whom I began working with later in my PhD. Thank you for believing in my vision for the 3D-printed conductive foams and for your support in advancing this part of the research.

I would also like to thank the members of the Cicoira research group, past and present, for creating such a stimulating and supportive research environment. Working alongside such talented and collaborative colleagues made my PhD an incredibly rewarding experience. I am grateful for the many discussions, technical advice, and shared moments in the lab that helped make this project possible. I would also like to especially thank Dr. Jiaxin Fan, whose guidance and support during my early time in the lab were incredibly valuable.

I would like to acknowledge the professors, researchers, technicians, and administrative staff whose dedication contributes to a supportive academic environment that enables students to thrive.

I gratefully acknowledge the generous support of the Vanier Canada Graduate Scholarship, which made this research possible and supported my doctoral studies. I would also like to acknowledge the support of MITACS through a MITACS internship in collaboration with EERS Global, which provided valuable industry exposure and additional support during my doctoral studies.

I would also like to express my heartfelt gratitude to my family: my late father, my mother, my sister, my brother, my brother-in-law, and my sister-in-law. Your support and encouragement have always been a major source of strength in my life. I would especially like to acknowledge my late father, whose constant encouragement throughout my life inspired me to pursue this PhD. He was always my biggest cheerleader, believing in me even before I believed in myself. Although he is no longer here to see this milestone, his influence and support remain with me every day, and I miss him deeply.

Last but not least, I would like to express my deepest gratitude to my husband, Tanner, for being my greatest source of strength throughout this journey. Your constant support, patience, and

encouragement carried me through the many challenges that came with pursuing this PhD. During the most demanding times, your reassurance and belief in me helped me keep moving forward. Whether through long conversations, words of motivation, or simply being there when I needed it most, you made this journey far more manageable. I am profoundly grateful for everything you have done and for always believing in my abilities.

RÉSUMÉ

Les technologies électroniques et bioélectroniques portables transforment rapidement la manière dont les signaux physiologiques sont surveillés, tant dans les environnements cliniques que dans la vie quotidienne. La mesure continue de signaux tels que l'électroencéphalographie (EEG), l'électromyographie (EMG) et l'électrocardiographie (ECG) nécessite des matériaux d'électrode capables de maintenir des performances électriques fiables tout en s'adaptant à la surface souple et dynamique du corps humain. Les systèmes d'électrodes conventionnels, en particulier les électrodes rigides Ag/AgCl qui reposent sur des gels conducteurs pour améliorer le contact peau-électrode, présentent souvent des limitations telles qu'une faible conformité mécanique, un inconfort lors d'une utilisation prolongée et une dégradation de la qualité du signal lorsque le gel se dessèche avec le temps. Ces défis ont motivé le développement de matériaux conducteurs souples, capables d'assurer un contact stable et confortable avec les tissus biologiques. Parmi les matériaux étudiés pour la bioélectronique portable, les polymères intrinsèquement conducteurs ont émergé comme des candidats prometteurs en raison de leur conductivité électronique et ionique combinée, de leur flexibilité mécanique et de leur facilité de mise en œuvre en solution.

Le poly(3,4-éthylènedioxythiophène):poly(styrène sulfonate) (PEDOT:PSS) est l'un des polymères conducteurs les plus étudiés pour les applications bioélectroniques. Ce matériau est constitué du polymère conducteur chargé positivement PEDOT stabilisé par le polyélectrolyte chargé négativement poly(styrène sulfonate), ce qui permet la formation de dispersions aqueuses stables et facilite des méthodes de mise en œuvre à grande échelle. Le PEDOT:PSS présente plusieurs propriétés qui le rendent particulièrement attrayant pour les applications de détection portables, notamment une conductivité électrique modulable, une bonne stabilité chimique et une compatibilité avec une large gamme de matrices polymères. Ces caractéristiques ont conduit à son utilisation répandue dans les domaines de l'électronique organique, des capteurs, des dispositifs énergétiques et des interfaces biomédicales.

Cette thèse explore le développement de nouvelles architectures matérielles à base de PEDOT:PSS conçues pour répondre aux exigences mécaniques et électriques des systèmes de détection portables. Plus précisément, ce travail examine comment l'ingénierie des structures des polymères conducteurs peut permettre le développement de nouvelles classes de matériaux conducteurs souples, adaptés aux dispositifs électroniques portables et aux interfaces bioélectroniques. Les

travaux présentés dans cette thèse combinent une analyse de la littérature avec la conception et la caractérisation expérimentale de deux systèmes distincts à base de PEDOT:PSS : des mousses syntactiques conductrices et des fibres de xérogel conductrices hautement extensibles.

La première partie de cette thèse présente une revue approfondie des matériaux d'électrode utilisés pour l'électroencéphalographie (EEG), avec un focus particulier sur les systèmes EEG du cuir chevelu, du front et de l'oreille. L'EEG est une technique largement utilisée pour surveiller évaluer l'activité neuronale, mais les technologies d'électrodes conventionnelles se basent souvent sur des gels conducteurs et des matériaux rigides, ce qui limite le confort et l'utilisation à long terme pour les patients. Les nouveaux systèmes EEG portables cherchent à surmonter ces limitations en développant des électrodes sèches et souples capables de maintenir un contact électrique stable avec la peau. Cette revue discute de l'évolution des technologies d'électrodes EEG et met en évidence l'importance croissante des matériaux conformables pour les systèmes de surveillance neuronale portables et discrets, en particulier dans les configurations émergentes telles que l'EEG auriculaire

S'appuyant sur les défis identifiés dans la littérature, la deuxième partie de cette thèse se concentre sur le développement de matériaux conducteurs poreux basés sur des mousses syntactiques PEDOT:PSS structurées par des microspheres, une classe de mousses dans lesquelles des microsphères creuses sont intégrées dans une matrice polymère afin de créer une structure poreuse légère. Dans cette approche, le PEDOT:PSS est synthétisé à la surface de microsphères polymères, qui sont ensuite incorporées dans une matrice polymère thermoplastique, le poly(ε-caprolactone), afin de créer des mousses conductrices légères avec une porosité modulable. Les mousses syntactiques obtenues présentent une architecture unique dans laquelle les enveloppes conductrices de PEDOT:PSS qui entourent les microsphères forment des voies conductrices interconnectées au sein de la structure poreuse. En contrôlant la fraction volumique de microsphères, les propriétés électriques et mécaniques des mousses peuvent être ajustées sur une large plage. Ces matériaux présentent des modules élastiques faibles comparables à ceux des tissus biologiques mous tout en conservant une conductivité électrique adaptée aux applications de détection bioélectronique. De plus, l'architecture des mousses syntactiques permet leur compatibilité avec des procédés thermoplastiques et des techniques de fabrication additive. Des filaments conducteurs dérivés de ces mousses ont été utilisés avec succès pour la fabrication par dépôt de fil fondu (fused filament), démontrant la possibilité de produire des structures conductrices personnalisables par impression

3D. En plus de leur structure légère et de leurs propriétés modulables, ces mousses présentent une recyclabilité par reconditionnement chimique et thermique, démontrant leur potentiel pour une électronique souple durable.

La dernière partie de cette thèse examine le développement de fibres de xérogel conductrices hautement extensibles basées sur des réseaux polymères de PEDOT:PSS. Dans ce système, le poly(vinyl alcool) (PVA), le PEDOT:PSS et le glycérol sont combinés pour former des hydrogels conducteurs par un procédé de congélation-décongélation induisant une réticulation physique au sein du réseau polymère. Un traitement ultérieur au borax introduit des réticulations supplémentaires, produisant une structure à double réseau qui améliore la robustesse mécanique tout en préservant la fonctionnalité électrique. Après une déshydratation dans des conditions ambiantes, les fibres de xérogel obtenues présentent des propriétés mécaniques exceptionnelles, notamment des résistances à la traction supérieures à 15 MPa et des allongements dépassant 1100 %. Parallèlement, les fibres conservent une conductivité électrique stable et présentent des variations reproductibles de résistance en fonction de la déformation. Ces caractéristiques permettent aux fibres de fonctionner comme des capteurs de déformation hautement sensibles capables de détecter une large gamme de mouvements humains, notamment ceux des doigts, du poignet et du coude. Ces résultats mettent en évidence le potentiel des xérogels PEDOT:PSS à double réseau comme matériaux conducteurs mécaniquement robustes et hautement extensibles pour des applications de détection portable.

Dans l'ensemble, cette thèse démontre que le PEDOT:PSS peut être utilisé sous une grande variété de formes structurales au-delà des films minces conventionnels, ouvrant ainsi de nouvelles perspectives pour le développement de matériaux conducteurs souples. Grâce à la conception de mousses conductrices structurées par des microsphères, et de fibres de xérogel à double réseau, ce travail montre comment l'ingénierie structurale peut être utilisée pour ajuster simultanément les propriétés mécaniques, les performances électriques et la facilité de mise en œuvre. Ces résultats contribuent au domaine en pleine expansion de l'électronique souple et proposent de nouvelles stratégies pour le développement de matériaux adaptés aux dispositifs bioélectroniques portables de prochaine génération.

ABSTRACT

Wearable electronic and bioelectronic technologies are rapidly transforming the way physiological signals are monitored in both clinical and everyday environments. Continuous measurement of signals such as electroencephalography (EEG), electromyography (EMG), and electrocardiography (ECG) requires electrode materials that can maintain reliable electrical performance while conforming to the soft and dynamic surface of the human body. Conventional electrode systems, particularly rigid Ag/AgCl electrodes that rely on conductive gels to improve electrode-skin contact, often suffer from limitations such as poor mechanical compliance, discomfort during prolonged use, and degradation of signal quality as the gel dries over time. These challenges have motivated significant research efforts toward the development of soft conductive materials capable of maintaining stable and comfortable contacts with biological tissues. Among the materials investigated for wearable bioelectronics, intrinsically conductive polymers have emerged as promising candidates due to their combined electronic and ionic conductivity, mechanical flexibility, and solution processability.

Poly(3,4-ethylenedioxythiophene):poly(styrene sulfonate) (PEDOT:PSS) is one of the most widely studied conductive polymers for bioelectronic applications. The material consists of the positively charged conductive polymer PEDOT stabilized by the negatively charged polyelectrolyte poly(styrene sulfonate), which enables the formation of stable aqueous dispersions and facilitates scalable processing methods. PEDOT:PSS exhibits several properties that make it attractive for wearable sensing applications, including tunable electrical conductivity, chemical stability, and compatibility with a wide range of polymer matrices. These characteristics have led to its widespread use in organic electronics, sensors, energy devices, and biomedical interfaces.

This thesis investigates the development of novel PEDOT:PSS-based material architectures designed to address the mechanical and electrical requirements of wearable sensing systems. In particular, the work explores how structural engineering of conductive polymers can enable new classes of soft conductive materials suitable for wearable electronics and bioelectronic interfaces. The research presented in this thesis combines literature analysis with the design and experimental characterization of two distinct PEDOT:PSS-based material systems: conductive syntactic foams and highly stretchable and conductive xerogel fibers.

The first part of this thesis presents a comprehensive review of electrode materials used for electroencephalography (EEG), with a particular focus on scalp, forehead, and ear-centered EEG systems. EEG is a widely used technique for monitoring neural activity, but conventional electrode technologies often rely on conductive gels and rigid materials that limit comfort and long-term usability. Emerging wearable EEG systems aim to overcome these limitations by developing dry and soft electrode materials capable of maintaining stable electrical contact with the skin. The review discusses the evolution of EEG electrode technologies and highlights the increasing importance of conformable materials for wearable and unobtrusive neural monitoring systems, particularly in emerging configurations such as ear-centered EEG.

Building on the challenges identified in the literature, the second part of this thesis focuses on the development of porous conductive materials based on microsphere-templated PEDOT:PSS syntactic foams, a class of foams in which hollow microspheres are embedded within a polymer matrix to create a lightweight porous structure. In this approach, PEDOT:PSS was synthesized on the surface of polymer microspheres, which were subsequently incorporated into a thermoplastic polymer matrix, poly(ε-caprolactone), to create lightweight conductive foams with tunable porosity. The resulting syntactic foams exhibit a unique architecture in which the conductive PEDOT:PSS shells surrounding the microspheres form electrically connected pathways within the porous structure. By controlling the volume fraction of the microspheres, the electrical and mechanical properties of the foams can be tuned over a wide range. These materials demonstrate low elastic moduli comparable to soft biological tissues while maintaining electrical conductivity suitable for bioelectronic sensing applications. Furthermore, the syntactic foam architecture enables compatibility with thermoplastic processing techniques and additive manufacturing. Conductive filaments derived from these foams were successfully used for fused filament fabrication, demonstrating the feasibility of producing customizable conductive structures through 3D printing. In addition to their lightweight structure and tunable properties, the foams exhibit recyclability through both chemical and thermal reprocessing, highlighting their potential for sustainable soft electronics.

The final part of this thesis investigates the development of highly stretchable conductive xerogel fibers based on PEDOT:PSS polymer networks. In this system, poly(vinyl alcohol) (PVA), PEDOT:PSS, and glycerol were combined to form conductive hydrogels through a freeze-thaw process that induces physical crosslinking within the polymer network. Subsequent treatment with

borax introduces additional crosslinks, producing a double-network structure that enhances mechanical robustness while maintaining electrical functionality. After dehydration under ambient conditions, the resulting xerogel fibers exhibit exceptional mechanical properties, including tensile strengths exceeding 15 MPa and elongations greater than 1100%. At the same time, the fibers maintain stable electrical conductivity and demonstrate reproducible strain-dependent resistance changes. These characteristics enable the fibers to function as highly sensitive strain sensors capable of detecting a wide range of human motions, including finger, wrist, and elbow movements. The results highlight the potential of double-network PEDOT:PSS xerogels as mechanically robust and highly stretchable conductive materials for wearable sensing applications.

Overall, this thesis demonstrates that PEDOT:PSS can be engineered into a wide variety of structural forms beyond conventional thin films, enabling new opportunities for the development of soft conductive materials. Through the design of microsphere-templated conductive foams and double-network xerogel fibers, this work illustrates how structural design can be used to simultaneously tailor mechanical properties, electrical performance, and processability. These findings contribute to the growing field of soft electronics and provide new strategies for developing materials suitable for next-generation wearable bioelectronic devices.

TABLE OF CONTENTS

LIST OF TABLES

LIST OF FIGURES

LISTE OF SYMBOLS AND ABBREVIATIONS

Ag/AgCl	Silver/silver chloride
APS	Ammonium persulfate
BCI	Brain-computer interfaces
CNC	Computer numerical control
CNTs	Carbon nanotubes
DC	Direct current
DEG	Diethylene glycol
DMSO	Dimethyl sulfoxide
DSC	Differential scanning calorimetry
ECG	Electrocardiography
EDOT	3,4-Ethylenedioxythiophene
EDS	Energy-dispersive spectrometer
EEG	Electroencephalography
EG	Ethylene glycol
EMG	Electromyography
EMI	Electromagnetic interference
EOEC	Eyes-open/eyes-closed
EOG	Electrooculography
ESD	Equilibrium swelling degree
FFF	Fused filament fabrication
F-T	Freeze-thaw
FTIR	Fourier-transform infrared

GF	Gauge factor
HCl	Hydrochloric acid
ICPS	Intrinsically conductive polymers
ITE	In-the-ear
LED	Light-emitting diode
MRI	Magnetic Resonance Imaging
PCB	Printed circuit board
PCL	Poly(ε-caprolactone)
PDA	Polydopamine
PDMS	Polydimethylsiloxane
PEDOT:PSS	Poly(3,4-ethylenedioxythiophene):poly(styrene sulfonate)
PEG	Polyethylene glycol
PET	Positron Emission Tomography
PLA	Polylactic acid
PolyAMPS	Poly(2-acrylamido-2-methyl-1-propanesulfonic acid)
PU	Polyurethane
PUD	Polyurethane diol
PVA	Polyvinyl alcohol
PVP	Polyvinylpyrrolidone
PSS	Poly(4-styrenesulfonic acid) sodium salt
RGO	Reduced graphene oxide
SEM	Scanning Electron Microscopy
SNR	Signal-to-noise ratio

TGA	Thermogravimetric analysis
TPU	Thermoplastic polyurethane

LIST OF APPENDICES

CHAPTER 1INTRODUCTION

1.1 Wearable electronics

Wearable electronics have emerged as a transformative class of technologies enabling continuous, real-time monitoring of physiological and biomechanical signals directly from the human body. By integrating electronics into soft, body-conformal platforms, these systems allow long-term health tracking outside of clinical settings, supporting applications in personalized health monitoring [1], [2], rehabilitation [3], sports performance [4], and human-machine interfacing [5], [6]. These wearable devices must operate under repeated mechanical deformation while maintaining stable electrical performance and user comfort.

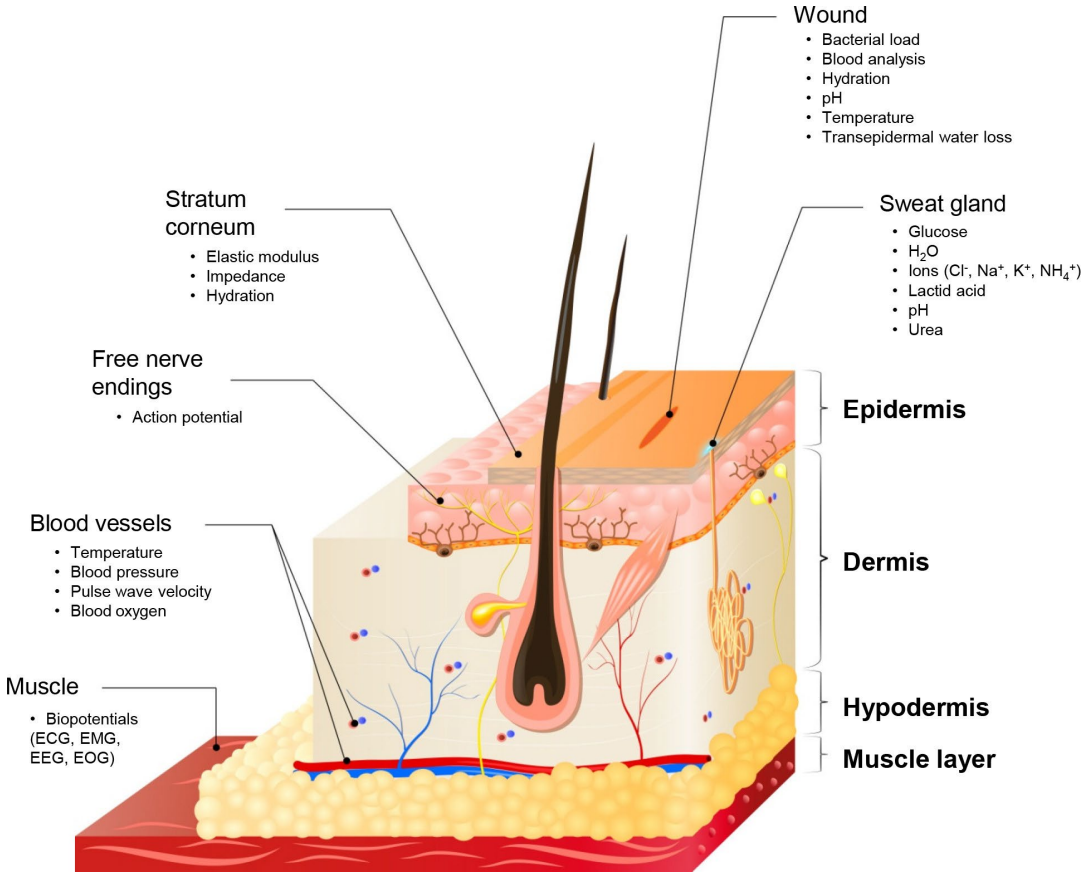

Figure 1-1 Schematic of skin anatomy and representative physiological signals accessible for bioelectronic monitoring. Reproduced with permission from [7].

The human skin serves as the primary interface for most wearable systems. Mechanically, skin is a soft, viscoelastic, and multilayered tissue whose Young's modulus varies significantly across its

structure. Reported values range from approximately 2-80 kPa in the dermis to 0.1-4 MPa in the epidermis, depending on factors such as age, hydration level, skin type, and overall health [8], [9]. Electrically, the skin acts as a barrier that can distort physiological signals before they reach an external sensor [10]. The outer stratum corneum, composed of relatively dry cells, contributes significantly to contact resistance, while the deeper hydrated layers provide more conductive pathways [11]. Physiological signals generated within the body must propagate through this heterogeneous interface before detection by an external sensor. Reliable signal acquisition therefore depends critically on intimate conformal contact, low interfacial impedance, and mechanical compatibility between the device and the skin. Figure 1.1 summarizes the skin's layered structure and key physiological signal sources, highlighting how surface hydration and the stratum corneum dominate electrode impedance and ultimately influence the fidelity of recorded biopotentials.

Despite these advances, the performance and long-term reliability of wearable bioelectronic devices strongly depend on the mechanical compatibility between the electronic components and the human body. Biological tissues are inherently soft, dynamic, and continuously deforming during daily activities such as movement, breathing, and muscle contraction. Conventional rigid electronic materials often fail to conform to these soft and curved surfaces, leading to poor contact, motion artifacts, and user discomfort. Consequently, the development of soft and mechanically compliant electrode materials has become a critical focus in wearable bioelectronics.

1.2 Electrode materials for soft interfaces

The emergence of soft mechanical sensors can be viewed as a continuation of decades of research on conventional mechanical sensing technologies that were historically developed using rigid electronic platforms. Early mechanical sensors were primarily fabricated from silicon-based microelectronics using established manufacturing processes and have been widely utilized since the 1970s in applications ranging from aerospace systems to medical equipment [12]. Although these devices offer high sensitivity and reliability, their rigid structures limit their ability to interface effectively with soft and deformable biological tissues. As interest in wearable and biomedical technologies has grown, significant efforts have been directed toward developing mechanically compliant sensors capable of adapting to dynamic physiological environments. These soft and deformable sensing systems enable improved contact with biological surfaces, more

accurate detection of mechanical signals, and greater comfort and compatibility during long-term use in biomedical applications. Figure 1-2 summarizes the key design considerations for soft on-skin electrodes, highlighting the interplay between material selection, fabrication approaches, and device requirements needed to achieve conformability, low impedance, biocompatibility, and long-term stability.

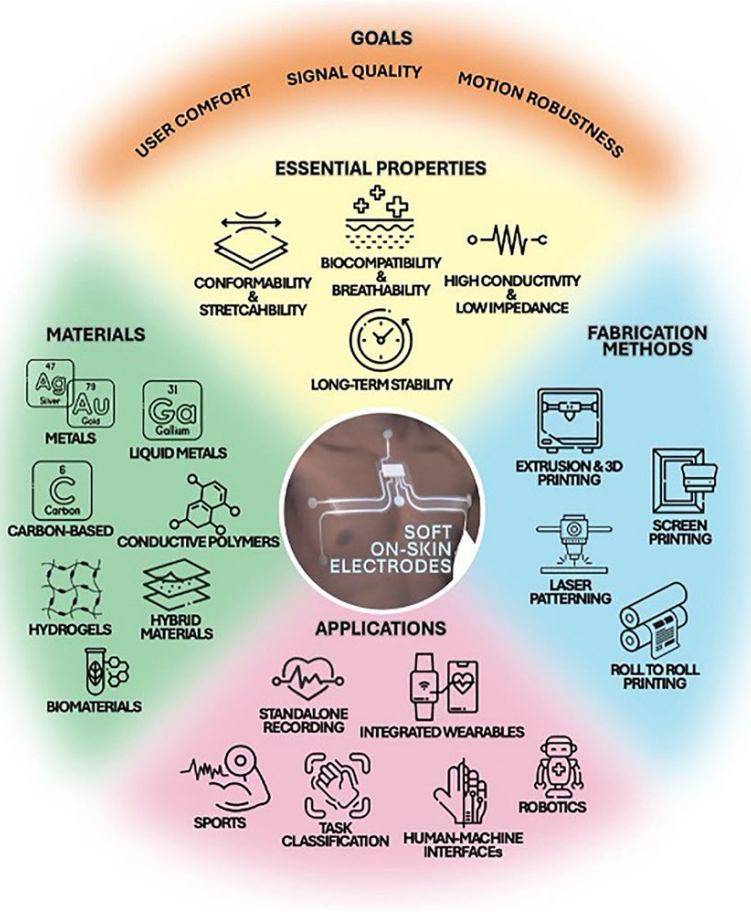

Figure 1-2 Overview of soft on-skin electrodes for wearable sensing applications, illustrating the relationships between target device performance (user comfort, signal quality, and motion robustness), essential material properties, candidate material systems, fabrication methods, and potential applications. Reproduced with permission from [13].

To address these challenges, a wide range of soft material systems have been explored for flexible and stretchable sensing platforms. These include elastomer-based composites [14], [15], [16], conductive hydrogels [17], [18], [19], foams [20], [21], [22], and intrinsically conductive polymers

integrated into soft matrices [23], [24], [25]. Such materials enable the fabrication of devices that can deform together with biological tissues while maintaining electrical functionality.

Foams, a class of cellular materials characterized by a high volume fraction of gas-filled voids within a solid framework, represent an attractive platform for the design of soft and flexible sensing materials [26]. Their highly porous and lightweight structures result in very low effective elastic moduli, enabling mechanical properties that more closely match those of soft biological tissues and thereby improving comfort and mechanical compatibility in wearable devices [27]. In addition, the porous framework provides a large internal surface area that can enhance electrical interactions and signal transmission, improving the sensitivity of flexible sensors such as strain and pressure sensors, as well as gas and biochemical sensors [28]. Owing to these characteristics, foams have been widely explored for flexible electronic devices including wearable electrodes and various sensing platforms.

In addition to foams, hydrogels and hydrogel-derived materials such as xerogels have also attracted attention as soft conductive platforms for wearable electronics [29]. Hydrogels are polymer networks capable of retaining large amounts of water, resulting in soft, tissue-like mechanical properties that are well suited for bioelectronic interfaces. When dried, these materials form xerogels that retain aspects of the original network structure while exhibiting improved mechanical stability and processability. Conductive xerogels based on polymer networks combined with conductive components therefore represent a promising platform for flexible sensors, soft electrodes, and wearable electronic devices [30], [31], [32].

In wearable electronics, sensing systems can be broadly categorized based on the type of signals they monitor. One major class focuses on biopotential sensing, where electrical activity from the heart, muscles, or brain is recorded at the skin surface. Another class includes biomechanical sensing, such as strain and pressure detection, which captures body motion and mechanical deformation. Although these modalities rely on different sensing mechanisms, both require soft, conductive materials capable of maintaining stable performance under repeated deformation and prolonged skin contact during continuous monitoring.

1.2.1 Biopotential sensing

Biopotential sensing relies on the detection of small electrical signals generated by the body. These signals reflect the activity of excitable tissues (primarily nervous and muscle tissues) and enable access to physiological information without the need for invasive procedures [33]. Electroencephalography (EEG) captures brain activity, electrocardiography (ECG) monitors cardiac rhythms, electromyography (EMG) measures muscle activation, and electrooculography (EOG) records eye movements. As summarized in Figure 1-3, these measurements span different frequency ranges and provide complementary insights into physiological function, from neural activity to muscle motion and cardiac dynamics. In all these measurements, signal quality is governed less by the recording hardware than by the electrode and the interface that couples the body to the electronics [33]. Because biopotentials are low-amplitude and the body is mechanically dynamic, even minor changes in contact, which are simply caused by motion, pressure variation, or shifts in skin hydration, can lead to impedance drift and artifacts that mask the physiological signal [34]. In laboratory settings, these impedance changes can be evaluated using electrochemical impedance spectroscopy (EIS) or impedance measurements with an LCR meter/potentiostat, typically by monitoring electrode-skin or electrode-gel impedance over time under controlled pressure, motion, and hydration conditions. Developing electrode materials that remain electrically stable while staying soft and comfortable during wear is therefore a central challenge for reliable biopotential sensing in practical, real-world settings.

The electrode problem becomes more visible as electrophysiology moves toward wearable and ambulatory systems. In controlled environments, a trained operator can prepare the skin, carefully place electrodes, apply conductive gels, and minimize motion. In daily life, none of these conditions are guaranteed. Biopotential amplitudes can be small, particularly in EEG, and the recordings are easily dominated by motion artifacts, impedance fluctuations, cable microphonics, and baseline drift [35]. For practical wearables, the electrode must support stable electrical coupling while also being comfortable enough to wear for hours. This combination is demanding because it merges electrical engineering requirements (low noise, stable contact impedance, reliable transduction) with soft-matter requirements (conformability, gentle contact mechanics, durability, and skin compatibility).

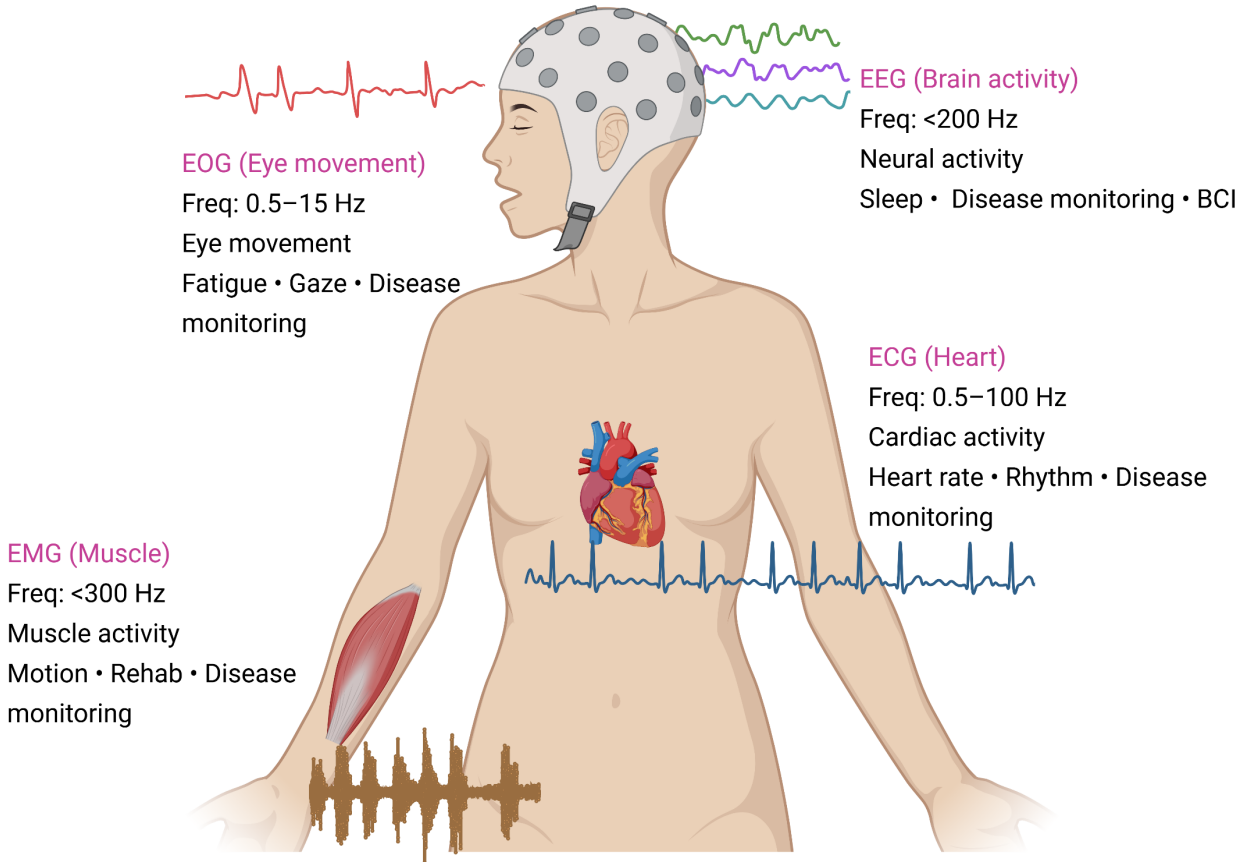

Figure 1-3 Overview of common biopotential signals and their physiological origins. EEG, ECG, EMG, and EOG capture electrical activity from the brain, heart, muscles, and eyes, respectively. Figure created by the author (Petrossian, G. (2026) https://BioRender.com/u468ic6).

1.2.2 Strain sensors

The growing development of consumer electronics, artificial intelligence, soft robotics, and wearable healthcare systems has increased the demand for stretchable and skin-conformable strain sensors capable of monitoring real-time mechanical deformation [36]. Such sensors play a key role in understanding physical motion and structural changes in both biological and engineered systems [7]. Strain sensors convert mechanical deformation into measurable electrical signals, enabling the monitoring of physiological movements such as joint bending, muscle contraction, respiration, and subtle body motions.

The sensing mechanism of most flexible strain sensors is based on piezoresistive, capacitive, piezoelectric, or triboelectric effects [37], with piezoresistive sensors being the most commonly

used in wearable systems due to their simple structure and high sensitivity. In piezoresistive strain sensors, mechanical deformation causes changes in the electrical resistance of the sensing material. This resistance variation typically results from mechanisms such as the rearrangement of conductive networks, variation in tunneling distance between conductive fillers, or geometric changes in conductive pathways [38], [39].

Recent advances in strain sensor design have focused on achieving high stretchability, sensitivity, and durability while maintaining biocompatibility for skin-contact applications.

Conventional flexible strain sensors have been fabricated by integrating conductive functional materials with elastic polymer substrates to form deformable conductive networks. Common conductive components include carbon-based nanomaterials such as carbon nanotubes (CNTs) [40] and graphene [41], metallic nanostructures such as silver nanowires (AgNWs) [42], [43], and more recently two-dimensional materials such as MXenes [44], [45], [46]. These conductive elements are typically incorporated into stretchable polymer matrices including thermoplastic polyurethane (TPU) [47], [48], and polydimethylsiloxane (PDMS) [49], [50], [51], which provide mechanical flexibility and structural support. Numerous studies have demonstrated that such composite structures enable strain sensors capable of detecting mechanical deformation with high sensitivity and mechanical compliance.

Although these composite-based sensors offer a relatively simple fabrication strategy and can provide good electrical conductivity, their stretchability is often limited, typically ranging from only a few percent to a few hundred percent depending on the material system [52], [53]. Such mechanical limitations can restrict their performance in applications that require large and repeated deformation. Consequently, there is increasing interest in developing softer and more deformable sensing materials capable of sustaining higher strains while maintaining stable electrical responses. In this context, hydrogel-based systems have emerged as promising candidates for next-generation flexible strain sensors. Hydrogels are three-dimensional polymer networks capable of retaining large amounts of water, giving them soft, tissue-like mechanical properties and high stretchability that are well suited for wearable bioelectronics [54].

Owing to their ability to sustain large deformation without mechanical failure, hydrogels have been widely explored as platforms for flexible strain sensors. In these systems, PEDOT:PSS has become one of the most commonly used conductive components due to its excellent solution

processability, compatibility with polymer networks, and ability to form conductive pathways that respond sensitively to mechanical deformation. As a result, PEDOT:PSS-based hydrogels have been extensively investigated for strain sensing applications capable of detecting both subtle and large mechanical motions [55], [56], [57]. Furthermore, these hydrogel systems often exhibit additional functional characteristics, including adhesive behavior [58], [59], self-healing capability [55], [60], and rapid structural recovery [61], [62], which are advantageous for wearable sensing applications.

Despite significant progress, designing strain sensors that simultaneously provide high stretchability, stable conductivity, mechanical robustness, and long-term durability remains challenging. Many conductive composites suffer from structural instability or conductivity degradation under repeated deformation, particularly at large strains. Although hydrogel-based sensors offer excellent stretchability and mechanical compliance, their high water content can lead to dehydration over time, resulting in changes in mechanical and electrical performance. Conversely, non-hydrogel systems often provide improved electrical stability but typically exhibit reduced flexibility and stretchability, highlighting a fundamental trade-off between mechanical compliance and electrical performance. Consequently, there is growing interest in developing soft conductive polymer networks that can sustain large mechanical deformation while maintaining reliable electrical properties for wearable bioelectronic applications.

1.3 PEDOT:PSS and its properties

Intrinsically conductive polymers (ICPs) are a class of materials capable of transporting electrical charge through conjugated π-electron systems along the polymer backbone. Since the discovery of conducting polymers in the late 1970s [63], later recognized by the Nobel Prize in Chemistry awarded to Heeger, MacDiarmid, and Shirakawa in 2000, conjugated polymers have attracted significant interest for applications in organic electronics. Over the past decades, numerous conductive polymers have been developed and investigated due to their combination of electrical conductivity, mechanical flexibility, and compatibility with solution-based processing.

Among these materials, poly(3,4-ethylenedioxythiophene):poly(styrene sulfonate) (PEDOT:PSS) has emerged as one of the most widely studied conductive polymers. PEDOT:PSS consists of the positively charged conductive polymer poly(3,4-ethylenedioxythiophene) (PEDOT), first synthesized in 1988 by Jonas et al. [64], combined with the negatively charged, water-soluble

polyelectrolyte poly(styrene sulfonate) (PSS). This combination enables the material to retain the high electrical conductivity of PEDOT while benefiting from the aqueous solubility and processability provided by PSS. As a result, PEDOT:PSS is considered as one of the most successful and widely used conducting polymers [65], with a wide range of applications in transistors [66], [67], solar cells [68], [69], sensors [70], [71], electromagnetic interference shielding [72], [73], etc.

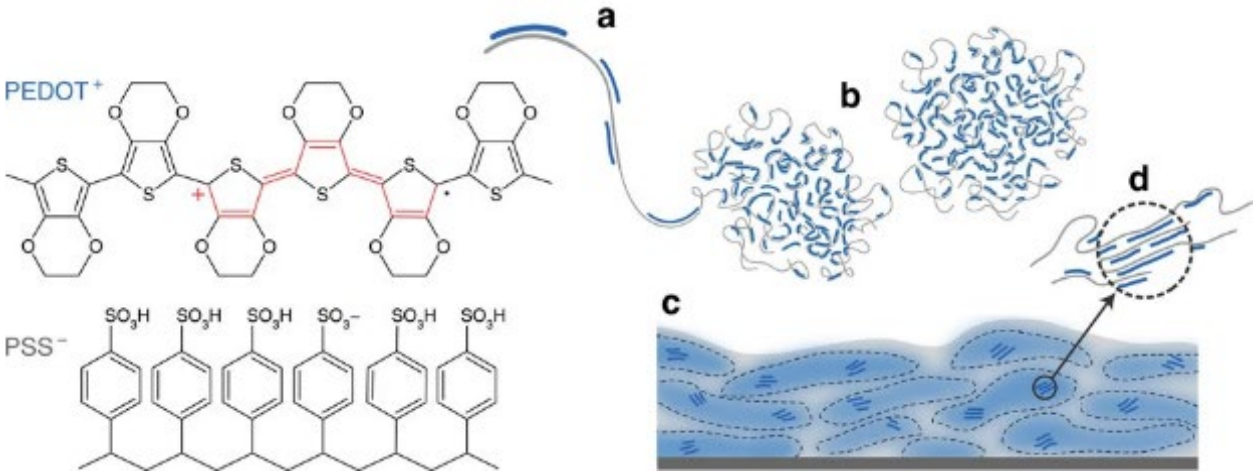

Figure 1-4 Chemical structure of PEDOT:PSS. The blue represents the PEDOT-rich domains, and the gray represents the PSS-rich domains. (a) PEDOT chains are synthesized on the PSS template, forming a polyelectrolyte complex. (b) In aqueous dispersion, PEDOT:PSS forms colloidal gel-like particles. (c) After film formation, the material consists of PEDOT-rich domains shown in blue and PSS-rich regions shown in gray. (d) PEDOT-rich aggregates/crystallites provide pathways for enhanced electronic transport. Reproduced with permission from [74].

The PEDOT:PSS complex exhibits a heterogeneous microstructure consisting of conductive PEDOT-rich domains surrounded by insulating PSS-rich regions (Figure 1-5). Electrical transport occurs primarily through interconnected PEDOT pathways, while PSS stabilizes the dispersion and enables solution-based processing. As a result, PEDOT:PSS can be readily processed using a variety of scalable coating, printing, and casting techniques. Beyond its processability in aqueous dispersions, PEDOT:PSS also exhibits several advantageous properties in its dried film form, including tunable electrical conductivity, mechanical compliance, high optical transparency, environmental stability, and good biocompatibility [75]. These characteristics have contributed

significantly to the widespread adoption of PEDOT:PSS in flexible electronics, printed devices, and bioelectronic applications [76], [77].

One of the most attractive characteristics of PEDOT:PSS is its tunable electrical conductivity. Kim et al.[78] were the first to explore the conductivity enhancement of PEDOT:PSS by adding a high boiling point solvent, dimethyl sulfoxide (DMSO). This increased the conductivity from 0.8 to 80 S cm^{-1}. Since then, various polar organic solvents such as ethylene glycol (EG), diethylene glycol (DEG), glycerol, and sorbitol have been studied [79]. These additives modify the microstructure of the film by inducing morphological rearrangements, increasing PEDOT crystallinity, and facilitating charge transport [80]. Continued advances in processing have led to much higher conductivities. For example, solution-sheared PEDOT:PSS films have reached 4,600 ± 100 S cm^{-1} [81], while more recent acid-treated PEDOT:PSS films have been reported to exceed 15,000 S cm^{-1} [82], among the highest conductivity values reported for this material system. Although these values are still below those of silver, copper, and gold (~10^5 S cm^{-1}), they are remarkable for a solution-processable conductive polymer. These results highlight the remarkable tunability of PEDOT:PSS and show that its electrical performance can be dramatically improved through microstructural and post-treatment engineering.

In addition to its tunable electrical properties and solution processability, PEDOT:PSS can be readily integrated with a wide range of materials and processing approaches, enabling the development of diverse functional architectures. As these systems continue to be tailored for different electronic and bioelectronic applications, PEDOT:PSS-based dispersions have been processed into numerous morphological forms, including powders, thin films, fibers, hydrogels, aerogels, elastomers, and sponges. The ability to fabricate PEDOT:PSS into such a broad range of structures highlights the remarkable versatility of this conducting polymer and continues to drive its exploration in advanced electronic, energy, and bioelectronic devices.

Overall, these considerations highlight the need for soft conductive materials that combine stable electrical performance, mechanical compliance, processability, and long-term reliability for wearable bioelectronic applications. PEDOT:PSS provides a promising foundation for such materials because of its conductivity, solution processability, and compatibility with diverse polymer systems. However, its performance depends strongly on how it is structured and integrated into larger material architectures. The following chapter therefore reviews recent

developments in wearable EEG electrode materials, with particular attention to the material and interface challenges that motivate the experimental work presented in this thesis.

CHAPTER 2LITERATURE REVIEW

A comprehensive overview of electrode materials for EEG applications was previously presented in our 2023 review article [83], which examined the state of the art in scalp, around-ear, and in-ear EEG electrode technologies and highlighted key challenges in achieving reliable skin-electrode interfaces. This review article is included in this thesis as **Article 1 in Chapter 4**. Since the publication of that work, the field of wearable electrophysiology has continued to evolve rapidly, with new materials strategies, device architectures, and fabrication approaches being reported. To place the present research within this broader context, the following sections summarize recent developments in wearable biopotential electrodes reported in the literature since that review.

It is important to note that while ear-EEG offers important advantages for discreet and long-term electrophysiological monitoring, it should not be considered a direct replacement for conventional scalp-EEG. Scalp-EEG remains the standard approach when high-density electrode coverage and spatially resolved information about brain activity are required. Because ear-EEG electrodes are positioned in or around the ear, their sensitivity is more limited to signals that can be detected from these locations, particularly activity originating from temporal regions. Therefore, the suitability of ear-EEG strongly depends on the target application and the specific EEG features of interest. In this context, the main potential of ear-EEG lies not in replacing scalp-based systems, but in enabling more wearable, comfortable, and long-duration recordings for applications where reduced spatial coverage is acceptable. From a materials perspective, improving electrode conductivity, mechanical conformability, and signal stability is therefore an important step toward expanding the practical use of ear-EEG, while recognizing that signal detectability and spatial specificity remain key considerations for future system-level studies.

2.1.1 Scalp-EEG

Since the publication of our earlier review, research on scalp EEG electrodes has increasingly focused on reducing preparation time and enabling long-term wearable monitoring. Conventional gel-based Ag/AgCl (silver/silver chloride) electrodes still remain the gold standard for high-quality EEG recordings because they provide low skin-electrode impedance and stable signal acquisition. However, traditional conductive gels and pastes suffer from several limitations, including drying over time, signal degradation during long recordings, and the need for skin preparation and post-

measurement cleaning. As a result, recent research on wet electrode systems has largely focused on the development of hydrogel-based interfaces, which offer improved mechanical compliance, enhanced moisture retention, and more stable electrical contact with the skin compared to conventional gels and pastes.

Several recent works have focused on incorporating adhesive properties into hydrogel electrodes to improve skin contact and signal stability. Ahn et al. [84] developed skin-conformal adhesive hydrogel electrodes by incorporating PEDOT:PSS and the surfactant Triton X-100 into an acrylic acid matrix. Addition of Triton X-100 led to a hydrogel that exhibited low skin-electrode impedance due to the formation of effective and continuous conductive pathways within the hydrogel network, enabling reliable EEG signal acquisition. The hydrogel showed an electrical conductivity of 9.1 S/m, a shear adhesion strength of 22.4 N cm^{-2}, and a Young's modulus of ~36 kPa, striking a good balance between electrical and mechanical properties. Similarly, Han et al. [85] developed a flexible and self-adhesive hydrogel electrode based on a polyvinyl alcohol (PVA), polyvinylpyrrolidone (PVP), and polydopamine nanoparticles network designed to achieve tissue-like mechanical properties and stable skin contact. The hydrogel electrode exhibited strong adhesion and mechanical flexibility, with a skin-electrode contact impedance of 3-4 kΩ over the 1-100 Hz frequency range. Notably, the impedance remained stable even after seven days of continuous use, demonstrating the potential of this hydrogel system for long-term EEG signal acquisition.

Ahmed et al. [86] developed bioadhesive hairlike EEG electrodes designed to attach directly to the scalp with an average adhesion force of 0.7 N cm^{-1} (Figure 2-1a). The device consists of a PEDOT:PSS-based conductive polymer hydrogel electrode encapsulated in flexible PDMS layers and integrated with a strong bioadhesive layer that ensures stable attachment to the scalp. The hair-mimicking geometry allows the electrodes to conform to hairy scalp regions while remaining nearly invisible during wear. The system exhibited stable skin-electrode impedance (~16.7 kΩ at 10 Hz) and maintained reliable EEG signal acquisition for up to 24 h of continuous use. Another miniaturized adhesive approach was developed by Tang et al. [87], who designed a bioadhesive hydrogel interface composed of poly(2-acrylamido-2-methyl-1-propanesulfonic acid) (polyAMPS) and glycerol to enable stable long-term coupling between the scalp and a wearable neuromodulation device (Figure 2-1b). The hydrogel exhibited strong skin adhesion (~0.96 N cm^{-}

[1]) and low signal attenuation (<13%), maintaining stable coupling for up to 35 days. This robust hydrogel interface enabled reliable long-term neuromodulation and monitoring, demonstrating the potential of adhesive hydrogel systems for wearable scalp-mounted neurotechnology.

Another research direction has focused on hydrogel systems that undergo in situ fluid-to-gel phase transitions, allowing the electrode to be applied as a liquid that subsequently solidifies on the skin to form a conformal and stable interface. Various triggering mechanisms have been explored to induce this transition, including pH-induced gelation [88], thermosensitive phase transitions [89], and near-infrared-induced polymerization [90]. For example, Li et al. [88] developed a hydrogel adhesive capable of undergoing autonomous fluid-to-gel transitions to form a programmable bioelectronic interface. The system is driven by antagonistic enzyme reaction networks, which dynamically modulate pH to control reversible boronate esterification between polymers, enabling spatiotemporal tuning of the hydrogel's mechanical and adhesive properties. This adaptive transition allows the material to be applied in a liquid state to conform to complex surfaces before solidifying into a stable hydrogel network, providing a robust interface for bioelectronic signal acquisition. Hsieh et al. [91] developed an injectable hydrogel electrode (AIRTrode) that forms in situ at the skin-electrode interface, enabling conformal contact even on hairy scalp regions. The AIRTrode can be either injectable or pre-formed by adjusting its composition ratio, allowing flexibility for different usage scenarios. The hydrogel exhibited a skin-electrode impedance of approximately 17.5 kΩ during more than 8 h of recording and strong adhesion to skin (~0.92 N cm^{-1}). In addition, the electrode achieved a higher signal-to-noise ratio (23.97 dB) than commercial wet electrodes, demonstrating its potential for stable EEG signal acquisition.

Overall, recent advances in wet scalp EEG electrodes have largely focused on hydrogel-based systems due to their improved moisture retention, mechanical compliance, and ability to maintain stable skin–electrode impedance. In addition to these hydrogel approaches, semi-dry electrodes have also been explored, using controlled electrolyte release to maintain conductivity while improving long-term stability.

Semi-dry electrodes have been proposed as an intermediate solution between traditional wet electrodes and fully dry systems. While this approach was already explored in earlier studies summarized in our previous review, recent work has focused on improving electrolyte management, structural design, and long-term stability for wearable EEG applications [92], [93],

[94] These electrodes incorporate a small electrolyte reservoir that gradually releases conductive liquid at the skin-electrode interface, maintaining hydration while avoiding the excessive gel application required by conventional wet electrodes.

For example, Zhu et al. [95] developed a semi-dry electrode composed of a reduced graphene oxide (RGO) network integrated within a porous polyurethane sponge, which acts as a saline-based electrolyte reservoir (Figure 2-1c). The flexible electrode exhibited a skin-electrode impedance below 5.6 kΩ for up to 4 hours and produced EEG signals highly correlated with those recorded using conventional wet electrodes, demonstrating comparable signal quality. However, these semi-dry electrode designs still rely on a limited electrolyte reservoir, which gradually depletes during use and therefore requires periodic replenishment to maintain low skin-electrode impedance.

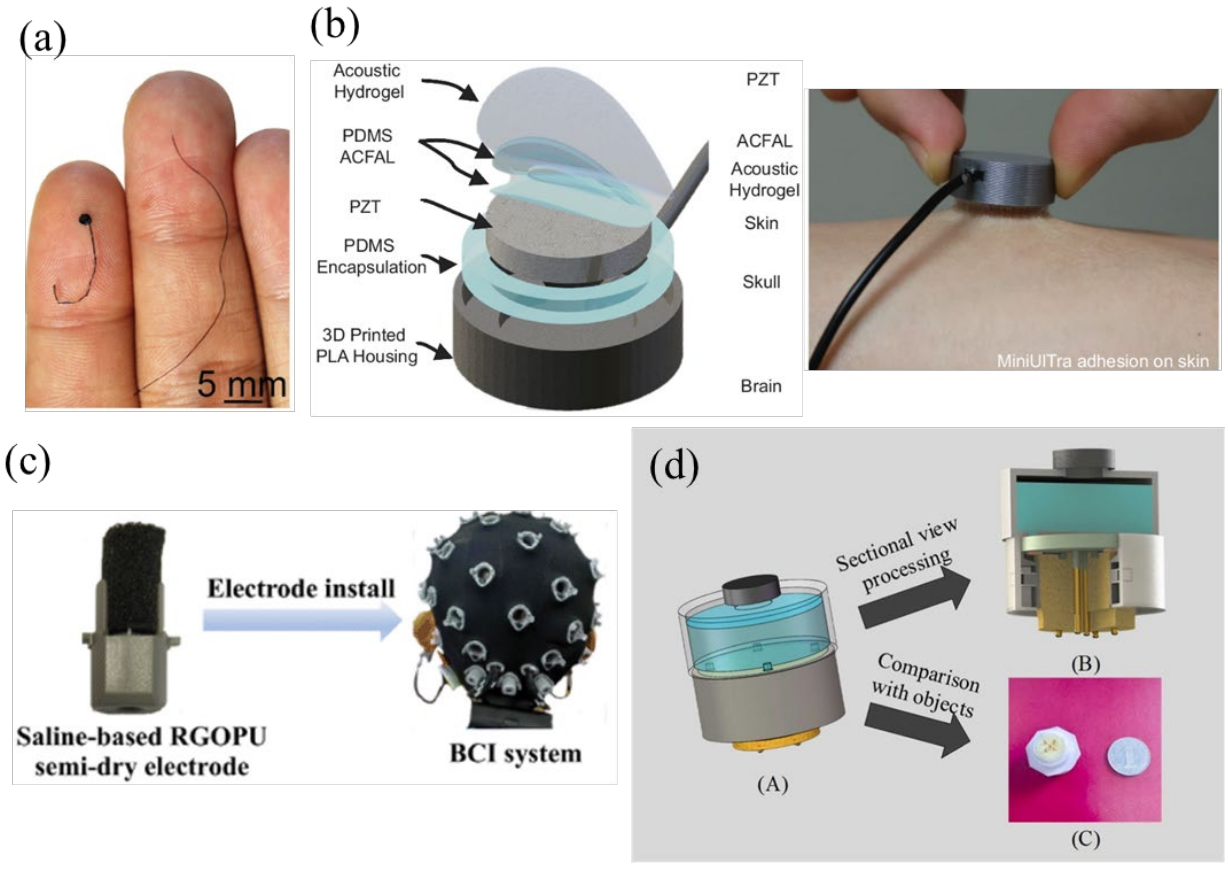

Figure 2-1 Wet and semi-dry scalp-EEG electrodes. (a) Photograph of a hairlike dry scalp electrode. (b) Schematic illustration of the layered structure an ultrasound transducer EEG electrode including a bioadhesive acoustic hydrogel (left) and its adhesin on skin (right). (c) A

Salin-based semi-dry electrode integrated into a brain-computer interfaces (BCI) system. (d) A semi-dry electrode, equipped with an automatically replenishing conductive fluid reservoir (A) sectional view of the internal composition (B) and size comparison with an object (C). Reproduced with permission from (a) [86], (b) [87], (c) [95], and (d) [96].

To address this limitation, recent work [96], [97], [98] has explored semi-dry electrode systems capable of automatically replenishing the electrolyte at the interface. For example, Wang et al. [96] developed a semi-dry electrode incorporating a flow-controllable electrolyte delivery mechanism that enables rapid conductive liquid replenishment during operation (Figure 2-1d). This design allows the electrode to maintain a stable conductive interface with the scalp while reducing the need for manual electrolyte refilling, achieving an impedance of 13.43 kΩ at 800 Hz.

With the growing interest in ambulatory EEG for applications such as long-term neurological disease monitoring and diagnosis [99], [100], [101], sleep studies [102], [103], and brain-computer interfaces [104], [105], there has been increasing demand for electrode systems that can operate reliably outside controlled clinical environments. In this context, some of the recent research has focused on the development of dry EEG electrodes, which eliminate the need for gels or liquid electrolytes and simplify device setup. These systems aim to enable comfortable, low-maintenance recordings while maintaining sufficient signal quality during prolonged wearable monitoring.

Multipin electrode architectures represent an important pillar in the development of dry EEG electrodes, as arrays of conductive pins help penetrate hair and improve contact with the scalp [106], [107], [108], [109], [110]. Warsito et al. [111] developed a multipin “flower” electrode consisting of 30 tilted pins arranged in a radial, flower-like geometry to improve scalp contact and wearing comfort (Figure 2-2a). The angled multipin architecture increases the contact area with the scalp while allowing the pins to navigate through hair, enabling reliable EEG acquisition, with an average skin-electrode impedance of ~650 kΩ. Similarly, Wang et al. [112] designed an active claw-shaped multipin dry electrode intended to improve electrode-scalp contact in hair-covered regions (Figure 2-2b). The electrode consists of several conductive claw-like protrusions mounted on a flexible substrate and combined with an active amplification circuit to improve impedance matching. The design achieved electrode-skin contact impedances of approximately 18.62 kΩ at 1 Hz on hairless regions and 122.15 kΩ at 1 Hz on hair-covered scalp, demonstrating its capability for reliable EEG signal acquisition.

Another approach for dry EEG electrodes involves the use of conductive textile or fabric-based electrodes, which leverage the inherent flexibility, breathability, and conformability of fabrics to improve user comfort during long-term monitoring. For example, Zeng et al. [113] developed a flexible and washable fabric dry EEG electrode by coating conductive polyester fabric with a PEDOT:PSS-PVA composite. The conductive coating produced a uniform conductive layer with a resistivity of ~0.09 Ω cm, enabling low and stable skin-electrode impedance during prolonged measurements. Similarly, Motiepor et al. [114] developed a textile-based stretchable dry electrode integrated into a wearable cap structure to enable comfortable long-term EEG monitoring.

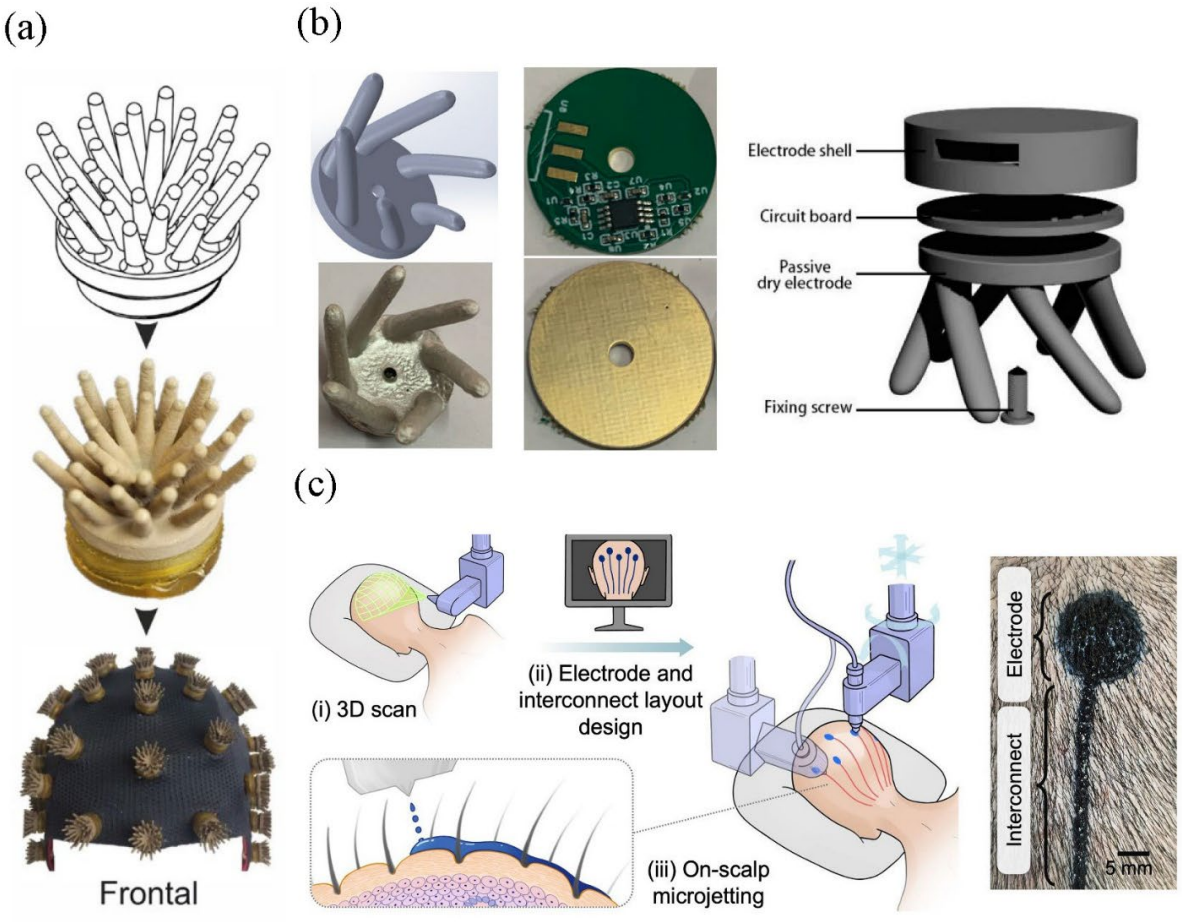

Figure 2-2 Dry scalp-EEG electrodes. (a) 3D schematic (top) and photograph (middle) of the flower electrode, and a photograph of flower cap (bottom). (b) The claw-shaped electrode (left), the electrode circuit (middle), and a schematic of the electrode (right). (c) A schematic of the on-scalp EEG e-tattoo printer setup (left), and a close-up photograph of the printed electrode (right). Reproduced with permission from (a) [111], (b) [112], and (c) [115].

A novel approach involves directly constructing electrodes on the scalp, where conductive materials are deposited or patterned directly onto the skin to form a conformal electrode interface. Vasconcelos et al. [115] developed a method for printing personalized PEDOT:PSS e-tattoo electrodes directly on the scalp, enabling conformal and ultrathin on-skin EEG interfaces without the need for conventional caps or gels (Figure 2-2c). The personalized electrodes closely follow the scalp topography and exhibited a skin-electrode impedance of approximately 24.6 kΩ, allowing stable EEG signal acquisition.

2.1.2 Ear-EEG

Ear-centered EEG (ear-EEG) has emerged as a promising alternative to conventional scalp EEG for wearable and long-term brain monitoring. By placing electrodes in or around the ear, ear-EEG systems enable unobtrusive and stable acquisition of neural signals while maintaining high user comfort and social acceptability [116]. The ear also provides a mechanically stable recording location that is less affected by motion than the scalp, making it particularly attractive for ambulatory and real-world monitoring applications. Early ear-EEG studies primarily focused on demonstrating proof-of-concept signal acquisition and validating the feasibility of recording neural activity from ear-mounted sensors. Despite growing interest in this approach, the field remains in its early stages, and relatively limited work has been devoted specifically to the development of electrode materials and structures optimized for ear-EEG applications.

Several recent studies have demonstrated the feasibility of ear-centered EEG using readily available or commercially available electrode systems rather than newly developed electrode materials. For example, Hestermann et al. [117] fabricated an in-ear EEG earpiece using a commercially available conductive fabric integrated into a custom ear mold, enabling stable neural signal acquisition while maintaining comfort and conformability within the ear canal. Similarly, Moumane et al. [118] evaluated an in-ear EEG system using a commercially available ear-EEG platform developed by Naox Technologies, demonstrating reliable neural signal acquisition during both wakefulness and sleep monitoring. In another study, Leung et al. [119] used commercially available gold-tipped foam earplugs as ear-EEG electrodes and demonstrated that these electrodes could capture brain activity such as alpha rhythms, further confirming the feasibility of recording EEG signals from the ear. Likewise, Liang et al. [120] implemented an ear-EEG recording system using conventional AgCl disk electrodes integrated into an ear-mounted configuration, further

demonstrating that neural activity can be reliably captured from the ear using standard electrode components.

Recent studies have begun to explore ear-EEG systems specifically designed for the unique geometry and mechanical constraints of the ear canal. Zhuo et al. [121] developed a mechanically adaptable in-ear electronic sensor that softens upon contact with the ear canal to reduce mechanical mismatch between the device and the skin. The system is based on a thermoplastic polyurethane-Ecoflex foam structure that transitions from an elastic modulus of 1.2 MPa to a softer state (~0.86 MPa) at body temperature, improving conformal contact within the ear canal. This mechanical adaptability increases the device-skin contact area and reduces interface impedance, enabling stable EEG recordings while minimizing motion artifacts during daily activities.

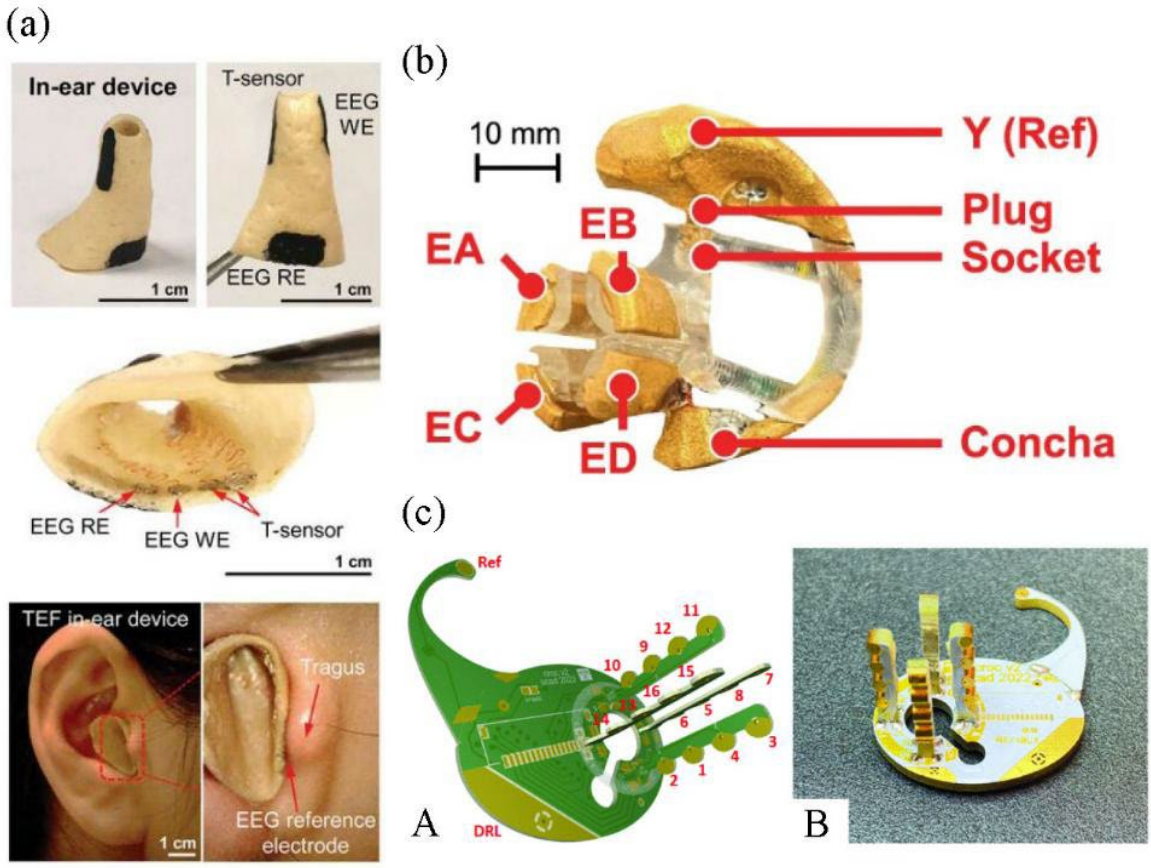

Figure 2-3 In-ear EEG devices and electrode configurations. (a) Photographs of mechanical adaptability-reinforced in-ear device, the electrodes and internal wiring. (b) Multi-electrode ear-centered device illustrating electrode placement around different regions of the ear, including the concha and outer ear structures, along with the reference electrode location. (c) Schematic of a

printed circuit board-based ear-EEG electrode design illustrating the EEG channel numbers (A) and a photograph of the assembled earpiece (B). Reproduced with permission from (a) [122], (b) [123], and (c) [124].

Another important development was reported by Kaveh et al. [123], who demonstrated a wireless in-ear EEG platform based on dry electrode earpieces designed for real-world monitoring applications such as drowsiness detection. fabricated by 3D printing a methacrylate polymer structure followed by metal plating, forming conductive contacts within an earbud-like device that enables continuous brain monitoring. The authors showed that the ear-mounted sensors could reliably detect neural signatures associated with fatigue and cognitive state, highlighting the potential of ear-EEG for ambulatory neurotechnology and wearable brain monitoring.

Other studies have focused on optimizing the geometry of the electrodes and the structure of the earpiece substrate to improve contact stability and signal quality within the ear. For example, Lee et al. [124] developed an in-ear EEG system based on a miniaturized printed circuit board (PCB) electrode component integrated into a custom earpiece structure. The PCB-based electrode design allowed precise positioning of the conductive contacts within the ear canal while maintaining a compact and mechanically robust architecture suitable for wearable monitoring. Similarly, Xu et al. [125] reported a flexible ear-centered electrode array designed to conform to the complex geometry around the ear. The array consists of multiple closely spaced electrodes arranged on a thin flexible substrate, enabling improved spatial sampling of neural signals and more stable signal acquisition compared with single-electrode designs.

Around-the-ear electrode configurations remain less popular because they partially lose the unobtrusive advantage of in-ear designs, as the electrodes remain visible on the outer ear. Nevertheless, a few studies have investigated wearable platforms that position electrodes around the ear canal. For example, Nguyen et al. [126] developed an ear-mounted EEG platform that integrates electrodes within a wearable around-the-ear structure, enabling stable signal acquisition while maintaining user comfort during ambulatory monitoring. Similarly, Mai et al. [127] proposed an around-the-ear EEG system designed to improve electrode positioning and signal stability by optimizing the geometry of the electrode layout around the auricle. In another study, Zhu et al. [128] developed a wearable ear-mounted EEG configuration incorporating multiple

electrodes distributed around the ear to improve spatial sampling of neural signals and enable reliable brain-activity monitoring during everyday activities.

Overall, recent developments in ear-centered EEG have demonstrated the feasibility of recording neural activity using in-ear and around-the-ear configurations, with growing attention devoted to device integration and structural design. However, much of the existing work has relied on commercially available electrodes or focused primarily on system-level validation rather than the development of optimized electrode materials specifically tailored to the mechanical and electrical constraints of the ear. As ear-EEG moves toward practical long-term wearable applications, there remains a clear need for soft, conformal, and conductive electrode materials capable of maintaining stable contact within the unique geometry of the ear.

CHAPTER 3RESEARCH OBJECTIVES AND COHERENCE OF ARTICLES

3.1 Research objectives

Wearable bioelectronic devices require materials that can simultaneously provide reliable electrical conductivity, mechanical compliance, and stable interfaces with biological tissues. Conventional rigid electrode materials often exhibit poor mechanical compatibility with soft biological environments, leading to signal instability and discomfort during long-term use. As a result, there is increasing interest in developing soft conductive materials that can conform to the body while maintaining stable electrical performance. Conductive polymers, particularly PEDOT:PSS, have emerged as promising candidates for such applications due to their combined electronic and ionic conductivity, solution processability, and compatibility with a wide range of polymer systems.

While PEDOT:PSS offers many attractive properties, further material engineering can expand its functionality for wearable bioelectronic applications. However, a key challenge remains in achieving both high electrical performance and mechanical compliance within the same material while maintaining scalable processing. In particular, new material architectures could help striking a balance between electrical conductivity, mechanical performance, and scalable fabrication. The central hypothesis of this thesis is that architecting PEDOT:PSS into structured and composite material systems can significantly expand its functionality for wearable sensing and bioelectrode applications. In particular, tailoring the microstructure, porosity, and polymer network architecture of PEDOT:PSS-based systems can enable conductive materials that combine electrical performance with enhanced mechanical performance, structural adaptability, and scalable manufacturing. Therefore, the main objective of this thesis is to demonstrate that the performance of PEDOT:PSS-based soft materials can be advanced not only through chemistry, but also through material architecture. To address this objective, the thesis is organized around the following specific objectives:

Objective 1: To address this hypothesis, the first objective of this thesis was to establish a comprehensive understanding of electrode materials used for wearable and bioelectronic signal acquisition. This objective was achieved through a comprehensive review of existing electrode technologies used for physiological monitoring. Beyond summarizing the state of the art, this

analysis critically identifies the limitations of current electrode materials in terms of mechanical mismatch, interface instability, and long-term usability, thereby defining the key material design criteria that guide this thesis. The review summarizes the advantages and limitations of current electrode materials and device configurations. This analysis provides the scientific and technological context that motivates the development of new PEDOT:PSS-based material platforms explored in the subsequent chapters of this thesis.

Objective 2: The second objective of this thesis was to develop lightweight and conductive porous materials based on PEDOT:PSS-coated polymer microspheres for wearable bioelectrode applications. In this work, conductive coatings were introduced onto expandable polymer microspheres to create electrically conductive building blocks that could be assembled into syntactic foam architectures. This objective specifically explores how microsphere-templated architecture can localize conductivity at particle surfaces while controlling porosity, mechanical compliance, and processability. This work introduces a microsphere-templated materials design strategy, in which electrical pathways are confined to the coated shells while porosity is independently controlled through the microsphere architecture. This microsphere-templated design allows fabrication of porous materials while maintaining electrical conductivity through PEDOT:PSS-coated shells. The resulting conductive foam combines low density, mechanical flexibility, and electrical functionality while also enabling scalable processing and compatibility with additive manufacturing techniques. This approach introduces a new class of microsphere-templated conductive foams, expanding the design space of PEDOT:PSS-based materials for soft bioelectronic interfaces. This approach represents a new class of lightweight, microsphere-templated conductive materials and provides insight into how porosity and architecture influence electrical percolation and mechanical response in PEDOT:PSS-based systems.

Objective 3: The third objective of this thesis was to develop highly stretchable conductive xerogel fibers based on PEDOT:PSS for wearable strain sensing applications. In this work, conductive polymer networks were engineered using a freeze-thaw processing strategy combined with additional crosslinking to form mechanically robust double-network xerogels. This objective specifically examines how polymer network architecture can improve stretchability and mechanical robustness while maintaining electrical functionality. This work establishes a double-network materials design strategy that enables the simultaneous enhancement of mechanical

robustness and stretchability while preserving electrical functionality, addressing a key limitation of conventional conductive polymer networks. By controlling the network structure and crosslinking conditions, the resulting fibers exhibited a favorable combination of electrical conductivity, large stretchability, and mechanical durability. These properties enabled their integration into wearable strain sensors capable of monitoring human motion through stable and repeatable electromechanical responses.

Together, these research efforts demonstrate how the structural and compositional design of PEDOT:PSS-based materials can enable the development of new soft conductive systems for wearable electronics and bioelectronic devices. This thesis introduces two distinct but complementary materials platforms and establishes general design principles for engineering PEDOT:PSS into mechanically compliant, structurally adaptable, and electrically functional materials. By exploring multiple material architectures and processing strategies, this thesis contributes to expanding the design space of PEDOT:PSS materials and highlights their potential for next-generation flexible and wearable sensing technologies.

3.2 Structure of the thesis

This thesis is organized into 8 chapters. Chapter 1 introduces the main themes and scientific background of the thesis. It presents an overview of wearable sensing technologies, including both biopotential sensing and strain sensing systems, and discusses the material requirements for soft and conformable electronic devices. The chapter also reviews conductive polymer materials, with particular emphasis on PEDOT:PSS, which serves as the primary material system investigated in this work.

Chapter 2 includes an updated literature review on electrode materials for electroencephalography (EEG), covering recent developments in the field since the publication of the review article included in this thesis, thereby providing an up-to-date context for the research presented. The research objectives and overall hypothesis of the thesis are also presented.

Chapter 4 is the reprint of the following article:

Article 1: Gayaneh Petrossiana, Pierre Kateb, Floriane Miquet-Westphal, Fabio Cicoira, “Advances in Electrode Materials for Scalp, Forehead, and Ear EEG: A Mini-Review,” *ACS Applied Bio Materials*, vol. 6, no. 8, p. 3019-3032, 2023.

Article 1 presents a review of electrode materials used for electroencephalography (EEG), with particular focus on scalp, forehead, and ear EEG systems. This chapter examines the material and design requirements for EEG electrodes and discusses the broad range of electrode types used in conventional scalp EEG as well as emerging forehead- and ear-centered configurations. Various electrode material classes and device approaches are reviewed in the context of signal quality, wearability, and long-term use. This chapter provides the scientific background for understanding the opportunities and limitations of current EEG electrode technologies and helps position the material developments presented in the following chapters.

Chapters 5 and 6 present the primary experimental research conducted in this thesis and are based on manuscripts submitted to scientific journals.

Chapter 5 is based on the following manuscript, currently under review:

Article 2: Gayaneh Petrossian, Yassine Diouri, Bolan Xu, Sara Ebrahimi, Atharva Pande, Floriane Miquet-Westphal, Hang Xu, and Fabio Cicoira, "Microsphere-Templated Conductive Syntactic Foams for Recyclable and Additively Manufactured Soft Electronics," under review at *Advanced Healthcare Materials*.

Article 2 investigates the development of lightweight conductive foams based on PEDOT:PSS-coated polymer microspheres. In this work, expandable polymer microspheres are coated with PEDOT:PSS to form conductive building blocks that can be incorporated into syntactic foam architectures. The resulting materials exhibit low density, tunable porosity, and electrical conductivity while maintaining mechanical compliance. The foams are further processed into filaments compatible with additive manufacturing, demonstrating their potential for scalable fabrication of customizable bioelectronic devices.

Chapter 6 is based on the following manuscript:

Article 3: Gayaneh Petrossian, Sara Ebrahimi, Floriane Miquet-Westphal, Hang Xu, and Fabio Circoira, "Double-Network PEDOT:PSS Xerogel Fibers with High Stretchability and Electrical Stability for Wearable Strain Sensing," under review at *Materials Advances*.

Article 3 explores the development of highly stretchable PEDOT:PSS-based xerogel fibers for wearable strain sensing applications. Conductive xerogels are fabricated using a freeze-thaw processing method followed by borax crosslinking to create a double-network polymer structure.

The resulting fibers combine high stretchability, mechanical robustness, and stable electrical conductivity. Their electromechanical response under deformation is investigated, and their potential for monitoring human motion in wearable sensing systems is demonstrated.

Chapter 7 provides a general discussion of the results obtained throughout the thesis and highlights the relationships between the different material architectures investigated. The broader implications of these findings for the development of soft conductive materials for wearable electronics are discussed.

Finally, Chapter 8 summarizes the main contributions of this work and outlines potential directions for future research in the design and development of PEDOT:PSS-based materials for wearable bioelectronic applications.

CHAPTER 4ARTICLE 1: ADVANCES IN ELECTRODE MATERIALS FOR SCALP, FOREHEAD, AND EAR EEG: A MINI-REVIEW

4.1 Authors

Gayaneh Petrossian[a], Pierre Kateb[a], Floriane Miquet-Westphal[a], Fabio Cicoira[a]*

[a]Department of Chemical Engineering, Polytechnique Montréal, Montréal, Québec H3C 3A7, Canada

*Email: fabio.cicoira@polymtl.ca

Published July 26, 2023, *ACS Applied Bio Materials*

KEYWORDS: Electroencephalography (EEG), wearable electronics, electrodes, Ear-EEG, Mobile-EEG

4.2 Abstract

Electroencephalogram (EEG) records the electrical activity of the neurons in the cerebral cortex and is used extensively to diagnose, treat, and monitor psychiatric and neurological conditions. Reliable contact between the skin and the electrodes is essential for achieving consistency and obtaining electroencephalographic information. There has been increasing demand for effective equipment and electrodes to overcome the time-consuming and cumbersome application of traditional systems.

Recently, ear-centered EEG has met with growing interest, since it can provide good signal quality due to the proximity of the ear to the brain. In addition, it can facilitate mobile and unobtrusive usage due to its smaller size and ease of use, since it can be used without interfering with the patient's daily activities. The purpose of this mini-review is to first discuss the broad range of electrodes used in conventional (scalp) EEG and subsequently introduce the state-of-the-art literature about around and in-the-ear EEG.

4.3 Introduction

Electroencephalography (EEG) is a method of measuring the brain's electrical activities, first reported for humans by the German psychiatrist Hans Berger in 1929. Amongst all available brain

monitoring techniques, including Magnetic Resonance Imaging (MRI) and Positron Emission Tomography (PET), EEG was the first to be utilized for neurological diagnoses and operations. Since its introduction, it has provided us with substantial knowledge about the brain, which has resulted in breakthroughs in neuroscience and neuromedicine.

A painless and safe technique, EEG is used to diagnose and control various neurological disorders, such as Parkinson's disease, epilepsy and autism. Additionally, it can be used in biometrics, brain-computer interfaces (BCI) and biofeedback therapy for mental disorders, such as insomnia, depression, and schizophrenia. Novel studies are opening new doors for the use of EEG in eye state detection,[129] identity authentication,[130] and emotion recognition.[131]

EEG uses electrodes to record signals primarily originating from the cerebral cortex. Fast action potentials generated by excitable cells (e.g., neurons or muscle cells) create electrical impulses, which are measured as voltage fluctuations and sent to an amplifier.[132] The recorded signals include the desired signal (related to the brain activity) and several undesired signals, called artifacts.[133] Artifacts are divided into two categories, depending on their origin: physiological (internal), resulting from physiological sources such as eye blinking, respiration, and jaw movement, and non-physiological (external), originating from the surrounding environment, such as electrical interferences and incorrect electrode placement. As artifacts mimic or distort EEG recording, it is essential to distinguish them from primary brain signals.

There are five common types of EEG: routine, invasive, video, sleep/sleep-deprived and ambulatory.

1) Routine EEG is the most common one. The patient is resting during the entire procedure, which typically takes between 20 minutes to 1 hour, as recommended by the American Clinical Neurophysiology Society.[134], [135]
2) Invasive EEG uses electrodes that are surgically implanted inside (depth EEG) or on the surface (subdural EEG) of the brain. It is used for the diagnosis of severe brain disorders, for instance to localize where the seizures start in epileptic patients.[136], [137]
3) Video EEG is achieved by filming the patient during the test, to gather more information about the relationship between the environment and EEG signals.[138]
4) Sleep EEG is conducted when the patient is asleep, while sleep-deprived EEG, primarily used for epilepsy diagnosis, is conducted when the patient has been awake for a prolonged time.[139]

5) Ambulatory EEG is a long-term test that provides continuous and real-life monitoring. It is typically an outpatient procedure in the patient's personal environment (e.g., performed at home). Generally, ambulatory EEG is performed in conjunction with video EEG.[139], [140]

For non-invasive procedures, EEG electrodes can be placed on the scalp (including the forehead), around the ear, and in the ear. In scalp EEG, several electrodes, placed along the scalp, are used to record brain signals. The number of electrodes used in this technique depends on the type of measurement. Oosteveld et al.[141] proposed a system with 345 electrodes for high-resolution measurements of event-related potential, i.e., resulting from events such as visual or auditory stimulations. Alba et al.[142] were able to use only 3 electrodes to estimate simple mental concentration levels.

EEG signals can be divided into different frequency bands, each associated with various mental states and cognitive processes.[143]

Delta waves (0.5-4 Hz), at the lowest frequencies, are typically observed during deep non-rapid eye movement (REM) sleep, and are associated with unconscious processes, deep restorative sleep, and healing. Theta waves (4-8 Hz) are commonly observed during light sleep and drowsiness. Alpha waves (8-12 Hz) are prominent during quiet wakefulness, especially when the eyes are closed, or during relaxation. These waves are associated with a calm, relaxed, and alert state of mind, as well as to the transition between wakefulness and sleep. Beta waves (12-35 Hz) are the most common brainwave pattern during active wakefulness and are associated with focused attention, conscious thoughts, and engaged thinking. Finally, gamma waves (30-80 Hz) are the fastest brainwave frequencies and are associated with peak concentration.

Despite its clinical value, long history and standardized protocols for data collection and analysis, current scalp EEG systems may be obtrusive and bulky, especially for non-clinic applications. The drawbacks include: the need to attach numerous electrodes to one's head, the use of pastes or gels between the electrode and the scalp (see below) and the presence of long cables connecting the electrodes to the recording unit. Another major drawback is the intricate and costly setup process, which is typically performed by a trained health- professional. To overcome these barriers, recent studies have focused on in-ear and around-ear EEG. There are three main advantages of such techniques: 1) mitigating the cumbersome process of applying and removing scalp EEG electrodes, 2) achieving signals is independent of one's hair type or atypical ear anatomy, 3) enabling long-

term monitoring by providing portability. Ear-centered EEG is particularly promising for ambulatory EEG, where standard in-hospital techniques fail to capture enough information or when continuous monitoring is required to observe a patient's condition.

This article examines a variety of electrodes used in three different types of EEG: scalp, around-ear, and in-ear. The first part summarizes the state-of-the-art scalp EEG electrodes and supplies a holistic look into the available electrode materials. The second section presents a comprehensive summary of materials used in around-ear and in-ear EEG electrodes, with the aim to provide a comprehensive review of the recent developments in EEG electrodes.

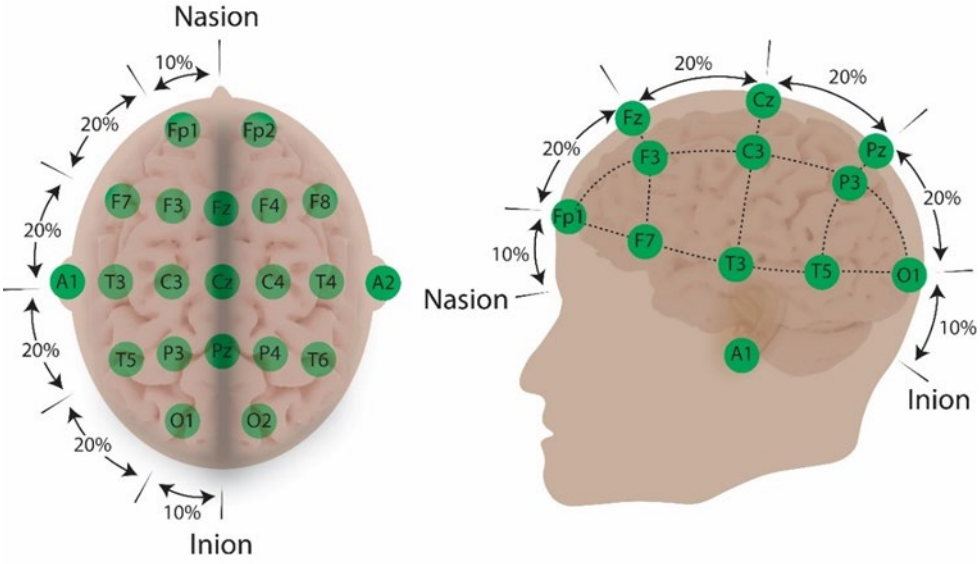

Figure 4-1 Electrode placements for EEG according to the international 10-20 system. The letters refer to pre-frontal (Fp), frontal (F), temporal (T), parietal (P), occipital (O), central (C), and reference (A).

4.4 Scalp EEG

Scalp EEG, the most used at present, requires electrodes affixed on the patient's scalp, typically placed according to the international standard 10-20 system.[144] The 10 and 20 refer to the distance between adjacent electrodes in the percentage of the total length between the nasion, i.e., the depressed area between the eyes and above the nasal bridge) and the inion, i.e., the most prominent point of the external occipital protuberance on the back of the skull (Figure 4-1).

The electrodes used for scalp EEG can be divided into wet and dry, based on whether or not an electrolyte is required between the electrode and the skin. The quality of the electrical contact at

the electrode/skin interface, very critical for EEG electrodes, is typically assessed by measuring the contact impedance at the skin-electrode interface. A high contact impedance reveals a high resistance to the flow of charges through the interface. An obstacle to achieve a good contact is the stratum corneum, the outer layer of the epidermis composed of dead skin cells, which is highly electrically resistive and not very permeable to ions. Progress in research on electrode materials and geometries is therefore important to create strategies to bypass this skin layer to decrease the skin-electrode impedance. Nevertheless, we must stress that the comparison between the skin-electrode impedance data reported in the literature is not straightforward, as the values strongly depend on the subject's skin and are often expressed in different units (e.g., normalized with respect to the contact surface). Table 4-1 provides a list of contact impedance values reported in the literature discussed in this work.

4.4.1 Wet Electrodes

In wet electrodes, ionic conductors in the form of electrolytic solutions, gels, or pastes are used to decrease the contact impedance between the skin and the electrode. This effect improves the quality of the recorded signals. Figure 4-2 illustrates the electrodes mentioned in this section.

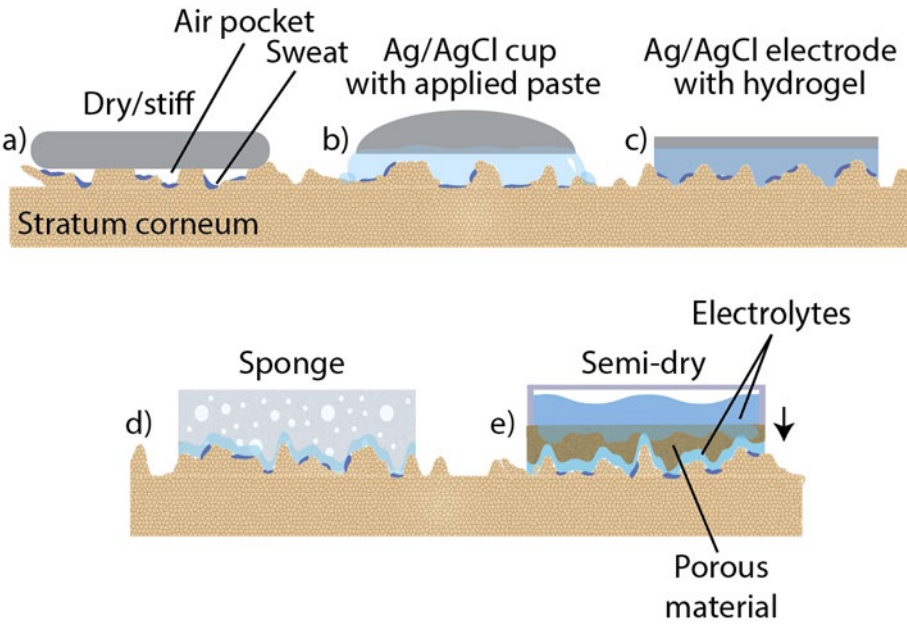

Figure 4-2 Four types of wet electrodes compared to a dry/stiff electrode on an irregular stratum corneum layer of the skin. a) dry, b) paste-based, c) hydrogel-based, d) sponge, and e) semi-dry.

Paste-based electrodes: In paste-based electrodes, a viscous paste is used as the conductive medium between the skin and the electrode for electrical signal transmission. Although the exact composition of the pastes may vary between manufacturers, some common ingredients include an aqueous electrolyte solution (NaCl or KCl), thickeners, such as hydroxyethyl cellulose, carboxymethyl cellulose or other polymers, humectants, like glycerol or sorbitol, which retain moisture in the paste and prevent it from drying out during use, and preservatives, to prolong the shelf life of the paste and prevent bacterial or fungal growth.[145], [146]

Silver/Silver chloride (Ag/AgCl) electrodes, combined with pastes, are the gold standard for EEG measurements in clinical and research applications. They typically yield a high signal-to-noise ratio (ratio of the desired signal to the undesired signal) and low electrode-skin interfacial impedance.[147] Metals such as gold (Au), tin (Sn) and, platinum (Pt) are also used in clinical settings for wet electrodes, although they tend to have lower direct current (DC) stability than Ag/AgCl ones.[148] A low DC stability translates into an electrode output susceptible to drift or change over time, which can introduce noise and artifacts into the recorded signals.

As opposed to dry electrodes, such as metal disks (discussed in detail in the next section), which would leave gaps between the skin and the electrode (Figure 4-2a), paste-based electrodes, often with a cup shape (Figure 4-2b), fill these gaps and can effectively hydrate the skin surface, further increasing the active contact area through the penetration of electrolytes into the pores of the skin. This, in turn helps reducing the impedance.[142]

Studies about ionically conductive pastes for EEG applications are still limited. Lau et al.[149] systematically compared two commercial pastes, Ten20® and Elefix®, used in combination with two adhesives, Collodion® and Hypafix®. Ten20® and Elefix® pastes are generally composed of short-chain polyoxyethylene compounds, water, glycerol, calcium carbonate, and sodium chloride.[145], [146] The tests were performed by installing 25 disposable Ag/AgCl disk electrodes on 100 test subjects according to the international 10-20 system, after preparation of the skin with an abrasive paste. As installing EEG on a scalp is time-consuming, the setup time for each paste with adhesive was measured and compared. Collodion adhesive with Ten20® paste showed the best performance as it yielded the lowest percentage of patients who required a replacement for dried, fallen-off or otherwise damaged electrodes.

The main drawbacks of paste-based electrodes are the long setup time, the need for skin preparation prior to measurement, the difficult removal of the paste from skin and hair at the end of the measurements and the signal degradation over time due to drying of the paste.

Gel-based electrodes: Tough ionic hydrogels or organogels can be an alternative to pastes as ion conductive media between electrodes and skin. The pastes described above (Figure 4-2c) are more elastic and easier to handle, although more prone to drying. Shen et al.[150] synthesized an organogel consisting of a matrix of polymerized N-acryloyl glycinamide and potassium carbonate as the source of ions. This material showed an average skin-electrode impedance around 13 $k\Omega \cdot cm^2$ at a frequency of 10 Hz in the hairy region of the scalp, which remained stable over 8 hours. In addition, glycerol was added to increase the moisture retention ability and provide a hydrating effect on the stratum corneum layer and thus lowering the impedance. Similarly, Jakab et al.[151] produced a polyvinyl alcohol-based hydrogel by integrating glycerol and NaCl and reported a ten-fold increase in impedance after 25 days, showing moderate sensitivity to dehydration. Alba et al.[142] investigated hydrogel-based EEG electrodes using a cross-linked sodium polyacrylate gel, which was swelled with electrolytes containing urea. Electrical characterization showed that the low contact impedance of about 15 $k\Omega \cdot cm^2$ at 10 Hz was maintained for at least 8 hours. The impedance of this hydrogel was one order of magnitude lower than that of a commercially available paste on non-abraded skin.

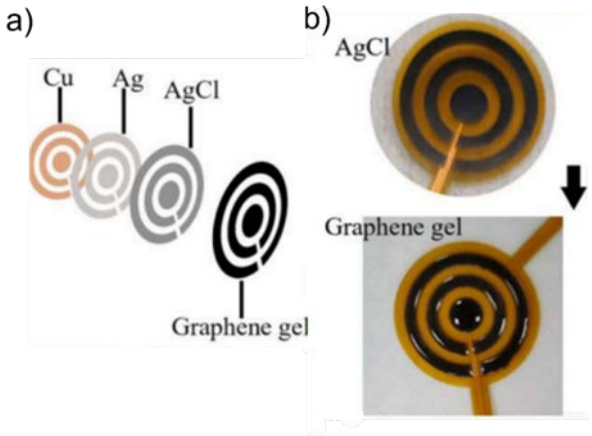

Figure 4-3 a) Design of the tri-polar concentric ring electrode arrays. B) Self-adhesive graphene gel on the tri-polar concentric rings. Reproduced with permission from [152].

Wang et al.[152] reported a different approach for reducing the contact impedance and improving the spatial resolution, based on a tri-polar concentric ring electrode array (Figure 4-3a) with a

flexible self-adhesive graphene gel (Figure 4-3b). The tri-polar concentric rings, based on a discrete array of nine-point electrodes,[153] were able to accurately localize and distinguish between sources from different locations on the head, therefore exhibiting high spatial resolution. The large number of micropores in the graphene gel allowed for abundant storage of electrolytic solution, helping with skin hydration. Electrical characterization showed minimal potential drift and relatively constant noise amplitude, with better noise levels than commercial Ag/AgCl gel electrodes. The self-adhesive gels showed a similar impedance to commercially available Ag/AgCl gel electrodes, with 6 $k\Omega \cdot cm^2$ for the graphene gel and 4 $k\Omega \cdot cm^2$ for the tested commercial gel.

Sponge electrodes: Sponge electrodes (Figure 4-2d) consist of a conductive sponge in contact with the skin, typically saturated with saline solution to improve ionic conductivity. These electrodes are in general not suitable for long-term measurement, as the impedance increases drastically as the solution dries out. Krishnan et al.[154] developed electrodes made of carbon nanofibers dispersed in a hydrophilic polyurethane foam, which allowed applications for both moist and dried out electrode interfaces while maintaining a low electrode-skin impedance over time. The hydrophilic polyurethane is used for its ability to retain water, while the carbon fibers make the foam electrically conductive. The skin-electrode impedance was 14 kΩ at 1 kHz, even after 20 hours.

Semi-dry electrodes: Semi-dry electrodes are generally composed of a reservoir of electrolyte and a porous material which gradually releases the electrolyte on the skin to counter dehydration. They provide the excellent contact impedance of wet electrodes and the durability for long-term use of dry ones. As they do not require skin preparation, semi-dry electrodes offer rapid setup and self-application. They have low skin-electrode impedance, which stems from the release of a small amount of electrolytic solution onto the skin. Approximately a few tens of microliters of solution are necessary for semi-dry electrodes, as opposed to 1-2 mL for electrodes requiring conductive gels (Figure 4-2c).[155] First-generation semi-dry electrodes released the electrolytic solution under pressure but often suffered from uncontrollable release, while second-generation ones consist of porous materials, which released the solution continuously and in a controllable fashion.[155], [156]

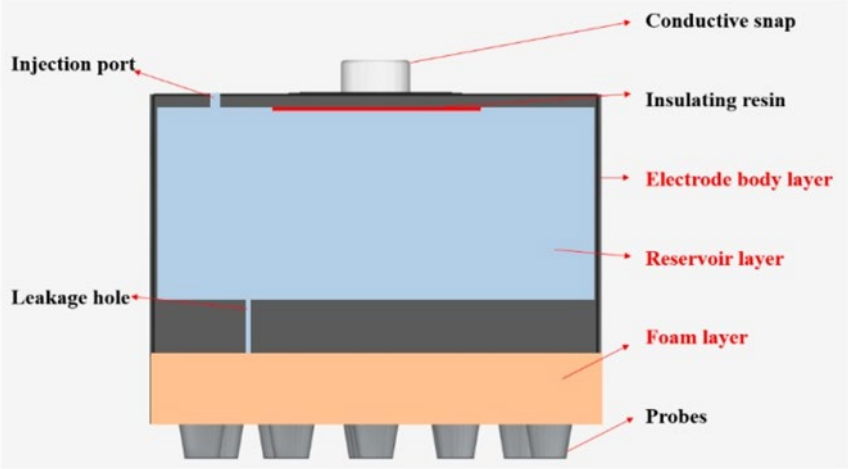

Figure 4-4 Schematic illustration of a multi-layer semi-dry electrode. Reproduced with permission from[157].

Hua et al.[157] developed flexible multi-layer semi-dry devices (Figure 4-4) for scalp EEG measurements at hairy sites using separate flexible electrode, foam, and reservoir layers. The electrode body layer and probes were made of a polydimethylsiloxane (PDMS) and 40 wt% Ag nanoparticles composite. The Ag/PDMS composite showed good electrical conductivity and stability. The probes were covered with a foam material (not specified) coated with Cu and Ni nanoparticles, to improve the conductivity. A 0.9% NaCl solution was stored in a reservoir layer, separated from the conductive snap by an insulated layer, to avoid electrochemical noise during the signal acquisition. During the monitoring, the electrolytic solution was continuously released through the foam layer to maintain a low contact impedance. The skin-electrode impedance of these electrodes was 23.89 ± 7.44 kΩ at 10 Hz and remained below 40 kΩ over 5 hours. Similarly, Gao et al.[158] presented a bristle-shaped semi-dry electrode of carbon-coated nylon bristles connected to a reservoir of water-imbibed cotton. They achieved a contact impedance of 15 kΩ at 10 Hz.

Overall, semi-dry electrodes offer an excellent solution to prevent drying of the electrolyte by using a reservoir of electrolytic solution that slowly exudes to keep an effective skin-electrode contact. Nonetheless, they remain sensitive to drying when the electrolyte gets exhausted from the reservoir. Furthermore, the precipitated salts left on the skin could induce irritation.[159], [160]

Summary and remarks about wet electrodes: Wet electrodes, such as paste, gel, sponge, and semi-dry, offer a variety of alternatives for improving the electrical contact between the skin and

the electrode. The selection of electrode type relies on the specific application requirements and needs to take into account several factors, such as signal quality, setup time, ease of use, and long-term durability.

In summary, wet EEG electrodes offer several advantages compared to their dry counterparts. The presence of a conductive gel, paste or electrolytic solution promotes a better skin-electrode interface and results in lower contact impedance and higher accuracy of recorded brain activity. It also makes the electrodes more comfortable for the user and helps to minimize drift and electrode movement.

However wet electrodes have a few disadvantages worth considering. One drawback is the long setup and cleaning time. Additionally, the ionically conductive medium can dry out over time, leading to an increase in impedance and reduced signal quality. The maintenance and cleaning of wet electrodes are also crucial to prevent contamination or degradation of the gel, requiring additional effort and resources.

Table 4-1 Summary of the average contact impedance at given frequency of the electrodes discussed in this review. The values are either in kΩ or kΩ.cm^2, as reported in the literature.

Electrode Type	Materials	Average Contact Impedance	Frequency (Hz)	References
Commercial paste	Ten20®	<10 kΩ	10	Pilloni et al.[161]
Hydrogel	Glycerol/Polymerized N-Acryloyl Glycinamide	13.15 ± 3.72 kΩ.cm^2	10	Shen et al.[150]
	Solid Contact Gel/Silver-Coated Polylactic Acid	20-200 kΩ.cm^2	10	Jakab et al.[151]
	Polyacrylate gel	15 kΩ.cm^2	10	Alba et al.[142]
	Tri-polar Concentric Rings/Self-Adhesive Graphene Gel	< 6 kΩ	10	Wang et al.[152]
Sponge	Carbon Nanofibers/Hydrophilic Polyurethane Foam	5-20 kΩ	1000	Krishnan et al.[154]
Semi-dry	Flexible Body Layer, Foam Layer, Reservoir Layer	23.89 ± 7.44 kΩ	10	Hua et al.[157]
	Carbon Coated Nylon Conductive Fibers	15 kΩ	10	Gao et al.[158]
Comb, Fingered, Spike	Thermoplastic Polyurethane/Carbon Black	70-90 kΩ	30	Xing et al.[162]
	Ethylene Propylene Diene Monomer Rubber/Carbon Black	10-100 kΩ.cm^2	10	Chen et al.[163]
Bristle	Polymer Bristles Coated with Silver-Based Conductive Ink	115 kΩ.cm^2	10	Grozea et al.[164]
	Carbon Fiber/Polyurethane/Carbon Nanotube/Gold	133 kΩ	31	Gao et al.[165]
Micro-Spike	Polyurethane/Epoxy/Ag-coating	7-25 kΩ	N/A	Ng et al.[166]
	SU-8 needles/silver film/Nanoporous Parylene Film	6 kΩ	15	Arai et al.[167]

	3D-printed acrylic-based photopolymer with titanium and gold coating	62 kΩ	10	Salvo et al.[168]
Foam	Polyurethane Foam/Taffeta Fabric Coated with Ni/Cu	4-26 kΩ	0.5 to 10000	Lin et al.[169]
	Polyurethane foam coated with polyaniline	1450 kΩ	N/A	Muthukumar et al.[170]
Tattoo	Inkjet-printed electrodes on commercial temporary tattoo paper using (PEDOT:PSS)	16.7×10^3 kΩ.cm^2	10	Ferrari et al.[171]
Dry Adhesive	PDMS/Silver Particles	50 kΩ.cm^2	10	Stauffer et al.[172]
Non-Contact	Carbon Nanotube/PDMS adhesive	117.21 (lowest) kΩ	0.1	Lee et al.[173]

4.4.2 Dry Electrodes

Dry electrodes use traces of moisture and sweat as electrolytes at the skin-electrode interface, therefore they do not require gels or pastes.[174],[155], [160] These electrodes are less prone to change over time because of electrolyte evaporation and cause minimal skin irritation. However, it is necessary to compensate for the lack of electrolytes by improving the skin's contact.

Dry electrodes are more accessible to the general population, as they do not require the intervention of a trained technician and can be placed on the skin without special preparation, such as skin abrasion or gel or paste application, which would dirt the scalp and become a source of discomfort.[175]

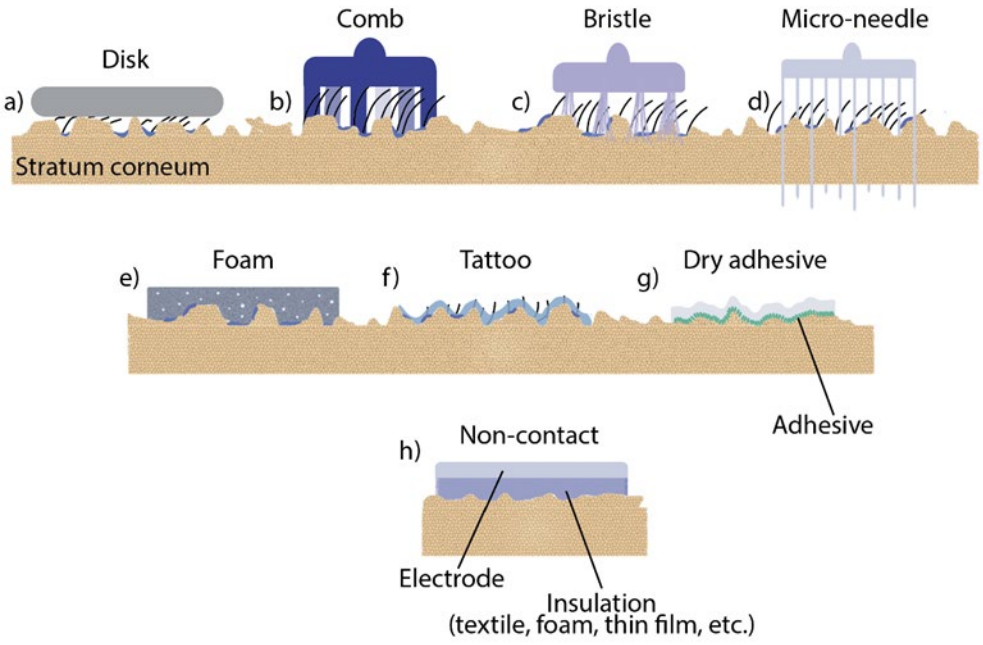

Figure 4-5 Eight types of dry electrodes on an irregular stratum corneum layer of the skin. a) Metal disk, b) comb, c) bristle, d) micro-needles, micro-spikes or micro-seepage, e) foam, f) tattoo, g) dry adhesive, and h) non-contact.

However, as dry electrodes are not tightly attached to the scalp, the signal is more prone to motion artifacts. In addition, the mechanical mismatch[176] between the electrode and the softer scalp causes mechanical distress to the electrode structure for long-term use. Dry electrodes with improved contact with skin have been designed to address these issues. Dry electrodes for EEG can be divided into two categories related to their mechanism: contact (resistive) and non-contact (capacitive) electrodes.

Contact electrodes: Contact electrodes are available in various shapes (Figure 4-5a-g), the simplest one being the disk electrode (Figure 4-5a), typically connected to the scalp using an adhesive or an electrode cap. The disk can be made of various materials, with Ag/AgCl currently leading the market.[159] Despite improvements, disk electrodes do not account for the presence of hair on the scalp, which is a significant obstacle for EEG measurements. This issue can be overcome with the use of comb electrodes.

Comb, Fingered or Spike Electrodes: Comb, fingered, or spike electrodes (Figure 4-5b) are designed to easily reach the scalp.[162], [163], [177], [178], [179] Xing et al.[162] reported a 3D-printed comb using a composite of thermoplastic polyurethane with embedded carbon black for conductivity. Despite a high skin-electrode impedance between 70 and 90 $k\Omega \cdot cm^2$ at 30 Hz, these electrodes are customizable, easy to use, and do not require a conductive gel or coatings.[162] Similarly, Chen et al.[163] fabricated two kinds of comb-electrodes: 1) a polymer 3D-printed using stereolithography coated with metal (TiW/Cu/TiW/Au), and 2) a compression- molded conductive composite of ethylene propylene diene monomer rubber mixed with carbon black. A skin-electrode impedance between 10 and 100 $k\Omega \cdot cm^2$ for the latter depending on the carbon black content. While further investigation is required, these electrodes are interesting due to their rapid and straightforward application.

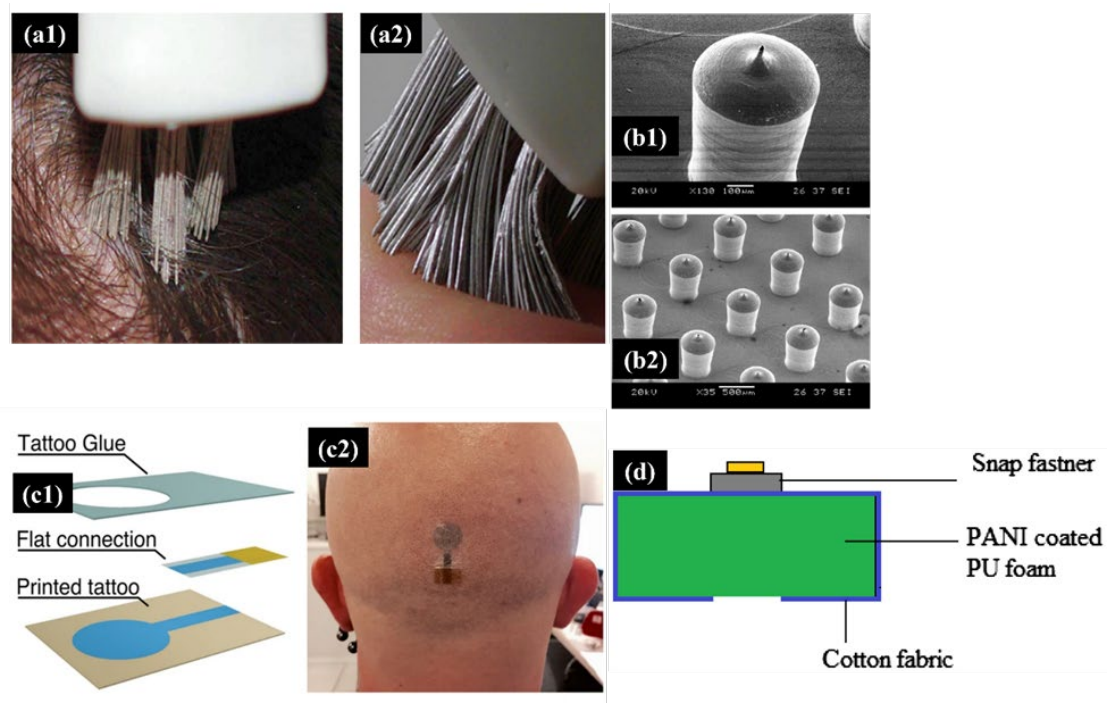

Figure 4-6 (a1) Silver-coated polymer bristle electrode through hair, (a2) flexing. (b1) Scanning electron microscopy images of zoomed in single micro-spike, (b2) several micro-spikes. (c1) Layered structure of a temporary tattoo electrode (TTE), (c2) a TTE on the scalp, (d) Design of foam electrode. Reproduced with permission from (a) [164], (b) [166], (c) [171], and (d) [170].

Bristle Electrodes: Bristle electrodes use a strategy similar to comb electrodes (Figure 4-5c). They feature small, brush-like bristles to distribute pressure evenly on the scalp without causing discomfort or breaking the skin barrier. The flexible bristle structures can fit the irregular surface of the scalp and increase the contact area. Grozea et al.[164] reported silver-coated flexible polymer bristles for long-term use (Figure 4-6a1,a2). The bristles helped reach the scalp through thick hair and led to skin-electrode impedances similar to wet electrodes (around 11.5 kΩ·cm^2 at 10 Hz). Gao et al.[165] prepared dry polyurethane/carbon nanotube and carbon fiber-based bristle electrodes, which were electroplated with Au to obtain a skin-electrode impedance of 133 kΩ.
Even though comb and bristle electrodes penetrate through hair, another source of high contact impedance is the epidermal stratum corneum layer.[160] This layer is often abraded with a paste to increase the signal quality. An alternative to abrasion is using electrodes exhibiting micro-needles or micro-spikes, which penetrate through the stratum corneum (Figure 4-5d) and ensure mechanical stability.

Micro-Needle or Micro-Spike Electrodes: As mentioned previously, the stratum corneum is highly resistive and only semi-permeable to ions. It would therefore greatly lower the contact impedance if this skin layer was bypassed. This is achieved through micro-needles or micro-spikes, which can be obtained through various fabrication methods such as photolithography, laser machining, electrical discharge machining, 3D printing, micromolding, and many other.[180]

Ng et al.[166] elaborated upon a vacuum-casting technology to fabricate Ag/AgCl-coated epoxy resin micro-spike electrodes for EEG (Figure 4-6b1,b2). Vacuum casting is a process used to cast elastomers into a mold previously made from a master pattern. A vacuum is applied to draw a liquid into the intricate details of the mold. Computer numerical control (CNC) micromachining was carried out to fabricate the master pattern for an electrode with dozens of spikes of a diameter of 6 μm to penetrate the stratum corneum. Arai et al.[181] and Stavrinidis et al.[182] fabricated a similar microneedle electrode using SU-8 and photolithography. Arai et al. measured a stable impedance of 6 kΩ at 15 Hz as opposed to over 200 kΩ when the stratum corneum was not penetrated and a contact impedance of 10 kΩ for wet Ag/AgCl electrodes.

Salvo et al.[168] reported a 3D-printed micro-needle electrode consisting of 180 conical needles with a height of 3 mm, a base diameter of 600 μm and a tip diameter of approximately 100 μm. The needles were printed using a stereolithography-based 3D printer with a biocompatible acrylic-based photopolymer. As this polymer is insulating, it was sputter-coated with titanium to promote the adhesion of the final gold layer which was evaporated on the micro-needles. However, they were not sharp enough to penetrate the skin. They reported a skin-electrode impedance of 62 kΩ at 10 Hz. Similarly, Kavaldzhieh et al.[183] 3D printed a biocompatible micro-needle electrode with an average tip diameter of 580 nm which was able to penetrate the skin. Two-photon polymerization lithography was used to obtain cylindrical micro-needles which were subsequently coated with Fe to make them electrically conductive. Despite the constraints posed by the limited availability of 3D-printable materials and the need for a post-treatment process that imparts electrical conductivity to the electrode, the utilization of such 3D-printed electrodes represents a significant advancement in the realm of rapid prototyping and customized electrode development. Therefore, micro-spikes that penetrate this highly resistive skin layer improve the signal quality by reducing the skin-electrode impedance and motion artifacts. Nevertheless, as they puncture the skin, they are a cause for irritation as well as hygienic and safety concerns over time.

Other Types of Dry Electrodes: One prevalent non-invasive strategy for achieving conformal contact with the skin is using conductive foams. The foam allows for high conformity to the irregular surface of the scalp (Figure 4-5e) and maintains low skin-electrode impedance. Lin et al.[169] prepared a dry electrode made of polyurethane foam, covered with a 0.2 mm thick taffeta fabric, and coated with Ni/Cu. The electrodes were secured to the head using adhesive tape. They reported a skin-electrode impedance for frequencies of 0.5 to 10 kHz of around 29 $k\Omega \cdot cm^2$ and 4.5 $k\Omega \cdot cm^2$, respectively.

Using a different technique, Muthukumar et al.[170] developed a foam-based electrode by polymerizing aniline in situ into a polyurethane foam (Figure 4-6d). The polyurethane foam was first soaked into a bath of aniline monomer solution and hydrochloric acid. Afterwards an aqueous solution of ammonium persulfate (oxidizing agent) was added to initiate the polymerization. The obtained polyaniline-coated polyurethane foam had a skin-electrode impedance of 1.45MΩ.

Temporary tattoos (Figure 4-5f) have been utilized for monitoring electrophysiological signals, as they provide conformal and imperceptible contact to the skin using van der Waals forces,[184] and permit the hair to grow through them.[171], [185], [186] Ferrari et al.[171] used inkjet-printed electrodes on 1.5 μm thick commercial temporary tattoo paper using a poly(3,4-ethylenedioxythiophene):polystyrene sulfonate (PEDOT:PSS) aqueous dispersion and confirmed their electrical stability for up to 48 hours (Figure 4-6c1,c2). They reported a skin-electrode impedance of around 17×10^3 $k\Omega \cdot cm^2$ and 1.3×10^3 $k\Omega \cdot cm^2$ at 10 Hz for their printed tattoo electrode and a commercial wet Ag/AgCl electrode, respectively. A higher signal-to-noise ratio (SNR) of 4.07 was obtained for the tattoo electrodes as opposed to 3.36 for Ag/AgCl electrodes.

Yet another strategy is the use of dry adhesive electrodes (Figure 4-5g) combined with a conductive element. Using photolithography, Stauffer et al.[172] fabricated a dry silicone/silver microparticle electrode with micropillar geometry inspired by gecko feet and grasshopper tarsus from which dry adhesion stems. They obtained a skin-electrode impedance of 50 $k\Omega \cdot cm^2$ at 10 Hz. This shows interesting potential for using dry adhesives in developing dry contact electrodes for EEG.

Non-contact electrodes: Dry capacitive or non-contact electrodes do not have direct electrical contact with the skin (Figure 4-5h). They can be integrated into clothing, rapidly installed, and reused. In addition, they eliminate the risk of skin irritation. Nonetheless, they are more prone to

motion artifacts than adhesive or wet electrodes. As the EEG is measured through capacitance, complete contact with the scalp is unnecessary. In capacitive electrodes, the hair, air, and insulator layer cause high impedance between the conductive layer and the scalp, which is unavoidable. Therefore, larger electrodes, shorter gaps between the skin and the electrode, or preamplifiers, are essential to achieve similar results to contact electrodes.

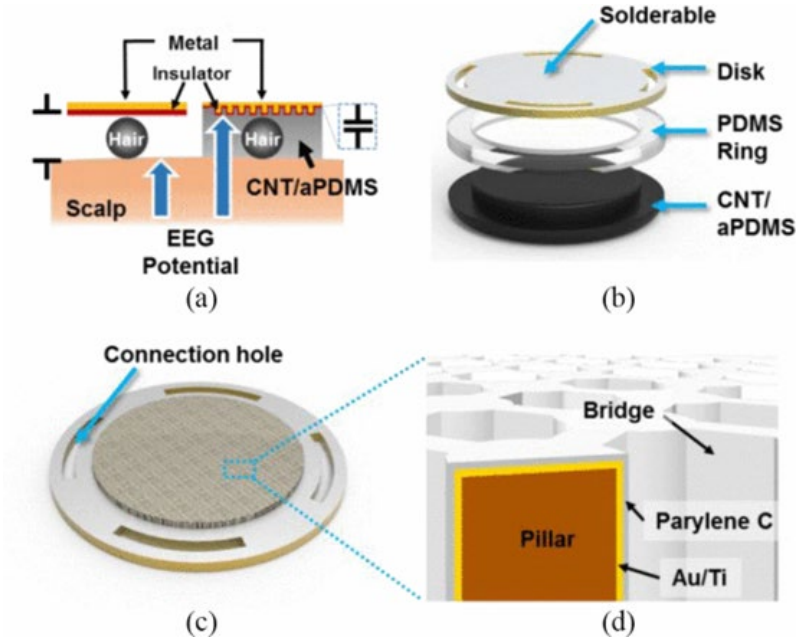

Figure 4-7 (a) Schematic of the implemented concept for a non-contact electrode. (b) Structural illustration, (c) bottom view, and (d) cross-sectional view of the electrodes. Reproduced with permission from ref [173].

These dry capacitive electrodes consist of a conductive base capacitively coupled with a dielectric or electrode plate covered with an insulating material such as foam, textile, or adhesive, which will be in contact with the scalp.[187]

As an improvement of typical non-contact electrodes, where the gap is mostly filled with hair and air, Lee and al.[173] fabricated a self-adhesive insulated electrode using a PDMS/carbon nanotube composite in the gap as a conductive adhesive that attached to the hair and ensured close contact with the skin, separated from the main electrode by a Parylene C insulating layer (Figure 4-7). The main electrode and the composite in contact with the skin acted as the two plates of a capacitor. A pillar and bridge structure were adopted for the disk electrode to increase the contact area and therefore the capacitance between the carbon PDMS/carbon nanotube composite and the metal electrode. They achieved an impedance of 117.21 kΩ at 0.1 Hz.

Summary and remarks about dry electrodes: Dry EEG electrodes offer several advantages over wet electrodes. Firstly, they eliminate the need for gels or pastes, making them more practical and convenient. This feature also allows for easy and fast setup, decreasing the preparation time and facilitating rapid application, while offering enhanced durability and reusability. Consequently, dry electrodes have the potential to increase the accessibility of EEG technology and expand its range of applications for long-term monitoring and home-based EEG assessments, due to their simplified application and maintenance.

However, dry EEG electrodes also present some disadvantages. The absence of an ion conductive medium at the electrode/skin interface impedes the electrode's ability to establish a low-impedance connection with the scalp, resulting in a reduced signal quality compared to wet electrodes. This can lead to increased noise, lower signal-to-noise ratio, and reduced accuracy in capturing subtle brain activity. Lastly, dry electrodes are more susceptible to motion artifacts due to their less secure attachment to the scalp.

4.4.3 Consumer Forehead EEG Devices

Consumer-friendly forehead EEG devices[188] (characteristics summarized in Table 4-2) have been gaining popularity among the general public for various applications, such as meditation, entertainment,[189], [190] and research.[191], [192], [193], [194], [195] The available information about the electrodes hardware is scarce since most of the work is proprietary. Other than BrainCo Focus 1, all listed electrodes are dry, mainly made of metals (the type of metal not specified).

The accuracy and functionality of readily available EEG headbands have been studied. Some clear advantages of these devices include relatively low cost (especially compared to clinically available counterparts), user-friendliness, versatile applications, non-invasive and ease of incorporation into daily life. However, a few disadvantages prevent their widespread use, mostly in research and clinical environments. They can be uncomfortable (especially during sleep) with an awkward look, which will prevent prolonged use. Moreover, these devices can lack accuracy, since the shape of the forehead hinders good contact between electrode and skin, in addition to the testing error introduced by the user’s misplacement of the headband.

Table 4-2 Summary of the most common EEG headbands.

Device name	Application	Electrode material	Number of electrodes
Muse Gen 2	Meditation Sleep tracking Stress management Medical	Conductive gold	7 (2 on forehead, 2 behind ears, 3 reference)
Macrotellect	EEG detection Entertainment Meditation	Dry electrodes	Three dry EEG electrodes (active, reference, and ground) 0.3mm electrodes[196]
Neurosky Mindwave	Health and wellness Education Entertainment	Stainless steel dry electrodes[197]	Single electrode neutral points on ears by ear clips[198]
Emotiv EPOC+	Research	Saline soaked felt pads	14 channels Other versions with 2, 5, or 32 channels
BrainCo Focus 1	Mental health Sports Meditation	Proprietary hydrogel	3 electrodes
Dreem	Sleep studies	Dry - silicone	5 (2 frontal, 1 ground, 2 occipital) high consistency silicone with soft, flexible protrusions on electrodes[199]
OpenBCI EEG Headband	Research	Comb and flat snap Ag/AgCl	8 channels

4.5 Around-Ear EEG

This section reviews research on around-ear EEG, which is a non-invasive brain monitoring technology that involves placing electrodes around the ear to record electrical signals from the brain. The region surrounding the ear is an excellent location for EEG research because of its proximity to the brain. Moreover, the skin in this region is mostly hairless, smooth, and easy to clean.

4.5.1 cEEGrids

cEEGrids, introduced by Debener et al. in 2016, are c-shaped flexible behind-ear arrangements, with 10 electrodes distributed on the "C" (Figure 4-8).[200] The electrodes, screen printed on flexible polyimide, consisted of conductive Ag/AgCl-based polymer thick film with copper traces and gold-plated ends and were embedded in a base material of a biocompatible polyimide. No further details about the materials and the fabrication procedure are given. Finally, an electrolyte gel was used to ensure the contact with the skin. This setup was later studied further by other researchers. The cEEGrid was used in comparison with scalp EEG[201] and in-ear EEG[202] and showed comparable signal quality.

A central requirement of any EEG device is the ability to collect good quality, stable and reliable brain signals. The objective of the research for novel electrode materials is to ensure comfort and signal efficiency by reducing electrode-skin abrasion. The most challenging issues for cEEGrids are the fragility of the adhesive used to hold the electrodes in place, and the effect of disturbance by hair and interference due to natural sweating.

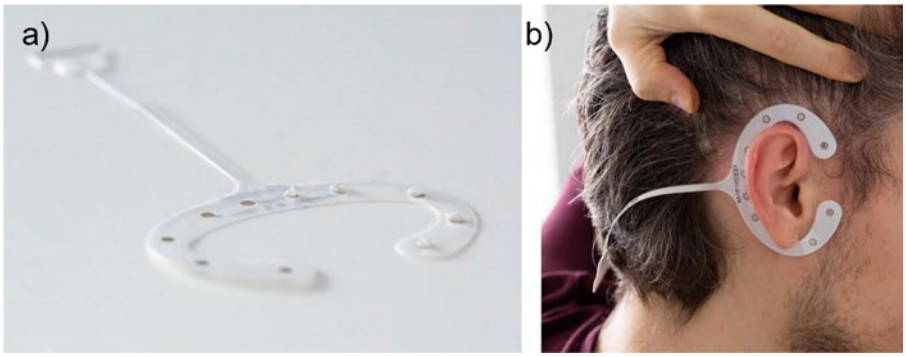

Figure 4-8 a) cEEGrid preparation with gel and b) its positioning behind the ear. Reproduced with permission from [203].

4.5.2 Other Around-Ear Systems

A few other around-ear systems have been studied besides cEEGrid. Such systems typically work with 2 or 3 electrodes on each side attached via glue or tape[204], [205], [206] to the area behind the ear. Other devices have electrodes housed in a 3D-printed package, such as earpieces[207], [208] and headphones.[209] There is little information about the type of electrodes, as most of the studies are aimed at proof-of-concept for the feasibility of using around-ear-EEG compared to scalp EEG. Gu et al.[204] compared around-ear and scalp EGG to continuously monitor potential seizures in epileptic patients. Tests were performed simultaneously, and the same ground and reference electrodes were used. For around-ear EEG, two electrodes (of unknown material) were glued (of unknown material) to the skin behind the ear. Figure 4-9a depicts the electrodes behind the left ear. The two techniques yielded similar results.

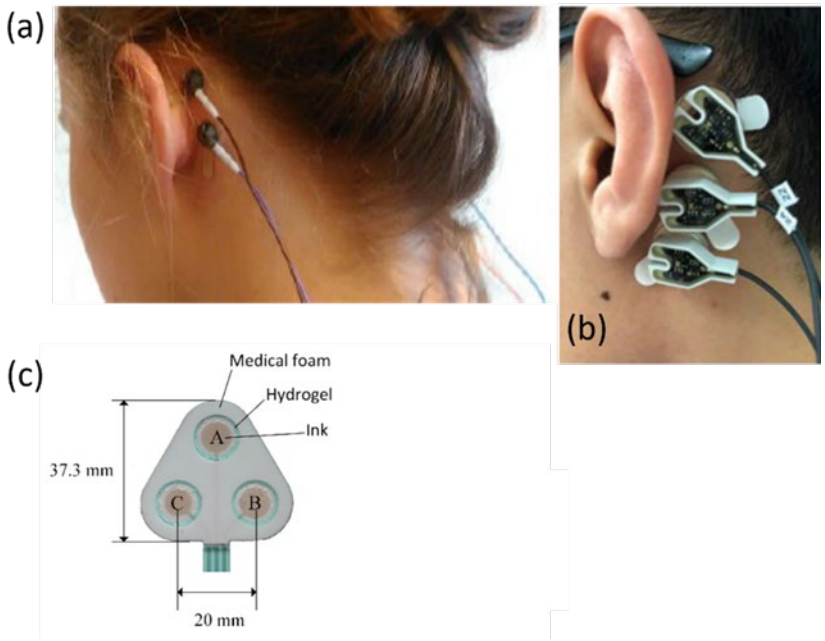

Figure 4-9 (a) Around-ear-EEG setup glued on the skin, (b) Ring holder and electrodes attached to the skin using double-sided tape, (c) screen-printed Ag/AgCl electrodes. Reproduced with permission from (a) [204], (b) [205], and (c) [206].

Choi et al.[205], [210] used double-sided tape to attach six rubber ring holders (three on each side) behind the ear (Figure 4-9b), utilized to hold the electrodes in place. The primary objective of this study was to optimize the conditions of the reference electrode to minimize the cancellation or

blockage of brain signals. This setup is not suitable for a continuous portable EEG system, especially during sleep since it is very bulky and would be very unstable and uncomfortable.

Klevo et al.[206], [211] studied the effect of sweat on six different configurations of Ag/AgCl screen-printed electrodes (Figure 4-9c). The electrodes were printed on flexible polyethylene terephthalate (PET) films, covered by a non-conductive medical foam, and their area was surrounded by an adhesive hydrogel membrane to ensure contact with the skin. Three types of electrodes (A, B, and C in Figure 4-9c) with different layer configurations were used in each specimen. The overall skin-electrode impedance decreased after sweating.

Valentin et al.[208] introduced a novel design for an around-ear prototype, which did not require glue, tape, or a headband. In this approach, an imprint of the area behind the ear was taken using modeling paste. Average ear geometry of eight volunteers was used to prepare a geometrical model. This produced a generic behind-the-ear piece that fits most people. Using this prototype, a frame was printed with stereolithography, using a malleable acrylic resin. The electrodes were made of a composite of 1.5-3% carbon fiber mixed in a silicone matrix and later were embedded in each earpiece.

4.6 In-Ear EEG (Ear-EEG)

In-ear EEG (or simply) ear-EEG refers to devices which capture brain signals from inside the ear canal. The skin surface of ears is generally hairless, so the patient's hairstyle will not introduce any hurdles. Furthermore, in-ear electrodes are considerably easier to use, primarily because of the minimal preparation and cleanup procedure. This section provides a comprehensive survey of the materials and configurations for ear-EEGs.

4.6.1 Personalized Earpieces

The research by Looney et al.[212] was the first study exploring the possibility of attaching electrodes on the outer surface of a personalized and individually molded earpiece to obtain EEG recording (Figure 4-10). Since ears appear in all shapes and sizes, first, an impression of the outer ear and ear canal was taken using a malleable and quick-setting material, such as silicone or wax. The mold was then scanned using a 3D scanner and manufactured using additive manufacturing. Afterward, three Ag/AgCl electrodes were mounted on the outer surface of the tailor-made piece, and a layer of gel (material not specified) was spread on the dry electrode. The ground electrode was placed on the chin, and the reference electrode on the right earlobe. The end of the earpiece was inserted inside the ear canal, while the electrodes were inserted no more than 10 mm inside

the ear to ensure comfortability and adherence to jurisdictional rules and regulations set for mitigating damage to ears. The feasibility of the proposed in-the-ear (ITE) recording platform was studied. To achieve this, a recording was performed simultaneously with ITE and scalp EEG, using mutual supporting hardware (leads, ground and reference electrodes and amplifier). The results showed excellent coherence between the results in the extraction of major EEG activity.

The strategy was subsequently followed by a few researchers, using similar personalized earpieces, with minimal changes, to study and build on the preliminary applications.[213], [214], [215], [216] Kidmose and Looney et al. investigated the suitability of using the personalized ear-EEG for auditory evoked potentials.[214], [215] They found the signal level of the ear-EEG to be of slightly lower amplitude (10-20 dB lower) than scalp EEG. However, the comparable signal-to-noise ratio, proved the new setup to be appropriate for this application.

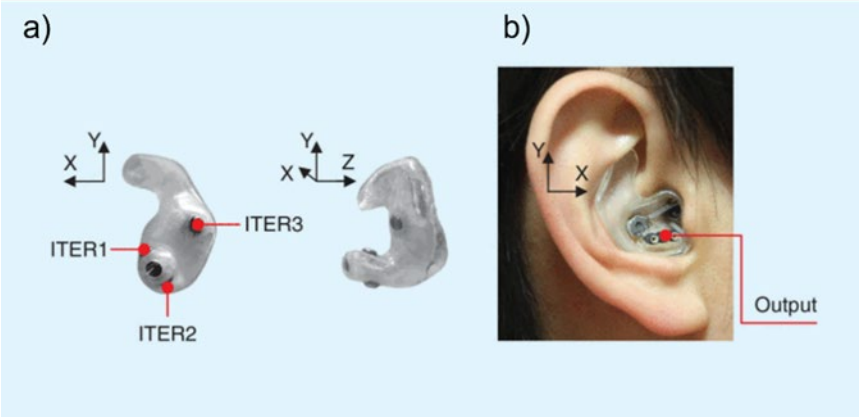

Figure 4-10 Ear-EEG earpiece for the preliminary studies. (a) The earpiece with the three mounted in-the-ear electrodes for the right ear (ITER); (b) The fitted earpiece. Reproduced with permission from [217].

Kappel et al.[218] studied the effectiveness of dry and wet ear-EEG electrodes by comparing their skin-electrode impedance. Silver was used as the dry electrode material, while for the wet electrodes, a commercially available electrode mixture paste (Elefix®) was applied to the dry silver electrodes. The dry electrode showed a variance in the impedance results, far higher than in wet electrodes, which is most likely caused by poor skin-electrode contact. Kappel et al. then targeted the noise and artifacts inherently present in EEG measurements. They compared artifacts in ear and scalp EEG[219] using the same silver electrode-conductive paste electrode setup. Four groups of physiological artifacts were studied (jaw artifacts, eye-blinking, eye-movement, and head

movement). The study revealed that ear-EEG was more prone to jaw-related artifacts and less prone to eye-blinking artifacts compared to state-of-the-art scalp-based systems.

Next, circular iridium-oxide (IrO_2) coated Ti-pin electrodes were fabricated and evaluated to study the characteristics of dry-contact electrodes.[220] The goal of dry-contact electrodes was to increase comfortability and accessibility and decrease the preparation time. A similar setup[221] using the same dry electrodes was used for sleep monitoring purposes and found the performance at levels analogous to scalp EEG.

4.6.2 Generic Earpieces

The personalization process is lengthy, costly, and strenuous. Using generic consumer earpieces with different electrodes attached, is an easier process for manufacturing ear-EEG.[222], [223], [224], [225], [226] TipTrodes, commonly used as generic conductive ear-pieces, are disposable gold foil-covered polyurethane foam earpieces, which are readily available and used in in-ear research recordings.[227], [228] They come in two cylinder sizes, 10 and 13 mm in diameter, and consists of a tubular insert to allow soundwaves to pass. The idea of a generic and off-the-shelf earpiece for ear-EEG was first introduced by Kidmose et al.[229] in hopes of establishing a practical prototype. The generic earpiece is based on a conical-shaped earplug made of a biocompatible silicone rubber, which fits any ear (Figure 4-11a). The results demonstrated a lower signal quality of generic piece compared to the personalized earpieces. The superior signal quality from the personalized earpiece was mainly due to the much higher degrees of freedom of the position the electrodes are put in. Generic pieces suffer from poor electrode to skin contact. Although this was a step towards a portable in-ear EEG device, the low signal quality limited its use.

Many studies have attempted to fabricate earpieces using softer materials to achieve ultimate comfortability. A composite of carbon nanotube and polydimethylsiloxane (CNT/PDMS) was fabricated in the shape of a commercial soft canal-type earphone cap.[222] Since the fabrication process of CNT/PDMS composites is costly and cumbersome, a combination of hard (silvered glass beads) and soft material (silicone rubber) was been suggested to address this issue.[223] Kaveh et al. also focused on ease of manufacturing and the scalability of ear-EEG.[230] Polycarbonate, as the supporting material, was thermoformed on a 3D printed master mold and Ag was deposited on the surface to act as the electrodes.

All the previously mentioned generic earpieces suffer from the non-uniformity of the pressure against the skin. Goverdovsky et al.[231] introduced a novel design for ear-EEG to target this issue. The two key components comprising the new device are a memory foam earbud and commercially available flexible conductive cloth electrodes, consisting of silver-coated nylon fibers and interwoven elastic (Figure 4-11b). After positioning, the memory foam expands and provides the sought-after electrode-skin contact. The same prototype was used in subsequent works to study sleep monitoring,[232], [233], [234] person authentication,[235] and real-life human activity classification.[236]

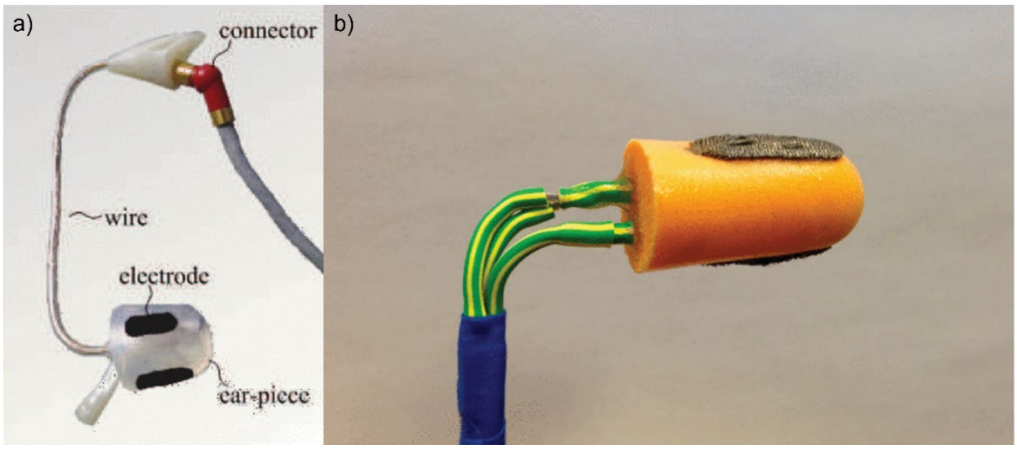

Figure 4-11 (a) Silicone rubber generic earpiece by Kidmose et al. (b) Memory foam earpiece by Goverdovsky et al. Reproduced with permission from (a) [229], and (b) [231].

4.7 Conclusion and Perspectives

Although incredible progress has been made since the emergence of EEG, especially in data characterization and interpretation, there are many challenges left pertaining to the setup and overall functionality of EEG hardware.

Electrodes are important components of an EEG system, as they serve as the interface between the brain's electrical activity and the recording equipment. Research in EEG electrodes is essential for several reasons, such as improving signal quality, reducing artifacts, enhancing user comfort, and expanding applicability.

Currently, there is one pressing need in EEG research: to engineer a device capable of recording long-term, mobile, and real-time data. If this goal is realized, it could revolutionize the world of diagnosis and treatment of neurological disorders and diseases. Ear-EEG has shown promising

results as a practical and convenient alternative to traditional scalp-EEG. Ear-EEG devices are small, lightweight, and portable, making them easy to wear and use in various settings. As the technology continues to improve, we can expect ear-EEG to become more accessible and affordable, making it an attractive option for brain monitoring and cognitive research. Ear-EEG has the potential to expand the applications of EEG technology beyond traditional clinical settings. It can be used for brain-computer interfaces, allowing individuals to control devices and interact with their environment using their brain signals.

Another future scenario for ear-EEG is the development of personalized and adaptive systems. By using machine learning algorithms and data-driven approaches, ear-EEG systems can be customized to individual users and adapt to their changing brain signals. This could lead to more accurate and precise brain monitoring and better outcomes for clinical and research applications.

One of the main challenges of ear-EEG is obtaining high-quality signals, due to the small surface area of the ear. To address this issue, we believe that materials based on conducting polymers, that can conform to the shape of the ear can provide better contact between the electrode and the skin. Conductive polymer electrodes, such as PEDOT:PSS-based materials, have shown promising results in improving signal quality and reducing noise, making them a potential solution for enhancing ear-EEG technology. These electrodes can offer some advantages over traditional metallic electrodes, such as improved comfort (due to their flexibility) and versatility (can be easily integrated into various form factors and devices). Additionally, they can potentially offer reduced motion artifacts due to their flexibility and improved adherence to the skin, which helps reduce the impact of motion artifacts on EEG signal recordings, making them suitable for applications where users are in motion.

In summary, ear-EEG is a promising technology with the potential to transform brain monitoring and cognitive research. With ongoing advancements in technology and research, we can expect to see incredible developments, which can ultimately benefit both clinicians and researchers in the study and treatment of brain function and neurological disorders.

4.8 Acknowledgments

This work was supported by the Natural Sciences and Engineering Research Council of Canada (NSERC) through a Discovery Grant (RGPIN-2017-06319).

CHAPTER 5ARTICLE 2: MICROSPHERE-TEMPLATED CONDUCTIVE SYNTACTIC FOAMS FOR RECYCLABLE AND ADDITIVELY MANUFACTURED SOFT ELECTRONICS

5.1 Authors

Gayaneh Petrossian, Yassine Diouri, Bolan Xu, Sara Ebrahimi, Atharva Pande, Floriane Miquet-Westphal, Hang Xu, and Fabio Cicoira*

G. Petrossian, Y. Diouri, S. Ebrahimi, F. Miquet-Westphal, F. Cicoira

Department of Chemical Engineering, Polytechnique Montréal, Montréal, Canada

E-mail: fabio.cicoira@polymtl.ca

B. Xu, A. Pande, H. Xu

Department of Mechanical, Industrial and Aerospace Engineering, Concordia University, Montreal, Canada

Keywords: PEDOT:PSS syntactic foams, 3D-printable bioelectrodes, Ear-EEG, Conductive microspheres, wearable electronics, sustainable electronics

Submitted February 20, 2026, under revision at *Advanced Healthcare Materials*

5.2 Abstract

Soft, conductive materials that simultaneously offer mechanical compliance, electrical conductivity, recyclability, and scalable manufacturing remain difficult to achieve. Here, we introduce recyclable, 3D-printable PEDOT:PSS syntactic foams based on polymer microspheres coated in situ, enabling precise control over porosity, mechanical properties, and electrical conductivity. Microsphere-templated conductive shells provide a unique materials architecture that unites porosity control, tailorable flexibility, electrical functionality, recyclability, and additive manufacturability, which are capabilities that are challenging to achieve in conventional conductive foams. The resulting foams exhibit low elastic moduli comparable to soft biological tissues, stable electrical conductivity over a wide void-fraction range, and excellent compatibility with fused filament fabrication. Importantly, the foams can be reprocessed through both chemical

recycling and thermal reshaping, while preserving structural integrity and electrical performance. To demonstrate functional relevance, the conductive foams are integrated into soft wearable electrodes, enabling reliable acquisition of electrocardiogram (ECG), electromyogram (EMG), and in-ear electroencephalogram (EEG) signals, including clear alpha-band modulation. Overall, this work establishes conductive syntactic foams as a recyclable and manufacturable materials platform for soft and wearable electronic systems.

5.3 Introduction

The increasing demand for materials that are versatile yet lightweight has driven the advancement of multifunctional cellular foams. Due to their tailorable constituents and porous-structure-induced low density, these foams offer a unique combination of properties such as shock absorption, thermal insulation, vibration damping, and cushioning, making them indispensable across various industrial sectors, ranging from packaging to construction.[237] More recently, attention has shifted toward functional foams that go beyond conventional applications, for example, by incorporating electrical conductivity to expand their potential uses in wearable bioelectronics[238], [239], [240], [241] and energy storage.[242], [243], [244] This multifunctionality positions conductive foams as a new generation of materials capable of addressing both structural and electronic demands in wearable devices, such as an ear-electroencephalograph (ear-EEG), which requires soft, low-density, and conformal electrodes that can maintain good electrical contact in the confined and curved ear canal geometry.[245], [246]

Conductive foams generally integrate conductive fillers, such as carbon nanotubes,[247] graphene,[248] and metallic powders,[249] in polymer matrices via various foaming techniques to achieve tailored electrical and mechanical properties. Producing conductive foams is inherently challenging due to the need for uniformly dispersed fillers that ensure a continuous conductive network (percolation) without compromising the foam's lightweight structure and desired porosity. Additionally, strong adhesion between the fillers and the polymer matrix is critical for maintaining durability and consistent performance under mechanical stress or environmental exposure.[250], [251] However, the presence of conductive fillers alters viscosity and destabilizes bubbles, thereby interfering with the foaming process and complicating the balance between conductivity and structural integrity. Material compatibility and scalability also pose hurdles, requiring precise control over processing parameters to achieve uniformity and stability in large-scale production.

These challenges necessitate innovative approaches to optimize the fabrication and functionality of conductive foams.

Recently, 3D-printable foams have gained significant attention because they offer design freedom, rapid prototyping, and the ability to tailor lightweight cellular structures.[252] The main strategies include syntactic foams,[253] post-foaming of printed solids,[254], [255] and in-situ foaming of gas- or blowing-agent–saturated filaments.[256], [257] Recycling is a critical consideration for sustainable foam production, yet conventional foams generally lose their cellular architecture when melted or dissolved, requiring energy-intensive re-foaming to restore functionality. When conventional foamed polymers are 3D-printed through extrusion and layered sequentially, such as via the fused filament fabrication (FFF) method, their fragile porous architecture often collapses or degrades. Gas bubbles can merge into larger voids or dissipate under heat and shear forces, leading to structural instability and inconsistency in the printed component. Therefore, controlling pore distribution and retention during FFF remains a significant challenge.

Syntactic foams, which incorporate hollow microspheres (comprising glass, polymer, or ceramic) into a matrix, offer a promising alternative. Initially used in marine structures by virtue of their buoyancy,[258] hollow microspheres have recently gained attention for their ease of processing, scalability, and superior mechanical properties.[259], [260], [261] The pre-engineered, thermally stable microspheres maintain their integrity during reprocessing, so the bulk matrix can be melted and reshaped without destroying the porous structure. When the ease of processing and the rapid prototyping advantages of additive manufacturing are combined with the inherent recyclability of syntactic foams, it results in a highly versatile platform that enables efficient reuse, reshaping, and even self-healing while preserving both mechanical and additional functional performance.

Building on these advantages, researchers have explored strategies to functionalize syntactic foams by coating microspheres with conductive or protective layers to improve interfacial properties and multifunctionality.[262], [263], [264], [265], [266], [267] For example, polydopamine (PDA) has been employed as a versatile surface treatment layer on hollow carbon microspheres to enhance interfacial adhesion with polymer matrices. In addition to improving mechanical integration, PDA can serve as an effective anchoring platform for secondary metallic coatings, such as silver, enabling the fabrication of lightweight foams with high electromagnetic interference (EMI)

shielding effectiveness.[266] Similarly, silver-coated hollow glass microspheres fabricated via in-situ composite technique in the presence of polyvinylpyrrolidone (PVP), have achieved tunable shell thickness and shielding effectiveness values up to 70–80 dB in the GHz range.[264] More recently, multifunctional syntactic foams have been reported using silver- and nickel-plated microspheres embedded in shape-memory vitrimer matrices, enabling multi-functionality of conductivity, ferromagnetism, and recyclability.[265] While these studies demonstrate the promise of conductive syntactic foams, they are often constrained by high costs due to the use of metals, overall heavier weight compared to conventional foams due to the presence of metals that increase density, and possible long-term instability arising from metal oxidation. Alternative conductive materials for coating hollow microspheres require further investigation.

To overcome these limitations, some researchers have begun incorporating Poly(3,4-ethylenedioxythiophene)-poly(styrenesulfonate) (PEDOT:PSS) into porous foam structures, which offer a promising route to combine electrical functionality with the mechanical benefits of lightweight, flexible, and conformable architecture. PEDOT:PSS is a widely studied conductive polymer known for its conductivity, biocompatibility, and ease of processing. While it has been extensively used in thin-film form for electronic and bioelectronic applications, its inherent brittleness has limited its utility in mechanically demanding or structurally complex environments. Overcoming these challenges is particularly critical for developing three-dimensional, multifunctional sensing platforms that require materials that are conductive, biocompatible, and also mechanically robust and adaptable. Recent research has therefore focused on using alternative processing methods, such as blending-molding,[268] and electrodeposition,[269] to adapt PEDOT:PSS into architectures with varied geometries and functionalities. Various fabrication methods, such as freeze-drying,[270] dip-coating,[271], [272] and addition of foaming agents[239], [273] have been employed to create PEDOT:PSS-based foams. While these studies demonstrate the materials' potential in wearable and flexible sensors, opportunities remain to further control pore size and distribution, which are key to optimizing both mechanical strength and electrical performance.

Here, we demonstrate conductive polymer foams that are simultaneously 3D-printable and fully recyclable, while retaining mechanical and electrical performance over multiple reprocessing cycles. By incorporating PEDOT:PSS-coated polymer microspheres into a thermoplastic poly(ε-

caprolactone) matrix, we establish a scalable and straightforward materials strategy for fabricating lightweight syntactic foams with tunable porosity, electrical conductivity, and mechanical robustness suited to flexible bioelectronics. Localizing electrical functionality at the microsphere surface simplifies the fabrication of conductive foams compared to conventional approaches that rely on complex formulations incorporating carbon-based or metallic fillers. Importantly, the foams preserve their functionality through dual recyclability, either by selective matrix dissolution to recover intact conductive microspheres or by thermal reshaping into new geometries without performance loss. Collectively, this combination of moderate conductivity, processability, additive manufacturability, and sustainable reusability establishes a gel-free, reprocessable materials platform for next-generation wearable electronics and environmentally responsible device design.

5.4 Results and Discussion

5.4.1 PEDOT:PSS-covered Microsphere Preparation

An in-situ oxidative polymerization strategy was employed to prepare PEDOT:PSS-coated microspheres, as schematically illustrated in Figure 5-1a. The visual evolution of the powders with different synthesis durations of 2, 4, 8, 12, and 24 hours, shown in Figure 5-1b, clearly reflects the progression of polymerization: the color gradually shifts from white to dark blue as the reaction time increases, indicative of PEDOT:PSS formation and increasing coating thickness.

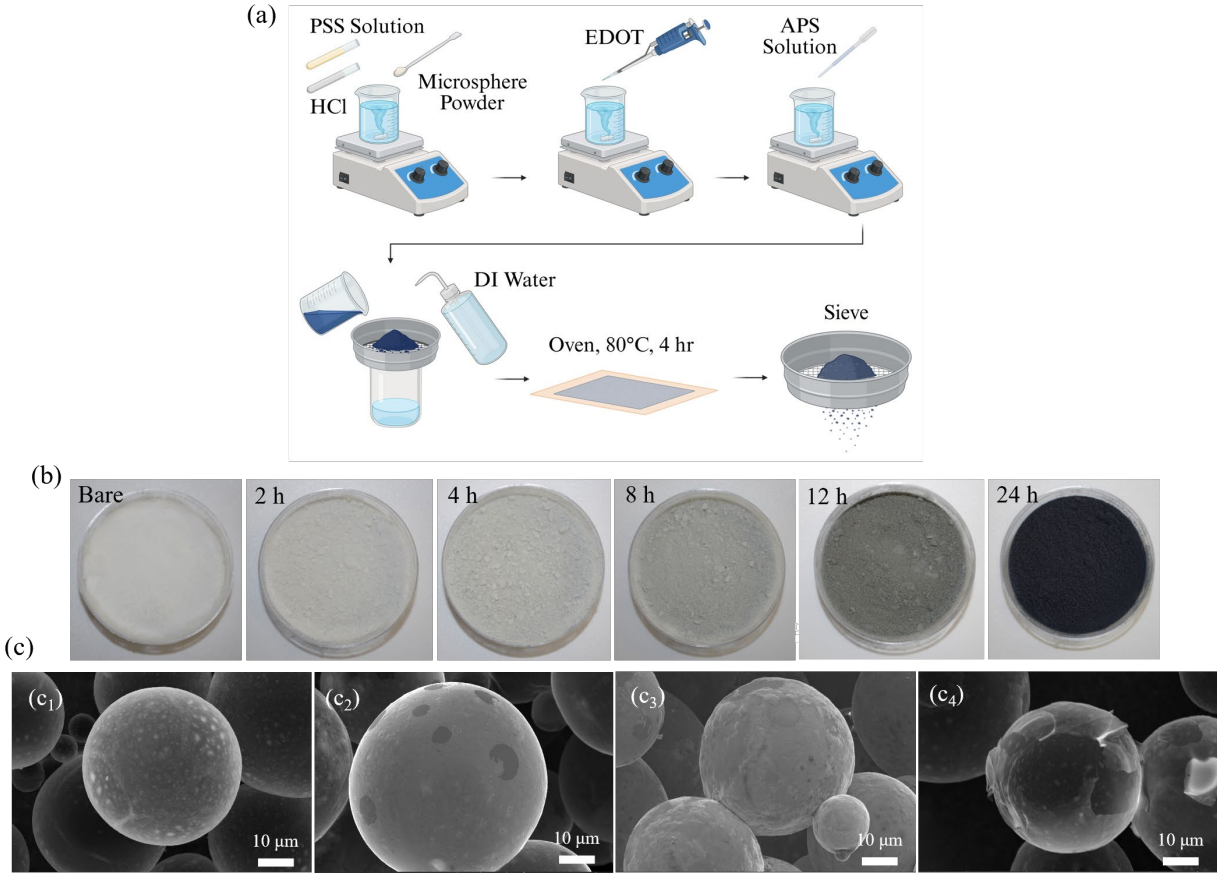

Figure 5-1 (a) Schematic of the preparation process of the conductive microsphere. (b) Digital images showing the color evolution of the powders from off-white (as-received bare microspheres) to dark blue with increasing polymerization time (2-24 h), indicating progressive formation and thickening of the PEDOT:PSS coating. Schematic created with BioRender. (c) SEM images of (c_1) bare microspheres (MS), (c_2-c_3) MS after 12, and 24 h of in-situ PEDOT:PSS polymerization, (c_4) MS coated with PEDOT:PSS PH1000.

Figure 5-1c presents SEM images of pristine microspheres (MS) and those subjected to in-situ PEDOT:PSS polymerization for various reaction durations, along with MS coated with commercial PEDOT:PSS. The pristine MS (Figure 5-1c_1) exhibited smooth surface morphologies with occasional shallow dimples, characteristic of the Expancel shell. With increased reaction time (Figure 5-1c_2), a thin PEDOT:PSS layer progressively formed on the surface, initially imparting only subtle texture changes. Dark, irregular patches were observed, indicating thicker PEDOT:PSS deposits. The small, round spots visible on the surface in Figure 5-1c_2 likely result from microspheres adhering to each other during drying and later being separated by sieving, which

causes PEDOT:PSS-coated regions to detach from one microsphere and reattach to another. After 24 hours (Figure 5-1c$_3$), the microspheres exhibited a significantly roughened and continuous coating layer, suggesting near-complete surface coverage and the formation of a conductive shell, which correlates with the onset of electrical conductivity observed for the corresponding samples. In contrast, the sample prepared by mixing MS with PEDOT:PSS PH1000 followed by drying (Figure 5-1c$_4$) displayed non-uniform PEDOT:PSS aggregates and large flakes loosely adhered to the surface. This comparison highlights the superior uniformity, coverage, and adhesion achieved via in-situ polymerization relative to the mixing method.

FTIR analysis (Figure 5-2a) successfully tracked the in-situ polymerization and deposition of PEDOT:PSS onto the MS over time. The bare MS spectrum established the baseline for the pristine polymer shell. As the synthesis time increased from 2 h to 24 h, the spectra clearly transitioned from being dominated by the native MS peaks to showing strong, characteristic signals of the conductive polymer. This confirms the formation of a continuous and thickening PEDOT:PSS layer on the MS surface.

This growth is spectroscopically confirmed by the progressive emergence and intensification of characteristic PEDOT:PSS vibrational bands, as validated through direct comparison with a reference PEDOT:PSS film synthesized separately under identical polymerization conditions.[274], [275], [276] Specifically, we observed a direct correlation between reaction time and the intensity of the C-C and C=C stretching vibrations of the PEDOT thiophene ring (~1350-1550 cm^{-1}, specifically at 1514 cm^{-1}), the asymmetric/symmetric S=O stretching vibrations of the PSS dopant (~1100-1200 cm^{-1} , specifically at 1190 cm^{-1}), and the C-O-C (~970 cm^{-1}) and C-S-C (~830 cm^{-1}) deformation vibrations of the PEDOT backbone. Additionally, the S-O bending vibrations of the PSS sulfonate group (~690 cm^{-1}) grew stronger. This comprehensive spectral evolution directly supports the morphological finding that extended synthesis time yields more pronounced surface coverage and thicker PEDOT:PSS deposits.

To further confirm PEDOT:PSS deposition and quantify its contribution to the total mass of the MS shell (e.g. the polymer wall of the hollow microspheres), helium pycnometer was used to measure the effective shell density before and after coating (Figure 5-2b). Because helium can permeate through the polymer shell and surface defects, the internal void volume is excluded from

the measured volume, and the measurement reflects only the density of the solid shell material. The pristine MS exhibited a shell density of 1.12 ± 0.02 g cm^{-3}, which, with polymerization time, gradually increased to 1.48 ± 0.08 (8 h), 2.15 ± 0.07 (12 h), and 2.23 ± 0.15 g cm^{-3} (24 h), reflecting progressive PEDOT:PSS deposition and correlating with SEM observations of thicker coatings. Although the overall density of the hollow microspheres is still largely governed by the internal void, the rise in shell density contributes to an increase in the total particle density once the coating is sufficiently thick.

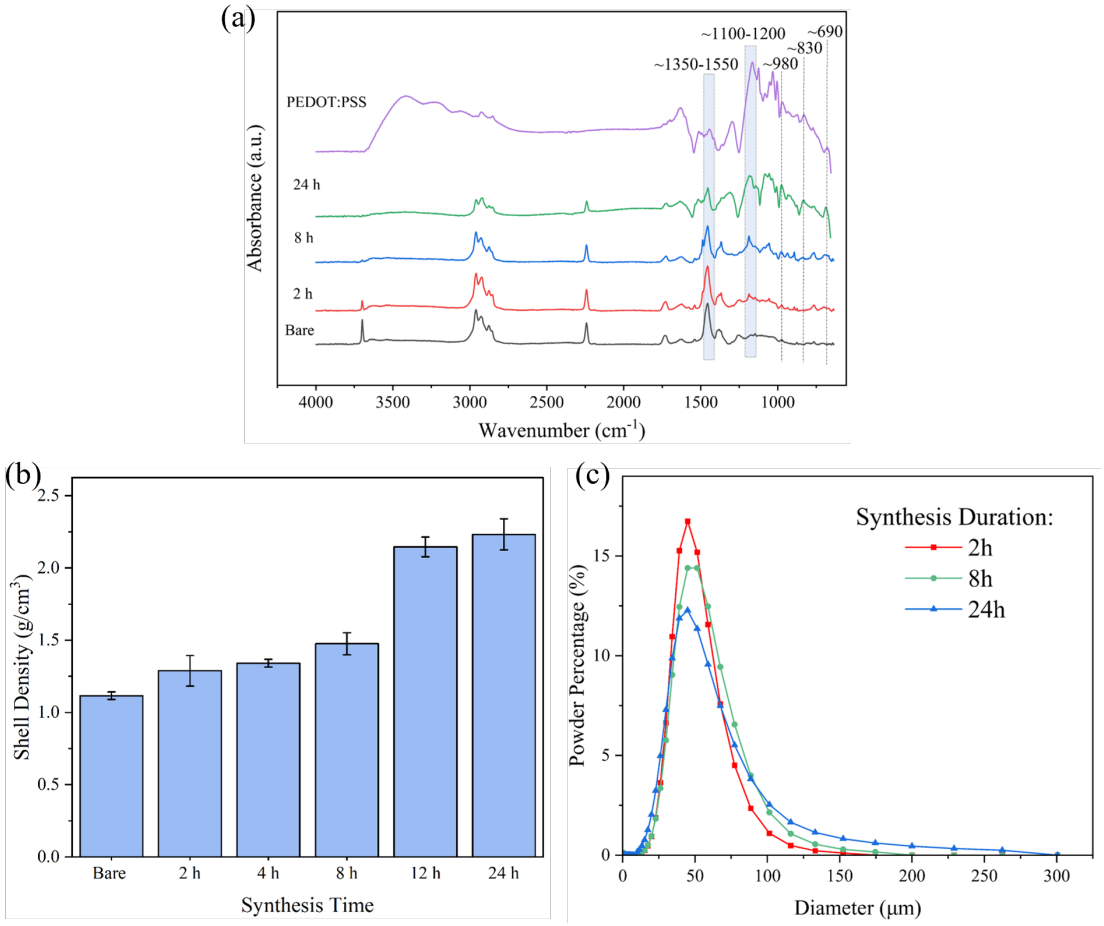

Figure 5-2 (a) FTIR spectra of bare MS, PEDOT:PSS film, and MS after 2, 8, and 12 h of synthesis. Effect of synthesis time on microsphere properties. (b) Shell density of microspheres as a function of synthesis duration, showing a gradual increase with longer polymerization times. Error bars represent the standard deviation of three independent measurements. (c) Particle size distributions of powders obtained after 2, 8, and 24 h of synthesis. Powder percentage represents the relative volume fraction of particles within each size range as measured by laser scattering.

The effect of polymerization time on particle size distribution, and consequently on the final microsphere size, was further evaluated by a laser scattering analyzer (Figure 5-2c). In this plot, the y-axis represents the relative proportion of particles within each size range, providing a measure of the particle size distribution for powders synthesized under different reaction times. After 2 hours of reaction, the size distribution exhibited a sharp peak centered at ~45 μm, indicating minimal growth of the PEDOT:PSS layer. Extending polymerization to 8 hours led to minor broadening of the distribution and a slight shift toward larger diameters, consistent with thicker and less uniform coverage. After 24 hours, this effect became more pronounced, with a broader tail extending to higher diameters, reflecting the continued surface deposition. Overall, despite continued PEDOT:PSS deposition, the overall microsphere size remains largely unchanged, reflecting the thin nature of the coating relative to the microsphere diameter. These findings are consistent with the pycnometer and SEM data, which confirm increased coating mass and thickness without major changes in particle size.

5.4.2 Morphology of Foams

Building upon the powder-level characterization, which confirmed successful PEDOT:PSS coating and controlled particle morphology, the next stage focused on understanding how these modified microspheres influence the structure of the resulting foams. The void fraction was quantified from the foam density by comparing the measured density of the porous foam with the density of the corresponding non-porous solid material. A lower foam density indicates a higher fraction of void space within the structure. DSC thermograms of PCL and PCL-PEDOT:PSS foams, showing a melting transition near 60 °C (Figure S1a, Supporting Information). This transition was used to define the temperature limit for thermal processing, ensuring sufficient polymer softening to enable foam shaping and consolidation. The morphology of foams with different void fractions was examined by SEM (Figure 5-3). Studying morphology at varying void fractions is essential, since wall thickness and microsphere packing directly influence the foam's density, mechanical compliance, and the ability to form continuous conductive pathways. At 70% void fraction (Figure 5-3a), the structure is composed of densely packed microspheres with relatively thick matrix walls that separate adjacent pores. This arrangement preserves mechanical stability while still reducing the bulk density by introducing a considerable amount of void space. In contrast, at 85% void fraction (Figure 5-3b), the foam displays a highly porous structure in which thin matrix walls

surround the pores. The increased void content leads to extensive interconnection between neighboring microspheres, with the microspheres dominating the architecture as the solid matrix phase becomes progressively thinner.

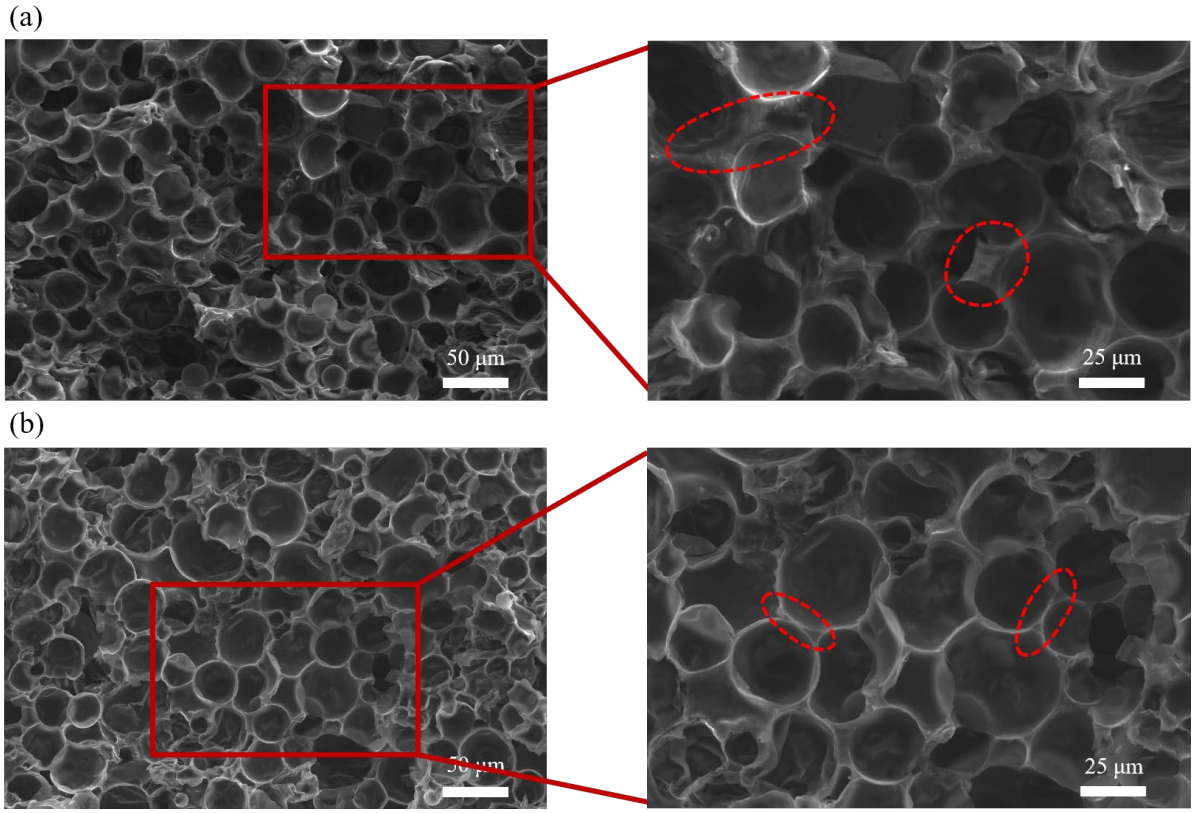

Figure 5-3 Cross-sectional SEM images of PEDOT:PSS-coated microsphere foams with (a) 70% and (b) 85% void fraction, showing the transition from thicker matrix walls to a highly porous structure with thin interconnecting walls. Enlarged views highlight increased microsphere packing at higher void fraction. Red dashed outlines mark regions of reduced matrix thickness between adjacent microspheres.

Thermogravimetric analysis (TGA) was carried out to evaluate the thermal stability of CMS and the foams (Figure S1b-c, Supporting Information). Since the coated microspheres can also be incorporated into other polymer matrices, it was important to assess their intrinsic thermal stability separately from that of the PCL-based foams. PEDOT:PSS-covered microspheres (Figure S1b, Supporting Information) exhibited continuous weight loss across the entire temperature range, leaving a presumably carbonaceous solid residue yield of approximately 29% at 800 °C, consistent with previous reports.[277] Since foams with an 85% void fraction were used for all subsequent

tests, this composition, chosen as a representative balance between high porosity, mechanical integrity, and electrical performance, was also selected for TGA analysis to ensure consistency. For the 85% void fraction foams (Figure S1c, Supporting Information), both uncoated and coated samples showed a major degradation step between 400-450 °C, characteristic of PCL decomposition. However, the foam containing PEDOT:PSS retained a higher solid yield (19%) compared to the neat PCL foam (8%). This difference reflects the contribution of both the PEDOT:PSS coating and the Expancel microspheres, which both contribute to the formation of thermally stable residues during decomposition.

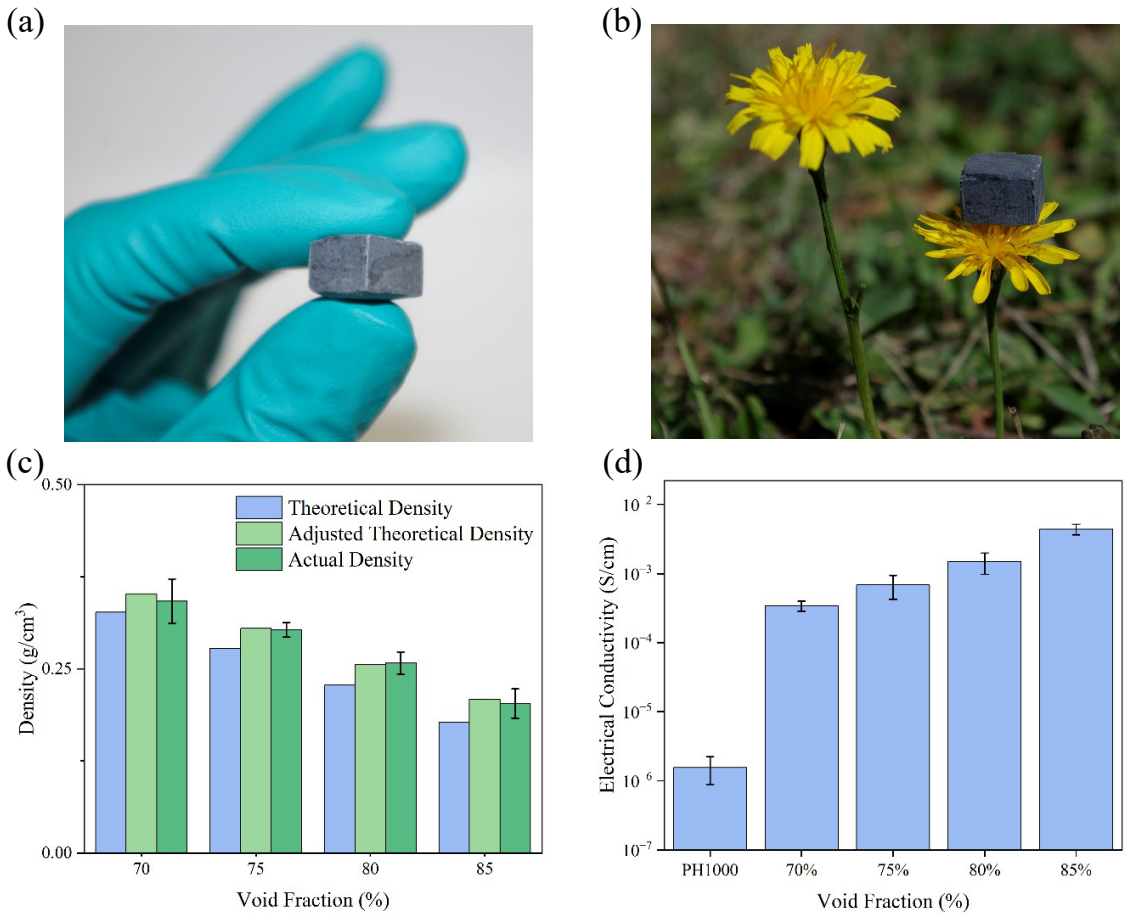

Figure 5-4 Digital images of (a) the 85% foam and (b) 85% foam on a flower. (c) Comparison of theoretical, adjusted theoretical, and measured foam densities (n=3) at different void fractions (70%, 75%, 80%, 85%). Actual density values are averaged from the density values of 3 cubic samples. (d) Electrical conductivity of foams as a function of void fraction, compared with a control prepared by simply mixing PH1000 with uncoated microspheres (mean of 3 measurements).

Figure 5-4a displays a representative sample of the 85% void fraction foam, illustrating its uniformity and mechanical stability even at high porosity, while Figure 5-4b visually demonstrates the ultralight nature of the foam by balancing it atop a delicate flower. Density measurements (Figure 5-4c) provide additional insight into the role of the coated microspheres. The initial theoretical density of the foams was estimated using the density of uncoated Expancel microspheres (30 kg m^{-3}). After foams fabrication, the density of each sample was measured and used to back-calculate the effective volume fraction and average density of the CMS. This analysis yielded an effective conductive microsphere density of ~66 kg m^{-3}, more than double that of uncoated Expancel, consistent with the added PEDOT:PSS. Using this corrected CMS density, new adjusted theoretical foam densities were calculated, which showed very good agreement with experimental values, shown in Figure 5-4c. This confirms both the successful incorporation of PEDOT:PSS onto the microsphere surfaces and the accuracy of the foaming process in producing controlled structures across varying void fractions.

Conductive foams reported in the literature (Table 5-1) span a broad density range, from ultralight graphene or PEDOT:PSS aerogel-like systems (~0.02-0.03 g cm^{-3})[278] to more conventional polymeric foams (up to ~0.48 g cm^{-3}).[279] Our foams, with densities around ~0.2 g cm^{-3}, occupy an intermediate region that balances lightweight porosity with mechanical compliance and scalable processing. This places them in a favorable position for applications requiring both structural functionality and electrical performance, not as fragile as ultralight aerogels, yet significantly lighter than typical solid foams.

Table 5-1 Summary of conductive foams showing foaming method, average conductivity and density.

Materials	**Foaming Method**	**Conductivity (S cm^{-1})**	**Density (g cm^{-3})**	**Ref.**
PCL/PEDOT:PSS	Syntactic foams	10^{-2}-10^{-3}	0.2	This work
TPU/0.06vol%CNT	Freeze-drying	10^{-3}	0.123	Huang et al.[280]
TPU/rGO	Freeze-drying/dip-coating	0.07	0.162	Lu et al.[281]
TPU/PDA/3.45wt%MXene	Freeze-drying/dip-coating	$2.5x10^{-3}$	0.106	Chen et al.[282]

MXene/auxetic PU	Dip-coating/triaxial compression	0.106	0.063	Kim et al.[283]
Melamine/PEDOT:PSS	Dip-coating	0.58	0.12	Gu et al.[284]
TPU/CNT	3D printing	10^{-8}-10^{-5}	0.25-1	Aghvami-Panah et al. [285]

Electrical conductivity measurements (Figure 5-4d) further highlight the advantage of PEDOT:PSS in situ polymerization. The control sample, prepared by mixing pristine microspheres with PH1000, exhibited low conductivity (~10^{-6} S cm^{-1}), reflecting the absence of a continuous conductive network due to poor filler dispersion and weak interfacial contact. In contrast, foams fabricated with synthesized in situ PEDOT:PSS-coated microspheres showed conductivities several orders of magnitude higher, systematically increasing from ~10^{-4} S cm^{-1} at 70% void fraction to ~10^{-2} S cm^{-1} at 85%. This trend reflects the formation of percolating conductive pathways along the PEDOT:PSS coatings. Although increasing void fraction usually reduces conductivity in conventional foams, here the opposite trend occurs because the conductive phase is localized on the microsphere surfaces. At higher void fraction, the microspheres are more closely packed, increasing contact between PEDOT:PSS-coated shells and forming more continuous conductive pathways. At lower void fractions, conductive contacts are sparse, while at higher void fractions, increased microsphere packing enhances connectivity and facilitates efficient charge transport. In this system, a higher void fraction corresponds to a larger volume fraction of conductive microspheres, since the same component provides both porosity and conductivity. Consequently, increasing the void fraction not only increases porosity but also enriches the density of the conductive component, thereby improving electrical connectivity. Compared with other polymer foams reported in the literature (Table 5-1), our PEDOT:PSS-PCL syntactic foams achieve conductivities on the order of 10^{-2}-10^{-3} S cm^{-1}, which are among the highest for polymer-based conductive foams without metallic or carbon-based fillers.

5.4.3 Mechanical Properties

Figure 5-5a shows the compressive behavior of the foams to assess the influence of void fraction and PEDOT:PSS incorporation on mechanical performance (refer to the Experimental Section/Methods for more information on mechanical characterization). PCL+PEDOT:PSS foams

exhibit the characteristic three-region stress-strain response of cellular solids: an initial elastic region, a plateau region, and a final densification region.[286] Foams with lower void fractions (e.g., 70%) show higher stiffness and compressive resistance, whereas those with higher void fractions (e.g., 85%) display lower stress-strain slopes, reflecting reduced load-bearing capacity due to the smaller matrix content.

In the elastic regime (0-10% strain), lower porosity foams exhibited steeper stress slopes, reflecting a higher initial modulus. With increased porosity, the modulus decreased and the plateau region became more pronounced, consistent with progressive buckling of the thin inter-void walls of PCL. At higher strains (~40-50%), the foams transitioned into the densification region, where collapsed pores were compacted and the material stiffened rapidly. This region appeared earlier and was more pronounced in lower porosity foams (70% and 75%) due to their greater solid content, while leads higher void fraction foams (80% and 85%) exhibited delayed densification, consistent with their higher porosity and enhanced capacity for deformation.

As shown in Figure 5-5b, compared to the dense, non-porous PCL sample, which showed a linear and brittle stress-strain profile without a plateau, all foams demonstrated significantly greater deformability. The incorporation of PEDOT:PSS-coated microspheres altered the mechanical response, particularly at high porosity. For instance, the elastic modulus of the 85% void fraction foam increased relative to its uncoated counterpart (Figure 5-5b), suggesting a higher shell rigidity. This trend was confirmed by compressive modulus values (Figure 5-5c), where PEDOT:PSS-containing foams consistently showed higher modulus compared to the uncoated foams across all porosities. These results highlight the dual role of PEDOT:PSS as both a conductive and mechanically reinforcing component.

Under compressive loading, the conductive foam exhibits a pronounced piezoresistive response, as shown in Figure 5-5d. A rapid reduction in resistance occurs at low compressive strain, followed by a more gradual and stable decrease at higher strains, reaching $\Delta R/R_0 \approx -90\%$, which is characteristic of porous conducting polymer foams.[287], [288] This behavior can be attributed to compression-induced densification of the foam and increased interparticle contacts within the conductive microsphere network, which facilitate charge transport. The reproducible response highlights the suitability of the foam for compression or strain-based electromechanical sensing.

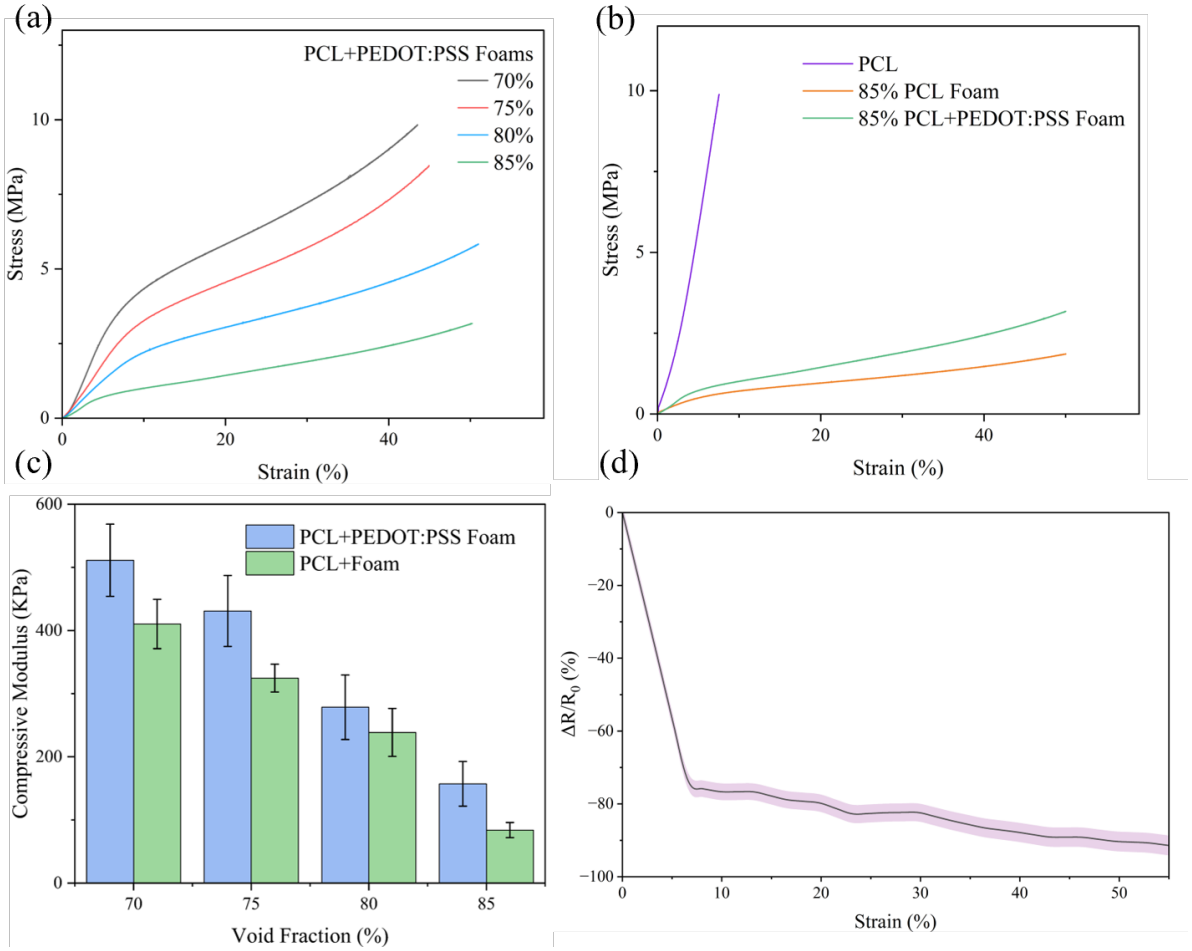

Figure 5-5 Mechanical properties of foams. (a) Compressive stress-strain curves of PCL+PEDOT:PSS foams with different void fractions. (b) Comparison of compressive stress-strain curves of PCL, PCL foam, and PCL+PEDOT:PSS foam at 85% void fraction. (c) Comparison of compressive modulus (error bars represent standard deviation from 4 measurements). (d) Resistance change ($\Delta R/R_0$) vs. compressive strain of 85% PCL+PEDOT:PSS foam. Data are reported as mean ± standard deviation of 4 measurements (the shaded area around the curve represents the standard deviation).

Importantly, the Young's modulus of the developed PEDOT:PSS foams fall well within the range accepted for skin-contact applications. Recent literature reports that the effective Young's modulus of hydrated human skin spans broadly from 10 kPa to 1 MPa, depending on anatomical site and hydration state.[27], [289] By matching their moduli to this spectrum, these foams minimize mechanical mismatch at the skin–electrode interface, thereby improving comfort, conformability, and reducing motion artifacts during the collection of physiological signals. The compressive

moduli observed for all foam variants in this study are accordingly well-suited for epidermal electronics and wearable biosensor platforms, as they support both stable device contact and imperceptible integration with the user's skin.

5.4.4 Additive Manufacturing

The additive manufacturing process yielded PCL and PCL+PEDOT:PSS syntactic foams with consistent microstructure and excellent compatibility for commercialized 3D printers (refer to the Experimental Section/Methods for more information on additive manufacturing). The SEM micrograph (Figure 5-6a) highlights the integrity of PEDOT:PSS-coated microspheres, while printed dogbone specimens (Figure 5-6b) display smooth surfaces and dimensional uniformity, underscoring reliable process control. Tensile testing was used here primarily to assess fabrication repeatability and consistency across printed samples. The tensile stress-strain curves (Figure 5-6c) feature shaded regions denoting standard deviation, which remains around 5% across measurements, showing quantitative evidence of reproducible fabrication and uniform mechanical properties vital for real-world device applications. The curves exhibit an initial elastic regime followed by a stable plastic plateau, consistent with the tensile deformation behavior of polymer foams.

Mechanical benchmarking reveals that adding PEDOT:PSS-coated microspheres increases tensile modulus and yield strength but lowers strain-at-break compared to pure PCL foam (Figure 5-6d-e). This is typical for conductive composite foams, since rigid filler particles introduce local stress concentrations and constrain matrix mobility, causing earlier microcrack formation and reduced elongation.[290] While this leads to lower ductility, the resulting strain-at-break still meets the requirements for wearable and skin-interfaced sensors, maintaining a balance between flexibility and robustness for soft bioelectronic applications. Different stiffnesses can be achieved by altering the void fractions, highlighting the material's designability.

Importantly, electrical conductivity measurements revealed that the 3D-printed foams exhibit conductivities ($3.48\times10^{-4} \pm 5.36\times10^{-5}$ S cm^{-1}) comparable to those of the corresponding hot-pressed 75% void-fraction foams ($6.84\times10^{-4} \pm 2.60\times10^{-5}$ S cm^{-1}), indicating that the extrusion and printing steps do not disrupt the percolated PEDOT:PSS network. This preservation of electrical

performance confirms that the conductive pathways formed by the coated microspheres remain intact throughout filament fabrication and printing.

Overall, the low variability in mechanical testing demonstrates that the materials and 3D printing approach enable scalable, repeatable fabrication of electrodes with tunable mechanical and electrical properties. This positions the developed syntactic foams as promising platforms for bioelectronic devices, where reliable strength, flexibility, and processability are essential for future development.

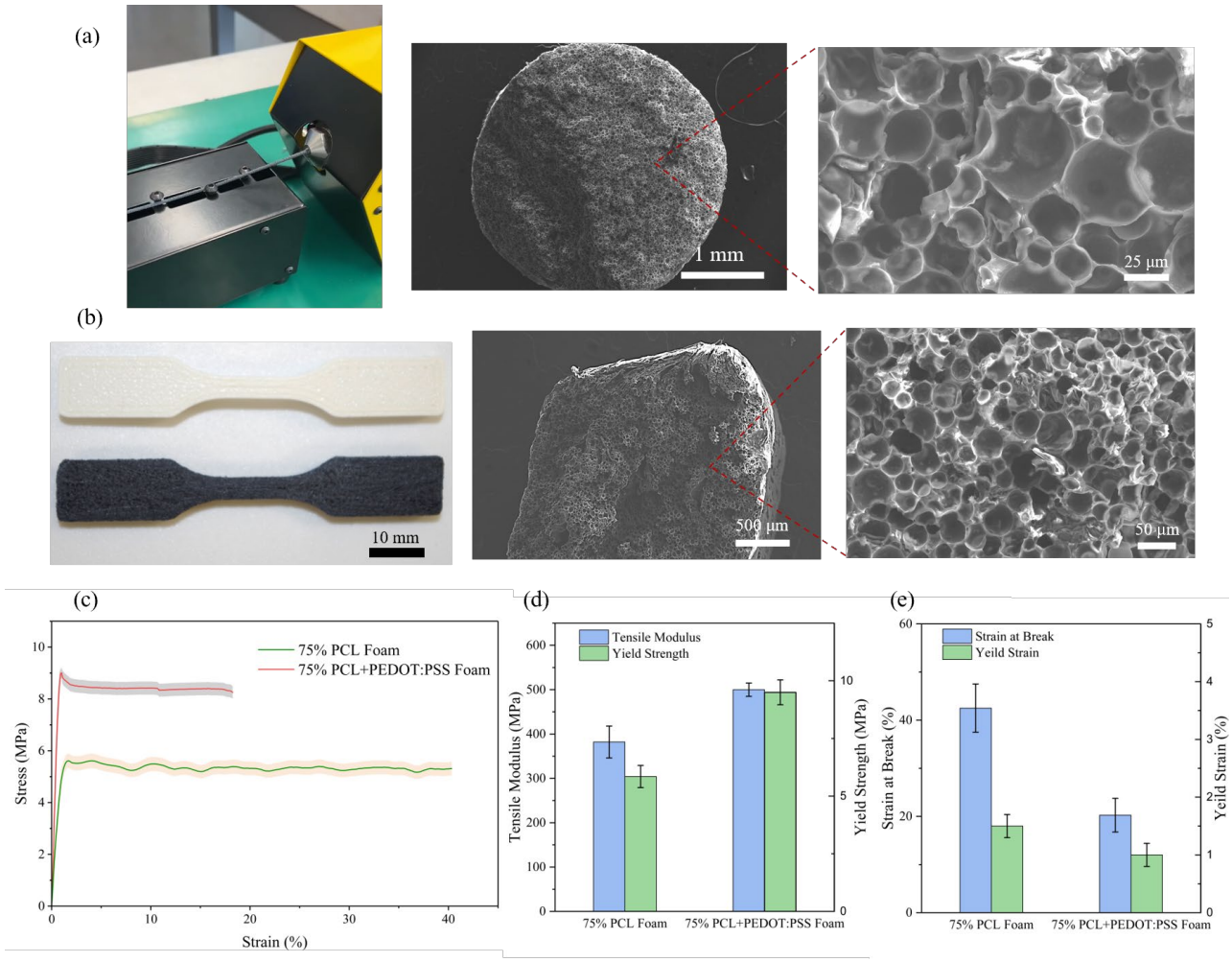

Figure 5-6 Fabrication, morphology, and mechanical characterization of 3D-printed 75% void fraction foams. (a) Extrusion of conductive foam filament prior to printing. The corresponding SEM image shows the cross-section of a representative 75% PCL+PEDOT:PSS foam filament, with enlarged views showing the internal porous structure. (b) Photographs of 3D-printed tensile dogbone specimens fabricated from neat PCL foam (top) and PCL + PEDOT:PSS foam (bottom).

The corresponding SEM image shows the cross-sectional morphology of the printed conductive foam sample. (c) Representative tensile stress-strain curves of 75% PCL and 75% PCL+PEDOT:PSS foams (shaded regions represent standard deviation). (d) Comparison of tensile modulus and yield strength (number of measurements n = 3), and (e) corresponding strain at break and yield strain values (n = 3).

5.4.5 Chemical and Mechanical Recycling

To evaluate the recyclability of the composite foams, a chemical separation method was implemented to isolate and recover the conductive PEDOT:PSS-coated microspheres from the PCL matrix (Figure 5-7a). The foams were first cut into small pieces and submerged in ethyl acetate, a green solvent (relatively low-toxicity and more environmentally benign solvent) that selectively dissolves PCL while leaving the microspheres intact. After complete dissolution of the polymer matrix, the suspension was filtered through a stainless-steel mesh to physically separate the microspheres from the polymer solution. The recovered microspheres were deposited onto a Kapton substrate and heated at 70 °C to remove residual solvent. The integrity of the PEDOT:PSS coating following the recycling process was examined by SEM. The images confirmed that the microspheres remained coated with the conductive polymer, with no sign of aggregation, cracking, or delamination. This indicates that the solvent treatment and mild heating did not degrade the conductive coating.

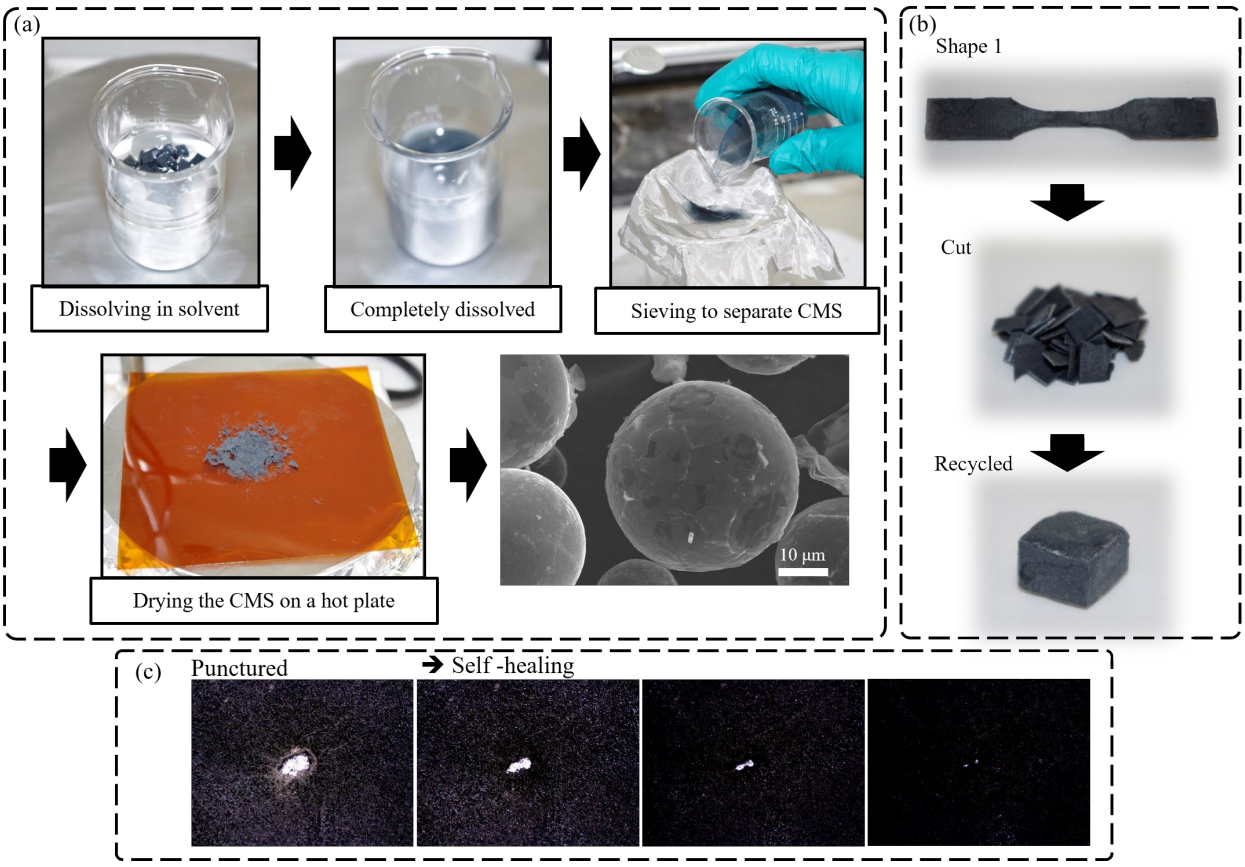

Figure 5-7 (a) Chemical recycling of the foams via dissolution of the PCL matrix, allowing recovery of PEDOT:PSS-coated microspheres for reuse in new formulations. (b) Physical recycling through melting and reshaping of the foam into new geometries. (c) Optical microscope images showing the time-lapse progression of defect closure in a punctured foam during thermally assisted repair (0-20 s), demonstrating rapid defect closure upon localized heating.

In parallel, physical recycling was explored by mechanically cutting used foams into small fragments and reprocessing them through hot pressing. The fragments were successfully reshaped into uniform films and cubes without visible degradation, delamination, or cracking (Figure 5-7b). This route exploited the thermoplasticity of PCL, enabling reshaping while preserving the distribution of conductive microspheres. As shown in Figure S2 (Supporting Information), the compressive modulus of the foams remains within the same range after the first and fifth recycling cycles, indicating negligible mechanical degradation. In addition, time-dependent current measurements reveal stable electrical responses across recycling cycles, confirming the preservation of conductive pathways upon repeated reprocessing. Together, these results

demonstrate that the foams are recyclable through both chemical and physical pathways, providing practical routes to extend their service life maintaining structural and functional integrity.

The thermally assisted repair capability of the foam was demonstrated by intentionally puncturing a film (thickness of ~5 mm) with a sewing needle and then applying localized heat to facilitate repair (Figure 5-7c). Various heat sources, including a hot plate, hot press, oven, or heat gun, can be used to trigger thermally assisted repair. In this experiment, a heat gun was directed at the punctured foam for 20 seconds, during which a series of images captured the gradual closure of the defect (Video S1, Supporting Information). The surface temperature during heating ranged between 80 °C and 100 °C (depending on the distance between the heat source and the sample), exceeding the melting temperature of the polymer matrix. Under these conditions, repair occurs through localized melting and reflow of the polymer. This thermally assisted repair enables rapid restoration of structural integrity and is relevant for practical repair and reprocessing scenarios.

5.4.6 Electrophysiological Signal Recording

To demonstrate the practical applicability of the developed conductive foams, we fabricated an epidermal electrode using the optimized 85% void-fraction foam and evaluated its performance for epidermal biosensing. The foam electrode was integrated into a standard snap-type configuration and used to record physiological signals, including electrocardiography (ECG) and electromyography (EMG). Representative ECG recordings clearly resolve characteristic P-QRS-T waveforms with stable amplitudes and low baseline noise (Figure S3a, Supporting Information), while EMG measurements exhibit distinct, repeatable bursts corresponding to voluntary muscle activation (Figure S3b, Supporting Information). These results confirm that the porous conductive foam provides reliable skin-electrode contact and sufficient electrical performance for high-fidelity acquisition of epidermal bioelectrical signals.

Brain electrical activity can be recorded noninvasively using electroencephalography (EEG), a proven technique widely employed in both clinical diagnostics and cognitive monitoring.[83], [291] Among the different EEG rhythms, alpha-band oscillations in the 8-13 Hz range are closely associated with relaxed wakefulness and are commonly used as benchmarks for assessing signal quality [292], [293] While conventional EEG systems rely on scalp-mounted, clinician-dependent and highly disruptive electrode caps, recent work has highlighted the ear canal as a particularly

attractive sensing site due to its close anatomical proximity to the central nervous system and its potential for unobtrusive, long-term monitoring.[122], [217], [233], [245], [294] A comprehensive review of electrode materials and form factors for scalp, around and in-ear EEG was conducted by the authors and published.[83] It outlined key design requirements for wearable ear-EEG systems which could all be met with conformable conductive foam.

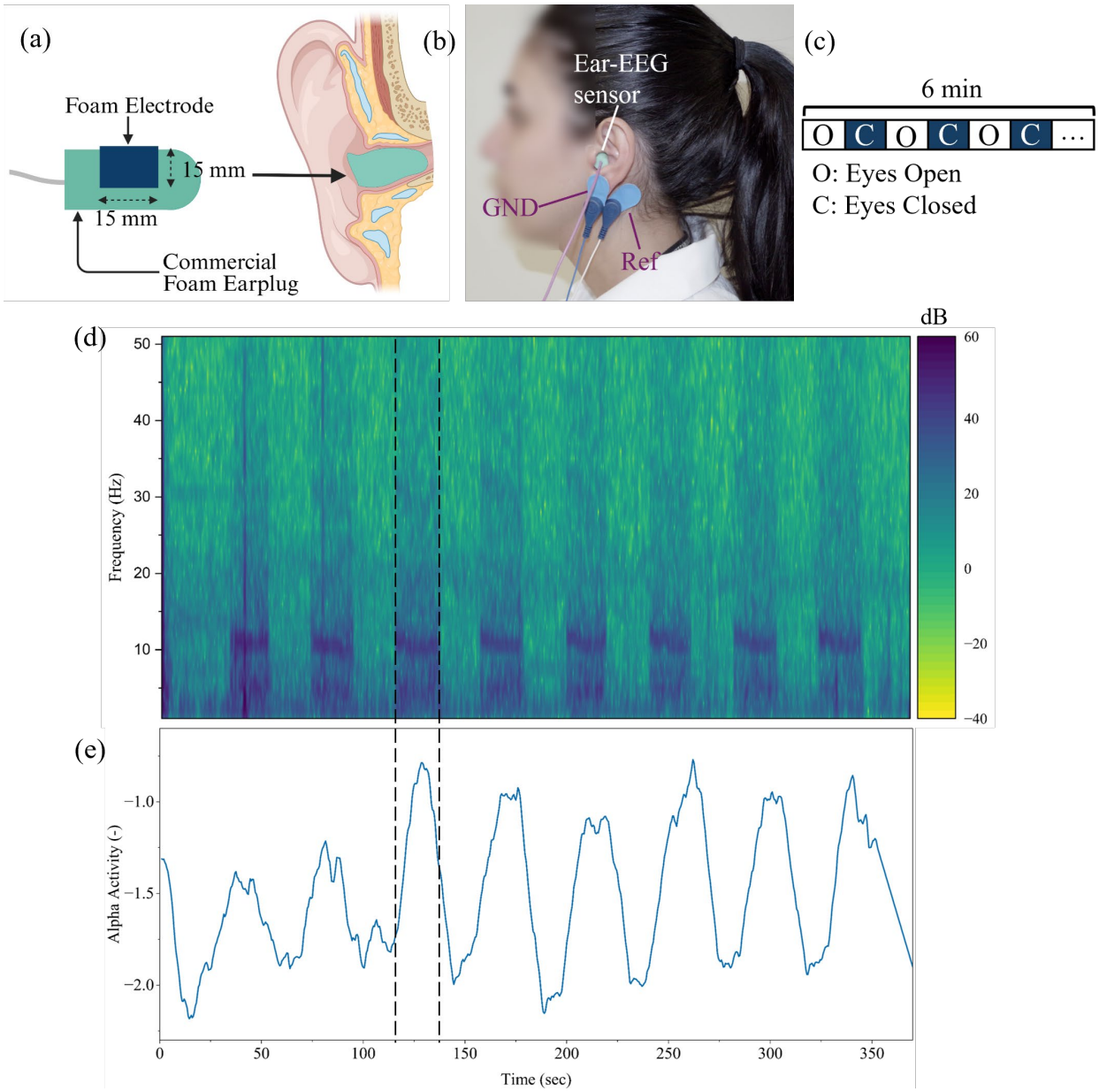

Figure 5-8 (a) Schematic of the foam-based in-ear EEG electrode. Schematic created with BioRender. (b) Illustration and photograph of electrode placement for ear-EEG recording, including reference (Ref) and ground (GND) electrodes. (c) Experimental protocol for eyes open

(O) and eyes closed (C) conditions. (d) Time-frequency spectrogram of the EEG signal showing power distribution across frequencies. (e) Temporal evolution of alpha-band (8-12 Hz) activity. Dashed lines indicate one episode of the eyes-closed condition.

The ear-EEG device developed here is entirely foam-based and ultralight, which allows it to be worn comfortably for extended periods of time during everyday activities. The compliant foam structure enables effortless insertion into the ear canal and adapts to its unique geometry, promoting close-range, stable yet inconspicuous contact with the skin (Figure 5-8a,b). This combination of conformability and low mechanical burden makes the platform well suited for long-term in-ear EEG sensing outside of laboratory and clinical constraints.

Time-frequency analysis of in-ear EEG recordings demonstrates the foam-based electrode's ability to capture physiologically meaningful brain rhythms (see Supporting Information for full signal analysis). The eyes-open/eyes-closed (EOEC) paradigm is widely recognized as an initial validation test to ensure new EEG systems are recording brain activity. The paradigm is simple, robust, and alpha modulation is well-characterized.[295], [296], [297] A single in-ear channel was recorded continuously over alternating 20 s blocks of eyes-open and eyes-closed (Figure 5-8c) while the subject remained seated and relaxed. The spectrogram (Figure 5-8d) shows clear power modulation in the alpha band (8-12 Hz) over time, with repeated increases in alpha activity corresponding to periods of eye closure and attenuation during eye opening, as indicated by the experimental protocol. This expected alternation between eyes-open and eyes-closed alpha activity is a well-established EEG hallmark and confirms that the in-ear foam electrode can reliably detect dynamic changes in actual cortical activity.

To quantify this behavior, the temporal evolution of alpha-band power was extracted and is shown in Figure 5-8e. The alpha activity exhibits consistent and repeatable fluctuations aligned with the task sequence, further supporting stable electrode-skin contact and low susceptibility to motion-related artifacts during the recording. Collectively, these observations indicate that the foam-based in-ear electrode supports reliable extraction of both temporal and spectral EEG features associated with relaxed wakefulness.

5.5 Conclusion

In summary, we have developed a class of recyclable and 3D-printable conductive syntactic foams based on PEDOT:PSS-coated polymer microspheres embedded in a thermoplastic matrix. By localizing conductivity at the microsphere surface, this architecture enables simultaneous control over porosity, mechanical compliance, and electrical performance while preserving low density and scalable processability. Importantly, microsphere-templated conductive shells provide a materials design strategy that decouples electrical functionality from bulk polymer loading, overcoming limitations commonly encountered in conventional conductive foams. Beyond performance, these materials introduce practical routes toward circular soft electronics. The foams can be reprocessed through both chemical recycling, via selective matrix dissolution and microsphere recovery, and physical recycling through thermal reshaping, without loss of structural integrity or conductivity. Compatibility with fused filament fabrication further enables rapid prototyping and geometric versatility using standard additive manufacturing tools. Demonstrated here in soft wearable electrodes for electrophysiological signal acquisition, including in-ear EEG, this work establishes conductive syntactic foams as a versatile and sustainable materials platform. Because PEDOT:PSS is hygroscopic, future work should also examine how humidity, storage conditions, and prolonged skin contact affect aging, electrode-skin impedance, and long-term signal fidelity. More broadly, the microsphere-templated approach outlined here offers a general framework for designing lightweight, compliant, and recyclable functional materials for next-generation soft and wearable electronic systems.

5.6 Experimental Section/Methods

Materials: Poly(4-styrenesulfonic acid) sodium salt (PSS), 3,4-Ethylenedioxythiophene (EDOT), ammonium persulfate (APS), and hydrochloric acid (HCl) were purchased from Millipore Sigma (St. Louis, MO, USA) and used as received. Expanded hollow microspheres (Expancel® grade 920 DE 40 d30, particle size 35-55 μm, density 27-33 kg m^{-3}) were supplied by AkzoNobel, Duluth, GA, USA. Poly(ε-caprolactone) (PCL, CAPA® 6500; density 1.02 g cm^{-3}; melt flow index of 7 g 10 min^{-1}; melting point 58-60 °C) was supplied by Ingevity, USA. PEDOT:PSS (Clevios™ PH1000 aqueous suspension; PEDOT:PSS content 1-1.3%) was purchased from Heraeus Precious Metals (Germany). Ethyl acetate was purchased from VWR (Radnor, PA, USA). For simplicity,

uncoated hollow microspheres are referred to as MS (microspheres), while the PEDOT:PSS-coated conductive microspheres are denoted as CMS (conductive microspheres) throughout this work.

Microsphere preparation: To coat Expancel® microspheres with PEDOT:PSS, 15 mL of 1 wt% PSS sodium salt solution in DI water was first prepared, followed by the addition of 1 mL of 1 M HCl. Next, 50 mg of Expancel microspheres were dispersed in the prepared PSS-HCl solution, which was sonicated for 5 minutes to ensure complete wetting of microsphere surfaces. Subsequently, 50 µL of EDOT monomer was added to the dispersion, which was stirred gently without oxidant for 60 minutes at room temperature to promote EDOT adsorption onto the microsphere surfaces. The oxidant solution, prepared by dissolving 70 mg of APS in 10 mL of DI water, was then added dropwise to the Expancel suspension over 30 minutes under gentle stirring to initiate in-situ oxidative polymerization on the surface of the MS. The reaction mixture was then covered with aluminum foil and left to polymerize at room temperature under gentle stirring. This PEDOT:PSS synthesis procedure was adapted from prior reports[298], [299] with modifications to accommodate microspheres as the template. To investigate the effect of polymerization duration, samples were prepared with reaction times of 2, 4, 8, 12, and 24 h under otherwise identical conditions. During polymerization, the solution gradually changed color from white to dark blue, which is characteristic of PEDOT:PSS formation and indicates the increase in the coating thickness with reaction time. The reaction was terminated by adding 5 mL of methanol to quench the polymerization. The mixture was sieved through a 500-mesh screen to collect the coated microspheres, which were thoroughly washed with DI water to remove residual reagents. The microspheres were subsequently dried at room temperature for 24 h, then passed through a 300-mesh screen to break apart agglomerates. The resulting powder was collected as the final conductive microsphere (CMS) product.

For comparison, a conductive microsphere powder was also prepared by physically mixing uncoated Expancel microspheres with PH1000. Microspheres and PEDOT:PSS dispersion were combined precisely in a 1:3 weight ratio (microspheres:PH1000) and hand-mixed with a spatula until a homogeneous paste-like consistency was obtained. This ratio was selected because it provided sufficient PEDOT:PSS to cover the microsphere surfaces while avoiding excess free PEDOT:PSS in the control sample. The mixture was spread onto a Kapton film and dried in an oven at 80 °C for 4 h. The dried film was carefully scraped from the substrate, sieved through a

300-mesh screen to remove aggregates, and processed into a fine, uniform powder. This powder was used in foam fabrication as a control material to benchmark against the in-situ PEDOT:PSS-coated microspheres produced via the synthesis route.

The density of the conductive powder was measured using a Micromeritics AccuPyc II 1345 gas pycnometer (Norcross, GA, USA) equipped with a 10 cm^3 sample cell, where helium gas displacement was used to determine the sample volume and calculate its density. Particle size distribution was determined using a LA-950 laser diffraction analyzer (HORIBA Instruments, Irvine, CA, USA). Briefly, a small amount of powder was dispersed in deionized water, the suspension was gently homogenized and ultrasonicated to minimize agglomeration and then introduced into the instrument for measurement.

Foam Preparation: Conductive foams were fabricated by a solution-casting method. PCL pellets were dissolved in ethyl acetate at room temperature using a magnetic stirrer. PCL and ethyl acetate were selected by virtue of their biodegradability, low toxicity, and compatibility with low-temperature processing, enabling an energy-efficient and environmentally conscious fabrication route.[300], [301] Once PCL was completely dissolved, the CMS powder was added to the solution and mixed to form a viscous slurry. The void fraction of the foam, defined as the ratio of the volume of void space to the total foam volume, was controlled by adjusting the volume ratio of microspheres to PCL, with higher CMS content yielding greater void fraction. The slurry was ultrasonicated with Branson 2510 Ultrasonic Cleaner (70 W) at 40 °C for 10 minutes and then dried in a Thermo Scientific Heratherm oven for 5 hours at 50 °C to remove residual solvent. Finally, the dried samples were pressed at 100°C using a heat press (Combo heat press machine) to mold into the desired shapes.

The foam density was determined by measuring the mass of 3 cuboidal specimens (~10 × 10 × 10 mm), dividing each by its respective volume, and reporting the average values for each sample type. A puncture test was performed by manually piercing the film through its full thickness using a standard sewing needle, followed by immediate needle removal. Images were taken using a digital microscope (Dino-Lite Edge 3.0 AM73915MT8, USA). The healing was triggered by a hot air gun (SEEKONE Heat Gun SDL-2816). The surface temperature during heating ranged from 80 to 100 °C, depending on the distance between the heat source and the sample.

Thermogravimetric analysis (TGA, 5500, TA Instruments, USA) was performed on both CMS and foams to evaluate their thermal stability. Measurements were performed in an open platinum crucible from 40-600 °C with a heating rate of 20 °C min^{-1}, under a nitrogen atmosphere (40 mL min^{-1}). Additionally, differential scanning calorimetry (DSC, Q2000, TA instruments, USA) was conducted to study the thermal properties of the foams. 5-10 mg of samples were placed in a closed-lid standard aluminum pan and subjected to nitrogen flow. To remove the influence of prior thermal history and obtain a reliable representation of the intrinsic thermal behavior, the samples were initially cooled to 0 °C and heated to 250 °C at a rate of 10 °C min^{-1}. A second heating cycle was then carried out under the same conditions, from 0 °C to 150 °C at 10 °C min^{-1}, and the data from this second run were used for analysis.

Scanning Electron Microscopy (SEM): The morphology of the foams was examined using a Quattro (Thermo Scientific) scanning electron microscope (SEM) equipped with an energy-dispersive spectrometer (EDS). The CMS powder was manually spread onto adhesive carbon tape (commonly used for SEM sample mounting) using gentle fingertip pressure to ensure uniform surface coverage. The foams were cryo-fractured using liquid nitrogen to achieve a clean representative cross-section of their internal structure.

Mechanical and Electrical Characterization: Mechanical tests were performed using a Mach-1 V500csst MA009 mechanical tester (Biomomentum Inc., Canada) equipped with a 250 N load cell. Compression tests were performed on cubic specimens (10 × 10 × 10 mm) at a compression rate of 0.1 mm s^{-1}. A flat circular indenter with a diameter of 32 mm was used. Prior to testing, all samples were hot-pressed at 100 °C in molds to achieve the desired shapes.

Electrical conductivity measurements were carried out using a tailored tensile grip with electrodes (model MA068, Biomomentum Inc., Canada), interfaced with a source measure unit (B2902A, Agilent). The conductivity (σ) of the films was determined as follows:

$$\sigma = \frac{L}{R \times A} \tag{5.1}$$

Where R denotes the average resistance, and L and A are the length and cross-sectional area of the foams between two grips, respectively. The reported conductivity values correspond to the average of 3 measurements, with error bars representing the standard deviation.

To validate the uniformity and repeatability of the 3D printing process, tensile tests were conducted on printed dogbone specimens prepared according to the testing standard ASTM D638 Type V, using an Instron 3365 universal testing machine (Norwood, MA) with a 500 N load cell. The tests were performed at a crosshead displacement rate of 10 mm s^{-1}. Each measurement was repeated at least four times, to ensure consistent evaluation of the mechanical performance across samples.

Fourier-transform infrared (FTIR) spectroscopy: Fourier-transform infrared (FTIR) spectroscopy was performed in absorption mode using a PerkinElmer Spectrum 65 spectrometer. A background spectrum was obtained prior to sample measurement. Spectra were acquired at room temperature over the range of 4000–600 cm^{-1} with a resolution of 4 cm^{-1}, across 32 scans per measurement. The powder samples were placed directly onto the ATR crystal for measurement without additional preparation. Each sample was analyzed three times under identical conditions. For the PEDOT:PSS reference spectrum, the PEDOT:PSS dispersion was drop-casted onto a clean glass slide, dried at room temperature to form a free-standing film, and subsequently analyzed under identical conditions.

Additive Manufacturing: The foams were additively manufactured via the Fused Filament Fabrication (FFF) method. As depicted in Figure 5-9, the process includes the fabrication of filaments via an extruder (Figure 5-9a) and then the deposition of molten filaments layer by layer via a 3D printer (Figure 5-9b). Pure PCL and solution-cast foams with a 75% void fraction were cut into pellets (about 5 × 5 mm) for filament extrusion. The pellets were gravity-fed into a single-screw extruder (3Dpany Extruder, with screw diameter of 20 mm and length-diameter ratio of L/D = 15:1), where they were conveyed and melted under controlled heating.

To preserve the microspheres, the heating temperatures (listed in Table 5-2), mainly determined by the melting temperature of PCL (~60 °C), are relatively low compared to those of commonly used FFF filaments, such as polylactic acid (PLA, printing temperature of 190 °C). The molten material was pushed through a circular die with a diameter of 1.75 mm under coordinately controlled screw speed and traction speed, which determine the production rate and adjust filament diameter, to produce continuous filaments suitable for commercial 3D printers. The hot extrudate was cooled by directed airflow at different fan speeds to stabilize its geometry while avoiding brittleness or deformation. Cooled filaments were then collected by a synchronized winding system that maintained constant tension and ensured uniform filament diameter. Table 5-2 shows the

processing parameters used for PCL and foam filament fabrication. The diameters of the filaments were obtained by averaging the measurements taken at five different positions.

Table 5-2 Processing parameters of the single-screw extruder.

Sample	Compression Zone Temperature (°C)	Nozzle Temperature (°C)	Screw Speed (rpm)	Traction Speed (mm/s)	Fan Speed (%)	Average Filament Diameter (mm)
PCL	70	85	4	1.3	70	1.76±0.04
Foam	73	90	12	1.3	100	1.73±0.04

A Bambu Lab A1 mini 3D printer was used to fabricate both foamed filaments with 75% void fraction and benchmarking PCL samples. A hotend with a nozzle diameter of 0.8 mm was utilized to alleviate flow resistance and avoid clogging. Bambu Studio slicing software was employed to convert the 3D digital models into layered printing instructions. Other key 3D-printing parameters include the bed-temperature of 30 °C, infill density of 100%, printing temperature of 70 °C, layer height of 0.15 mm, and printing speed of 50 mm s^{-1}.

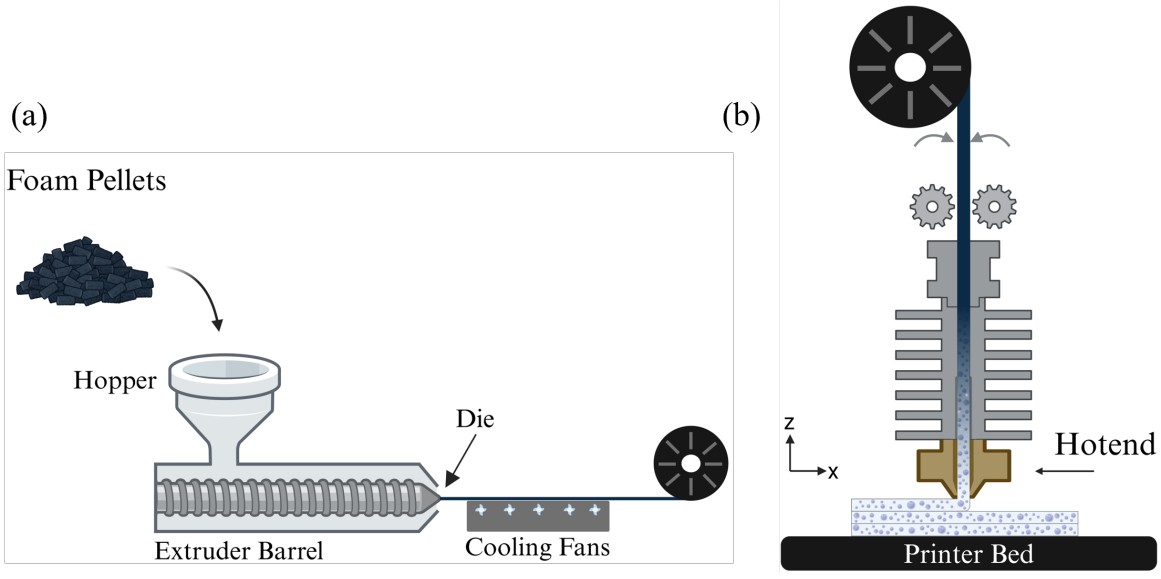

Figure 5-9 Schematic illustration of (a) foam pellet extrusion into filaments and (b) fused filament fabrication (FFF) 3D printing. Schematic created with BioRender.

Electrophysiological Signal Recording: Electrophysiological recordings, including electrocardiography (ECG), electromyography (EMG), and electroencephalography (EEG), were

performed to evaluate the performance of the developed electrodes in representative biosensing applications. All measurements were conducted on a healthy volunteer, and signals were acquired using a biosensing board (Cyton, OpenBCI, USA) at a sampling rate of 250 Hz. Foams with an 85% void fraction were cut into disks (8 mm diameter, 5 mm thickness). Electrical contacts were established using silver (Ag) traces connected to the snap button of a commercial Ambu® electrode (Figure S4a, Supporting Information). These assemblies were used for ECG and EMG measurements, and additionally as reference and ground electrodes in EEG recordings.

ECG signals were recorded using a standard limb-lead configuration (Figure S4b, Supporting Information). The ground and positive electrodes were placed on the left forearm, while the negative electrode was positioned on the right forearm. The electrodes were connected to the biosensing monitor, and cardiac signals were recorded in real time. During acquisition, a bandpass filter of 5-50 Hz was applied, along with a 60 Hz notch filter to suppress power-line interference. Offline signal processing was performed using a second-order digital Butterworth high-pass filter with a cutoff frequency of 0.5 Hz to remove baseline drift.

Surface EMG measurements were conducted on the flexor carpi muscle of the right forearm (Figure S4c, Supporting Information). Three electrodes were placed along the muscle. EMG signals were recorded while the participant performed repeated voluntary hand and wrist flexion–extension movements for durations of 1-2 s. Data acquisition was carried out with a bandpass filter of 15-50 Hz. Offline processing involved applying a second-order digital Butterworth high-pass filter with a cutoff frequency of 10 Hz to eliminate baseline drift.

Ear-EEG measurements were performed using the developed 85% void-fraction conductive foam electrode, integrated onto a commercial Onhear® foam earplug to enable in-ear recording (Figure 5-8a and Figure S4d, Supporting Information). The foam electrode (15 mm × 15 mm) was glued onto the foam base of the earplug to ensure conformal contact with the ear canal. The recording electrode was positioned within the ear canal, with a reference electrode placed on the ipsilateral mastoid and a ground electrode attached to the earlobe (Figure 5-8b). EEG signals were acquired during a 10-min recording session. Brain activity was analyzed in the 0-25 Hz frequency range, with particular emphasis on alpha-band activity (8-12 Hz), a hallmark of relaxed wakefulness (see Supporting Information for full signal analysis).

5.7 Acknowledgements

The protocol for human experiments was approved by the research ethics board of Polytechnique Montreal (certificate CER-2021-04-D), in accordance with the Tri-Council Policy Statement: Ethical Conduct for Research Involving Humans (TCPS). Written consent was obtained from the participant. The authors acknowledge the use of BioRender.com to create the schematics used in Figure 1a (Petrossian, G. (2026) https://BioRender.com/gee6a7p), Figure 8a (Petrossian, G. (2026) https://BioRender.com/dxxm4ml), and Figure 9 (Petrossian, G. (2026) https://BioRender.com/jg02o3w).

5.8 Funding

This research was supported by the Natural Science and Engineering Research Council of Canada (NSERC) through Discovery Grants awarded to FC (grant No. RGPIN-2025-05607) and HX (grant No. RGPIN-2024-06567). The equipment and infrastructure used in this study were acquired and maintained by the Canada Foundation for Innovation, FRQNT and NSERC. GP acknowledges support from the NSERC Vanier Canada Graduate Scholarship. Y.D. acknowledges support from CREPEC for the Complément de bourse (Maitrise) scholarship. S.E. and F.M.W. acknowledge the Fonds de recherche du Québec - Nature et technologies (FRQNT) for a Doctoral Scholarship. BX acknowledges support from NSERC Undergraduate Student Research Awards (USRA).

CHAPTER 6ARTICLE 3: DOUBLE-NETWORK PEDOT:PSS XEROGEL FIBERS WITH HIGH STRETCHABILITY AND ELECTRICAL STABILITY FOR WEARABLE STRAIN SENSING

6.1 Authors

Gayaneh Petrossian,[a] Sara Ebrahimi,[a] Floriane Miquet-Westphal,[a] Hang Xu,[b] and Fabio Circoira *[a]

[a] Department of Chemical Engineering, Polytechnique Montréal, Montréal, Québec H3C 3A7, Canada

[b] Department of Mechanical, Industrial and Aerospace Engineering, Concordia University, Montreal, QC H3A 0C3, Canada

*Corresponding author: fabio.cicoira@polymtl.ca

Submitted March 17, 2026, under revision at *Materials Advances*

6.2 Abstract

Conductive polymer xerogels provide a promising route toward mechanically stable and water-independent alternatives to conventional hydrogels for wearable bioelectronics. However, achieving high stretchability, mechanical robustness, and stable electrical performance in xerogel fibers remains challenging. Here, we develop highly stretchable and conductive double-network PEDOT:PSS xerogel fibers fabricated through freeze-thaw-induced physical crosslinking of poly vinyl alcohol (PVA) followed by borax-mediated crosslink formation. The resulting fibers exhibit enhanced network integrity and mechanical robustness, enabling tensile strength up to ~16 MPa and elongation at break exceeding 1100% at an optimized borax concentration, while maintaining stable electrical conductivity (~0.8 S m^{-1}). The fibers display reproducible strain-dependent resistance changes with gauge factors up to ~19 at high strain. When integrated as wearable sensors, the xerogel fibers enable reliable real-time monitoring of human motion, including finger, wrist, and elbow movements. This double-network xerogel strategy provides a simple and scalable approach to engineering mechanically robust conductive fibers for next-generation wearable sensing and bioelectronic applications.

6.3 Introduction

Flexible and stretchable conductive materials composed of conductive polymers and elastic matrices are increasingly explored for applications in wearable health monitoring, implantable bioelectronics, and human-machine interfaces.[302], [303], [304], [305], [306], [307], [308], [309], [310], [311] Conducting polymer-based hydrogels have attracted significant attention due to their combination of softness, stretchability, and ionic/electronic conductivity. Among these materials, poly(3,4-ethylenedioxythiophene):polystyrene sulfonate (PEDOT:PSS) has emerged for its tunable electrical conductivity, aqueous processability, biocompatibility, and potential for self-healing. However, in its pristine form, PEDOT:PSS generally exhibits moderate conductivity (~1 S cm^{-1}) and limited stretchability (~5%).[312], [313] Moreover, most PEDOT:PSS-based hydrogel conductors remain strongly dependent on water content to maintain their mechanical compliance and electrical performance, making them vulnerable to dehydration, dimensional instability, and long-term performance degradation in ambient environments. To overcome these limitations, various additives have been introduced. Small-molecule polyols such as glycerol,[314] ethylene glycol (EG),[315] and xylitol[316] primarily act as conductivity enhancers, while polymeric additives such as polyvinyl alcohol (PVA),[317] polyurethane (PU)[268], polyurethane diol (PUD)[318], and polyethylene glycol (PEG)[319] are commonly incorporated to improve mechanical compliance, stretchability, and structural stability of the conductive network.

Xerogels, the dry analogs of hydrogels, are polymer networks obtained by removing water from a hydrogel while preserving the underlying crosslinked structure. Unlike aerogels, which require supercritical drying to maintain an open-pore architecture, xerogels are typically produced through ambient drying or mild thermal drying, making them simpler and more cost-effective to manufacture.[320] The removal of water results in a denser and mechanically stable material that is no longer dependent on hydration for structural integrity. Consequently, xerogels overcome key limitations of hydrogels, including dehydration, dimensional instability, and degradation of mechanical and electrical performance over time. These advantages make conductive xerogels particularly attractive for wearable and bioelectronic applications requiring stable performance under ambient conditions.

To enhance the mechanical performance of polymer-based hydrogels and xerogels, both physical and chemical crosslinking methods have been employed.[321], [322] Physical crosslinking

methods, such as freeze-thaw cycling,[323] rely on non-covalent interactions, including hydrogen bonding and crystallite formation, to establish network structures without the introduction of additional chemicals. In PVA systems, freeze-thaw processing promotes the formation of microcrystalline domains that serve as physical junction points, resulting in enhanced elasticity and mechanical strength.[324] Chemical crosslinking involves the formation of covalent or reversible bonds using crosslinkers such as glutaraldehyde,[325] citric acid,[326] or borax.[327], [328], [329] Borax forms reversible di-diol complexes with PVA chains, enabling dynamic and tunable mechanical behavior.[330] Combining both physical and chemical crosslinking approaches can therefore produce hybrid networks that balance flexibility, strength, and structural stability.[331], [332]

Conductive fibers are particularly attractive for wearable sensing applications due to their inherent flexibility, lightweight nature, and ability to conform to complex and dynamic surfaces. Compared with bulk films, fiber-shaped sensors can accommodate larger deformation, provide improved mechanical compatibility with soft tissues, and enable reliable signal acquisition during motion. Fiber geometries also facilitate the integration into wearable platforms, such as textiles and skin-mounted devices. For example, fiber-like conductive hydrogels fabricated through freeze-thaw processing and weaving strategies have been reported as mechanically robust and stretchable sensors for human motion monitoring.[333] Similarly, PEDOT:PSS/PVA hydrogel fibers have demonstrated high mechanical strength and sensitivity for physiological sensing applications.[334] Despite these advances, developing conductive xerogel fibers that simultaneously exhibit high mechanical robustness, large stretchability, and stable electrical performance remains challenging, particularly in water-independent systems.

Here, we report highly stretchable and conductive double-network PEDOT:PSS xerogel fibers for wearable strain sensing applications. The fibers are fabricated through a double-network design combining freeze–thaw-induced physical crosslinking of PVA with borax-mediated dynamic crosslink formation. This strategy produces mechanically robust and electrically stable xerogel fibers that operate under water-independent conditions, addressing a key limitation of conventional PEDOT:PSS hydrogel strain sensors. By varying the borax concentration, the crosslink density can be systematically tuned, enabling control over the mechanical and electromechanical properties of the fibers. The resulting xerogel fibers exhibit tensile strains exceeding 1100% while maintaining

stable electrical conductivity and reliable strain-dependent resistance changes. When integrated as wearable sensors, the fibers enable accurate real-time monitoring of human motion, demonstrating their potential for robust wearable bioelectronic applications.

6.4 Materials and methods

6.4.1 Materials

Poly(vinyl alcohol) (PVA, 89,000-98,000 average molecular weight and 99+% hydrolyzed), glycerol, and sodium tetraborate decahydrate (borax) were purchased from Millipore Sigma (St. Louis, MO, USA). PEDOT:PSS dispersion (conductive grade, SKU 483095, 1.3 wt% solids) was purchased from Millipore Sigma (St. Louis, MO, USA). Silicone elastomer Ecoflex Gel was purchased from Smooth-On (Macungie, PA, USA). Copper tape (88.9 μm, 10 mΩ sq^{-1}) was purchased from McMaster-Carr. The glass capillary tubes with an inside diameter of 1 mm were supplied by Iouyup (China).

6.4.2 Xerogel preparation

Initially, a 15wt% aqueous solution of polyvinyl alcohol was prepared by dissolving PVA in distilled water in an oil bath at 90°C with continuous stirring for 2 hours until a clear solution was obtained. A precursor solution was prepared by mixing 1 g of the PVA solution, 1 g of PEDOT:PSS dispersion, and 0.1 g of glycerol under magnetic stirring at 50 °C for 5 min.

After thorough mixing, the homogeneous solution was injected using a syringe into molds with desired shapes, where the mold geometry defined the final form of the xerogel. For the preparation of the fibers, the mixture was injected into glass capillary tubes with an inside diameter of 1 mm and a length of 10 cm. For certain characterization techniques, films were also prepared by casting the solution into flat molds to obtain xerogel films with uniform thickness. Consequently, the materials were subjected to freeze-thaw (F-T) processing, consisting of freezing at -80 °C for 8 h followed by thawing at room temperature for 30 minutes, repeated for five cycles, resulting in physically crosslinked hydrogels. After freeze-thaw treatment, the samples formed fully solid, self-supporting structures that could be easily removed from the molds without deformation or damage. These samples were designated PPG. Following gel formation, the hydrogels were immersed for 30 s in aqueous borax solutions (concentrations of 0, 0.1, 0.25, and 0.5 M), followed by ambient drying to obtain the xerogels. For comparison, cast-only (CO) control samples were prepared by

casting the precursor solution into films and allowing them to dry at room temperature without undergoing freeze-thaw treatment. Because no crosslinking occurred under these conditions, the materials did not form stable fibers. These samples were designated CO-PPG.

6.4.3 Characterization

The morphology of the xerogels was analyzed using a Quattro (Thermo Scientific) scanning electron microscope (SEM). The samples were cryo-fractured using liquid nitrogen to achieve a clean representative cross-section of their internal structure.

The thermal stability of the xerogels was evaluated using thermogravimetric analysis (TGA, 5500, TA Instruments, USA). Measurements were performed in an open platinum crucible from 40-600 °C with a heating rate of 20 °C min^{-1}, under a nitrogen atmosphere (40 mL min^{-1}). Differential scanning calorimetry (DSC, Q2000, TA Instruments, USA) was used to determine the crystallinity percentage (X_c), using the following equation:

$$\boldsymbol{X_c = \frac{\Delta H_f}{\Delta H_f^{100}} \times 100} \qquad (6.1)$$

where ΔH_f is the heat of fusion, measured by the area under the melting peaks in DSC, and ΔH_f^{100} is the heat of fusion for a 100% crystalline PVA, obtained from the literature (ΔH_f^{100}=161.4J g^{-1}).[335]

To study the chemical structure and bond formations, Fourier-transform infrared (FTIR) spectroscopy was performed on the samples using a PerkinElmer Spectrum 65 spectrometer. Before acquiring sample data, a background spectrum was recorded. The sample spectra were measured at room temperature with a scanning range of 4000-600 cm^{-1} and a resolution of 4 cm^{-1} across 32 scans. Each sample underwent three scans under the same conditions.

Water content percentages (WC%) of the hydrogels were determined using:

$$\boldsymbol{WC = \frac{W_h - W_x}{W_x} \times 100} \qquad (6.2)$$

where W_h and W_x are the weights of the hydrogels and xerogels, respectively. In addition, the swelling degree (SD) was calculated using:

$$\boldsymbol{SD = \frac{W_s - W_x}{W_x} \times 100} \qquad (6.3)$$

where W_s is the weight of the swollen samples. The swollen samples were prepared by immersing 1.0 g of xerogel in distilled water at room temperature. The swollen samples were removed, patted dry with absorbent paper, and weighed, after specific time intervals. The measurements continued until the swollen gel's weight stabilized, indicating that equilibrium swelling had been reached. The equilibrium swelling degree was defined as the plateau value in the swelling ratio versus time curve.

Mechanical and electrical tests were performed using a Mach-1 V500csst MA009 mechanical tester (Biomomentum Inc., Canada). Uniaxial tensile tests were performed on xerogel fibers to evaluate their mechanical response, using a constant crosshead speed of 30 mm min^{-1}. For xerogel fibers, a custom double-needle tensile mounting approach was used to enable reliable handling of small-diameter filaments (Figure S1). Briefly, two syringe needle tips were positioned facing each other on the bench and separated by a predefined gauge gap of ~10 mm. The xerogel fiber was carefully threaded through both needle tips, and a single drop of cyanoacrylate adhesive was applied within the plastic cavity of each needle to immobilize the filament ends. The two needle tips were then seated onto a double-needle tip holder assembly (provided by Biomomentum Inc., Canada) designed for the Mach-1 tester. A 70N load cell was used for these experiments. The holders were mounted coaxially, facing each other at the center of the testing chamber, and the double-needle assembly was firmly inserted onto the holders to establish a stable tensile configuration for fiber testing.

Electrical conductivity measurements were carried out using a tailored tensile grip with electrodes (model MA068) made by Biomomentum Inc., interfaced with a source measure unit (B2902A, Agilent). For all electrical measurements, copper tape was used to tab the xerogel fibers at both ends to ensure stable electrical contact between the sample and the electrodes. The electrical resistance of the samples was measured using the source measure unit during the test. The conductivity (σ) was calculated using:

$$\boldsymbol{\sigma = \frac{L}{R \times A}} \qquad (\mathbf{6.4})$$

where R denotes the average resistance, and L and A are the length and cross-sectional area of the xerogels between two grips, respectively. The reported conductivity values correspond to the average of 3 measurements, with error bars representing the standard deviation. Electrical continuity was further demonstrated by incorporating the xerogel conductor into a simple circuit

connected to a light-emitting diode (LED), where successful illumination confirmed effective charge transport through the material.

The electromechanical response was evaluated by monitoring the relative resistance change ($\Delta R/R_0$) during tensile deformation using the same mechanical testing system coupled to the source measure unit. The relative resistance change was defined as:

$$\frac{\Delta R}{R_0} = \frac{R - R_0}{R_0} \times 100 \quad (6.5)$$

where R is the instantaneous resistance and R_0 is the initial resistance at 0% strain. Additionally, the gauge factor (GF), indicating the sensitivity of the xerogel, was calculated using the following equation:

$$GF = \frac{\Delta R / R_0}{\varepsilon} \quad (6.6)$$

where ε represents the applied strain.

For wearable sensing demonstrations (refer to the results and discussion section for details), PPG-0.1 M borax xerogel fibers were placed on the skin and secured using a thin cured Ecoflex elastomer film. Copper tape was applied at both ends of the fiber to establish electrical connections to the source measure unit, and the real-time resistance was recorded during human motion.

6.5 Results and discussion

6.5.1 Preparation of PVA-PEDOT:PSS-Gly-Borax hydrogels and xerogels

Here, we introduce a reinforced xerogel fiber strategy based on a double network of physically and dynamically crosslinked PVA-PEDOT:PSS, enabling mechanically robust, stable sensing materials. Figure 6-1 illustrates the fabrication process and structural evolution of the xerogel fibers. A homogeneous aqueous solution of PVA, glycerol, and PEDOT:PSS was subjected to freeze-thaw cycling to induce physical crosslinking through the formation of PVA crystallite, producing free-standing hydrogels. Freezing drives phase separation and chain packing, generating crystalline junctions within a three-dimensional network that balance strength and elasticity. Although glycerol can participate in hydrogen bonding with PVA, substantial concentrations are typically required to markedly alter the hydrogen-bonded network.[336], [337] In the present system, glycerol primarily acts as a plasticizer, improving chain mobility and flexibility within the

matrix, while also acting as an electrical conductivity enhancer.[338], [339] PEDOT:PSS provides the conductive phase. To further reinforce the network, the hydrogels were post-treated with sodium tetraborate decahydrate (borax), which forms borate-diol crosslinks with PVA chains.[340] This process yields mechanically robust and conductive double-network xerogel fibers.

Scanning electron microscopy was used to examine the fracture morphology of the xerogels prepared under different conditions (Figure 6-2a-c). The cast-only sample exhibited a featureless fracture surface, indicating a dense and relatively homogeneous polymer network formed in the absence of any crosslinking. In contrast, the PVA-PEDOT:PSS-glycerol freeze-thaw sample (PPG) exhibited a textured fracture surface, reflecting the porous network typically formed in hydrogels during freeze-thaw gelation, where subsequent dehydration leads to partial pore collapse.[341], [342], [343] Following borax treatment, the PPG-0.1 M borax xerogel displayed an even more textured morphology, suggesting further modification and reinforcement of the network due to the formation of the double-network structure.

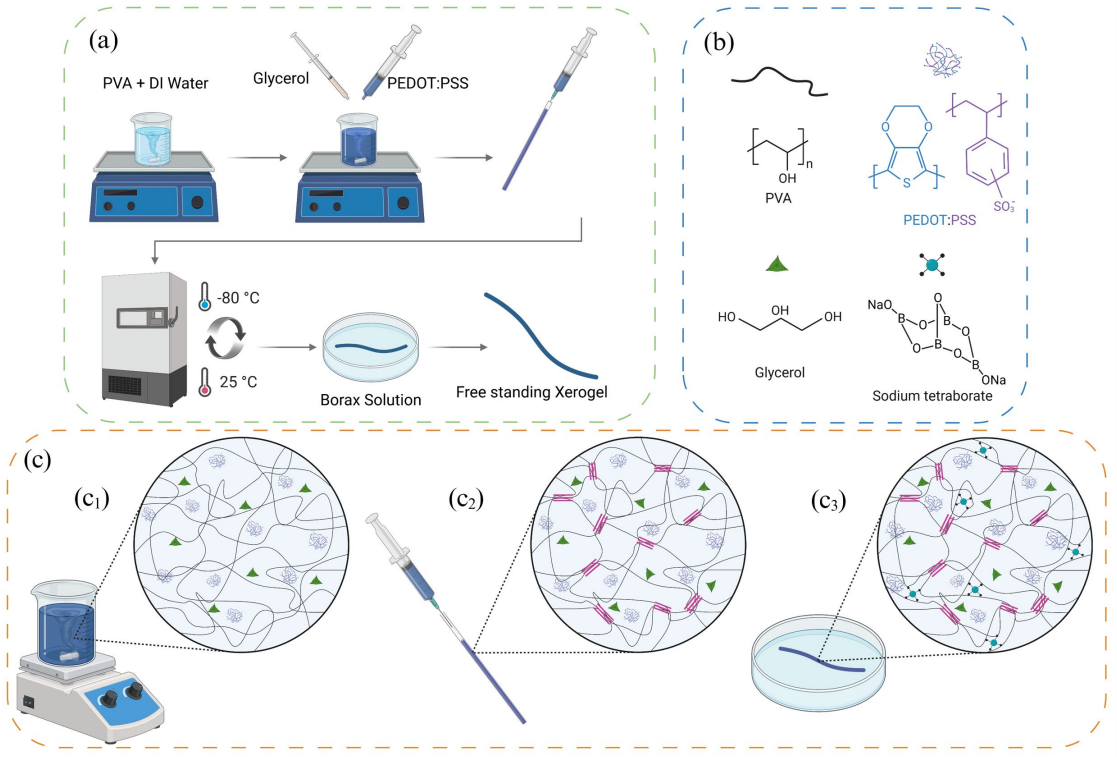

Figure 6-1 (a) Schematic illustration of the fabrication process of the xerogels. (b) Chemical structures of PVA, glycerol, sodium tetraborate (borax), and PEDOT:PSS. (c) schematic representation of the network evolution during processing: (c_1) homogeneous precursor solution

after mixing, (c_2) physically crosslinked network formed via freeze-thaw cycling, and (c_3) chemically crosslinked network after borax treatment. Schematic created with BioRender.

FTIR spectra of the cast-only sample (PPG-CO), freeze-thaw xerogel (PPG), and borax-treated xerogels (0.1-0.5 M) are shown in Figure 6-2d. The broad absorption band at 3000-3600 cm^{-1} is attributed to the stretching vibration of hydroxyl (-OH) groups in PVA.[344], [345], [346] The peak at 2915 cm^{-1} corresponds to the stretching vibration of -CH_2 groups.[347] The characteristic band at 1000-1150 cm^{-1} [347], [348] is associated with C-O stretching and crystalline domains of PVA. Additionally, the asymmetric stretching vibration of B-O-C at 1415 cm^{-1} confirms the crosslinking of PVA with borate ions through the formation of tetrahedral complexes.[349]

Thermogravimetric analysis (Figure S2) was conducted to evaluate the thermal stability of the xerogels before and after borax treatment. Both samples exhibited minimal mass loss below 150 °C, indicating a negligible amount of residual free water. The untreated PPG sample showed the onset of major weight loss at around 200 °C, whereas the borax-crosslinked xerogel exhibited a delayed degradation onset, indicating enhanced thermal stability due to the formation of additional crosslinks, consistent with previous reports.[350] The primary degradation stage between 300 and 500 °C corresponds to decomposition of the PVA backbone and PEDOT:PSS.[351], [352] Although the borax-treated sample showed a sharper mass loss within this main degradation region, this may be attributed to borate-assisted dehydration and decomposition of the PVA-rich network once thermal degradation begins. Notably, the borax-treated sample displayed a higher residual mass at elevated temperatures, confirming the formation of a more thermally stable network. These results demonstrate that borax treatment effectively improves the thermal resistance of the xerogel by increasing the crosslink density.

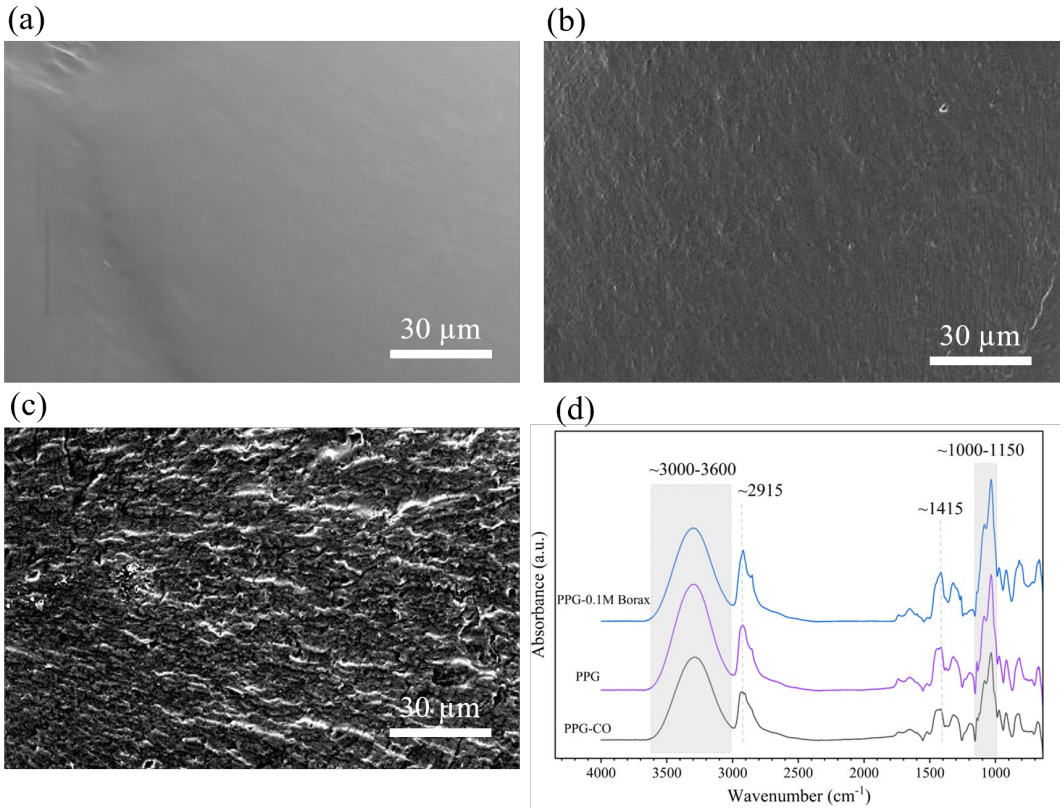

Figure 6-2 (a-c) SEM images showing the fracture morphology of (a) CO-PPG, (b) PPG, and (c) PPG-0.1M borax xerogels. (d) FTIR spectra of the CO-PPG film, PPG xerogel film, and PPG-0.1M borax xerogel film.

Differential scanning calorimetry (DSC) thermograms obtained during the second heating cycle are shown in Figure S3a. The untreated PPG sample exhibited no distinct melting transition, indicating that crystalline domains formed during freeze-thaw processing were either thermally unstable or highly constrained. This behavior can be attributed to the presence of physical crosslinks formed during freeze-thaw processing, which restrict the mobility of amorphous chain segments and inhibit the formation of well-defined crystalline domains detectable during the second heating cycle.[353] In contrast, borax-treated xerogels displayed a pronounced endothermic peak at approximately 160-190 °C, corresponding to the melting of crystalline domains formed within the more constrained network. The degree of crystallinity (Figure S3b) increased progressively with borax concentration, confirming that borax treatment promotes structural ordering. Additionally, the melting peak broadened with increasing borax concentration, indicating a wider distribution of crystalline domain sizes. This broadening is attributed to reduced chain

mobility caused by borate crosslinks, which disrupt uniform crystal growth and lead to crystals with varying sizes and stability.[354]

6.5.2 Swelling behavior

To evaluate the structural stability of the developed materials and to gain insight into the internal double-network architecture, the dehydration and swelling behaviors were investigated. For these swelling studies, samples were prepared as films using small square molds to obtain specimens with uniform geometry. Swelling analysis provides information about the internal polymer structure and crosslinking density, reflecting the relationship between network organization and water transport properties. Figure 6-3a shows representative photographs of the hydrogel, the corresponding xerogel after drying, and the swollen sample after rehydration. Figure 6-3b shows the temporal evolution of water content during ambient drying. All compositions exhibit a continuous and nearly linear decrease in water content, reaching near-complete dehydration and equilibrium with ambient humidity within approximately 8 hours. The similar drying profiles observed for all samples indicate that borax treatment does not significantly alter the overall evaporation kinetics.

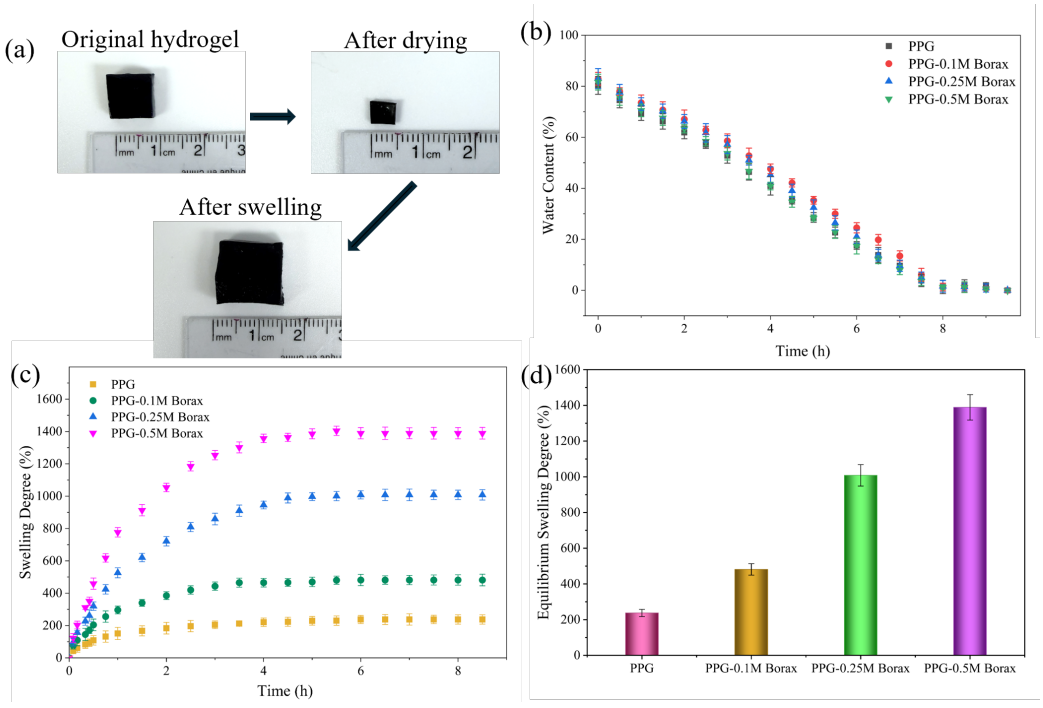

Figure 6-3 (a) Digital images of the PPG-0.1M borax hydrogel, the same sample after drying, and after swelling in water for 4 h. (b) Dehydration behavior of PPG and borax-treated xerogels (0–0.5

M) under ambient conditions, showing water content as a function of drying time until equilibrium with ambient humidity. (c) Swelling kinetics in deionized water, where samples were periodically weighed to determine swelling degree over time. (d) Equilibrium swelling degree of xerogels treated with different borax concentrations after reaching mass stabilization in water. Data represent mean ± standard deviation (n=3).

In contrast, the swelling behavior was strongly influenced by borax concentration (Figure 6-3c-d). Borax-treated xerogels exhibited faster swelling kinetics and higher equilibrium swelling degrees compared to the untreated PPG sample. The influence of borax on swelling in PVA-based systems is not universal, as both decreases[354], [355], [356] and increases[357], [358], [359] in swelling have been reported depending on network structure and processing conditions. In PVA networks crosslinked solely by borax, borax crosslinks often restrict chain mobility and reduce swelling. However, in the present freeze-thaw-derived network, borax treatment increases swelling capacity. This behavior likely arises from the interaction between borate ions and hydroxyl groups on PVA chains, which modifies the original hydrogen-bonding network formed during freeze-thaw gelation. The formation of borate crosslinks partially disrupts locally dense hydrogen-bonded regions, leading to a more open network structure that facilitates water penetration. As a result, the equilibrium swelling degree increases with borax concentration, reflecting greater water uptake within the double-network xerogel.

Appropriate swelling ability is important for sensing and bioelectronics applications, as it influences fluid transport, interfacial contact, and material stability in aqueous environments. Similar PVA-borax systems reported in the literature exhibit swelling ratios ranging from ~32% to 600%, demonstrating suitability for applications such as wound dressings and soft sensors.[355], [356], [360], [361] The swelling performance achieved here falls within this range, highlighting the suitability of these double network xerogel fibers for aqueous and bioelectronic applications.

6.5.3 Mechanical properties

The tensile behavior of the xerogel fibers was evaluated using a custom double-needle tensile mounting system (Figure 6-4a) designed to securely hold soft and compliant fibers without inducing stress concentrations or slippage. In this configuration, each fiber was fixed inside opposing syringe needle tips using adhesive and mounted onto the tensile tester. Representative

stress-strain curves under tensile loading are shown in Figure 6-4b. The curves are representative of three independent measurements, with statistical analysis presented in Figure 6-4c-d. Compared to the freeze-thaw-only PPG fibers, borax-treated samples displayed higher stress levels across the entire strain range, indicating effective reinforcement of the network.

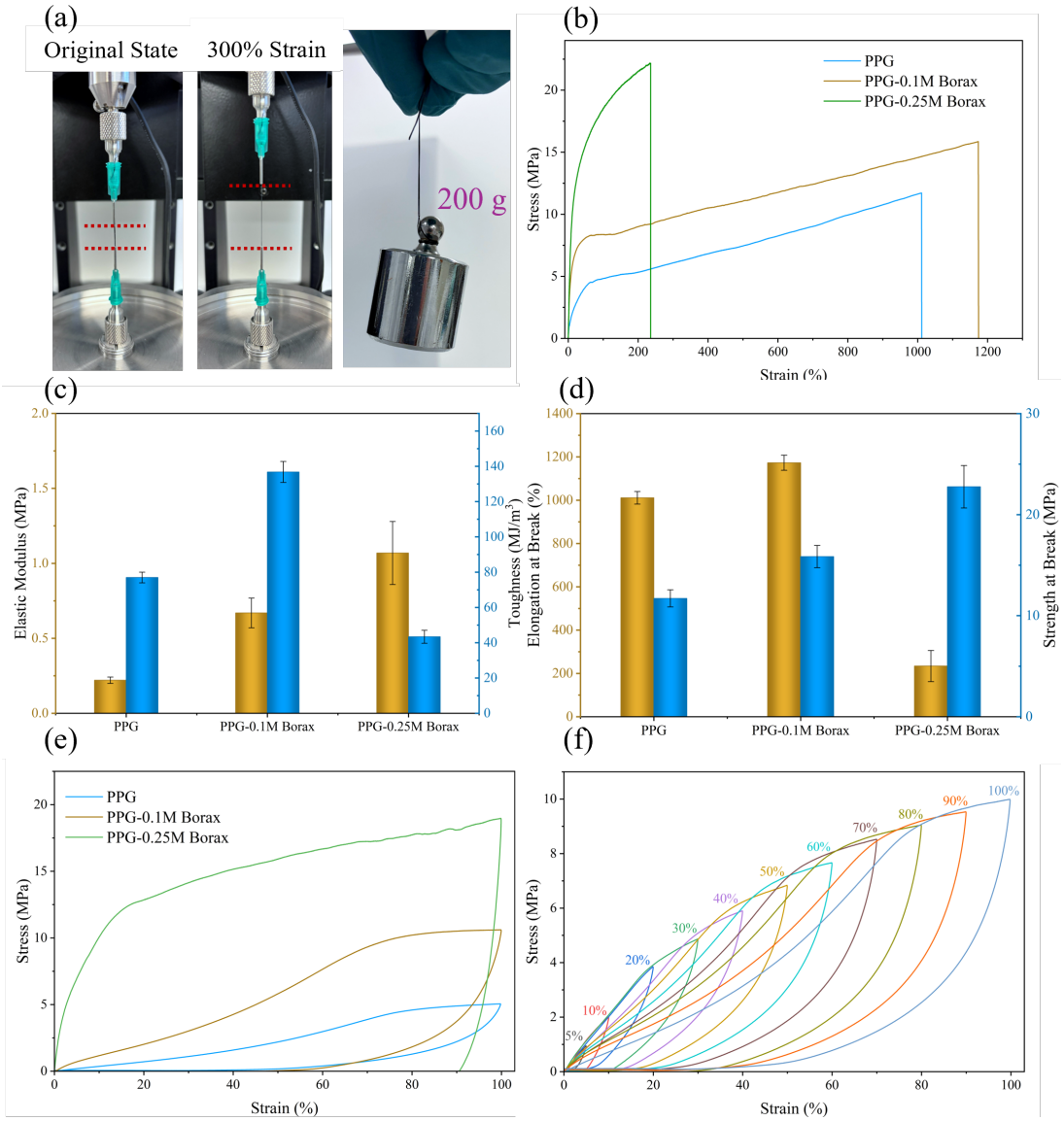

Figure 6-4 (a) Digital images of a PPG-0.1 M borax xerogel fiber during tensile testing, showing the original state and elongation to 300% strain (the red dashed lines indicate the gauge region of the fiber between the tensile grips), along with a demonstration of load-bearing capability (200 g). (b) Representative tensile stress-strain curves. (c) Elastic modulus and toughness (mean ±SD, n=3). (d) Elongation at break and strength at break (mean ±SD, n=3). (e) Loading-unloading tensile

curves of PPG xerogels with 0, 0.1 M, and 0.25 M borax. (f) Cyclic tensile behavior of PPG-0.1M borax fibers at increasing strain levels (5-100%). All tests were performed at an overhead speed of 30 mm min^{-1}.

Quantitative analysis further confirms this trend (Figure 6-4c-d). The elastic modulus, extracted from the slope of the initial linear region of the stress-strain curves (0-10% strain), increased substantially with borax concentration, reflecting the introduction of additional borate-diol interactions that strengthen the polymer network. The modulus increased by more than 4.5 times from the untreated PPG sample to the 0.25 M borax-treated xerogel, consistent with the increased effective crosslink density widely reported in PVA-borax systems.[362], [363] Similarly, the tensile strength at break increased progressively with borax concentration, approximately doubling from the untreated PPG sample to the 0.25 M borax-treated xerogel, demonstrating improved load-bearing capacity and tunable mechanical properties through borax-mediated crosslinking. The tensile strength achieved here is comparable to or higher than previously reported PVA-based fibers while maintaining similar or higher stretchability.[333], [334]

The elongation at break initially increased at moderate borax concentration (0.1 M) but decreased at higher concentration (0.25 M). At moderate borax content, additional borate-diol interactions reinforce the network while still allowing sufficient chain mobility, leading to improved extensibility. At higher borax concentration, the increased crosslink density imposes stronger network constraints, restricting chain mobility and resulting in more brittle behavior. This trend highlights the intrinsic trade-off between mechanical reinforcement and flexibility, where increased crosslink density enhances stiffness and strength but limits extensibility.[364] The toughness followed a similar trend, reaching a maximum (136.78 ± 5.95 MJ m^{-3}) at intermediate borax concentration before decreasing at higher borax concentration, indicating an optimal crosslinking window at moderate borax concentration, beyond which excessive crosslinking windows where the balance between strength and extensibility maximizes energy dissipation.

Subsequently, cyclic tensile tests were conducted to assess the energy dissipation behavior of the xerogel fibers (Figure 6-4e). All samples exhibit evident hysteresis loops during loading-unloading, and the loop area increases with borax concentration (PPG < PPG-0.1M < PPG-0.25M). The enlarged hysteresis indicates greater mechanical energy dissipation, consistent with a more highly crosslinked network that increases internal friction and limits molecular rearrangement during

deformation. These results further support that borax post-treatment strengthens the double-network structure by increasing crosslink density, leading to improved mechanical robustness and toughness. Overall, our xerogel fibers exhibited higher ultimate stress and strain than many previously reported PVA-based strain sensors (Table 6-1).

Table 6-1 Comparison of properties of recent PVA-based strain sensors.

Material	**Fabrication Method**	**Strength (MPa)**	**Strain (%)**	**Ref.**
PVA-HPC	Salt solution soaking	1.3	975	[365]
PVA-TA@talc	Molecular-level ion conductive channels + F-T	~0.7	~750	[366]
PVA-PEDOT:PSS-Gly	F-T	13.76	519.9	[334]
PVA-PA	Hot-pressing + F-T	~0.7	>1000	[367]
PVA	Crosslinking with alkaline metal hydroxide	~13	~350	[368]
PVA-Mxene-PEDOT:PSS-PDA	Dynamic supramolecular cross-linking	~1N	~700	[369]
PVA-HGNs	Doping nanofillers + Directional freezing + Salting out	9.5	2058	[333]
PVA-ANF	Electrospinning + Vacuum-assisted filtration	~5.5	~240	[370]
PVA-SL	Cross-linking with sodium lignosulfonate	~6	571	[371]
PVA-PEDOT:PSS-DMSO-Borax	Physical crosslinking + Borax crosslinking	~0.23	~300	[55]
PVA-SA-PESOT:PSS-$ZnSO_4$	F-T + Salting-out	34.22	402	[372]
PVA-IL-Borax	Borax crosslinking + F-T	3.1	~500	[373]
PVA-CS-Glycerol	One-pot synthesis + F-T	6.29	497	[374]
PVA-PEDOT:PSS-Glycerol-Borax	F-T + Borax crosslinking	15.85±1.12	1173.02±33.21	This work

To further evaluate mechanical stability, cyclic tensile tests at progressively increasing strain were performed on the PPG-0.1 M borax fibers, corresponding to the optimal crosslink density (Figure 6-4f). As the applied strain increased from 5% to 100%, the hysteresis loops progressively expanded and the maximum stress increased steadily, demonstrating stable load-bearing capability and mechanical integrity, consistent with previous reports.[375], [376], [377] The well-defined, closed loops indicate that the fibers maintain structural integrity throughout the loading-unloading

cycles, confirming that borax post-treatment produces a mechanically robust network capable of sustaining repeated deformation without failure. This combination of high stretchability and mechanical robustness is particularly advantageous for strain sensing applications, where large deformation and repeated loading are required.

6.5.4 Electromechanical properties

PEDOT:PSS endows the xerogel fibers with electrical conductivity by forming a continuous conductive network. All samples exhibited similar conductivities of approximately 0.8 S m^{-1}, indicating that the freeze-thaw process and borax crosslinking did not significantly disrupt electrical pathways. The moderate conductivity is likely due to the high fraction of insulating PVA and the dense xerogel network formed after drying, which favors mechanical robustness and structural stability over maximization of electrical transport. The electrical stability of the PPG-0.1 M borax fibers under deformation was qualitatively demonstrated using a simple LED circuit (Figure 6-5a). The LED remained illuminated when the fiber was stretched up to 200% strain, confirming the preservation of conductivity during large deformation, although its brightness gradually decreased due to the strain-induced increase in resistance.

To quantitatively characterize this behavior, the relative resistance change ($\Delta R/R_0$) was measured as a function of tensile strain (Figure 6-5b). The relative resistance increased progressively with increasing strain, confirming that the xerogel fibers are suitable for use as strain sensors. Since the $\Delta R/R_0$-strain response is nonlinear, GF values were extracted as apparent gauge factors over equal strain intervals rather than as a single value over the full strain range. The gauge factor (GF), calculated from the slope of the relative resistance-strain curve, remained modest at 0.86 and 2.06 in the 0-50% and 50-100% strain ranges, respectively, before increasing sharply to ~9 and ~19 at higher strains (100-150% and 150-200%). At low strain, the conductive PEDOT:PSS network deforms elastically together with the PVA matrix, and the resistance change is mainly governed by geometric effects, including elongation of the conductive pathway and reduction of the cross-sectional area. As the strain increases, the distance between PEDOT-rich conductive regions within the polymer network gradually increases, which reduces interchain contact and increases charge transport resistance through hopping or tunneling mechanisms. At larger strains, continued stretching of the polymer network further increases the transport distance between conductive

pathways, leading to a more pronounced resistance increase and the sharp rise in gauge factor observed at higher strain.[378], [379]

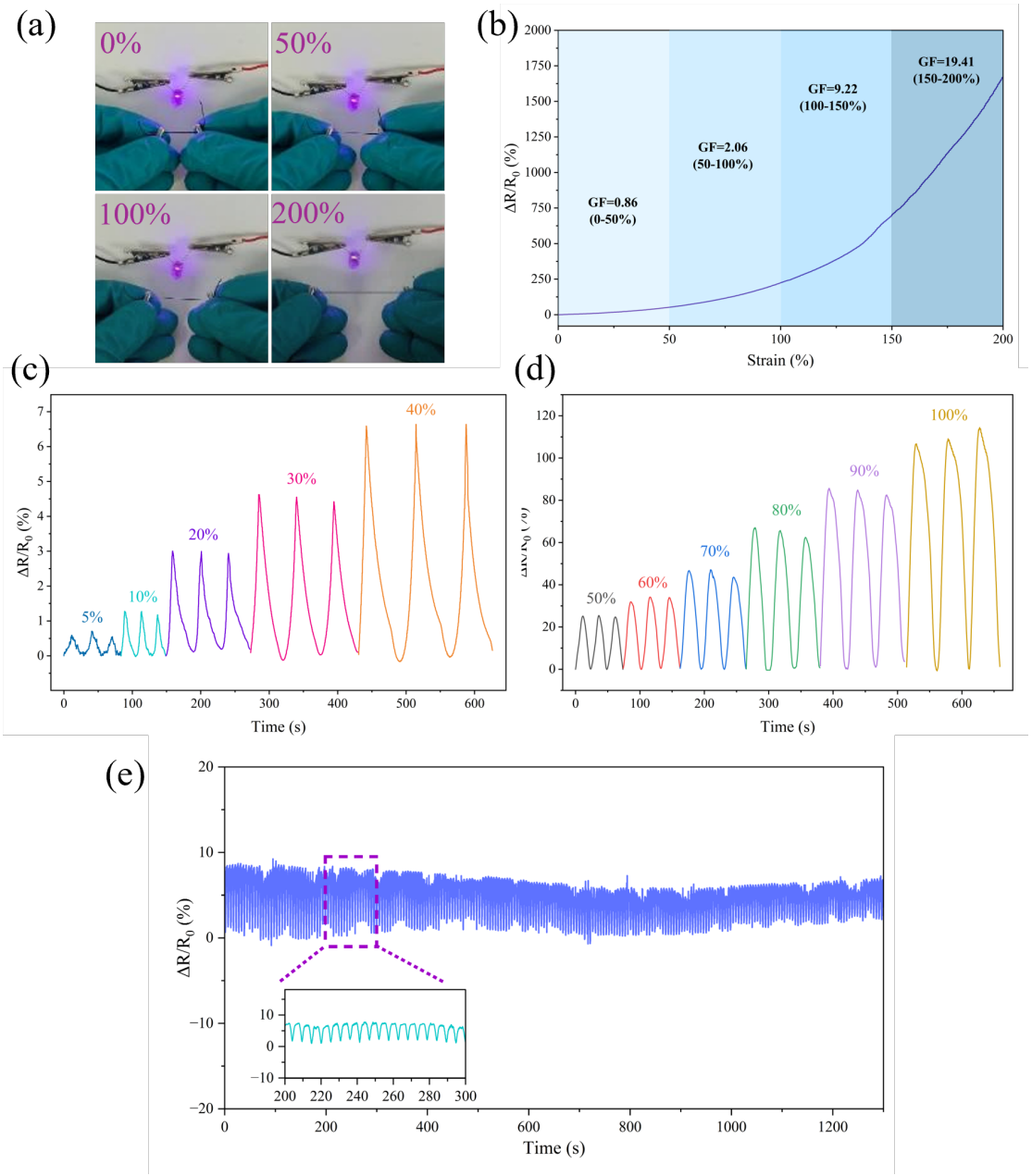

Figure 6-5 (a) Digital images of the strain sensor at 0%, 50%, 100%, and 200% tensile strain, demonstrating stable electrical response during deformation. (b) Relative resistance change (ΔR/R₀) as a function of strain, with calculated gauge factors in different strain regions. Variation in relative resistance of the xerogel fibers in response to (c) small strains (5-40%) and (d) large

strains (50-100%); (e) Cyclic electromechanical response of the PPG-0.1 M borax xerogel fiber during 300 stretching cycles at 30% strain, demonstrating signal stability.

The electrical response of the xerogel fibers under cyclic deformation was evaluated at different strain levels (Figure 6-5c-d). The fibers exhibited stable and repeatable resistance changes over multiple loading-unloading cycles, with the signal amplitude increasing systematically with increasing strain. Distinct and well-defined responses were observed even at low strains, while larger strains produced proportionally greater resistance variations. The consistent signal profiles and clear differentiation between strain levels demonstrate the reliability and sensitivity of the xerogel fibers for repeated strain sensing.

The electromechanical stability of the xerogel fibers was further evaluated during 300 consecutive loading–unloading cycles at 30% strain, where the resistance signal remained stable and reproducible with no noticeable drift or degradation (Figure 6-5e). The consistent peak amplitudes and waveform profiles indicate that the conductive network remains intact during repeated deformation. This stable electrical performance highlights the robustness of the xerogel fibers and their suitability for reliable strain sensing under repeated mechanical loading.

6.5.5 Application of xerogel fibers in motion monitoring

To evaluate the ability of the xerogel fibers to monitor human motion, the sensors were attached to different body locations for dynamic testing (Figure S4 and Figure 6-6). When mounted on the finger, the sensor produced distinct and repeatable resistance peaks corresponding to bending and releasing motions (Figure 6-6a). Similarly, clear and stable electrical responses were observed during hand opening and closing, with consistent signal amplitudes and good reproducibility over multiple cycles (Figure 6-6b). When positioned on larger joints such as the wrist and elbow, the fibers generate significantly higher resistance changes due to the greater deformation associated with these movements (Figure 6-6c-d). Upon release of each movement, the signal rapidly returned to its baseline value, indicating fast recovery, good repeatability, and stable electrical performance. These results demonstrate the capability of the xerogel fibers to reliably monitor both subtle and large-scale human motion, highlighting their potential for wearable strain sensing applications.

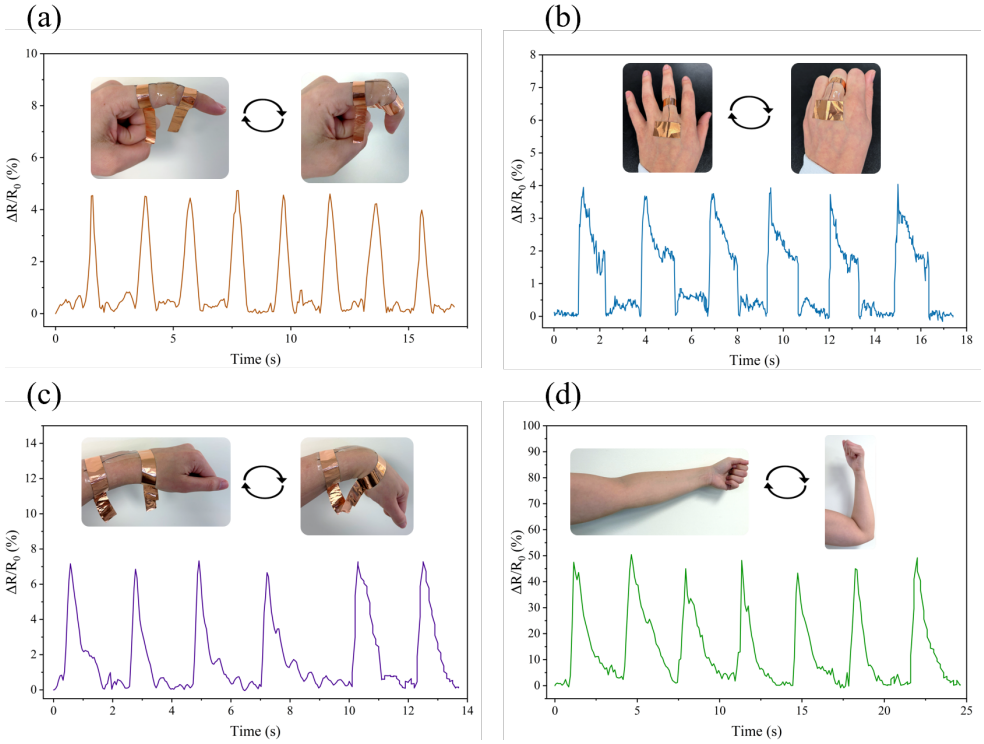

Figure 6-6 Real-time relative resistance changes of the xerogel fibers during human motion monitoring: (a) finger bending, (b) fist clenching, (c) wrist bending, and (d) elbow bending.

6.6 Conclusions

In summary, we developed highly stretchable and conductive double-network PEDOT:PSS xerogel fibers through freeze-thaw processing followed by borax-mediated crosslinking. By varying the borax concentration, the mechanical properties of the fibers could be systematically tuned. The combined physical and chemical crosslinking strategy produced mechanically robust fibers with elastic moduli ranging from ~0.2 to ~1 MPa and tensile strengths of ~12 to ~23 MPa, while maintaining elongation at break exceeding 1100%, demonstrating an effective balance between strength and extensibility. The xerogel fibers exhibited stable electrical conductivity and reproducible strain-dependent resistance changes with gauge factors ranging from 0.86 to ~19, along with excellent durability under repeated deformation. When integrated as wearable sensors, the fibers enabled reliable real-time monitoring of human motion. These results demonstrate that double-network conductive xerogel fibers provide a promising platform for mechanically robust and reliable wearable strain sensors.

6.7 Author contributions

Gayaneh Petrossian: conceptualization, data curation, formal analysis, methodology, investigation, visualization, writing – original draft. Sara Ebrahimi: methodology, writing – review & editing. Floriane Miquet-Westphal: methodology, writing – review & editing. Hang Xu: supervision, validation, writing – review & editing. Fabio Cicoira: project administration, resources, supervision, validation, writing – review & editing.

6.8 Conflict of interest

There are no conflicts to declare.

6.9 Data availability

The data supporting the findings of this study are provided in the Supplementary Information (SI). Additional data is available from the corresponding authors upon reasonable request.

6.10 Acknowledgements

This research was supported by the Natural Science and Engineering Research Council of Canada (NSERC) through Discovery Grants awarded to FC (grant No. RGPIN-2025-05607) and HX (grant No. RGPIN-2024-06567). The equipment and infrastructure used in this study were acquired and maintained by the Canada Foundation for Innovation, FRQNT and NSERC. GP acknowledges support from the NSERC Vanier Canada Graduate Scholarship. S.E. and F.M.W. acknowledge the Fonds de recherche du Québec - Nature et technologies (FRQNT) for a Doctoral Scholarship. F.M-W acknowledge the support of Hydro-Québec, Fondation Arbour, and the Club Saint-Denis and Foundation and Alumni of Polytechnique Montreal for an Excellence Award scholarship.

The protocol for human experiments was approved by the research ethics board of Polytechnique Montreal (certificate CER-2021-04-D), in accordance with the Tri-Council Policy Statement: Ethical Conduct for Research Involving Humans (TCPS). Written consent was obtained from the participant. The authors acknowledge the use of BioRender.com to create the schematics used in Fig. 1 (Petrossian, G. (2026) https://BioRender.com/tyscmea).

CHAPTER 7GENERAL DISCUSSION

The development of materials that are simultaneously soft and electrically conductive is central to advancing wearable electronic and bioelectronic technologies. As discussed in the literature review presented in this thesis, electrode materials used in physiological monitoring systems must meet several critical requirements, including reliable electrical conductivity, mechanical compliance with biological tissues, and long-term stability during use. Conductive polymers, particularly poly(3,4-ethylenedioxythiophene):poly(styrene sulfonate) (PEDOT:PSS), have emerged as promising candidates for addressing these requirements due to their combined electronic and ionic conductivity, solution processability, and compatibility with various polymer systems. Building on these characteristics, this thesis explored how tailoring the structure of PEDOT:PSS-based materials can enable new classes of soft conductive systems for wearable sensing applications.

The literature review presented in Article 1 highlights the diversity of electrode materials currently investigated for electroencephalography (EEG), including conventional wet electrodes, dry metallic electrodes, and emerging soft materials designed to improve comfort and long-term wearability. These studies demonstrate that the mechanical properties and structural design of electrode materials play a critical role in determining signal stability and user comfort. In particular, the growing interest in alternative EEG configurations such as forehead and ear-centered EEG systems further highlights the need for electrode materials that are soft, conformable, and capable of maintaining stable electrical contact with the skin. These requirements highlight the importance of developing new material systems that can better adapt to the complex geometry of the ear while enabling reliable long-term electrophysiological recordings.

Motivated by these considerations, the experimental chapters of this thesis investigated two distinct material strategies for developing soft conductive PEDOT:PSS-based systems. The first approach focused on the development of conductive foams based on PEDOT:PSS-coated polymer microspheres. In this work, expandable polymer microspheres were coated in situ with PEDOT:PSS and incorporated into syntactic foam architectures to create lightweight conductive materials with tunable porosity and mechanical flexibility. This microsphere-templated design enables precise control over the foam structure through adjustment of the void fraction while maintaining conductive pathways along the PEDOT:PSS-coated microsphere shells. The resulting

materials exhibit low elastic moduli comparable to soft biological tissues and electrical conductivities reaching ~10^{-2} S cm^{-1} at 85% void fractions. In addition to their lightweight and compliant structure, the foams are compatible with thermoplastic processing and fused filament fabrication, enabling additive manufacturing of personalized soft electrodes. Furthermore, the syntactic foam architecture allows the materials to be reprocessed through both chemical recycling and thermal reshaping while preserving their structural and electrical properties. Such porous conductive architecture offers a versatile platform for developing lightweight and mechanically adaptable electrodes for wearable sensing systems.

The second material strategy explored in this thesis involved the development of conductive xerogel fibers based on PEDOT:PSS polymer networks. The xerogel system is based on a continuous polymer network formed through freeze-thaw-induced physical crosslinking followed by borax-mediated fixed crosslink formation. In this work, a PVA-PEDOT:PSS-glycerol system was used to fabricate fiber-shaped hydrogels that were subsequently dehydrated under ambient conditions to obtain conductive xerogel fibers. The resulting double-network architecture significantly enhanced the mechanical robustness of the fibers, yielding tensile strengths up to ~15 MPa and elongations exceeding 1100% while maintaining stable electrical conductivity (~0.8 S m^{-1}). The xerogel fibers exhibited reproducible strain-dependent resistance changes with gauge factors up to ~19 and demonstrated stable performance under repeated mechanical deformation. When integrated into wearable platforms, these fibers enabled reliable monitoring of human motion, including finger, wrist, and elbow movements. These results highlight the potential of double-network PEDOT:PSS xerogel fibers as mechanically robust and highly stretchable conductors for wearable strain sensing systems.

Despite their differences, both material systems developed in this thesis rely on controlling the microstructure of PEDOT:PSS to achieve a combination of mechanical compliance and electrical functionality. In the syntactic foams, this is accomplished through the formation of conductive pathways along PEDOT:PSS-coated microsphere shells within a highly porous architecture, whereas in the xerogel fibers, conductivity is governed by a continuous polymer network reinforced through a double-network structure. These contrasting approaches highlight how microstructural design can be leveraged to tailor the balance between mechanical properties and electrical performance for different wearable sensing applications.

Together, the results presented in this thesis illustrate how the properties of PEDOT:PSS can be significantly expanded through structural design and material architecture. While PEDOT:PSS is commonly used in thin-film form, the work presented here demonstrates that alternative material formats, including porous foams and xerogel fibers, offer new opportunities to engineer conductive systems with tailored mechanical and electrical characteristics. These approaches illustrate the versatility of PEDOT:PSS as a platform material for the development of next-generation wearable electronic and bioelectronic devices.

Overall, this thesis contributes to the growing field of soft conductive materials by demonstrating how PEDOT:PSS-based systems can be engineered into diverse architectures to address different sensing requirements. By combining insights from the literature with the development of new material systems, this work highlights the importance of structural design in advancing the performance and functionality of conductive polymer materials for wearable sensing technologies.

CHAPTER 8CONCLUSION AND RECOMMENDATIONS

This thesis investigated the development of soft conductive materials based on poly(3,4-ethylenedioxythiophene):poly(styrene sulfonate) (PEDOT:PSS) for wearable sensing applications. The main contributions of this work are summarized as follows:

- Development of lightweight conductive syntactic foams based on PEDOT:PSS-coated microspheres

This work introduced porous conductive foams using PEDOT:PSS-coated polymer microspheres as functional fillers within a thermoplastic matrix. The resulting syntactic foams exhibited low density, tunable porosity, and electrical conductivity at high void fractions while maintaining mechanical compliance suitable for wearable applications. The materials were compatible with thermoplastic processing methods, including filament extrusion and 3D printing, enabling the fabrication of complex geometries. In addition, the foams demonstrated recyclability, highlighting their potential for more sustainable wearable bioelectronic systems.

- Fabrication of highly stretchable conductive xerogel fibers using a double-network design

A second material platform was developed based on PVA-PEDOT:PSS-glycerol systems, where freeze-thaw processing followed by borax-mediated crosslinking and dehydration produced conductive xerogel fibers. The resulting double-network structure provided a balance between mechanical robustness, high stretchability, and stable electrical conductivity. These fibers exhibited reliable strain-dependent electrical responses, excellent cyclic durability, and consistent performance under repeated deformation, demonstrating their suitability for wearable motion sensing applications.

- Expansion of PEDOT:PSS into diverse structural material architectures for wearable sensing

Overall, this thesis demonstrated that PEDOT:PSS can be tailored into multiple structural forms, including porous foams and fiber-based systems, extending its application beyond conventional thin films. These results highlight the versatility of PEDOT:PSS for the development of soft, conductive materials that meet the mechanical and electrical requirements of wearable bioelectronic devices.

Recommendations for Future Research:

While the results presented in this thesis demonstrate promising material platforms, several directions for future research could further expand the capabilities and applications of PEDOT:PSS-based systems.

- Optimization of conductive microsphere architectures and PEDOT:PSS conductivity

The electrical and mechanical properties of the syntactic foams are strongly influenced by the quality of the PEDOT:PSS coating on the microspheres, the void fraction, and the resulting distribution of conductive pathways throughout the structure. Future research could therefore focus on improving the uniformity and coverage of the PEDOT:PSS coating on the microspheres, as well as optimizing the foam architecture to enhance electrical performance. In addition, the electrical conductivity of PEDOT:PSS is known to be highly tunable through various post-treatment strategies, including the use of polar solvents or acid treatments that induce structural rearrangements within the polymer. Applying these conductivity enhancement methods to the PEDOT:PSS coatings on the microspheres could significantly improve the electrical performance of the resulting foams. Exploring different conductive polymer formulations, polymer matrices, and processing techniques may further enable control over both the mechanical and electrical properties of the material.

- Advanced investigation of additive manufacturing of conductive foams

In this work, fused filament fabrication was primarily used to demonstrate the printability of the conductive syntactic foams and the feasibility of producing customizable conductive structures. Future research should focus on a more systematic investigation of the additive manufacturing behavior of these materials. In particular, studying the influence of printing parameters, such as extrusion temperature, printing speed, and layer orientation, on the resulting microstructure and electrical performance could provide valuable insight into process-microstructure-property relationships. Directional or anisotropic printing strategies may also be explored to tailor the alignment and connectivity of conductive pathways within the printed structures. Such studies could enable improved control over both mechanical and electrical properties, further expanding the potential of these materials for engineered wearable electronic devices.

- Integration of conductive foams into EEG electrode systems

Future work should further investigate the use of the conductive foams developed in this thesis for EEG recording applications. While preliminary demonstrations of in-ear EEG recordings were performed, more systematic and in-depth studies are needed to fully evaluate their performance. In particular, integrating these materials into EEG caps could enable controlled comparisons between scalp-based electrode configurations and in-ear implementations using the same material platform. Such studies should include benchmarking against conventional electrode materials, such as Ag/AgCl and existing dry electrodes, while evaluating signal quality, electrode-skin impedance, long-term recording stability, and user comfort. These investigations would provide a clearer understanding of the advantages and limitations of conductive foam electrodes for different EEG monitoring configurations.

- Integration of the PEDOT:PSS xerogel fibers into textile-based systems

The conductive xerogel fibers developed in this work show strong potential for wearable strain sensing. Future work could explore the integration of these fibers into textile-based systems or wearable garments, enabling distributed sensing across larger areas of the body. In addition, modifying the polymer network composition or incorporating functional additives could allow the development of multifunctional sensing fibers capable of detecting additional physiological signals such as pressure, temperature, or biochemical markers.

- Long-term stability and environmental durability studies

Although the materials developed in this thesis demonstrated stable electrical performance under laboratory testing conditions, long-term durability remains an important consideration for wearable applications. Future studies should investigate the long-term electrical and mechanical stability of these materials under repeated deformation and extended use. In addition, their performance should be evaluated under different environmental conditions, including variations in temperature and humidity, which can significantly influence polymer properties and electrical behavior in wearable devices. Such studies would provide a more comprehensive understanding of the reliability and practical applicability of these materials in real-world operating environments.

Overall, this work demonstrates that controlled structural design of PEDOT:PSS-based materials provides a versatile strategy for developing soft conductive systems for wearable sensing technologies. Continued research in this area will contribute to the advancement of next-generation

wearable electronics capable of enabling long-term, comfortable, and reliable physiological monitoring.

REFERENCES

[1] A. Pantelopoulos and N. G. Bourbakis, “A Survey on Wearable Sensor-Based Systems for Health Monitoring and Prognosis,” *IEEE Trans. Syst. Man, Cybern. Part C Rev.*, vol. 40, no. 1, pp. 1–12, 2010, doi: 10.1109/TSMCC.2009.2032660.

[2] A. S. Farooq and P. Zhang, “A comprehensive review on the prospects of next-generation wearable electronics for individualized health monitoring, assistive robotics, and communication,” *Sensors Actuators A Phys.*, vol. 344, p. 113715, 2022, doi: https://doi.org/10.1016/j.sna.2022.113715.

[3] S. Patel, H. Park, P. Bonato, L. Chan, and M. Rodgers, “A review of wearable sensors and systems with application in rehabilitation,” *J. Neuroeng. Rehabil.*, vol. 9, no. 1, p. 21, 2012, doi: 10.1186/1743-0003-9-21.

[4] R. De Fazio, V. M. Mastronardi, M. De Vittorio, and P. Visconti, “Wearable Sensors and Smart Devices to Monitor Rehabilitation Parameters and Sports Performance: An Overview,” *Sensors*, vol. 23, no. 4, 2023, doi: 10.3390/s23041856.

[5] G. Mu, Y. Zhang, Z. Yan, Q. Yu, and Q. Wang, “Recent advancements in wearable sensors: integration with machine learning for human–machine interaction,” *RSC Adv.*, vol. 15, no. 10, pp. 7844–7854, 2025, doi: 10.1039/D5RA00167F.

[6] R. Yin, D. Wang, S. Zhao, Z. Lou, and G. Shen, “Wearable Sensors-Enabled Human–Machine Interaction Systems: From Design to Application,” *Adv. Funct. Mater.*, vol. 31, no. 11, p. 2008936, 2021, doi: https://doi.org/10.1002/adfm.202008936.

[7] Y. Liu, M. Pharr, and G. A. Salvatore, “Lab-on-Skin: A Review of Flexible and Stretchable Electronics for Wearable Health Monitoring,” *ACS Nano*, vol. 11, no. 10, pp. 9614–9635, 2017, doi: 10.1021/acsnano.7b04898.

[8] H.-R. Lim, H. S. Kim, R. Qazi, Y.-T. Kwon, J.-W. Jeong, and W.-H. Yeo, “Advanced Soft Materials, Sensor Integrations, and Applications of Wearable Flexible Hybrid Electronics in Healthcare, Energy, and Environment,” *Adv. Mater.*, vol. 32, no. 15, p. 1901924, 2020, doi: https://doi.org/10.1002/adma.201901924.

[9] X. Feng, G.-Y. Li, A. Ramier, A. M. Eltony, and S.-H. Yun, “In vivo stiffness measurement

of epidermis, dermis, and hypodermis using broadband Rayleigh-wave optical coherence elastography," *Acta Biomater.*, vol. 146, pp. 295–305, 2022, doi: https://doi.org/10.1016/j.actbio.2022.04.030.

[10] D. J. Bora and R. Dasgupta, "Estimation of skin impedance models with experimental data and a proposed model for human skin impedance," *IET Syst. Biol.*, vol. 14, no. 5, pp. 230–240, 2020, doi: https://doi.org/10.1049/iet-syb.2020.0049.

[11] F. Lu *et al.*, "Review of Stratum Corneum Impedance Measurement in Non-Invasive Penetration Application.," *Biosensors*, vol. 8, no. 2, Mar. 2018, doi: 10.3390/bios8020031.

[12] R. Papani, Y. Li, and S. Wang, "Soft mechanical sensors for wearable and implantable applications," *WIREs Nanomedicine and Nanobiotechnology*, vol. 16, no. 3, p. e1961, 2024, doi: https://doi.org/10.1002/wnan.1961.

[13] M. Reis Carneiro, M. Tavakoli, and C. Majidi, "Soft skin-interfacing electrodes for wearable bioelectronics," *Matter*, vol. 8, no. 10, Oct. 2025, doi: 10.1016/j.matt.2025.102409.

[14] Y. Yu, X. Liao, and W. Feng, "Recent development of elastomer-based smart sensing materials and structures," *Adv. Compos. Hybrid Mater.*, vol. 8, no. 1, p. 138, 2025, doi: 10.1007/s42114-024-01168-y.

[15] G. Rizzello, "A Review of Cooperative Actuator and Sensor Systems Based on Dielectric Elastomer Transducers," *Actuators*, vol. 12, no. 2, 2023, doi: 10.3390/act12020046.

[16] H. Böse and J. Ehrlich, "Dielectric Elastomer Sensors with Advanced Designs and Their Applications," *Actuators*, vol. 12, no. 3, 2023, doi: 10.3390/act12030115.

[17] P. Zhou, Z. Zhang, F. Mo, and Y. Wang, "A Review of Functional Hydrogels for Flexible Chemical Sensors," *Adv. Sens. Res.*, vol. 3, no. 3, p. 2300021, 2024, doi: https://doi.org/10.1002/adsr.202300021.

[18] J. Zeng, X. Jing, L. Lin, G. Wang, Y. Zhang, and P. Feng, "Smart sensing hydrogel actuators conferred by MXene gradient arrangement," *J. Colloid Interface Sci.*, vol. 677, pp. 816–826, 2025, doi: https://doi.org/10.1016/j.jcis.2024.08.117.

[19] H. Wang *et al.*, "Flexible chitosan sensing hydrogel enabled by phytic acid coordination effect with high-conductivity and ultra-sensitivity for self-powered handwriting recognition

and multimodal sensors," *Nano Energy*, vol. 128, p. 109843, 2024, doi: https://doi.org/10.1016/j.nanoen.2024.109843.

[20] L. A. Kurup, C. M. Cole, J. N. Arthur, and S. D. Yambem, "Graphene Porous Foams for Capacitive Pressure Sensing," *ACS Appl. Nano Mater.*, vol. 5, no. 2, pp. 2973–2983, Feb. 2022, doi: 10.1021/acsanm.2c00247.

[21] A. Huang *et al.*, "A unique, flexible, and porous pressure sensor with enhanced sensitivity and durability by synergy of surface microstructure and supercritical fluid foaming," *Appl. Surf. Sci.*, vol. 618, p. 156661, 2023, doi: https://doi.org/10.1016/j.apsusc.2023.156661.

[22] X. Liang *et al.*, "Advanced Stretchable Aerogels and Foams for Flexible Electronics and Beyond," *Adv. Funct. Mater.*, vol. 34, no. 48, p. 2408707, 2024, doi: https://doi.org/10.1002/adfm.202408707.

[23] Y. Maithani, A. Singh, B. R. Mehta, and J. P. Singh, "PEDOT: PSS treated cotton-based textile dry electrode for ECG sensing," *Mater. Today Proc.*, vol. 62, pp. 4052–4057, 2022, doi: https://doi.org/10.1016/j.matpr.2022.04.611.

[24] K.-H. Teng and M.-H. Lee, "PEDOT:PSS treated Xuan paper as a green electronics material for wearable dry electrocardiogram electrodes and flexible strain sensors," *J. Environ. Chem. Eng.*, vol. 13, no. 2, p. 115716, 2025, doi: https://doi.org/10.1016/j.jece.2025.115716.

[25] P. Kateb, J. Fan, J. Kim, X. Zhou, G. A. Lodygensky, and F. Cicoira, "Printable, adhesive, and self-healing dry epidermal electrodes based on PEDOT:PSS and polyurethane diol," *Flex. Print. Electron.*, vol. 8, no. 4, p. 45006, Nov. 2023, doi: 10.1088/2058-8585/ad05d6.

[26] H. Guo *et al.*, "Artificially innervated self-healing foams as synthetic piezo-impedance sensor skins.," *Nat. Commun.*, vol. 11, no. 1, p. 5747, Nov. 2020, doi: 10.1038/s41467-020-19531-0.

[27] J. Kim *et al.*, "Ultrathin Soft Wearable Sensor Materials and Structures: A Review of Current Trends and Prospectives," *ACS Appl. Mater. Interfaces*, vol. 17, no. 44, pp. 59994–60027, Nov. 2025, doi: 10.1021/acsami.5c14329.

[28] S. Bilent, T. H. N. Dinh, E. Martincic, and P.-Y. Joubert, "Influence of the Porosity of Polymer Foams on the Performances of Capacitive Flexible Pressure Sensors.," *Sensors*,

vol. 19, no. 9, Apr. 2019, doi: 10.3390/s19091968.

[29] Q. Li, B. Tian, J. Liang, and W. Wu, “Functional conductive hydrogels: from performance to flexible sensor applications,” *Mater. Chem. Front.*, vol. 7, no. 15, pp. 2925–2957, 2023, doi: 10.1039/D3QM00109A.

[30] G. Mummaleti and F. Kong, “Fabrication, properties and applications of xerogels in food processing,” *J. Agric. Food Res.*, vol. 11, p. 100506, 2023, doi: https://doi.org/10.1016/j.jafr.2023.100506.

[31] Q. M. Dang, A. H. Wemple, and M. C. Leopold, “Nanomaterial-Doped Xerogels for Biosensing Measurements of Xanthine in Clinical and Industrial Applications,” *Gels*, vol. 9, no. 6, 2023, doi: 10.3390/gels9060437.

[32] G. Kumar and S. Panda, “Probing the ionic activation enthalpies in anionic polysaccharide xerogel-based single ion conductor for temperature sensing,” *Carbohydr. Polym.*, vol. 340, p. 122258, 2024, doi: https://doi.org/10.1016/j.carbpol.2024.122258.

[33] C. M. Vidhya, Y. Maithani, and J. P. Singh, “Recent Advances and Challenges in Textile Electrodes for Wearable Biopotential Signal Monitoring: A Comprehensive Review.,” *Biosensors*, vol. 13, no. 7, Jun. 2023, doi: 10.3390/bios13070679.

[34] L. Zhang *et al.*, “Fully organic compliant dry electrodes self-adhesive to skin for long-term motion-robust epidermal biopotential monitoring,” *Nat. Commun.*, vol. 11, no. 1, p. 4683, 2020, doi: 10.1038/s41467-020-18503-8.

[35] A. Giangrande, A. Botter, H. Piitulainen, and G. L. Cerone, “Motion Artifacts in Dynamic EEG Recordings: Experimental Observations, Electrical Modelling, and Design Considerations.,” *Sensors*, vol. 24, no. 19, Sep. 2024, doi: 10.3390/s24196363.

[36] A. Maji, C. Kuila, N. C. Murmu, and T. Kuila, “Stretch, sense, and innovate: Advances in next-generation strain sensors,” *Compos. Part B Eng.*, vol. 306, p. 112749, 2025, doi: https://doi.org/10.1016/j.compositesb.2025.112749.

[37] Z. Shen *et al.*, “Progress of flexible strain sensors for physiological signal monitoring,” *Biosens. Bioelectron.*, vol. 211, p. 114298, 2022, doi: https://doi.org/10.1016/j.bios.2022.114298.

[38] A. B. Oskouyi, U. Sundararaj, and P. Mertiny, “Tunneling Conductivity and Piezoresistivity of Composites Containing Randomly Dispersed Conductive Nano-Platelets.,” *Mater.*, vol. 7, no. 4, pp. 2501–2521, Mar. 2014, doi: 10.3390/ma7042501.

[39] H. Ji *et al.*, “Development and application of flexible piezoresistive sensors based on synergistic effect of CB and MWCNTs,” *Sensors Actuators A Phys.*, vol. 382, p. 116180, 2025, doi: https://doi.org/10.1016/j.sna.2024.116180.

[40] R. Wang *et al.*, “Carbon Nanotube-Based Strain Sensors: Structures, Fabrication, and Applications,” *Adv. Mater. Technol.*, vol. 8, no. 1, p. 2200855, 2023, doi: https://doi.org/10.1002/admt.202200855.

[41] H. Chen *et al.*, “Advances in graphene-based flexible and wearable strain sensors,” *Chem. Eng. J.*, vol. 464, p. 142576, 2023, doi: https://doi.org/10.1016/j.cej.2023.142576.

[42] S. Raman and R. S. Arunagirinathan, “Silver Nanowires in Stretchable Resistive Strain Sensors,” *Nanomaterials*, vol. 12, no. 11, 2022, doi: 10.3390/nano12111932.

[43] H. Wang, J. Jiang, and J. Wang, “The role and progress of silver nanowires in wearable strain sensors for human motion detection,” *Alexandria Eng. J.*, vol. 108, pp. 706–716, 2024, doi: https://doi.org/10.1016/j.aej.2024.09.039.

[44] T. Wang *et al.*, “High Sensitivity, Wide Linear-Range Strain Sensor Based on MXene/AgNW Composite Film with Hierarchical Microcrack,” *Small*, vol. 19, no. 50, p. 2304033, 2023, doi: https://doi.org/10.1002/smll.202304033.

[45] Y. Yao *et al.*, “Flexible Strain Sensor Based on AgNWs/MXene/SEBS with High Sensitivity and Wide Strain Range,” *Electron. Mater. Lett.*, vol. 20, no. 6, pp. 684–693, 2024, doi: 10.1007/s13391-024-00514-y.

[46] W. Qin *et al.*, “Flexible multifunctional TPU strain sensors with improved sensitivity and wide sensing range based on MXene/AgNWs,” *J. Mater. Sci. Mater. Electron.*, vol. 34, no. 6, p. 564, 2023, doi: 10.1007/s10854-023-09950-2.

[47] Z. Zhou, W. Tang, T. Xu, W. Zhao, J. Zhang, and C. Bai, “Flexible Strain Sensors Based on Thermoplastic Polyurethane Fabricated by Electrospinning: A Review,” *Sensors*, vol. 24, no. 15, 2024, doi: 10.3390/s24154793.

[48] J. Tang, Y. Wu, S. Ma, T. Yan, and Z. Pan, “Flexible strain sensor based on CNT/TPU composite nanofiber yarn for smart sports bandage,” *Compos. Part B Eng.*, vol. 232, p. 109605, 2022, doi: https://doi.org/10.1016/j.compositesb.2021.109605.

[49] G. Wang, M. Wang, M. Zheng, S. Yao, and B. Ebo, “High-Sensitivity GNPs/PDMS Flexible Strain Sensor with a Microdome Array,” *ACS Appl. Electron. Mater.*, vol. 4, no. 9, pp. 4576–4587, Sep. 2022, doi: 10.1021/acsaelm.2c00782.

[50] S. Zhang, C. Ge, and R. Liu, “Mechanical characterization of the stress-strain behavior of the polydimethylsiloxane (PDMS) substate of wearable strain sensors under uniaxial loading conditions,” *Sensors Actuators A Phys.*, vol. 341, p. 113580, 2022, doi: https://doi.org/10.1016/j.sna.2022.113580.

[51] X. Wang *et al.*, “PDMS-based conductive elastomeric composite with 3D reduced graphene oxide conductive network for flexible strain sensor,” *Compos. Part A Appl. Sci. Manuf.*, vol. 161, p. 107113, 2022, doi: https://doi.org/10.1016/j.compositesa.2022.107113.

[52] M. Amjadi, K.-U. Kyung, I. Park, and M. Sitti, “Stretchable, Skin-Mountable, and Wearable Strain Sensors and Their Potential Applications: A Review,” *Adv. Funct. Mater.*, vol. 26, no. 11, pp. 1678–1698, 2016, doi: https://doi.org/10.1002/adfm.201504755.

[53] L. Tang, S. Wu, J. Qu, L. Gong, and J. Tang, “A Review of Conductive Hydrogel Used in Flexible Strain Sensor,” *Materials*, vol. 13, no. 18, 2020, doi: 10.3390/ma13183947.

[54] B. Chen *et al.*, “Recent Progress of Biomaterial-Based Hydrogels for Wearable and Implantable Bioelectronics.,” *Gels*, vol. 11, no. 6, Jun. 2025, doi: 10.3390/gels11060442.

[55] J. Cao *et al.*, “Self-Healable PEDOT:PSS-PVA Nanocomposite Hydrogel Strain Sensor for Human Motion Monitoring,” *Nanomaterials*, vol. 13, no. 17, 2023, doi: 10.3390/nano13172465.

[56] F. E. Jurin, C. C. Buron, E. Frau, S. del Rossi, and S. Schintke, “The Electrical and Mechanical Characteristics of Conductive PVA/PEDOT:PSS Hydrogel Foams for Soft Strain Sensors,” *Sensors*, vol. 24, no. 2, 2024, doi: 10.3390/s24020570.

[57] M. Zhang *et al.*, “Strong, conductive, and freezing-tolerant polyacrylamide/PEDOT:PSS/cellulose nanofibrils hydrogels for wearable strain sensors,”

Carbohydr. Polym., vol. 305, p. 120567, 2023, doi: https://doi.org/10.1016/j.carbpol.2023.120567.

[58] R. Zhao, X. Yan, H. Lin, Z. Zhao, and S. Song, "Mechanical tough, stretchable, and adhesive PEDOT:PSS-based hydrogel flexible electronics towards multi-modal wearable application," *Chem. Eng. J.*, vol. 510, p. 161645, 2025, doi: https://doi.org/10.1016/j.cej.2025.161645.

[59] Q. Gao, C. Li, M. Wang, J. Zhu, and C. Gao, "A low-hysteresis, self-adhesive and conductive PAA/PEDOT:PSS hydrogel enabled body-conformable electronics," *J. Mater. Chem. C*, vol. 11, no. 27, pp. 9355–9365, 2023, doi: 10.1039/D3TC00850A.

[60] K. Zhao, Y. Zhao, J. Xu, R. Qian, Z. Yu, and C. Ye, "Stretchable, adhesive and self-healing conductive hydrogels based on PEDOT:PSS-stabilized liquid metals for human motion detection," *Chem. Eng. J.*, vol. 494, p. 152971, 2024, doi: https://doi.org/10.1016/j.cej.2024.152971.

[61] Y. Hu *et al.*, "Dual Physically Cross-Linked Hydrogels with High Stretchability, Toughness, and Good Self-Recoverability," *Macromolecules*, vol. 49, no. 15, pp. 5660–5668, Aug. 2016, doi: 10.1021/acs.macromol.6b00584.

[62] Q. Chen *et al.*, "A Novel Design Strategy for Fully Physically Linked Double Network Hydrogels with Tough, Fatigue Resistant, and Self-Healing Properties," *Adv. Funct. Mater.*, vol. 25, no. 10, pp. 1598–1607, 2015, doi: https://doi.org/10.1002/adfm.201404357.

[63] H. Shirakawa, E. J. Louis, A. G. MacDiarmid, C. K. Chiang, and A. J. Heeger, "Synthesis of electrically conducting organic polymers: halogen derivatives of polyacetylene, (CH)," *J. Chem. Soc. Chem. Commun.*, no. 16, pp. 578–580, 1977, doi: 10.1039/C39770000578.

[64] F. Jonas, G. Heywang, and S. Werner, "Novel polythiophenes, process for their preparation, and their use," *Bayer AG Ger. Pat. 3813589A1*, vol. 22, 1988.

[65] Z. Fan and J. Ouyang, "Thermoelectric properties of PEDOT: PSS," *Adv. Electron. Mater.*, vol. 5, no. 11, p. 1800769, 2019.

[66] M. Wang *et al.*, "Robust and flexible organic electrochemical transistors enabled by electropolymerized PEDOT," *npj Flex. Electron.*, vol. 9, no. 1, p. 74, 2025, doi:

10.1038/s41528-025-00457-w.

[67] S. L. Bidinger, S. Han, G. G. Malliaras, and T. Hasan, “Highly stable PEDOT:PSS electrochemical transistors,” *Appl. Phys. Lett.*, vol. 120, no. 7, p. 73302, Feb. 2022, doi: 10.1063/5.0079011.

[68] Q. Bin Ke, J.-R. Wu, C.-C. Lin, and S. H. Chang, “Understanding the PEDOT:PSS, PTAA and P3CT-X Hole-Transport-Layer-Based Inverted Perovskite Solar Cells,” *Polymers*, vol. 14, no. 4, 2022, doi: 10.3390/polym14040823.

[69] K. Kim, M. Kim, H. Lee, D. Chung, and J. Kim, “Multi-Functional PEDOT:PSS as the Efficient Perovskite Solar Cells,” *Small*, vol. 20, no. 38, p. 2402341, 2024, doi: https://doi.org/10.1002/smll.202402341.

[70] Z. Shen *et al.*, “High-Stretchability, Ultralow-Hysteresis ConductingPolymer Hydrogel Strain Sensors for Soft Machines,” *Adv. Mater.*, vol. 34, no. 32, p. 2203650, 2022, doi: https://doi.org/10.1002/adma.202203650.

[71] J. Kim *et al.*, “Self-healing{,} stretchable and recyclable polyurethane-PEDOT:PSS conductive blends,” *Mater. Horiz.*, vol. 11, no. 15, pp. 3548–3560, 2024, doi: 10.1039/D4MH00203B.

[72] B. Sarkar, F. Miquet-Westphal, J. Fan, G. Petrossian, and F. Cicoira, “Electromagnetic interference shielding in soft, lightweight, and flexible conducting polymer-based sponges,” *Flex. Print. Electron.*, vol. 10, no. 2, p. 25002, Apr. 2025, doi: 10.1088/2058-8585/adc589.

[73] P. J. Bora, A. G. Anil, K. J. Vinoy, and P. C. Ramamurthy, “Outstanding Absolute Electromagnetic Interference Shielding Effectiveness of Cross-Linked PEDOT:PSS Film,” *Adv. Mater. Interfaces*, vol. 6, no. 22, p. 1901353, 2019, doi: https://doi.org/10.1002/admi.201901353.

[74] J. Rivnay *et al.*, “Structural control of mixed ionic and electronic transport in conducting polymers,” *Nat. Commun.*, vol. 7, no. 1, p. 11287, 2016, doi: 10.1038/ncomms11287.

[75] S. Chen *et al.*, “PEDOT:PSS-based electronic materials: Preparation, performance tuning, processing, applications, and future prospect,” *Prog. Polym. Sci.*, vol. 166, p. 101990, 2025, doi: https://doi.org/10.1016/j.progpolymsci.2025.101990.

[76] X. Fan *et al.*, "PEDOT:PSS materials for optoelectronics{,} thermoelectrics{,} and flexible and stretchable electronics," *J. Mater. Chem. A*, vol. 11, no. 35, pp. 18561–18591, 2023, doi: 10.1039/D3TA03213B.

[77] Y. Huang, L. Tang, and Y. Jiang, "Chemical Strategies of Tailoring PEDOT:PSS for Bioelectronic Applications: Synthesis, Processing and Device Fabrication," *CCS Chem.*, vol. 6, no. 8, pp. 1844–1867, 2024, doi: 10.31635/ccschem.024.202403858.

[78] J. Y. Kim, J. H. Jung, D. E. Lee, and J. Joo, "Enhancement of electrical conductivity of poly (3, 4-ethylenedioxythiophene)/poly (4-styrenesulfonate) by a change of solvents," *Synth. Met.*, vol. 126, no. 2–3, pp. 311–316, 2002, doi:10.1016/S0379-6779(01)00576-8.

[79] N. A. Shahrim, Z. Ahmad, A. Wong Azman, Y. Fachmi Buys, and N. Sarifuddin, "Mechanisms for doped PEDOT:PSS electrical conductivity improvement," *Mater. Adv.*, vol. 2, no. 22, pp. 7118–7138, 2021, doi: 10.1039/d1ma00290b.

[80] E. Gutierrez-Fernandez, T. A. Ezquerra, and M.C. García-Gutiérrez, "Additive Effect on the Structure of PEDOT:PSS Dispersions and Its Correlation with the Structure and Morphology of Thin Films," *Polymers*, vol. 14, no. 1, pp. 141, 2022. doi: 10.3390/polym14010141.

[81] B. J. Worfolk *et al.*, "Ultrahigh electrical conductivity in solution-sheared polymeric transparent films," *Proc. Natl. Acad. Sci.*, vol. 112, no. 46, pp. 14138–14143, 2015, doi: 10.1073/pnas.1509958112.

[82] X. Qian *et al.*, "Metal-Like Conductivity in Acid-Treated PEDOT:PSS Films: Surpassing 15,000 S/Cm," *ACS Appl. Mater. Interfaces*, vol. 17, no. 11, pp. 17164–17178, Mar. 2025, doi: 10.1021/acsami.4c19958.

[83] G. Petrossian, P. Kateb, F. Miquet-Westphal, and F. Cicoira, "Advances in Electrode Materials for Scalp, Forehead, and Ear EEG: A Mini-Review.," *ACS Appl. bio Mater.*, vol. 6, no. 8, pp. 3019–3032, Aug. 2023, doi: 10.1021/acsabm.3c00322.

[84] J.-Y. Ahn, J. Oh, M.-R. An, K.-W. Nam, J.-W. Kim, and S.-H. Park, "Skin-Conformal Hydrogel-Based Electroencephalography Electrodes with Surfactant-Reorganized PEDOT:PSS.," *Mater.*, vol. 18, no. 20, Oct. 2025, doi: 10.3390/ma18204781.

[85] Q. Han *et al.*, “Hydrogel Nanoarchitectonics of a Flexible and Self-Adhesive Electrode for Long-Term Wireless Electroencephalogram Recording and High-Accuracy Sustained Attention Evaluation,” *Adv. Mater.*, vol. 35, no. 12, p. 2209606, 2023, doi: https://doi.org/10.1002/adma.202209606.

[86] S. Ahmed *et al.*, “Stick-and-play bioadhesive hairlike electrodes for chronic EEG recording on human,” *npj Biomed. Innov.*, vol. 2, no. 1, p. 9, 2025, doi: 10.1038/s44385-025-00009-x.

[87] K. W. K. Tang *et al.*, “Bioadhesive hydrogel-coupled and miniaturized ultrasound transducer system for long-term, wearable neuromodulation,” *Nat. Commun.*, vol. 16, no. 1, p. 4940, 2025, doi: 10.1038/s41467-025-60181-x.

[88] M. Li, G. Tian, X. Jiang, D. Qi, B. Yang, and Y. Li, “An Autonomously Liquefied Hydrogel Adhesive for Programmable Bioelectronic Interface,” *Angew. Chemie Int. Ed.*, vol. 64, no. 26, p. e202503010, 2025, doi: https://doi.org/10.1002/anie.202503010.

[89] K. Zheng *et al.*, “Machine Learning Enabled Reusable Adhesion, Entangled Network-Based Hydrogel for Long-Term, High-Fidelity EEG Recording and Attention Assessment,” *Nano-Micro Lett.*, vol. 17, no. 1, p. 281, 2025, doi: 10.1007/s40820-025-01780-7.

[90] H. Tang *et al.*, “In Situ Forming Epidermal Bioelectronics for Daily Monitoring and Comprehensive Exercise,” *ACS Nano*, vol. 16, no. 11, pp. 17931–17947, Nov. 2022, doi: 10.1021/acsnano.2c03414.

[91] J.-C. Hsieh *et al.*, “Design of an injectable, self-adhesive, and highly stable hydrogel electrode for sleep recording,” *Device*, vol. 2, no. 2, p. 100182, 2024, doi: https://doi.org/10.1016/j.device.2023.100182.

[92] D. Wang *et al.*, “A tough semi-dry hydrogel electrode with anti-bacterial properties for long-term repeatable non-invasive EEG acquisition,” *Microsystems Nanoeng.*, vol. 11, no. 1, p. 105, 2025, doi: 10.1038/s41378-025-00908-4.

[93] G. Li *et al.*, “Polyvinyl alcohol/polyacrylamide double-network hydrogel-based semi-dry electrodes for robust electroencephalography recording at hairy scalp for noninvasive brain–computer interfaces,” *J. Neural Eng.*, vol. 20, no. 2, p. 26017, Mar. 2023, doi: 10.1088/1741-2552/acc098.

[94] J.-B. Lu, Y. Tsao, and Y. Te Wang, “Design and Evaluate Semi-dry Watermill-like EEG Electrodes,” in *2024 46th Annual International Conference of the IEEE Engineering in Medicine and Biology Society (EMBC)*, 2024, pp. 1–4. doi: 10.1109/EMBC53108.2024.10782960.

[95] Y. Zhu *et al.*, “A flexible, stable, semi-dry electrode with low impedance for electroencephalography recording,” *RSC Adv.*, vol. 14, no. 46, pp. 34415–34427, 2024, doi: 10.1039/D4RA05560H.

[96] F. Wang, Q. Guo, and R. Fu, “A new semi-dry electrode for driving fatigue detection on urban roads,” *Sensors Actuators A Phys.*, vol. 393, p. 116794, 2025, doi: https://doi.org/10.1016/j.sna.2025.116794.

[97] Y. Cai *et al.*, “A smart electrolyte-replenishing semi-dry electrode based on a temperature-responsive hydrogel for sustainable electrophysiological signal acquisition,” *J. Mater. Chem. C*, vol. 12, no. 45, pp. 18446–18457, 2024, doi: 10.1039/D4TC02801E.

[98] F. Wang, D. Chen, R. Fu, and X. Zhang, “Study on a Novel Flow-Controllable Semidry Electrode for EEG Signal Acquisition,” *IEEE Sens. J.*, vol. 24, no. 23, pp. 38646–38657, 2024, doi: 10.1109/JSEN.2024.3480308.

[99] E. S. Nurse, D. R. Freestone, G. Dabscheck, and M. J. Cook, “Clinical findings of long-term ambulatory video EEG following routine EEG.,” *Epilepsy Behav.*, vol. 161, p. 110104, Dec. 2024, doi: 10.1016/j.yebeh.2024.110104.

[100] A. Lawley, S. Evans, F. Manfredonia, and A. E. Cavanna, “The role of outpatient ambulatory electroencephalography in the diagnosis and management of adults with epilepsy or nonepileptic attack disorder: A systematic literature review,” *Epilepsy Behav.*, vol. 53, pp. 26–30, 2015, doi: https://doi.org/10.1016/j.yebeh.2015.09.032.

[101] L. Hernández-Ronquillo *et al.*, “Diagnostic Accuracy of the Ambulatory EEG vs. Routine EEG for First Single Unprovoked Seizures and Seizure Recurrence: The DX-Seizure Study.,” *Front. Neurol.*, vol. 11, p. 223, 2020, doi: 10.3389/fneur.2020.00223.

[102] C. J. de Gans *et al.*, “Sleep assessment using EEG-based wearables – A systematic review,” *Sleep Med. Rev.*, vol. 76, p. 101951, 2024, doi: https://doi.org/10.1016/j.smrv.2024.101951.

[103] A. Cakir *et al.*, “1076 Feasibility of Sleep Staging EEG Acquired by a Dry-electrode Wearable Device Using a PSG-trained Algorithm,” *Sleep*, vol. 47, no. Supplement_1, pp. A462–A462, 2024, doi: 10.1093/sleep/zsae067.01076.

[104] D. Yang *et al.*, “Neural electrodes for brain-computer interface system: From rigid to soft,” *BMEMat*, vol. 3, no. 3, p. e12130, 2025, doi: https://doi.org/10.1002/bmm2.12130.

[105] S. Li, G. Liu, F. Feng, Z. Chang, W. Li, and F. Duan, “An Interventional Brain-Computer Interface for Long-Term EEG Collection and Motion Classification of a Quadruped Mammal.,” *IEEE Trans. neural Syst. Rehabil. Eng. a Publ. IEEE Eng. Med. Biol. Soc.*, vol. 33, pp. 1633–1642, 2025, doi: 10.1109/TNSRE.2025.3562922.

[106] G. Gnonhoue, I. Tabiai, J. Voix, and É. David, “Electrical and thermo-mechanical properties of styrene-ethylene-butylene-styrene/carbon nanotube and styrene-ethylene-butylene-styrene/carbon black multipin electrodes for electroencephalography,” *Sensors Actuators A Phys.*, vol. 399, p. 117446, 2026, doi: https://doi.org/10.1016/j.sna.2025.117446.

[107] L. C. Alarcón-Segovia, R. Morel, R. Spies, and I. Rintoul, “The challenging scalp–electrode interface and the evolution of materials and electrode integrated icts for electroencephalography,” *Surf. Rev. Lett.*, vol. 31, no. 09, p. 2430009, 2024, doi: 10.1142/S0218625X24300090.

[108] G. Gnonhoue, É. David, J. Voix, and I. Tabiai, “Flexible Dry Electrodes Based on Styrene-Ethylene-Butylene-Styrene/Carbon Black and Ethylene-Vinyl Acetate/Carbon Black for Electroencephalography: Electrical, Thermal and Mechanical Properties,” *J. Appl. Polym. Sci.*, vol. 143, no. 9, p. e70163, 2026, doi: https://doi.org/10.1002/app.70163.

[109] A. Tong, P. Perera, Z. Sarsenbayeva, A. McEwan, A. C. De Silva, and A. Withana, “Fully 3D-Printed Dry EEG Electrodes,” *Sensors*, vol. 23, no. 11, 2023, doi: 10.3390/s23115175.

[110] R. B. Damalerio, R. Lim, Y. Gao, T.-T. Zhang, and M.-Y. Cheng, “Development of Low-Contact-Impedance Dry Electrodes for Electroencephalogram Signal Acquisition,” *Sensors*, vol. 23, no. 9, 2023, doi: 10.3390/s23094453.

[111] I. F. Warsito, M. Komosar, M. A. Bernhard, P. Fiedler, and J. Haueisen, “Flower electrodes for comfortable dry electroencephalography,” *Sci. Rep.*, vol. 13, no. 1, p. 16589, 2023, doi: 10.1038/s41598-023-42732-8.

[112] Z. Wang, Y. Ding, W. Yuan, H. Chen, W. Chen, and C. Chen, “Active Claw-Shaped Dry Electrodes for EEG Measurement in Hair Areas.,” *Bioeng.*, vol. 11, no. 3, Mar. 2024, doi: 10.3390/bioengineering11030276.

[113] F. Zeng, G. Wang, C. Sun, J. Gao, S. Ji, and Q. Zhang, “Flexible and Washable Poly(3,4-ethylenedioxythiophene): Polystyrene Sulfonate/Polyvinyl Alcohol Fabric Dry Electrode for Long-Term Electroencephalography Signals Measurement.,” *Polymers*, vol. 17, no. 5, Mar. 2025, doi: 10.3390/polym17050683.

[114] K. Motiepor, S. Bakhtiyari, A. Jahanshahi, and R. Bagherzadeh, “Stretchable clutter-free E-textile EEG cap: Advancing seamless wearable solutions for emerging neuroimaging applications,” *Sensors Actuators A Phys.*, vol. 387, p. 116454, 2025, doi: https://doi.org/10.1016/j.sna.2025.116454.

[115] L. Scalco de Vasconcelos *et al.*, “On-scalp printing of personalized electroencephalography e-tattoos,” *Cell Biomater.*, vol. 1, no. 1, p. 100004, 2025, doi: https://doi.org/10.1016/j.celbio.2024.100004.

[116] A. S. Mihai, O. Geman, R. Toderean, L. Miron, and S. SharghiLavan, “The Next Frontier in Brain Monitoring: A Comprehensive Look at In-Ear EEG Electrodes and Their Applications,” *Sensors*, vol. 25, no. 11, 2025, doi: 10.3390/s25113321.

[117] E. Hestermann, K. Schreve, and D. Vandenheever, “Enhancing Deep Sleep Induction Through a Wireless In-Ear EEG Device Delivering Binaural Beats and ASMR: A Proof-of-Concept Study,” *Sensors*, vol. 24, no. 23, 2024, doi: 10.3390/s24237471.

[118] H. Moumane, J. Pazuelo, M. Nassar, J. Y. Juez, M. Valderrama, and M. Le Van Quyen, “Signal quality evaluation of an in-ear EEG device in comparison to a conventional cap system,” *Front. Neurosci.*, vol. Volume 18, 2024, doi: 10.3389/fnins.2024.1441897.

[119] J. Leung, L. J. Holanda, L. Wheeler, and T. Chau, “Wireless in-ear EEG system for auditory brain-computer interface applications in adolescents,” *Biomed. Phys. Eng. Express*, vol. 12, no. 1, p. 15062, Feb. 2026, doi: 10.1088/2057-1976/ae3b45.

[120] H. Liang, Y. Wang, H. Li, Y. Wang, P. X. Liu, and R. Liu, “Development and Characterization of a Dry Ear-EEG Sensor With a Generic Flexible Earpiece,” *IEEE Trans. Instrum. Meas.*, vol. 72, pp. 1–12, 2023, doi: 10.1109/TIM.2023.3277949.

[121] S. Zhuo, Z. Wu, C. Williams, C. Sundaresan, and S. K. Ameri, “In-Ear Electronics with Mechanical Adaptability for Physiological Sensing,” *Adv. Healthc. Mater.*, vol. 14, no. 3, p. 2404296, 2025, doi: https://doi.org/10.1002/adhm.202404296.

[122] S. Zhuo, Z. Wu, C. Williams, C. Sundaresan, and S. K. Ameri, “In-Ear Electronics with Mechanical Adaptability for Physiological Sensing,” *Adv. Healthc. Mater.*, vol. 14, no. 3, pp. 1–11, 2025, doi: 10.1002/adhm.202404296.

[123] R. Kaveh, C. Schwendeman, L. Pu, A. C. Arias, and R. Muller, “Wireless ear EEG to monitor drowsiness,” *Nat. Commun.*, vol. 15, no. 1, p. 6520, 2024, doi: 10.1038/s41467-024-48682-7.

[124] M. S. Lee, A. Paul, T. H. Joung, Y. Xu, J. Wu, W. D. Hairston, and G. Cauwenberghs, “Scalable Anatomically-Tunable Fully In-Ear Dry-Electrode Array for User-Generic Unobtrusive Electrophysiology,” in *2023 45th Annual International Conference of the IEEE Engineering in Medicine & Biology Society (EMBC)*, 2023, pp. 1–4. doi: 10.1109/EMBC40787.2023.10340888.

[125] Xu, Y., De la Paz, E., Paul, A., Mahato, K., Sempionatto, J.R., Tostado, N., Lee, M., Hota, G., Lin, M., Uppal, A. and Chen, W., “In-ear integrated sensor array for the continuous monitoring of brain activity and of lactate in sweat,” *Nat. Biomed. Eng.*, vol. 7, no. 10, pp. 1307–1320, 2023, doi: 10.1038/s41551-023-01095-1.

[126] H.-T. Nguyen, N.-D. Mai, B. G. Lee, and W.-Y. Chung, “Behind-the-Ear EEG-Based Wearable Driver Drowsiness Detection System Using Embedded Tiny Neural Networks,” *IEEE Sens. J.*, vol. 23, no. 19, pp. 23875–23892, 2023, doi: 10.1109/JSEN.2023.3307766.

[127] N.-D. Mai and W.-Y. Chung, “On-Chip Mental Stress Detection: Integrating a Wearable Behind-The-Ear EEG Device With Embedded Tiny Neural Network,” *IEEE J. Biomed. Heal. Informatics*, vol. 29, no. 3, pp. 1872–1885, 2025, doi: 10.1109/JBHI.2024.3519600.

[128] Zhu, H., Yan, Y., Xu, X., Ge, Z., Tian, P., Wu, X. and Chen, J., “Using Ear-EEG to Decode Auditory Attention in Multiple-speaker Environment,” in *ICASSP 2025 - 2025 IEEE International Conference on Acoustics, Speech and Signal Processing (ICASSP)*, 2025, pp. 1–5. doi: 10.1109/ICASSP49660.2025.10890810.

[129] B. Kaur, D. Singh, and P. P. Roy, “Eyes open and eyes close activity recognition using EEG

signals," in *Cognitive Computing and Information Processing: Third International Conference, CCIP 2017, Bengaluru, India, December 15-16, 2017, Revised Selected Papers 3*, Springer, 2018, pp. 3–9.

[130] Zeng, Y., Wu, Q., Yang, K., Tong, L., Yan, B., Shu, J. and Yao, D., "EEG-based identity authentication framework using face rapid serial visual presentation with optimized channels," *Sensors*, vol. 19, no. 1, 2019, doi: 10.3390/s19010006.

[131] J. Seo, T. H. Laine, and K. A. Sohn, "Machine learning approaches for boredom classification using EEG," *J. Ambient Intell. Humaniz. Comput.*, vol. 10, no. 10, pp. 3831–3846, 2019, doi: 10.1007/s12652-019-01196-3.

[132] G. Buzsáki, C. A. Anastassiou, and C. Koch, "The origin of extracellular fields and currents-EEG, ECoG, LFP and spikes," *Nat. Rev. Neurosci.*, vol. 13, no. 6, pp. 407–420, 2012.

[133] H. Alsuradi, W. Park, and M. Eid, "EEG-Based Neurohaptics Research: A Literature Review," *IEEE Access*, vol. 8, pp. 49313–49328, 2020, doi: 10.1109/ACCESS.2020.2979855.

[134] American Clinical Neurophysiology Society. "Guideline 1: minimum technical requirements for performing clinical electroencephalography.," *Am. J. Electroneurodiagnostic Technol.*, vol. 46, no. 3, pp. 198–204, Sep. 2006.

[135] Burkholder, D.B., Britton, J.W., Rajasekaran, V., Fabris, R.R., Cherian, P.J., Kelly-Williams, K.M., So, E.L., Nickels, K.C., Wong-Kisiel, L.C., Lagerlund, T.D. and Cascino, G.D., "Routine vs extended outpatient EEG for the detection of interictal epileptiform discharges.," *Neurology*, vol. 86, no. 16, pp. 1524–1530, Apr. 2016, doi: 10.1212/WNL.0000000000002592.

[136] G. Ramantani, L. Maillard, and L. Koessler, "Correlation of invasive EEG and scalp EEG," *Seizure*, vol. 41, pp. 196–200, 2016, doi: https://doi.org/10.1016/j.seizure.2016.05.018.

[137] N. Rossetti, P. Kateb, and F. Cicoira, "Neural and electromyography PEDOT electrodes for invasive stimulation and recording," *J. Mater. Chem. C*, vol. 9, no. 23, pp. 7243–7263, 2021.

[138] G. D. Cascino, "Video-EEG monitoring in adults," *Epilepsia*, vol. 43, no. SUPPL. 3, pp. 80–93, 2002, doi: 10.1046/j.1528-1157.43.s.3.14.x.

[139] V. Michel, L. Mazzola, M. Lemesle, and L. Vercueil, “Long-term EEG in adults: Sleep-deprived EEG (SDE), ambulatory EEG (Amb-EEG) and long-term video-EEG recording (LTVER),” *Neurophysiol. Clin. Neurophysiol.*, vol. 45, no. 1, pp. 47–64, 2015, doi: https://doi.org/10.1016/j.neucli.2014.11.004.

[140] U. Seneviratne and W. J. D’Souza, “Chapter 10 - Ambulatory EEG,” in *Clinical Neurophysiology: Basis and Technical Aspects*, vol. 160, K. H. Levin and P. B. T.-H. of C. N. Chauvel, Eds., Elsevier, 2019, pp. 161–170. doi: https://doi.org/10.1016/B978-0-444-64032-1.00010-2.

[141] R. Oostenveld and P. Praamstra, “The five percent electrode system for high-resolution EEG and ERP measurements,” *Clin. Neurophysiol.*, vol. 112, no. 4, pp. 713–719, 2001, doi: 10.1016/S1388-2457(00)00527-7.

[142] N. A. Alba, R. J. Sclabassi, M. Sun, and X. T. Cui, “Novel hydrogel-based preparation-free EEG electrode,” *IEEE Trans. Neural Syst. Rehabil. Eng.*, vol. 18, no. 4, pp. 415–423, Aug. 2010, doi: 10.1109/TNSRE.2010.2048579.

[143] P. A. Abhang, B. Gawali, and S. C. Mehrotra, *Introduction to EEG-and speech-based emotion recognition*. Academic Press, 2016.

[144] R. W. Homan, J. Herman, and P. Purdy, “Cerebral location of international 10–20 system electrode placement,” *Electroencephalogr. Clin. Neurophysiol.*, vol. 66, no. 4, pp. 376–382, 1987, doi: https://doi.org/10.1016/0013-4694(87)90206-9.

[145] “TEN20 Conductive Paste,” 2012. [Online]. Available: https://fscimage.fishersci.com/msds/60250.htm

[146] Elefix, “Electrode Paste,” 2012. [Online]. Available: https://shrinkwrapcontainments.com/Images/media/SDS Shrink Film.pdf

[147] A. Albulbul, “Evaluating major electrode types for idle biological signal measurements for modern medical technology,” *Bioengineering*, vol. 3, no. 3, 2016, doi: 10.3390/bioengineering3030020.

[148] P. Tallgren, S. Vanhatalo, K. Kaila, and J. Voipio, “Evaluation of commercially available electrodes and gels for recording of slow EEG potentials,” *Clin. Neurophysiol.*, vol. 116, no.

4, pp. 799–806, 2005, doi: https://doi.org/10.1016/j.clinph.2004.10.001.

[149] R. R. Lau, M. K. Powell, C. Terry, and D. Jahnke, “Neurotelemetry electrode application techniques compared,” *Neurodiagn. J.*, vol. 51, no. 3, pp. 165–182, Sep. 2011, doi: 10.1080/1086508x.2011.11079817.

[150] Shen, G., Gao, K., Zhao, N., Yi, Z., Jiang, C., Yang, B. and Liu, J., “A novel flexible hydrogel electrode with a strong moisturizing ability for long-term EEG recording,” *J. Neural Eng.*, vol. 18, no. 6, 2021, doi: 10.1088/1741-2552/ac41ab.

[151] K. Jakab, J. Csipor, I. Ulbert, Z. Keresztes, G. Mészáros, and G. Márton, “EEG sensor system development consisting of solid polyvinyl alcohol–glycerol–NaCl contact gel and 3D-printed, silver-coated polylactic acid electrode for potential brain–computer interface use,” *Mater. Today Chem.*, vol. 26, 2022, doi: 10.1016/j.mtchem.2022.101085.

[152] Z. Wang, N. Zhao, G. Shen, C. Jiang, and J. Liu, “MEMS-Based flexible wearable tri-polar concentric ring electrode array with self-adhesive graphene gel for EEG Monitoring,” *IEEE Sens. J.*, vol. 23, no. 3, pp. 3137–3146, 2022, doi: 10.1109/JSEN.2022.3230679.

[153] C. Carvalhaes and J. A. De Barros, “The surface Laplacian technique in EEG: Theory and methods,” *Int. J. Psychophysiol.*, vol. 97, no. 3, pp. 174–188, 2015, doi: 10.1016/j.ijpsycho.2015.04.023.

[154] A. Krishnan, K. Rozylowicz, S. K. Kelly, and P. Grover, “Hydrophilic Conductive Sponge Sensors for Fast Setup, Low Impedance Bio-potential Measurements,” *Proc. Annu. Int. Conf. IEEE Eng. Med. Biol. Soc. EMBS*, vol. 2020-July, pp. 3973–3976, 2020, doi: 10.1109/EMBC44109.2020.9176005.

[155] G. L. Li, J. T. Wu, Y. H. Xia, Q. G. He, and H. G. Jin, “Review of semi-dry electrodes for EEG recording,” *J. Neural Eng.*, vol. 17, no. 5, 2020, doi: 10.1088/1741-2552/abbd50.

[156] G. Li, S. Wang, M. Li, and Y. Y. Duan, “Towards real-life EEG applications: Novel superporous hydrogel-based semi-dry EEG electrodes enabling automatically ‘charge-discharge’ electrolyte,” *J. Neural Eng.*, vol. 18, no. 4, 2021, doi: 10.1088/1741-2552/abeeab.

[157] H. Hua, W. Tang, X. Xu, D. D. Feng, and L. Shu, “Flexible multi-layer semi-dry electrode for scalp EEG measurements at hairy sites,” *Micromachines*, vol. 10, no. 8, pp. 1–13, 2019,

doi: 10.3390/mi10080518.

[158] Gao, K.P., Yang, H.J., Liao, L.L., Jiang, C.P., Zhao, N., Wang, X.L., Li, X.Y., Chen, X., Yang, B. and Liu, J., "A Novel Bristle-Shaped Semi-Dry Electrode with Low Contact Impedance and Ease of Use Features for EEG Signal Measurements," *IEEE Trans. Biomed. Eng.*, vol. 67, no. 3, pp. 750–761, 2020, doi: 10.1109/TBME.2019.2920711.

[159] Wu, H., Yang, G., Zhu, K., Liu, S., Guo, W., Jiang, Z. and Li, Z., "Materials , Devices , and Systems of On-Skin Electrodes for Electrophysiological Monitoring and Human – Machine Interfaces," vol. 2001938, pp. 1–30, 2021, doi: 10.1002/advs.202001938.

[160] N. Meziane, J. G. Webster, M. Attari, and A. J. Nimunkar, "Dry electrodes for electrocardiography," *Physiol. Meas.*, vol. 34, no. 9, 2013, doi: 10.1088/0967-3334/34/9/R47.

[161] G. Pilloni, A. J. Woods, and L. Charvet, "No risk of skin lesion or burn with transcranial direct current stimulation (tDCS) using standardized protocols," *Brain Stimul. Basic, Transl. Clin. Res. Neuromodulation*, vol. 14, no. 3, pp. 511–512, 2021.

[162] L. Xing and A. J. Casson, "Directly conductive, flexible, 3D printed, EEG electrodes," *FLEPS 2022 - IEEE Int. Conf. Flex. Printable Sensors Syst. Proc.*, pp. 3–6, 2022, doi: 10.1109/FLEPS53764.2022.9781489.

[163] Y. H. Chen, M. Op De Beeck, L. Vanderheyden, V. Mihajlovic, B. Grundlehner, and C. Van Hoof, "Comb - shaped Polymer - based Dry Electrodes for EEG / ECG Measurements with High User Comfort," *Proc. Annu. Int. Conf. IEEE Eng. Med. Biol. Soc. EMBS*, vol. 2013, pp. 551-554. Available: https://doi.org/10.1109/embc.2013.6609559

[164] C. Grozea, C. D. Voinescu, and S. Fazli, "Bristle-sensors - low-cost flexible passive dry EEG electrodes for neurofeedback and BCI applications," *J. Neural Eng.*, 2011, doi: 10.1088/1741-2560/8/2/025008.

[165] K. Gao, H. Yang, X. Wang, B. Yang, and J. Liu, "Sensors and Actuators A : Physical Soft pin-shaped dry electrode with bristles for EEG signal measurements," *Sensors Actuators A. Phys.*, vol. 283, pp. 348–361, 2018, doi: 10.1016/j.sna.2018.09.045.

[166] Ng, W.C., Seet, H.L., Lee, K.S., Ning, N., Tai, W.X., Sutedja, M., Fuh, J.Y.H. and Li, X.P.,

"Micro-spike EEG electrode and the vacuum-casting technology for mass production," *J. Mater. Process. Technol.*, vol. 209, no. 9, pp. 4434–4438, 2009, doi: 10.1016/j.jmatprotec.2008.10.051.

[167] M. Arai, Y. Nishinaka, and N. Miki, "Electroencephalogram measurement using polymer-based dry microneedle electrode," *Jpn. J. Appl. Phys.*, vol. 54, no. 6S1, p. 06FP14, 2015.

[168] P. Salvo, R. Raedt, E. Carrette, D. Schaubroeck, J. Vanfleteren, and L. Cardon, "A 3D printed dry electrode for ECG/EEG recording," *Sensors Actuators A Phys.*, vol. 174, pp. 96–102, 2012, doi: https://doi.org/10.1016/j.sna.2011.12.017.

[169] C. T. Lin, L. De Liao, Y. H. Liu, I. J. Wang, B. S. Lin, and J. Y. Chang, "Novel dry polymer foam electrodes for long-term EEG measurement," *IEEE Trans. Biomed. Eng.*, vol. 58, no. 5, pp. 1200–1207, 2011, doi: 10.1109/TBME.2010.2102353.

[170] N. Muthukumar, G. Thilagavathi, and T. Kannaian, "Polyaniline-coated foam electrodes for electroencephalography (EEG) measurement," *J. Text. Inst.*, vol. 107, no. 3, pp. 283–290, Mar. 2016, doi: 10.1080/00405000.2015.1028248.

[171] L. M. Ferrari, "Conducting polymer tattoo electrodes in clinical electro- and magneto-encephalography," *npj Flex. Electron.*, pp. 1–9, 2020, doi: 10.1038/s41528-020-0067-z.

[172] Stauffer, F., Thielen, M., Sauter, C., Chardonnens, S., Bachmann, S., Tybrandt, K., Peters, C., Hierold, C. and Vörös, J., "Skin Conformal Polymer Electrodes for Clinical ECG and EEG Recordings," vol. 1700994, pp. 1–10, 2018, doi: 10.1002/adhm.201700994.

[173] Lee, S.M., Kim, J.H., Park, C., Hwang, J.Y., Hong, J.S., Lee, K.H. and Lee, S.H., "Self-adhesive and capacitive carbon nanotube-based electrode to record electroencephalograph signals from the hairy scalp," *IEEE Trans. Biomed. Eng.*, vol. 63, no. 1, pp. 138–147, 2016, doi: 10.1109/TBME.2015.2478406.

[174] B. Vasconcelos, P. Fiedler, R. Machts, J. Haueisen, and C. Fonseca, "The Arch Electrode: A Novel Dry Electrode Concept for Improved Wearing Comfort," *Front. Neurosci.*, vol. 15, no. October, pp. 1–14, 2021, doi: 10.3389/fnins.2021.748100.

[175] H. Hinrichs, M. Scholz, A. K. Baum, J. W. Y. Kam, R. T. Knight, and H. J. Heinze, "Comparison between a wireless dry electrode EEG system with a conventional wired wet

electrode EEG system for clinical applications," *Sci. Rep.*, vol. 10, no. 1, pp. 1–14, 2020, doi: 10.1038/s41598-020-62154-0.

[176] L. Wang, J. Wang, C. Fan, T. Xu, and X. Zhang, "Skin-like hydrogel-elastomer based electrochemical device for comfortable wearable biofluid monitoring," *Chem. Eng. J.*, vol. 455, no. November 2022, p. 140609, 2022, doi: 10.1016/j.cej.2022.140609.

[177] S. Krachunov and A. J. Casson, "3D Printed Dry EEG Electrodes," *Sensors*, vol. 16, no. 10, 2016, doi: 10.3390/s16101635.

[178] Shi, Z., Jiang, B., Liang, S., Zhang, J., Suo, D., Wu, J., Chen, D., Pei, G. and Yan, T., "Claw-shaped flexible and low-impedance conductive polymer electrodes for EEG recordings: Anemone dry electrode," *Sci. China Technol. Sci.*, vol. 66, no. 1, pp. 255–266, 2023, doi: 10.1007/s11431-022-2231-3.

[179] Y. J. Huang, C. Y. Wu, A. M. K. Wong, and B. S. Lin, "Novel active comb-shaped dry electrode for eeg measurement in Hairy site," *IEEE Trans. Biomed. Eng.*, vol. 62, no. 1, pp. 256–263, 2015, doi: 10.1109/TBME.2014.2347318.

[180] L. Ren, B. Liu, W. Zhou, and L. Jiang, "A Mini Review of Microneedle Array Electrode for Bio-Signal Recording: A Review," *IEEE Sens. J.*, vol. 20, no. 2, pp. 577–590, 2020, doi: 10.1109/JSEN.2019.2944847.

[181] M. Arai, Y. Nishinaka, and N. Miki, "Long-term electroencephalogram measurement using polymer-based dry microneedle electrode," *2015 Transducers - 2015 18th Int. Conf. Solid-State Sensors, Actuators Microsystems, Transducers 2015*, pp. 81–84, 2015, doi: 10.1109/TRANSDUCERS.2015.7180866.

[182] Stavrinidis, G., Michelakis, K., Kontomitrou, V., Giannakakis, G., Sevrisarianos, M., Sevrisarianos, G., Chaniotakis, N., Alifragis, Y. and Konstantinidis, G., "SU-8 microneedles based dry electrodes for Electroencephalogram," *Microelectron. Eng.*, vol. 159, pp. 114–120, 2016, doi: 10.1016/j.mee.2016.02.062.

[183] M. Kavaldzhiev, J. E. Perez, Y. Ivanov, A. Bertoncini, C. Liberale, and J. Kosel, "Biocompatible 3D printed magnetic micro needles," *Biomed. Phys. Eng. Express*, vol. 3, no. 2, 2017, doi: 10.1088/2057-1976/aa5ccb.

[184] Kabiri Ameri, S., Ho, R., Jang, H., Tao, L., Wang, Y., Wang, L., Schnyer, D.M., Akinwande, D. and Lu, N., "Graphene Electronic Tattoo Sensors," *ACS Nano*, vol. 11, no. 8, pp. 7634–7641, 2017, doi: 10.1021/acsnano.7b02182.

[185] Wang, Y., Yin, L., Bai, Y., Liu, S., Wang, L., Zhou, Y., Hou, C., Yang, Z., Wu, H., Ma, J. and Shen, Y., "Electrically compensated, tattoo-like electrodes for epidermal electrophysiology at scale," *Sci. Adv.*, vol. 6, no. 43, 2020, doi: 10.1126/sciadv.abd0996.

[186] A. Mascia, R. Collu, A. Spanu, M. Fraschini, M. Barbaro, and P. Cosseddu, "Wearable System Based on Ultra-Thin Parylene C Tattoo Electrodes for EEG Recording," *Sensors*, vol. 23, no. 2, pp. 1–9, 2023, doi: 10.3390/s23020766.

[187] Y. M. Chi, T. P. Jung, and G. Cauwenberghs, "Dry-contact and noncontact biopotential electrodes: Methodological review," *IEEE Rev. Biomed. Eng.*, vol. 3, pp. 106–119, 2010, doi: 10.1109/RBME.2010.2084078.

[188] S. Mandekar, A. Holland, M. Thielen, M. Behbahani, and M. Melnykowycz, "Advancing towards Ubiquitous EEG, Correlation of In-Ear EEG with Forehead EEG," *Sensors*, vol. 22, no. 4, pp. 1–19, 2022, doi: 10.3390/s22041568.

[189] T. McMahan, I. Parberry, and T. D. Parsons, "Modality specific assessment of video game player's experience using the Emotiv," *Entertain. Comput.*, vol. 7, pp. 1–6, 2015, doi: 10.1016/j.entcom.2015.03.001.

[190] G. Ruqeyya and S. M. U. Saeed, "Player Engagement Classification in Mobile Games Using MUSE Headband," *2022 17th Int. Conf. Emerg. Technol. ICET 2022*, pp. 83–88, 2022, doi: 10.1109/ICET56601.2022.10004658.

[191] S. M. Slobounov, W. Ray, B. Johnson, E. Slobounov, and K. M. Newell, "Modulation of cortical activity in 2D versus 3D virtual reality environments: An EEG study," *Int. J. Psychophysiol.*, vol. 95, no. 3, pp. 254–260, 2015, doi: 10.1016/j.ijpsycho.2014.11.003.

[192] Japaridze, G., Loeckx, D., Buckinx, T., Armand Larsen, S., Proost, R., Jansen, K., MacMullin, P., Paiva, N., Kasradze, S., Rotenberg, A. and Lagae, L., "Automated detection of absence seizures using a wearable electroencephalographic device: a phase 3 validation study and feasibility of automated behavioral testing," *Epilepsia*, no. January, pp. 1–7, 2022, doi: 10.1111/epi.17200.

[193] M. P. Barham, G. M. Clark, M. J. Hayden, P. G. Enticott, R. Conduit, and J. A. G. Lum, "Acquiring research-grade ERPs on a shoestring budget: A comparison of a modified Emotiv and commercial SynAmps EEG system," *Psychophysiology*, vol. 54, no. 9, pp. 1393–1404, 2017, doi: 10.1111/psyp.12888.

[194] A. Mascia, R. Collu, A. Spanu, M. Fraschini, M. Barbaro, and P. Cosseddu, "Wearable System Based on Ultra-Thin Parylene C Tattoo Electrodes for EEG Recording," *Sensors*, vol. 23, no. 2, p. 766, 2023.

[195] Aldridge, A., Barnes, E., Bethel, C.L., Carruth, D.W., Kocturova, M., Pleva, M. and Juhar, J., "Accessible electroencephalograms (EEGs): A comparative review with openbci's ultracortex mark IV headset," in *2019 29th International Conference Radioelektronika (RADIOELEKTRONIKA)*, IEEE, 2019, pp. 1–6.

[196] Li, M., Liang, Z., He, B., Zhao, C.G., Yao, W., Xu, G., Xie, J. and Cui, L., "Attention-Controlled Assistive Wrist Rehabilitation Using a Low-Cost EEG Sensor," *IEEE Sens. J.*, vol. 19, no. 15, pp. 6497–6507, 2019, doi: 10.1109/JSEN.2019.2910318.

[197] Rieiro, H., Diaz-Piedra, C., Morales, J.M., Catena, A., Romero, S., Roca-Gonzalez, J., Fuentes, L.J. and Di Stasi, L.L., "Validation of Electroencephalographic Recordings Obtained with a Consumer-Grade, Single Dry Electrode, Low-Cost Device: A Comparative Study," *Sensors*, vol. 19, no. 12, pp. 2808, 2019. doi: 10.3390/s19122808.

[198] J. Katona, T. Ujbanyi, G. Sziladi, and A. Kovari, "Speed control of Festo Robotino mobile robot using NeuroSky MindWave EEG headset based brain-computer interface," *7th IEEE Int. Conf. Cogn. Infocommunications, CogInfoCom 2016 - Proc.*, no. December 2021, pp. 251–256, 2017, doi: 10.1109/CogInfoCom.2016.7804557.

[199] Arnal, P.J., Thorey, V., Debellemaniere, E., Ballard, M.E., Bou Hernandez, A., Guillot, A., Jourde, H., Harris, M., Guillard, M., Van Beers, P. and Chennaoui, M., "The dreem headband compared to polysomnography for electroencephalographic signal acquisition and sleep staging," *Sleep*, vol. 43, no. 11, pp. 1–11, 2020, doi: 10.1093/sleep/zsaa097.

[200] S. Debener, R. Emkes, M. De Vos, and M. Bleichner, "Unobtrusive ambulatory EEG using a smartphone and flexible printed electrodes around the ear," *Sci. Rep.*, vol. 5, pp. 1–11, 2015, doi: 10.1038/srep16743.

[201] M. G. Bleichner, B. Mirkovic, and S. Debener, “Identifying auditory attention with ear-EEG: CEEGrid versus high-density cap-EEG comparison,” *J. Neural Eng.*, vol. 13, no. 6, 2016, doi: 10.1088/1741-2560/13/6/066004.

[202] F. Denk, M. Grzybowski, S. M. A. Ernst, B. Kollmeier, S. Debener, and M. G. Bleichner, “Event-Related Potentials Measured From In and Around the Ear Electrodes Integrated in a Live Hearing Device for Monitoring Sound Perception,” *Trends Hear.*, vol. 22, pp. 1–14, 2018, doi: 10.1177/2331216518788219.

[203] M. T. Knierim, M. Schemmer, and N. Bauer, “HardwareX A simplified design of a cEEGrid ear-electrode adapter for the OpenBCI biosensing platform,” *HardwareX*, vol. 12, p. e00357, 2022, doi: 10.1016/j.ohx.2022.e00357.

[204] Y. Gu, E. Cleeren, J. Dan, K. Claes, W. Van Paesschen, and S. Van Huffel, “Comparison between Scalp EEG and Behind-the-Ear EEG for Development of a Wearable Seizure Detection System for Patients with Focal Epilepsy,” *Sensors*, vol. 18, no. 1, pp. 1–17, 2017. doi: 10.3390/s18010029.

[205] S. Choi and H. Hwang, “Effects of Different Re-referencing Methods on Spontaneously Generated Ear-EEG,” *Frontiers in Neuroscience,* vol. 13, no. August, pp. 1–13, 2019, doi: 10.3389/fnins.2019.00822.

[206] Kalevo, L., Miettinen, T., Leino, A., Kainulainen, S., Korkalainen, H., Myllymaa, K., Töyräs, J., Leppänen, T., Laitinen, T. and Myllymaa, S., “Effect of Sweating on Electrode-Skin Contact Impedances and Artifacts in EEG Recordings With Various Screen-Printed Ag / Agcl Electrodes,” *Ieee Access,* vol. 8, pp. 0–9, 2020, doi: 10.1109/ACCESS.2020.2977172.

[207] B. G. D. Valle, S. S. Cash, and C. G. Sodini, “Wireless behind-the-ear EEG recording device with wireless interface to a mobile device (iPhone/iPod touch),” *2014 36th Annu. Int. Conf. IEEE Eng. Med. Biol. Soc. EMBC 2014*, pp. 5952–5955, 2014, doi: 10.1109/EMBC.2014.6944984.

[208] Valentin, O., Viallet, G., Delnavaz, A., Cretot-Richert, G., Ducharme, M., Monsarat-Chanon, H. and Voix, J., “Custom-fitted in-and around-the-ear sensors for unobtrusive and on-the-go eeg acquisitions: Development and validation,” *Sensors*, vol. 21, no. 9, 2021, doi:

10.3390/s21092953.

[209] N. Kaongoen, J. Choi, and S. Jo, “A novel online BCI system using speech imagery and ear-EEG for home appliances control,” *Comput. Methods Programs Biomed.*, vol. 224, p. 107022, 2022, doi: 10.1016/j.cmpb.2022.107022.

[210] Choi, S.I., Han, C.H., Choi, G.Y., Shin, J., Song, K.S., Im, C.H. and Hwang, H.J., “On the Feasibility of Using an Ear-EEG to Develop an Endogenous Brain-Computer Interface,” *Sensors*, vol. 18, no. 9, pp. 1–14, 2018. doi: 10.3390/s18092856.

[211] Kalevo, L., Miettinen, T., Leino, A., Kainulainen, S., Myllymaa, K., Töyräs, J., Leppänen, T. and Myllymaa, S., “Improved Sweat Artifact Tolerance of Screen-Printed EEG Electrodes by Material Selection-Comparison of Electrochemical Properties in Artificial Sweat,” *Ieee Access*, vol. 7, pp. 133237–133247, 2019, doi: 10.1109/ACCESS.2019.2941052.

[212] Looney, D., Park, C., Kidmose, P., Rank, M.L., Ungstrup, M., Rosenkranz, K. and Mandic, D.P., “An in-the-ear platform for recording electroencephalogram,” *Proc. Annu. Int. Conf. IEEE Eng. Med. Biol. Soc. EMBS*, pp. 6882–6885, 2011, doi: 10.1109/IEMBS.2011.6091733.

[213] K. B. Mikkelsen, S. L. Kappel, D. P. Mandic, and P. Kidmose, “EEG recorded from the ear: Characterizing the Ear-EEG Method,” *Front. Neurosci.*, vol. 9, no. NOV, pp. 1–8, 2015, doi: 10.3389/fnins.2015.00438.

[214] P. Kidmose, D. Looney, and D. P. Mandic, “Auditory evoked responses from Ear-EEG recordings,” *Proc. Annu. Int. Conf. IEEE Eng. Med. Biol. Soc. EMBS*, pp. 586–589, 2012, doi: 10.1109/EMBC.2012.6345999.

[215] P. Kidmose, D. Looney, M. Ungstrup, M. L. Rank, and D. P. Mandic, “A study of evoked potentials from ear-EEG,” *IEEE Trans. Biomed. Eng.*, vol. 60, no. 10, pp. 2824–2830, 2013, doi: 10.1109/TBME.2013.2264956.

[216] M. Eickenscheidt, P. Schäfer, Y. Baslan, C. Schwarz, and T. Stieglitz, “Highly porous platinum electrodes for dry ear-EEG measurements,” *Sensors*, vol. 20, no. 11, pp. 1–12, 2020, doi: 10.3390/s20113176.

[217] Looney, D., Kidmose, P., Park, C., Ungstrup, M., Rank, M.L., Rosenkranz, K. and Mandic, D.P., "The in-the-ear recording concept: User-centered and wearable brain monitoring," *IEEE Pulse*, vol. 3, no. 6, pp. 32–42, 2012, doi: 10.1109/MPUL.2012.2216717.

[218] S. L. Kappel and P. Kidmose, "Study of impedance spectra for dry and wet EarEEG electrodes," *Proc. Annu. Int. Conf. IEEE Eng. Med. Biol. Soc. EMBS*, vol. 2015-Novem, pp. 3161–3164, 2015, doi: 10.1109/EMBC.2015.7319063.

[219] S. L. Kappel, D. Looney, D. P. Mandic, and P. Kidmose, "Physiological artifacts in scalp EEG and ear-EEG," *Biomed. Eng. Online*, vol. 16, no. 1, p. 103, 2017, doi: 10.1186/s12938-017-0391-2.

[220] S. L. Kappel, M. L. Rank, H. O. Toft, M. Andersen, and P. Kidmose, "Dry-Contact Electrode Ear-EEG," *IEEE Trans. Biomed. Eng.*, vol. 66, no. 1, pp. 150–158, 2019, doi: 10.1109/TBME.2018.2835778.

[221] Mikkelsen, K.B., Tabar, Y.R., Kappel, S.L., Christensen, C.B., Toft, H.O., Hemmsen, M.C., Rank, M.L., Otto, M. and Kidmose, P., "Accurate whole-night sleep monitoring with dry-contact ear-EEG," *Sci. Rep.*, vol. 9, no. 1, pp. 1–12, 2019, doi: 10.1038/s41598-019-53115-3.

[222] J. H. Lee, S. M. Lee, H. J. Byeon, J. S. Hong, K. S. Park, and S. H. Lee, "CNT/PDMS-based canal-typed ear electrodes for inconspicuous EEG recording," *J. Neural Eng.*, vol. 11, no. 4, 2014, doi: 10.1088/1741-2560/11/4/046014.

[223] H. Dong, P. M. Matthews, and Y. Guo, "A new soft material based in-the-ear EEG recording technique," *Proc. Annu. Int. Conf. IEEE Eng. Med. Biol. Soc. EMBS*, vol. 2016-Octob, pp. 5709–5712, 2016, doi: 10.1109/EMBC.2016.7592023.

[224] Kim, J., Kim, H., Kim, D.H., Lee, S.K., Roh, J.Y., Kim, C.H., Chang, J.G. and Roh, D., "Effects of cranial electrotherapy stimulation with novel in-ear electrodes on anxiety and resting-state brain activity: A randomized double-blind placebo-controlled trial," *J. Affect. Disord.*, vol. 295, no. August, pp. 856–864, 2021, doi: 10.1016/j.jad.2021.08.141.

[225] A. Paul, G. Hota, B. Khaleghi, Y. Xu, T. Rosing, and G. Cauwenberghs, "Attention State Classification with In-Ear EEG," *BioCAS 2021 - IEEE Biomed. Circuits Syst. Conf. Proc.*, 2021, doi: 10.1109/BioCAS49922.2021.9644973.

[226] S. Mouli, R. Palaniappan, E. Molefi, and I. McLoughlin, “In-Ear Electrode EEG for Practical SSVEP BCI,” *Technologies*, vol. 8, no. 4, p. 63, 2020, doi: 10.3390/technologies8040063.

[227] J. Märcher-Rørsted, G. Encina-Llamas, T. Dau, M. C. Liberman, P. zhe Wu, and J. Hjortkjær, “Age-related reduction in frequency-following responses as a potential marker of cochlear neural degeneration,” *Hear. Res.*, vol. 414, 2022, doi: 10.1016/j.heares.2021.108411.

[228] L. M. Coraci and A. J. Beynon, “Use of an Extra-Tympanic Membrane Electrode to Record Cochlear Microphonics with Click, Tone Burst and Chirp Stimuli,” *Audiol. Res.*, vol. 11, no. 1, pp. 89–99, 2021, doi: 10.3390/audiolres11010010.

[229] P. Kidmose, D. Looney, L. Jochumsen, and D. P. Mandic, “Ear-EEG from generic earpieces: A feasibility study,” *Proc. Annu. Int. Conf. IEEE Eng. Med. Biol. Soc. EMBS*, pp. 543–546, 2013, doi: 10.1109/EMBC.2013.6609557.

[230] Kaveh, R., Doong, J., Zhou, A., Schwendeman, C., Gopalan, K., Burghardt, F.L., Arias, A.C., Maharbiz, M.M. and Muller, R., 2020. “Wireless User-Generic Ear EEG,” *IEEE Trans. Biomed. Circuits Syst.*, vol. 14, no. 4, pp. 727–737, 2020, doi: 10.1109/TBCAS.2020.3001265.

[231] V. Goverdovsky, D. Looney, P. Kidmose, and D. P. Mandic, “In-Ear EEG From Viscoelastic Generic Earpieces: Robust and Unobtrusive 24/7 Monitoring,” *IEEE Sens. J.*, vol. 16, no. 1, pp. 271–277, 2016, doi: 10.1109/JSEN.2015.2471183.

[232] D. Looney, V. Goverdovsky, I. Rosenzweig, M. J. Morrell, and D. P. Mandic, “Wearable in-ear encephalography sensor for monitoring sleep preliminary observations from nap studies,” *Ann. Am. Thorac. Soc.*, vol. 13, no. 12, pp. 2229–2233, 2016, doi: 10.1513/AnnalsATS.201605-342BC.

[233] T. Nakamura, V. Goverdovsky, M. J. Morrell, and D. P. Mandic, “Automatic Sleep Monitoring Using Ear-EEG,” *IEEE J. Transl. Eng. Heal. Med.*, vol. 5, no. July, pp. 1–8, 2017, doi: 10.1109/JTEHM.2017.2702558.

[234] Alqurashi, Y.D., Nakamura, T., Goverdovsky, V., Moss, J., Polkey, M.I., Mandic, D.P. and Morrell, M.J., “A novel in-ear sensor to determine sleep latency during the multiple sleep

latency test in healthy adults with and without sleep restriction," *Nat. Sci. Sleep*, vol. 10, pp. 385–396, 2018, doi: 10.2147/NSS.S175998.

[235] T. Nakamura, V. Goverdovsky, and D. P. Mandic, "In-ear EEG biometrics for feasible and readily collectable real-world person authentication," *IEEE Trans. Inf. Forensics Secur.*, vol. 13, no. 3, pp. 648–661, 2018, doi: 10.1109/TIFS.2017.2763124.

[236] G. M. Hammour and D. P. Mandic, "Hearables: Making Sense from Motion Artefacts in Ear-EEG for Real-Life Human Activity Classification," *Proc. Annu. Int. Conf. IEEE Eng. Med. Biol. Soc. EMBS*, pp. 6889–6893, 2021, doi: 10.1109/EMBC46164.2021.9629886.

[237] F.-L. Jin, M. Zhao, M. Park, and S.-J. Park, "Recent Trends of Foaming in Polymer Processing: A Review," *Polymers*, vol. 11, no. 6, 2019, doi: 10.3390/polym11060953.

[238] F. Lin and W. Cheng, "3D Sponge Electrodes for Soft Wearable Bioelectronics," *Advanced Electronic Materials,* vol. 2300334, pp. 1–21, 2023, doi: 10.1002/aelm.202300334.

[239] Ma, J., Yu, P., Zhou, M., Huang, H., Cai, Z., An, H., Shu, Z., Zhu, Y. and Tan, L., "Mechanically Robust and Ultrasensitive Natural Rubber / PEDOT : PSS Foam for Piezoresistive Sensors and Motion Monitoring," *ACS Applied Electronic Materials*, vol. *7*, no. 1, pp.313-321, 2025, doi: 10.1021/acsaelm.4c01780.

[240] Chen, R., He, Z., Luo, X., Wang, M., Liu, Z., Wu, Y., Dong, X., Zhang, D. and Liu, J., "Bio-Inspired Ion-Conducting Foam Elastomer for Human Motion Monitoring," *ACS Appl. Polym. Mater.*, vol. 5, no. 1, pp. 391–399, 2023, doi: 10.1021/ACSAPM.2C01568.

[241] Kim, S., Amjadi, M., Lee, T.I., Jeong, Y., Kwon, D., Kim, M.S., Kim, K., Kim, T.S., Oh, Y.S. and Park, I., "Wearable, Ultrawide-Range, and Bending-Insensitive Pressure Sensor Based on Carbon Nanotube Network-Coated Porous Elastomer Sponges for Human Interface and Healthcare Devices," *ACS Appl. Mater. Interfaces*, vol. 11, no. 26, pp. 23639–23648, 2019, doi: 10.1021/acsami.9b07636.

[242] X. Ma, Z. Jing, C. Feng, M. Qiao, and D. Xu, "Research and development progress of porous foam-based electrodes in advanced electrochemical energy storage devices: A critical review," *Renew. Sustain. Energy Rev.*, vol. 173, p. 113111, 2023, doi: https://doi.org/10.1016/j.rser.2022.113111.

[243] R. Banerjee, A. Gebrekrstos, J. T. Orasugh, and S. S. Ray, “Nanocarbon-Containing Polymer Composite Foams: A Review of Systems for Applications in Electromagnetic Interference Shielding, Energy Storage, and Piezoresistive Sensors,” *Ind. Eng. Chem. Res.*, vol. 62, no. 18, pp. 6807–6842, 2023, doi: 10.1021/acs.iecr.3c00089.

[244] Amaral, C., Pinto, S.C., Silva, T., Mohseni, F., Amaral, J.S., Amaral, V.S., Marques, P.A.A.P., Barros-Timmons, A. and Vicente, R., “Development of polyurethane foam incorporating phase change material for thermal energy storage,” *J. Energy Storage*, vol. 28, p. 101177, 2020, doi: https://doi.org/10.1016/j.est.2019.101177.

[245] Goverdovsky, V., Von Rosenberg, W., Nakamura, T., Looney, D., Sharp, D.J., Papavassiliou, C., Morrell, M.J. and Mandic, D.P., “Hearables: Multimodal physiological in-ear sensing,” *Sci. Rep.*, vol. 7, no. 1, pp. 1–10, 2017, doi: 10.1038/s41598-017-06925-2.

[246] H. J. Baek, H. J. Lee, Y. G. Lim, and K. S. Park, “Conductive Polymer Foam Surface Improves the Performance of a Capacitive EEG Electrode,” *IEEE Trans. Biomed. Eng.*, vol. 59, no. 12, pp. 3422–3431, 2012, doi: 10.1109/TBME.2012.2215032.

[247] Q. Ma, B. Hao, and P.C. Ma, “Flexible sensor based on polymer nanocomposites reinforced by carbon nanotube foam derivated from cotton,” *Compos. Sci. Technol.*, vol. 192, p. 108103, 2020, doi: https://doi.org/10.1016/j.compscitech.2020.108103.

[248] A. Idowu, B. Boesl, and A. Agarwal, “3D graphene foam-reinforced polymer composites – A review,” *Carbon*, vol. 135, pp. 52–71, 2018, doi: https://doi.org/10.1016/j.carbon.2018.04.024.

[249] T. M. Madkour, E. A. Abdelazeem, A. Tayel, G. Mustafa, and R. Siam, “In situ polymerization of polyurethane-silver nanocomposite foams with intact thermal stability , improved mechanical performance , and induced antimicrobial properties,” *Journal of Applied Polymer Science*, vol. 43125, pp. 1–9, 2016, doi: 10.1002/app.43125.

[250] A. Ameli, P. U. Jung, and C. B. Park, “Electrical properties and electromagnetic interference shielding effectiveness of polypropylene/carbon fiber composite foams,” *Carbon*, vol. 60, pp. 379–391, 2013, doi: 10.1016/j.carbon.2013.04.050.

[251] R. Banerjee, A. Gebrekrstos, J. T. Orasugh, and S. S. Ray, “Nanocarbon-Containing Polymer Composite Foams : A Review of Systems for Applications in Electromagnetic

Interference Shielding , Energy Storage , and Piezoresistive Sensors," 2023, doi: 10.1021/acs.iecr.3c00089.

[252] M. Nofar, J. Utz, N. Geis, V. Altstädt, and H. Ruckdäschel, "Foam 3D Printing of Thermoplastics : A Symbiosis of Additive Manufacturing and Foaming Technology," *Advanced Science,* vol. 2105701, pp. 1–18, 2022, doi: 10.1002/advs.202105701.

[253] H. S. Bharath, A. Sawardekar, S. Waddar, P. Jeyaraj, and M. Doddamani, "Mechanical behavior of 3D printed syntactic foam composites," *Compos. Struct.*, vol. 254, no. August, p. 112832, 2020, doi: 10.1016/j.compstruct.2020.112832.

[254] B. Sun and L. Wu, "Research progress of 3D printing combined with thermoplastic foaming," *Frontiers in Materials*, no. November, pp. 1–15, 2022, doi: 10.3389/fmats.2022.1083931.

[255] Zhou, C., Yang, K., Wang, K., Pei, X., Dong, Z., Hong, Y. and Zhang, X., "Combination of fused deposition modeling and gas foaming technique to fabricated hierarchical macro / microporous polymer scaffolds," *JMADE*, vol. 109, pp. 415–424, 2016, doi: 10.1016/j.matdes.2016.07.094.

[256] K. Kalia, B. Francoeur, A. Amirkhizi, and A. Ameli, "In Situ Foam 3D Printing of Microcellular Structures Using Material Extrusion Additive Manufacturing," *ACS Applied Materials & Interfaces*, 2022, doi: 10.1021/acsami.2c03014.

[257] D. E. Kwon and B. K. Park, "Solid-State Foaming of Acrylonitrile-Butadiene- Styrene / Recycled Polyethylene Terephthalate Using Carbon Dioxide as a Blowing Agent," *Polymers*, vol. 11, no. 2. pp. 291, 2019, doi: 10.3390/polym11020291.

[258] N. Gupta, S. E. Zeltmann, and V. C. Shunmugasamy, "Applications of Polymer Matrix Syntactic Foams," *Jom*, vol. 66, no. 2, pp. 245–254, 2014, doi: 10.1007/s11837-013-0796-8.

[259] R. Thiyagarajan and M. Senthil, "A Review on Closed Cell Metal Matrix Syntactic Foams : A Green Initiative towards Eco- Sustainability A Review on Closed Cell Metal Matrix Syntactic Foams : A Green Initiative towards Eco-," *Mater. Manuf. Process.*, vol. 36, no. 12, pp. 1333–1351, 2021, doi: 10.1080/10426914.2021.1928696.

[260] Zhang, Z., Dai, X., Li, L., Zhou, S., Xue, W., Liu, Y. and Liu, H., "Current Status of Research on the Modification of Thermal Properties of Epoxy Resin-Based Syntactic Foam Insulation Materials," *Polymers*, vol. 13, no. 18, 2021, doi: 10.3390/polym13183185.

[261] S. Anirudh, C. G. Jayalakshmi, A. Anand, B. Kandasubramanian, and S. O. Ismail, "Epoxy/hollow glass microsphere syntactic foams for structural and functional application-A review," *Eur. Polym. J.*, vol. 171, p. 111163, 2022, doi: https://doi.org/10.1016/j.eurpolymj.2022.111163.

[262] Cheng, C., Zhu, Z., Wang, M., Li, J., Sun, H., Jiao, R. and Li, A., "Enhanced flame retardancy and thermal insulation of flexible polyurethane foam decorated with DMMP-loaded CuO hollow spheres," *Colloids Surfaces A Physicochem. Eng. Asp.*, vol. 718, no. April, 2025, doi: 10.1016/j.colsurfa.2025.136961.

[263] Wang, Y., Wen, J., Zhao, S., Chen, Z., Ren, K., Sun, J. and Guan, J., "Surface Thiolation of Al Microspheres to Deposite Thin and Compact Ag Shells for High Conductivity," *Langmuir*, vol. 31, no. 49, pp. 13441–13451, 2015, doi: 10.1021/acs.langmuir.5b03590.

[264] Z. Huang, B. Chi, J. Guan, and Y. Liu, "Facile method to synthesize silver nanoparticles on the surface of hollow glass microspheres and their microwave shielding properties," *RSC Adv.*, vol. 4, no. 36, pp. 18645–18651, 2014, doi: 10.1039/c4ra01617c.

[265] S. Sarrafan and G. Li, "Conductive and Ferromagnetic Syntactic Foam with Shape Memory and Self-Healing/Recycling Capabilities," *Adv. Funct. Mater.*, vol. 34, no. 11, p. 2308085, 2024, doi: https://doi.org/10.1002/adfm.202308085.

[266] Zhang, L., Roy, S., Chen, Y., Chua, E.K., See, K.Y., Hu, X. and Liu, M., "Mussel-inspired polydopamine coated hollow carbon microspheres, a novel versatile filler for fabrication of high performance syntactic foams," *ACS Appl. Mater. Interfaces*, vol. 6, no. 21, pp. 18644–18652, 2014, doi: 10.1021/am503774a.

[267] Liu, Z., Yao, Z., Lv, Z., Huo, Z., Tan, S., Guo, S. and Qin, Y., "Structural and thermal enhancements in hollow glass microspheres via ZnO nanoparticle coating," *J. Coatings Technol. Res.*, 2025, doi: 10.1007/s11998-025-01095-7.

[268] Kim, J., Fan, J., Petrossian, G., Zhou, X., Kateb, P., Gagnon-Lafrenais, N. and Cicoira, F., "Self-healing, stretchable and recyclable polyurethane-PEDOT:PSS conductive blends,"

Mater. Horizons, vol. 11, no. 15, pp. 3548–3560, 2024, doi: 10.1039/d4mh00203b.

[269] Ebrahimi, S., Khoomortezaei, S., Fan, J., Dongnang, K., Garon, M., Quenneville, E. and Cicoira, F., "Conducting Polymer Coatings for Bioelectronic Arthroscopy Probes," *Adv. Healthc. Mater.*, vol. 02269, pp. 1–11, 2025, doi: 10.1002/adhm.202502269.

[270] J. S. Yun and S. H. Im, "Porous PEDOT : PSS smart thermal insulators enabling energy harvesting and detection," *Journal of Materials Chemistry A*, pp. 7837–7846, 2024, doi: 10.1039/d4ta00287c.

[271] Zhang, M., Yang, W., Wang, Z., Liu, H., Yin, R., Liu, C. and Shen, C., "Highly compressible and thermal insulative conductive MXene/PEDOT:PSS@melamine foam for promising wearable piezoresistive sensor," *Appl. Phys. Lett.*, vol. 122, no. 4, p. 43507, 2023, doi: 10.1063/5.0137571.

[272] Beccatelli, M., Villani, M., Gentile, F., Bruno, L., Seletti, D., Nikolaidou, D.M., Culiolo, M., Zappettini, A. and Coppede, N., "All-Polymeric Pressure Sensors Based on PEDOT : PSS-Modi fi ed Polyurethane Foam," *ACS Applied Polymer Materials*, vol. 3, 2021, doi: 10.1021/acsapm.0c01389.

[273] H. Li, R. Luo, J. Hu, S. Zhou, X. Zhou, and B. Du, "Lightweight, elastic and conductive pure PEDOT:PSS foam for dual-mode sensing," *J. Mater. Chem. A*, vol. 12, no. 25, pp. 15290–15299, 2024, doi: 10.1039/D4TA01631A.

[274] P. Sakunpongpitiporn, K. Phasuksom, N. Paradee, and A. Sirivat, "Facile synthesis of highly conductive PEDOT:PSS: Via surfactant templates," *RSC Adv.*, vol. 9, no. 11, pp. 6363–6378, 2019, doi: 10.1039/c8ra08801b.

[275] V. Forsberg, J. Mašlík, and M. Norgren, "Electronic performance of printed PEDOT:PSS lines correlated to the physical and chemical properties of coated inkjet papers," *RSC Adv.*, vol. 9, no. 41, pp. 23925–23938, 2019, doi: 10.1039/c9ra03801a.

[276] S. Ebrahimi, M. Nasiri, S. Agbolaghi, F. Abbasi, and R. Sarvari, "A focus on polystyrene tacticity in synthesized conductive PEDOT:PSS thin films," *J. Polym. Res.*, vol. 25, no. 11, pp. 18–20, 2018, doi: 10.1007/s10965-018-1598-z.

[277] L. E. Noble, R. Sarabia-riquelme, E. A. Morris, G. S. Rupasinghe, A. F. Paterson, and M.

C. Weisenberger, “Carbon fiber from direct carbonization of PEDOT : PSS precursor fibers,” *Carbon Trends*, vol. 19, no. December 2024, p. 100448, 2025, doi: 10.1016/j.cartre.2024.100448.

[278] Y. Wu *et al.*, “Ultralight Graphene Foam/Conductive Polymer Composites for Exceptional Electromagnetic Interference Shielding,” *ACS Appl. Mater. Interfaces*, vol. 9, no. 10, pp. 9059–9069, 2017, doi: 10.1021/acsami.7b01017.

[279] Aghvami-Panah, M., Wang, A., Panahi-Sarmad, M., Esfahani, S.A.S., Seraji, A.A., Shahbazi, M., Ghaffarian, R., Jamalpour, S. and Xiao, X., “A comparison study on polymeric nanocomposite foams with various carbon nanoparticles: adjusting radiation time and effect on electrical behavior and microcellular structure,” *Int. J. Smart Nano Mater.*, vol. 13, no. 3, pp. 504–528, 2022, doi: 10.1080/19475411.2022.2107110.

[280] Huang, W., Dai, K., Zhai, Y., Liu, H., Zhan, P., Gao, J., Zheng, G., Liu, C. and Shen, C., “Flexible and Lightweight Pressure Sensor Based on Carbon Nanotube / Thermoplastic Polyurethane-Aligned Conductive Foam with Superior Compressibility and Stability,” *ACS applied materials & interfaces*, vol. 9, no. 48, 2017, doi: 10.1021/acsami.7b16975.

[281] X. Lü, T. Yu, F. Meng, and W. Bao, “Wide-Range and High-Stability Flexible Conductive Graphene/Thermoplastic Polyurethane Foam for Piezoresistive Sensor Applications,” *Adv. Mater. Technol.*, vol. 6, no. 10, pp. 1–13, 2021, doi: 10.1002/admt.202100248.

[282] Q. Chen, Q. Gao, X. Wang, D. W. Schubert, and X. Liu, “Flexible, conductive, and anisotropic thermoplastic polyurethane/polydopamine /MXene foam for piezoresistive sensors and motion monitoring,” *Compos. Part A Appl. Sci. Manuf.*, vol. 155, no. November 2021, p. 106838, 2022, doi: 10.1016/j.compositesa.2022.106838.

[283] Kim, E., Zhang, H., Lee, J.H., Chen, H., Zhang, H., Javed, M.H., Shen, X. and Kim, J.K., “MXene/polyurethane auxetic composite foam for electromagnetic interference shielding and impact attenuation,” *Compos. Part A Appl. Sci. Manuf.*, vol. 147, no. April, p. 106430, 2021, doi: 10.1016/j.compositesa.2021.106430.

[284] Gu, W., Ong, S.J.H., Shen, Y., Guo, W., Fang, Y., Ji, G. and Xu, Z.J., “A Lightweight, Elastic, and Thermally Insulating Stealth Foam With High Infrared-Radar Compatibility,” *Adv. Sci.*, vol. 9, no. 35, pp. 1–14, 2022, doi: 10.1002/advs.202204165.

[285] M. Aghvami-Panah, M. Azami, K. Kalia, and A. Ameli, “In situ foam 3D printed microcellular multifunctional nanocomposites of thermoplastic polyurethane and carbon nanotube,” *Carbon*, vol. 230, p. 119619, 2024, doi: https://doi.org/10.1016/j.carbon.2024.119619.

[286] L.J. Gibson and M.F. Ashby, "Cellular solids: Structure and properties," *Adv. Polym. Technol.*, vol. 9, no. 2, pp. 165–166, 1989, doi: https://doi.org/10.1002/adv.1989.060090207.

[287] Y. He *et al.*, “CNT/PDMS conductive foam-based piezoresistive sensors with low detection limits, excellent durability, and multifunctional sensing capability,” *Sensors Actuators A Phys.*, vol. 358, p. 114408, 2023, doi: https://doi.org/10.1016/j.sna.2023.114408.

[288] P. Ghahramani, K. Behdinan, and H. E. Naguib, “Development of piezoresistive PDMS/MWCNT foam nanocomposite sensor with ultrahigh flexibility and compressibility.,” *J. Intell. Mater. Syst. Struct.*, vol. 33, no. 14, pp. 1751–1761, Aug. 2022, doi: 10.1177/1045389X211064345.

[289] Y. Li *et al.*, “Achieving tissue-level softness on stretchable electronics through a generalizable soft interlayer design,” *Nat. Commun.*, vol. 14, no. 1, p. 4488, 2023, doi: 10.1038/s41467-023-40191-3.

[290] H. Peidayesh, K. Mosnáčková, Z. Špitalský, A. Heydari, A. O. Šišková, and I. Chodák, “Thermoplastic Starch–Based Composite Reinforced by Conductive Filler Networks: Physical Properties and Electrical Conductivity Changes during Cyclic Deformation,” *Polymers*, vol. 13, no. 21, 2021, doi: 10.3390/polym13213819.

[291] R. Sharma and H. K. Meena, “Emerging Trends in EEG Signal Processing: A Systematic Review,” *SN Comput. Sci.*, vol. 5, no. 4, Apr. 2024, doi: 10.1007/s42979-024-02773-w.

[292] K. Mizokuchi, T. Tanaka, T. G. Sato, and Y. Shiraki, “Alpha band modulation caused by selective attention to music enables EEG classification.,” *Cogn. Neurodyn.*, vol. 18, no. 3, pp. 1005–1020, Jun. 2024, doi: 10.1007/s11571-023-09955-x.

[293] J. L. Cantero, M. Atienza, and R. M. Salas, “Human alpha oscillations in wakefulness, drowsiness period, and REM sleep: different electroencephalographic phenomena within the alpha band.,” *Neurophysiol. Clin.*, vol. 32, no. 1, pp. 54–71, Jan. 2002, doi:

10.1016/s0987-7053(01)00289-1.

[294] X. Xiao, Y. Zhou, J. Yin, X. Zhao, and J. Chen, “In-ear electrophysichochemical sensing.,” *Nat. Biomed. Eng.*, vol. 7, no. 10, pp. 1207–1209, Oct. 2023, doi: 10.1038/s41551-023-01097-z.

[295] R. J. Barry, A. R. Clarke, S. J. Johnstone, C. A. Magee, and J. A. Rushby, “EEG differences between eyes-closed and eyes-open resting conditions.,” *Clin. Neurophysiol. Off. J. Int. Fed. Clin. Neurophysiol.*, vol. 118, no. 12, pp. 2765–2773, Dec. 2007, doi: 10.1016/j.clinph.2007.07.028.

[296] S. Rimbert, R. Al-Chwa, M. Zaepffel, and L. Bougrain, “Electroencephalographic modulations during an open- or closed-eyes motor task.,” *PeerJ*, vol. 6, p. e4492, 2018, doi: 10.7717/peerj.4492.

[297] N. M. Petro *et al.*, “Eyes-closed versus eyes-open differences in spontaneous neural dynamics during development.,” *Neuroimage*, vol. 258, p. 119337, Sep. 2022, doi: 10.1016/j.neuroimage.2022.119337.

[298] S. C. Luo, H. H. Yu, A. C. A. Wan, Y. Han, and J. Y. Ying, “A general synthesis for PEDOT-coated nonconductive materials and PEDOT hollow particles by aqueous chemical polymerization,” *Small*, vol. 4, no. 11, pp. 2051–2058, Nov. 2008, doi: 10.1002/smll.200800033.

[299] Z. Zhang, G. Chen, H. Wang, and X. Li, “Template-directed in situ polymerization preparation of nanocomposites of PEDOT:PSS-coated multi-walled carbon nanotubes with enhanced thermoelectric property,” *Chem. - An Asian J.*, vol. 10, no. 1, pp. 149–153, 2015, doi: 10.1002/asia.201403100.

[300] R. A. Ilyas *et al.*, “Natural Fiber-Reinforced Polycaprolactone Green and Hybrid Biocomposites for Various Advanced Applications,” *Polymers*, vol. 14, no. 1, 2022, doi: 10.3390/polym14010182.

[301] S. Zhang, C. Campagne, and F. Salaün, “Preparation of Electrosprayed Poly(caprolactone) Microparticles Based on Green Solvents and Related Investigations on the Effects of Solution Properties as Well as Operating Parameters,” *Coatings*, vol. 9, no. 2, 2019, doi: 10.3390/coatings9020084.

[302] Y. Liu, H. Wang, W. Zhao, M. Zhang, H. Qin, and Y. Xie, "Flexible, Stretchable Sensors for Wearable Health Monitoring: Sensing Mechanisms, Materials, Fabrication Strategies and Features," *Sensors*, vol. 18, no. 2, 2018, doi: 10.3390/s18020645.

[303] A. Yu *et al.*, "Implantable Flexible Sensors for Health Monitoring," *Adv. Healthc. Mater.*, vol. 13, no. 2, pp. 1–21, 2024, doi: 10.1002/adhm.202302460.

[304] J. Li, Z. Fang, D. Wei, and Y. Liu, "Flexible Pressure, Humidity, and Temperature Sensors for Human Health Monitoring," *Adv. Healthc. Mater.*, vol. 2401532, pp. 1–37, 2024, doi: 10.1002/adhm.202401532.

[305] Y. Lu *et al.*, "Stretchable graphene–hydrogel interfaces for wearable and implantable bioelectronics," *Nat. Electron.*, vol. 7, no. 1, pp. 51–65, 2024, doi: 10.1038/s41928-023-01091-y.

[306] F. Lin *et al.*, "Muscle-Inspired Robust Anisotropic Cellulose Conductive Hydrogel for Multidirectional Strain Sensors and Implantable Bioelectronics," *Adv. Funct. Mater.*, vol. 2416419, pp. 1–16, 2024, doi: 10.1002/adfm.202416419.

[307] S.-H. Sunwoo *et al.*, "Soft bioelectronics for the management of cardiovascular diseases," *Nat. Rev. Bioeng.*, vol. 2, no. 1, pp. 8–24, 2024, doi: 10.1038/s44222-023-00102-z.

[308] M. Wang *et al.*, "Fusing Stretchable Sensing Technology with Machine Learning for Human–Machine Interfaces," *Adv. Funct. Mater.*, vol. 31, no. 39, pp. 1–13, 2021, doi: 10.1002/adfm.202008807.

[309] K. K. Kim, Y. Suh, and S. H. Ko, "Smart Stretchable Electronics for Advanced Human–Machine Interface," *Adv. Intell. Syst.*, vol. 3, no. 2, 2021, doi: 10.1002/aisy.202000157.

[310] L. Wang, F. Wei, Z. Zhai, R. Zhang, W. Liu, and Z. Zhao, "A flexible dual-mode triboelectric sensor for strain and tactile sensing toward human-machine interface applications," *Sensors Actuators A Phys.*, vol. 365, p. 114909, 2024, doi: https://doi.org/10.1016/j.sna.2023.114909.

[311] W. Heng, S. Solomon, and W. Gao, "Flexible Electronics and Devices as Human–Machine Interfaces for Medical Robotics," *Adv. Mater.*, vol. 34, no. 16, pp. 1–48, 2022, doi: 10.1002/adma.202107902.

[312] N. A. Shahrim, Z. Ahmad, A. Wong Azman, Y. Fachmi Buys, and N. Sarifuddin, “Mechanisms for doped PEDOT:PSS electrical conductivity improvement,” *Mater. Adv.*, vol. 2, no. 22, pp. 7118–7138, 2021, doi: 10.1039/D1MA00290B.

[313] N. Kim *et al.*, “Elastic conducting polymer composites in thermoelectric modules,” *Nat. Commun.*, vol. 11, no. 1, 2020, doi: 10.1038/s41467-020-15135-w.

[314] C. Volkert *et al.*, “Enhanced Electrical Performance and Stretchability by Plasticizer-Facilitated PEDOT:PSS Self-Alignment,” *Adv. Sci.*, vol. 2502853, pp. 1–9, 2025, doi: 10.1002/advs.202502853.

[315] K. Pattanarat, N. Petchsang, T. Osotchan, Y. H. Kim, and R. Jaisutti, “Wash-Durable Conductive Yarn with Ethylene Glycol-Treated PEDOT:PSS for Wearable Electric Heaters,” *ACS Appl. Mater. Interfaces*, vol. 13, no. 40, pp. 48053–48060, 2021, doi: 10.1021/acsami.1c13329.

[316] S. Ichikawa and N. Toshima, “Improvement of thermoelectric properties of composite films of PEDOT-PSS with xylitol by means of stretching and solvent treatment,” *Polym. J.*, vol. 47, no. 7, pp. 522–526, 2015, doi: 10.1038/pj.2015.28.

[317] Q. Liu, J. Qiu, C. Yang, L. Zang, G. Zhang, and E. Sakai, “High-Performance PVA/PEDOT:PSS Hydrogel Electrode for All-Gel-State Flexible Supercapacitors,” *Adv. Mater. Technol.*, vol. 6, no. 1, pp. 1–11, 2021, doi: 10.1002/admt.202000919.

[318] P. Kateb, J. Fan, J. Kim, X. Zhou, G. A. Lodygensky, and F. Cicoira, “Printable, adhesive, and self-healing dry epidermal electrodes based on PEDOT:PSS and polyurethane diol,” *Flex. Print. Electron.*, vol. 8, no. 4, 2023, doi: 10.1088/2058-8585/ad05d6.

[319] Y. Wang *et al.*, “Engineering PEDOT:PSS/PEG Fibers with a Textured Surface toward Comprehensive Personal Thermal Management,” *ACS Appl. Mater. Interfaces*, vol. 15, no. 13, pp. 17175–17187, 2023, doi: 10.1021/acsami.2c23269.

[320] C. I. Idumah, J. H. Low, and E. O. Emmanuel, "Recently emerging trends in xerogel polymeric nanoarchitectures and multifunctional applications," *Polymer Bulletin*, vol. 80, no. 11, 2023. doi: 10.1007/s00289-022-04625-0.

[321] W. Hu, Z. Wang, Y. Xiao, S. Zhang, and J. Wang, “Advances in crosslinking strategies of

biomedical hydrogels," *Biomater. Sci.*, vol. 7, no. 3, pp. 843–855, 2019, doi: 10.1039/c8bm01246f.

[322] H. Chamkouri, "A Review of Hydrogels, Their Properties and Applications in Medicine," *Am. J. Biomed. Sci. Res.*, vol. 11, no. 6, pp. 485–493, 2021, doi: 10.34297/ajbsr.2021.11.001682.

[323] W. X. Waresindo *et al.*, "Freeze-thaw hydrogel fabrication method: basic principles, synthesis parameters, properties, and biomedical applications," *Mater. Res. Express*, vol. 10, no. 2, 2023, doi: 10.1088/2053-1591/acb98e.

[324] F. Wu, J. Gao, Y. Xiang, and J. Yang, "Enhanced Mechanical Properties of PVA Hydrogel by Low-Temperature Segment Self-Assembly vs. Freeze–Thaw Cycles," *Polymers*, vol. 15, no. 18, 2023, doi: 10.3390/polym15183782.

[325] G. Mugnaini, R. Gelli, L. Mori, and M. Bonini, "How to Cross-Link Gelatin: The Effect of Glutaraldehyde and Glyceraldehyde on the Hydrogel Properties," *ACS Appl. Polym. Mater.*, vol. 5, no. 11, pp. 9192–9202, Nov. 2023, doi: 10.1021/acsapm.3c01676.

[326] A. Chang *et al.*, "Citric acid crosslinked sphingan WL gum hydrogel films supported ciprofloxacin for potential wound dressing application," *Carbohydr. Polym.*, vol. 291, p. 119520, 2022, doi: https://doi.org/10.1016/j.carbpol.2022.119520.

[327] X. Zhou *et al.*, "Self-healing, stretchable, and highly adhesive hydrogels for epidermal patch electrodes," *Acta Biomater.*, vol. 139, pp. 296–306, 2022, doi: 10.1016/j.actbio.2021.07.069.

[328] C. Liu, F. Lei, P. Li, K. Wang, and J. Jiang, "A review on preparations, properties, and applications of cis-ortho-hydroxyl polysaccharides hydrogels crosslinked with borax," *Int. J. Biol. Macromol.*, vol. 182, pp. 1179–1191, 2021, doi: https://doi.org/10.1016/j.ijbiomac.2021.04.090.

[329] S. Cho, S. Y. Hwang, D. X. Oh, and J. Park, "Recent progress in self-healing polymers and hydrogels based on reversible dynamic B-O bonds: boronic/boronate esters, borax, and benzoxaborole," *J. Mater. Chem. A*, vol. 9, no. 26, pp. 14630–14655, 2021, doi: 10.1039/d1ta02308j.

[330] M. B. Lawrence, “Influence of cross-linker concentration on the water contained within the pores of poly(vinyl alcohol)-borax hydrogels: a vibrational spectroscopic study,” *Polym. Bull.*, vol. 81, no. 15, pp. 13783–13801, 2024, doi: 10.1007/s00289-024-05364-0.

[331] J. Xu, X. Liu, X. Ren, and G. Gao, “The role of chemical and physical crosslinking in different deformation stages of hybrid hydrogels,” *Eur. Polym. J.*, vol. 100, pp. 86–95, 2018, doi: https://doi.org/10.1016/j.eurpolymj.2018.01.020.

[332] J. Hao and R. A. Weiss, “Mechanical behavior of hybrid hydrogels composed of a physical and a chemical network,” *Polymer*, vol. 54, no. 8, pp. 2174–2182, 2013, doi: https://doi.org/10.1016/j.polymer.2013.01.052.

[333] Y. Zhou *et al.*, “The weaving art of mechanically and electronically robust hydrogel realizes multi-dimensional response of stretchable sensors,” *Appl. Mater. Today*, vol. 34, no. May, p. 101894, 2023, doi: 10.1016/j.apmt.2023.101894.

[334] W. Shi *et al.*, “High-Sensitivity and Extreme Environment-Resistant Sensors Based on PEDOT:PSS@PVA Hydrogel Fibers for Physiological Monitoring,” *ACS Appl. Mater. Interfaces*, vol. 14, no. 30, pp. 35114–35125, 2022, doi: 10.1021/acsami.2c09556.

[335] H. S. Bu, W. Aycock, S. Z. D. Cheng, and B. Wunderlich, “Heat capacities of various solid linear macromolecules,” *Polymer*, vol. 29, no. 8, pp. 1485–1494, 1988, doi: https://doi.org/10.1016/0032-3861(88)90314-X.

[336] S. Peng, S. Liu, Y. Sun, N. Xiang, X. Jiang, and L. Hou, “Facile preparation and characterization of poly(vinyl alcohol)-NaCl-glycerol supramolecular hydrogel electrolyte,” *Eur. Polym. J.*, vol. 106, pp. 206–213, 2018, doi: https://doi.org/10.1016/j.eurpolymj.2018.07.024.

[337] S. Shi, X. Peng, T. Liu, Y.-N. Chen, C. He, and H. Wang, “Facile preparation of hydrogen-bonded supramolecular polyvinyl alcohol-glycerol gels with excellent thermoplasticity and mechanical properties,” *Polymer*, vol. 111, pp. 168–176, 2017, doi: https://doi.org/10.1016/j.polymer.2017.01.051.

[338] T. Yang, J. Wu, Y. Yao, K. Wang, Q. Zhang, and Q. Fu, “Towards the toughness-strength balance of poly(vinyl alcohol) films via synergic plasticization,” *Polymer*, vol. 301, p. 127031, 2024, doi: https://doi.org/10.1016/j.polymer.2024.127031.

[339] H. Li and M. A. Huneault, “Comparison of sorbitol and glycerol as plasticizers for thermoplastic starch in TPS/PLA blends,” *J. Appl. Polym. Sci.*, vol. 119, no. 4, pp. 2439–2448, 2011, doi: https://doi.org/10.1002/app.32956.

[340] H.-L. Lin, Y.-F. Liu, T. L. Yu, W.-H. Liu, and S.-P. Rwei, “Light scattering and viscoelasticity study of poly(vinyl alcohol)–borax aqueous solutions and gels,” *Polymer*, vol. 46, no. 15, pp. 5541–5549, 2005, doi: https://doi.org/10.1016/j.polymer.2005.04.074.

[341] F. Soto-Bustamante, G. Bassu, E. Fratini, and M. Laurati, “Effect of Composition and Freeze-Thaw on the Network Structure, Porosity and Mechanical Properties of Polyvinyl-Alcohol/Chitosan Hydrogels.,” *Gels*, vol. 9, no. 5, May 2023, doi: 10.3390/gels9050396.

[342] R. Ricciardi, F. Auriemma, C. De Rosa, and F. Lauprêtre, “X-ray Diffraction Analysis of Poly(vinyl alcohol) Hydrogels, Obtained by Freezing and Thawing Techniques,” *Macromolecules*, vol. 37, no. 5, pp. 1921–1927, Mar. 2004, doi: 10.1021/ma035663q.

[343] A. Górska *et al.*, “Physically Cross-Linked PVA Hydrogels as Potential Wound Dressings: How Freezing Conditions and Formulation Composition Define Cryogel Structure and Performance.,” *Pharmaceutics*, vol. 16, no. 11, Oct. 2024, doi: 10.3390/pharmaceutics16111388.

[344] X. Qi, X. Yao, S. Deng, T. Zhou, and Q. Fu, “Water-induced shape memory effect of graphene oxide reinforced polyvinyl alcohol nanocomposites,” *J. Mater. Chem. A*, vol. 2, no. 7, pp. 2240–2249, 2014, doi: 10.1039/C3TA14340F.

[345] S. N. Kale, J. Mona, S. Dhobale, T. Thite, and S. L. Laware, “Intramolecular and intermolecular crosslinked poly(vinyl alcohol)–borate complexes for the sustained release of fertilizers and enzymes,” *J. Appl. Polym. Sci.*, vol. 121, no. 4, pp. 2450–2457, 2011, doi: https://doi.org/10.1002/app.33776.

[346] G. Cai, J. Wang, K. Qian, J. Chen, S. Li, and P. S. Lee, “Extremely Stretchable Strain Sensors Based on Conductive Self-Healing Dynamic Cross-Links Hydrogels for Human-Motion Detection,” *Adv. Sci.*, vol. 4, no. 2, p. 1600190, 2017, doi: https://doi.org/10.1002/advs.201600190.

[347] X. Qi *et al.*, “Investigation of Salecan/poly(vinyl alcohol) hydrogels prepared by freeze/thaw method,” *Carbohydr. Polym.*, vol. 118, pp. 60–69, 2015, doi:

https://doi.org/10.1016/j.carbpol.2014.11.021.

[348] C. M. Hassan and N. A. Peppas, “Structure and Applications of Poly(vinyl alcohol) Hydrogels Produced by Conventional Crosslinking or by Freezing/Thawing Methods,” in *Biopolymers ·PVA Hydrogels, Anionic Polymerisation Nanocomposites*, Berlin, Heidelberg: Springer Berlin Heidelberg, 2000, pp. 37–65. doi: 10.1007/3-540-46414-X_2.

[349] E. Al-Emam, H. Soenen, J. Caen, and K. Janssens, “Characterization of polyvinyl alcohol-borax/agarose (PVA-B/AG) double network hydrogel utilized for the cleaning of works of art,” *Herit. Sci.*, vol. 8, no. 1, p. 106, 2020, doi: 10.1186/s40494-020-00447-3.

[350] N. Q. Vu, T. M. Le, A. N. B. Ngo, M. H. T. Nguyen, Y.-C. Liao, and T. T. Tran, “Engineering Functional PVA: A Comprehensive Review of Chemical Modifications and Prospective Developments,” *ACS Polym. Au*, vol. 6, no. 1, pp. 33–60, Feb. 2026, doi: 10.1021/acspolymersau.5c00133.

[351] J. L. Carter, C. A. Kelly, and M. J. Jenkins, “Processing optimization of PEDOT:PSS and PEDOT:PSS/Tween 80 films,” *Polym. J.*, vol. 55, no. 3, pp. 253–260, 2023, doi: 10.1038/s41428-022-00740-x.

[352] D. A. Ahmad Ruzaidi *et al.*, “Revealing the improved sensitivity of PEDOT:PSS/PVA thin films through secondary doping and their strain sensors application,” *RSC Adv.*, vol. 13, no. 12, pp. 8202–8219, 2023, doi: 10.1039/D3RA00584D.

[353] B. Sreedhar, M. Sairam, D. K. Chattopadhyay, P. A. S. Rathnam, and D. V. M. Rao, “Thermal, mechanical, and surface characterization of starch–poly(vinyl alcohol) blends and borax-crosslinked films,” *J. Appl. Polym. Sci.*, vol. 96, no. 4, pp. 1313–1322, 2005, doi: https://doi.org/10.1002/app.21439.

[354] M. Huang, Y. Hou, Y. Li, D. Wang, and L. Zhang, “High performances of dual network PVA hydrogel modified by PVP using borax as the structure-forming accelerator.,” *Des. monomers Polym.*, vol. 20, no. 1, pp. 505–513, 2017, doi: 10.1080/15685551.2017.1382433.

[355] O. Zandraa *et al.*, “Development of dual crosslinked mumio-based hydrogel dressing for wound healing application: Physico-chemistry and antimicrobial activity,” *Int. J. Pharm.*, vol. 607, p. 120952, 2021, doi: https://doi.org/10.1016/j.ijpharm.2021.120952.

[356] W. Liu, C. Yao, D. Wang, G. Du, Y. Ji, and Q. Li, "Dynamic Double-Networked Hydrogels by Hybridizing PVA and Herbal Polysaccharides: Improved Mechanical Properties and Selective Antibacterial Activity.," *Gels*, vol. 10, no. 12, Dec. 2024, doi: 10.3390/gels10120821.

[357] Y. Qin, J. Wang, C. Qiu, X. Xu, and Z. Jin, "A Dual Cross-Linked Strategy to Construct Moldable Hydrogels with High Stretchability, Good Self-Recovery, and Self-Healing Capability," *J. Agric. Food Chem.*, vol. 67, no. 14, pp. 3966–3980, Apr. 2019, doi: 10.1021/acs.jafc.8b05147.

[358] K. Ingtipi, B. J. Choudhury, and V. S. Moholkar, "Development of NaOH-borax crosslinked PVA-xanthan gum-lignin hydrogel as green fire retardant coating," *Prog. Org. Coatings*, vol. 174, p. 107268, 2023, doi: https://doi.org/10.1016/j.porgcoat.2022.107268.

[359] C. Wang *et al.*, "Facile fabrication and characterization of high-performance Borax-PVA hydrogel," *J. Sol-Gel Sci. Technol.*, vol. 101, no. 1, pp. 103–113, 2022, doi: 10.1007/s10971-021-05584-0.

[360] J. Tavakoli and Y. Tang, "Honey/PVA hybrid wound dressings with controlled release of antibiotics: Structural, physico-mechanical and in-vitro biomedical studies," *Mater. Sci. Eng. C*, vol. 77, pp. 318–325, 2017, doi: https://doi.org/10.1016/j.msec.2017.03.272.

[361] L. Tu *et al.*, "Production and Anti-Inflammatory Performance of PVA Hydrogels Loaded with Curcumin Encapsulated in Octenyl Succinic Anhydride Modified Schizophyllan as Wound Dressings," *Molecules*, vol. 28, no. 3, 2023, doi: 10.3390/molecules28031321.

[362] A. Li, J. Zhang, M. A. A. Newton, Y. Liu, T. Li, and B. Xin, "Multifunctional double network PVA-Borax/GO-cellulose nanofibrils hydrogel for wearable strain sensor," *Polymer*, vol. 337, p. 129027, 2025, doi: https://doi.org/10.1016/j.polymer.2025.129027.

[363] A. Dixit and D. S. Bag, "Highly stretchable and tough thermo-responsive double network (DN) hydrogels: Composed of PVA-borax and poly (AM-co-NIPAM) polymer networks," *Eur. Polym. J.*, vol. 175, p. 111347, 2022, doi: https://doi.org/10.1016/j.eurpolymj.2022.111347.

[364] Y. Wang *et al.*, "Multifunctional Nano-Conductive Hydrogels With High Mechanical Strength, Toughness and Fatigue Resistance as Self-Powered Wearable Sensors and Deep

Learning-Assisted Recognition System," *Adv. Funct. Mater.*, vol. 34, no. 49, p. 2409081, 2024, doi: https://doi.org/10.1002/adfm.202409081.

[365] Y. Zhou *et al.*, "Highly Stretchable, Elastic, and Ionic Conductive Hydrogel for Artificial Soft Electronics," *Adv. Funct. Mater.*, vol. 29, no. 1, p. 1806220, 2019, doi: https://doi.org/10.1002/adfm.201806220.

[366] X. Pan *et al.*, "An integrated transparent, UV-filtering organohydrogel sensor via molecular-level ion conductive channels," *J. Mater. Chem. A*, vol. 7, no. 9, pp. 4525–4535, 2019, doi: 10.1039/C8TA12360H.

[367] R. Hu, J. Zhao, Y. Wang, Z. Li, and J. Zheng, "A highly stretchable, self-healing, recyclable and interfacial adhesion gel: Preparation, characterization and applications," *Chem. Eng. J.*, vol. 360, pp. 334–341, 2019, doi: https://doi.org/10.1016/j.cej.2018.12.001.

[368] M. A. Darabi *et al.*, "An Alkaline Based Method for Generating Crystalline, Strong, and Shape Memory Polyvinyl Alcohol Biomaterials," *Adv. Sci.*, vol. 7, no. 21, p. 1902740, 2020, doi: https://doi.org/10.1002/advs.201902740.

[369] W. Zhao, D. Zhang, Y. Yang, C. Du, and B. Zhang, "A fast self-healing multifunctional polyvinyl alcohol nano-organic composite hydrogel as a building block for highly sensitive strain/pressure sensors," *J. Mater. Chem. A*, vol. 9, no. 38, pp. 22082–22094, 2021, doi: 10.1039/D1TA05586K.

[370] Q. Zhou *et al.*, "Mechanically Strong and Multifunctional Hybrid Hydrogels with Ultrahigh Electrical Conductivity," *Adv. Funct. Mater.*, vol. 31, no. 40, p. 2104536, 2021, doi: https://doi.org/10.1002/adfm.202104536.

[371] Q. He, L. Ren, J. Xu, N. Wu, L. Wang, and W. Song, "High-Strength, UV-Resistant Conductive PVA/Sodium Lignosulfonate Hydrogels for Wearable Strain Sensors," *ACS Appl. Polym. Mater.*, Feb. 2026, doi: 10.1021/acsapm.5c04413.

[372] Z. Cao *et al.*, "Ion–Electron Dual-Conductive High-Performance PVA-Based Conductive Hydrogel for Wearable Strain Sensors," *ACS Appl. Polym. Mater.*, Feb. 2026, doi: 10.1021/acsapm.5c03486.

[373] M. Meng, R. Fu, T. Xue, X. Liu, J. Jiang, and X. Liu, "Triple-network conductive hydrogel

with high strength and toughness for visual flexible strain sensor," *Chem. Eng. J.*, vol. 519, p. 165709, 2025, doi: https://doi.org/10.1016/j.cej.2025.165709.

[374] T. Wang *et al.*, "Reactive dye-reinforced PVA-based high-strength, highly conductive coloured hydrogel flexible sensors for joint monitoring and pressure sensing," *Compos. Struct.*, vol. 382, p. 120084, 2026, doi: https://doi.org/10.1016/j.compstruct.2026.120084.

[375] L. Dai *et al.*, "Twisted Conductive Fiber-Based Strain Sensor with High Sensitivity and Wide Working Range for Human Motion Recognition and Physiological Activity Monitoring," *ACS Appl. Mater. Interfaces*, vol. 17, no. 43, pp. 59747–59758, Oct. 2025, doi: 10.1021/acsami.5c13604.

[376] D. Bi *et al.*, "Tough and Strain-Sensitive Organohydrogels Based on MXene and PEDOT/PSS and Their Effects on Mechanical Properties and Strain-Sensing Performance," *ACS Appl. Mater. Interfaces*, vol. 16, no. 9, pp. 11914–11929, Mar. 2024, doi: 10.1021/acsami.3c18631.

[377] Y. Zhang *et al.*, "Multifunctional PVA/gelatin DN hydrogels with strong mechanical properties enhanced by Hofmeister effect," *Colloids Surfaces A Physicochem. Eng. Asp.*, vol. 691, p. 133833, 2024, doi: https://doi.org/10.1016/j.colsurfa.2024.133833.

[378] Y. Yang, G. Zhao, X. Cheng, H. Deng, and Q. Fu, "Stretchable and Healable Conductive Elastomer Based on PEDOT:PSS/Natural Rubber for Self-Powered Temperature and Strain Sensing," *ACS Appl. Mater. Interfaces*, vol. 13, no. 12, pp. 14599–14611, Mar. 2021, doi: 10.1021/acsami.1c00879.

[379] R. Luo, X. Li, H. Li, B. Du, and S. Zhou, "A stretchable and printable PEDOT:PSS/PDMS composite conductors and its application to wearable strain sensor," *Prog. Org. Coatings*, vol. 162, p. 106593, 2022, doi: https://doi.org/10.1016/j.porgcoat.2021.106593.

APPENDIX A SUPPORTING INFORMATION OF ARTICLE 2: MICROSPHERE-TEMPLATED CONDUCTIVE SYNTACTIC FOAMS FOR RECYCLABLE AND ADDITIVELY MANUFACTURED SOFT ELECTRONICS

Gayaneh Petrossian, Yassine Diouri, Bolan Xu, Sara Ebrahimi, Atharva Pande, Floriane Miquet-Westphal, Hang Xu, and Fabio Cicoira*

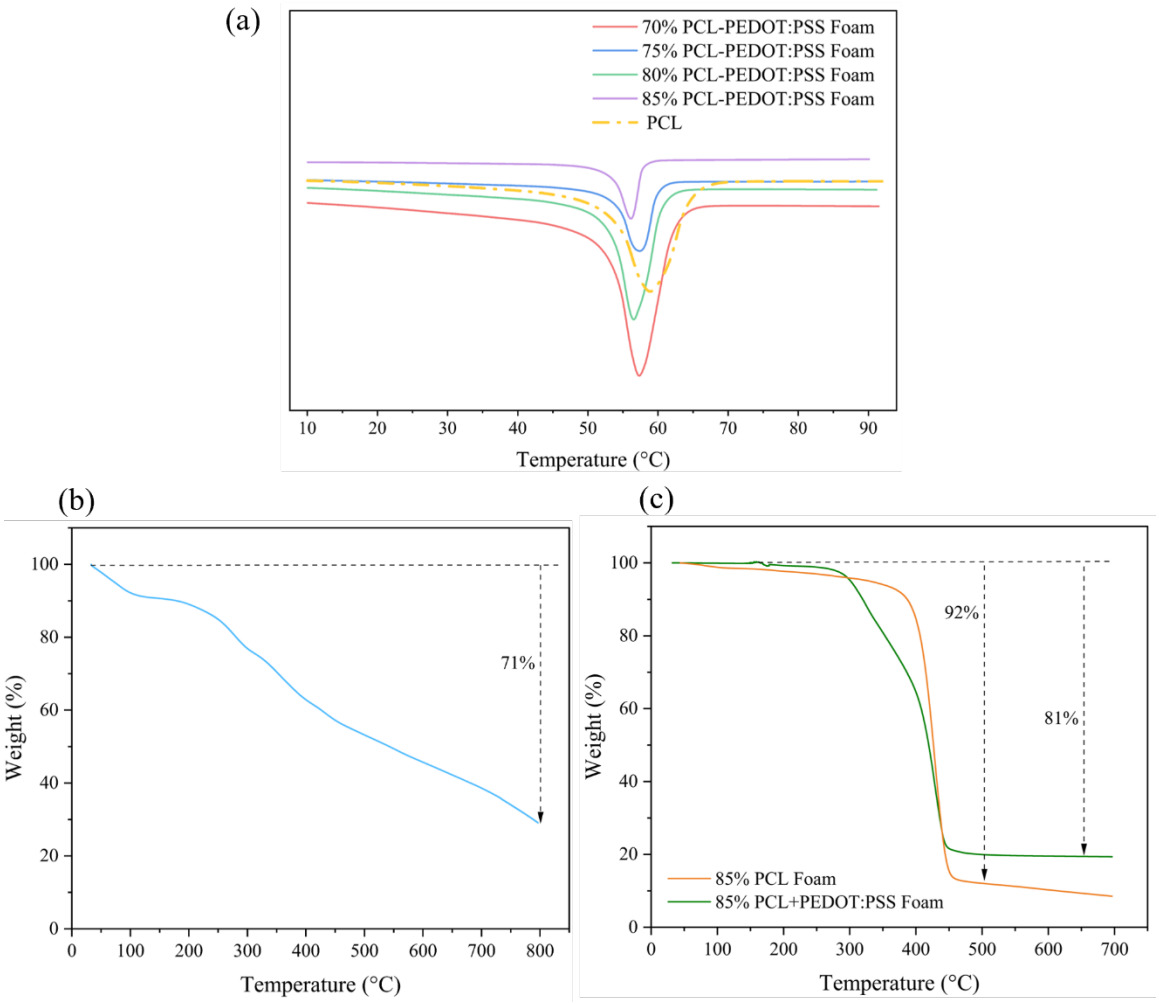

Figure A1 (a) DSC thermograms of neat PCL and PCL-PEDOT:PSS foams. (b) Thermogravimetric curve of PEDOT:PSS-coated microspheres, exhibiting continuous mass loss. (c) TGA curves of 85% void fraction foams with and without PEDOT:PSS.

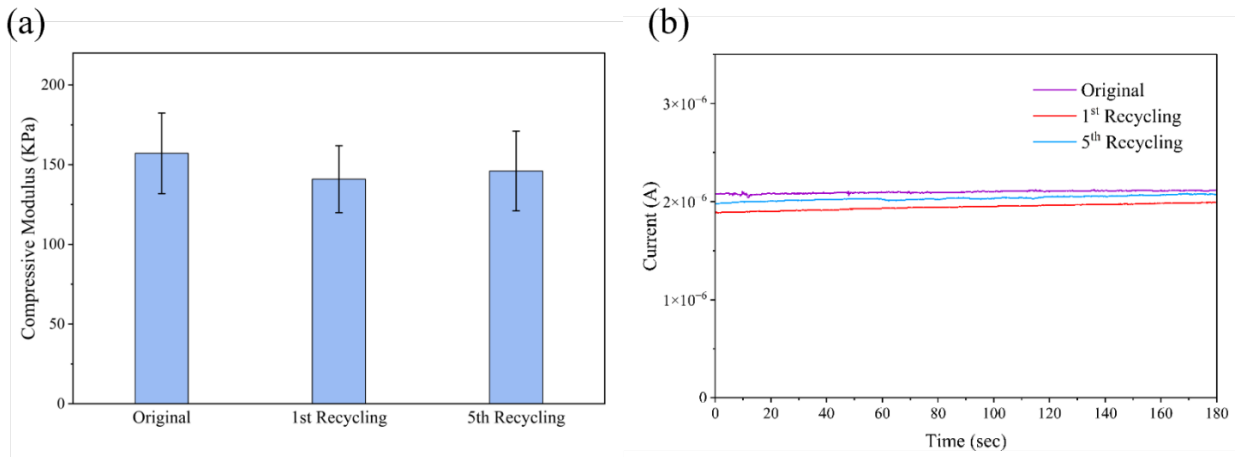

Figure A2 Comparison of (a) compression modulus and (b) current vs. time plot for 85% PCL-PEDOT:PSS foam before and after recycling (1, and 5 times) using a hot press at 100 °C.

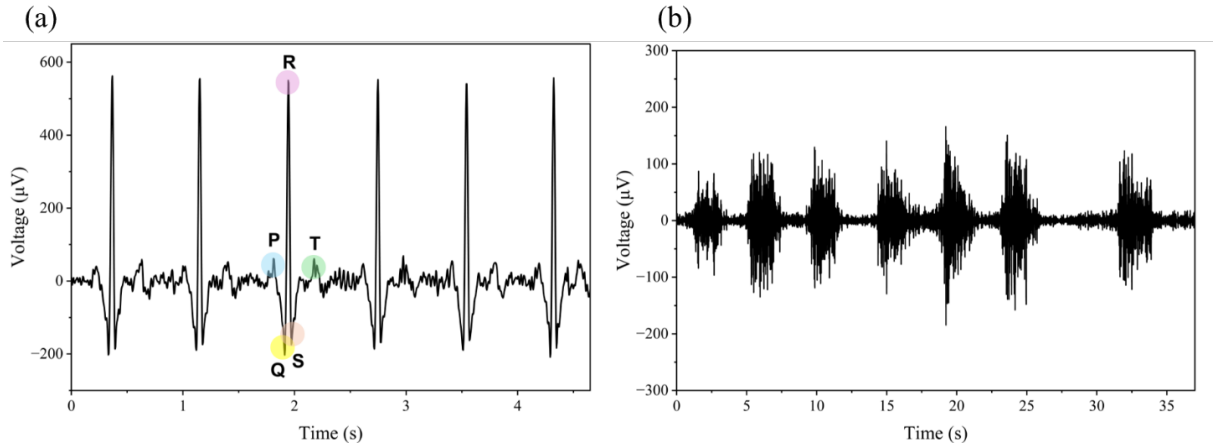

Figure A3 Representative biopotential signals recorded using the foam-based electrode. (a) ECG waveform, showing clearly resolved P, QRS, and T features. (b) EMG signal recorded during muscle activation.

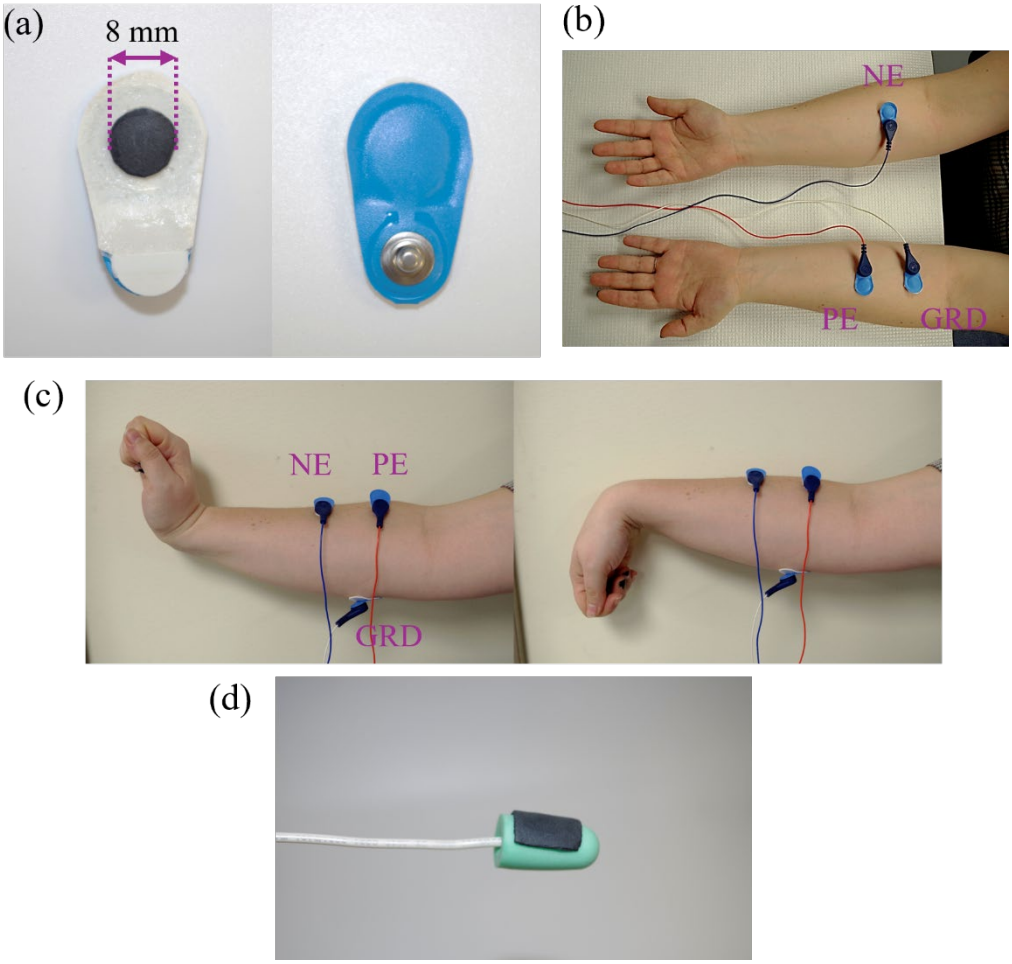

Figure A4 (a) Photograph of the 85% void-fraction conductive foam cut into a disk (8 mm diameter) and integrated into a commercial snap-type electrode. (b) Electrode placement on the forearms for ECG measurements, showing negative electrode (NE), positive electrode (PE), and ground (GRD). (c) Electrode configuration for EMG measurements during forearm muscle activation, with NE, PE, and GRD positions indicated. (d) In-Ear EEG electrode configuration.

EEG Signal Processing:

The raw EEG signal was preprocessed to remove low-frequency drift and high-frequency noise. The data were band-pass filtered between 0.5 and 40 Hz using a fourth-order zero-phase Butterworth filter, retaining the conventional EEG frequency range while attenuating slow baseline fluctuations, motion artifacts, and muscle activity. Time-frequency representations were then obtained using a spectrogram to visualize the temporal evolution of neural activity across frequencies.

For alpha-band analysis, the preprocessed signal was further band-pass filtered between 8 and 12 Hz using a fourth-order zero-phase Butterworth filter to isolate the canonical alpha rhythm associated with relaxed wakefulness. Alpha-band activity was quantified in the time domain by computing the mean squared amplitude of the filtered signal, defined as

$$P_\alpha = \frac{1}{T}\int_0^T x_\alpha^2(t)dt$$

where $x_\alpha(t)$is the alpha-band-filtered EEG signal and $T$is the analysis duration. This metric provides a robust measure of alpha activity and enables direct comparison of state-dependent changes, such as eyes-open versus eyes-closed conditions.

APPENDIX B SUPPORTING INFORMATION OF ARTICLE 3: DOUBLE-NETWORK PEDOT:PSS XEROGEL FIBERS WITH HIGH STRETCHABILITY AND ELECTRICAL STABILITY FOR WEARABLE STRAIN SENSING

Gayaneh Petrossian, Sara Ebrahimi, Floriane Miquet-Westphal, Hang Xu, and Fabio Cicoira *

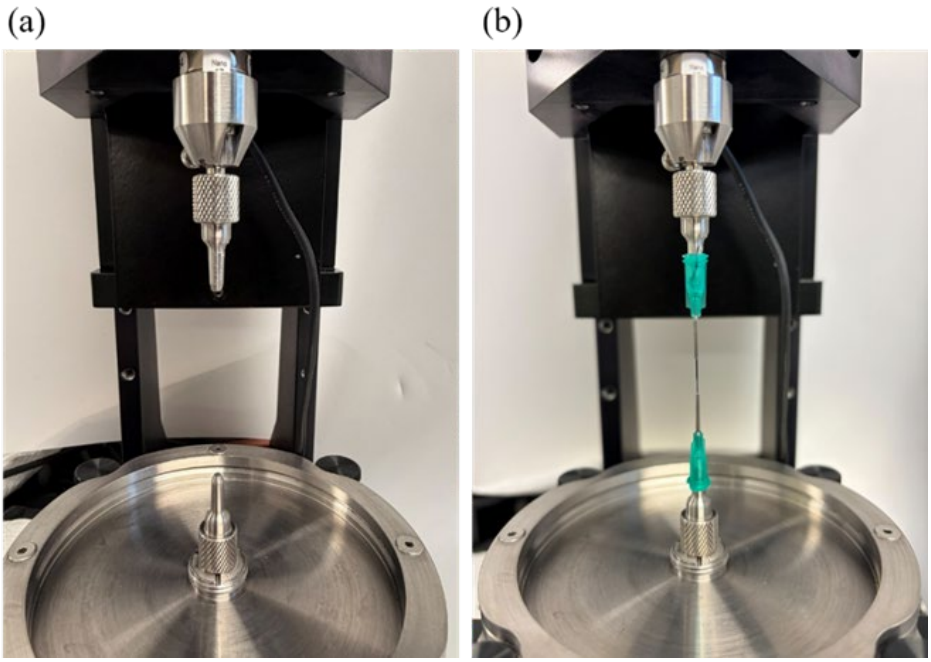

Figure B1 Tensile testing setup for xerogel fibers using a custom double-needle holder assembly on the Mach-1 mechanical tester. (a) Empty opposing tips, and (b) xerogel fiber secured between the needles using cyanoacrylate adhesive prior to tensile loading.

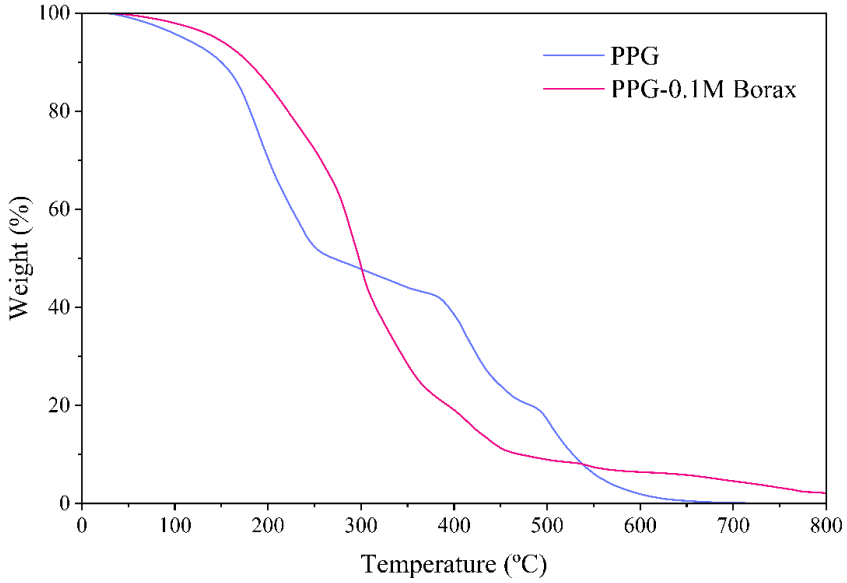

Figure B2 TGA thermograms of PPG and PPG-0.1M borax xerogels.

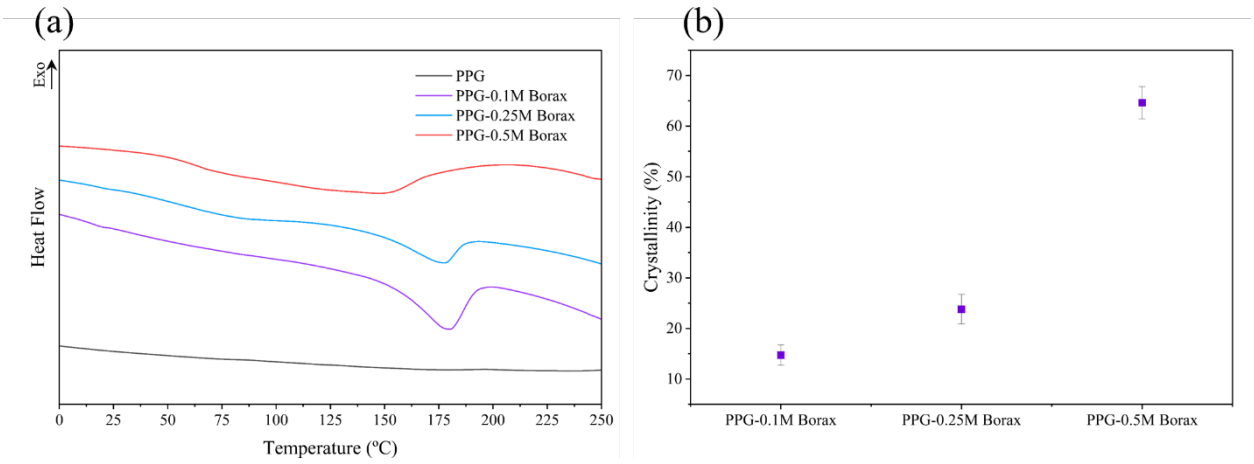

Figure B3 (a) DSC thermograms (second heating) of PPG and borax-treated xerogels. (b) Corresponding crystallinity of the xerogels calculated from the melting enthalpy. Error bars represent standard deviation (n = 3).

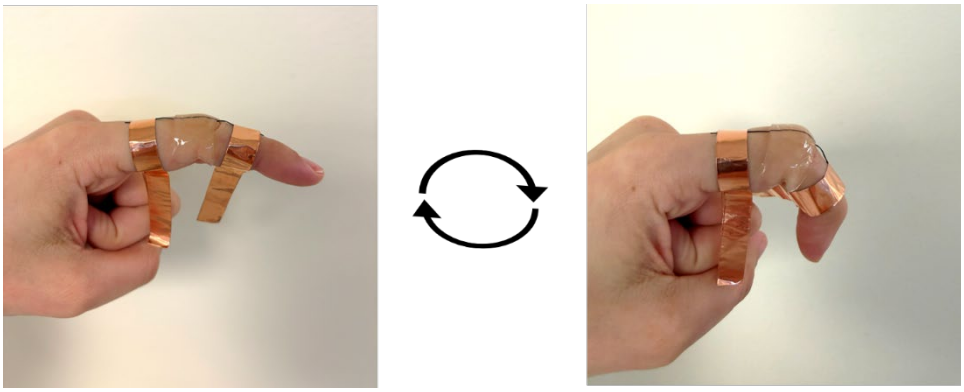

Figure B4 Photographs of the PPG-0.1 M borax xerogel fiber integrated as a wearable strain sensor on a finger in the relaxed (left) and bent (right) states. The resistance of the fiber changes with finger bending, enabling detection of human motion.